THE UNIVERSITY *of* EDINBURGH

Investigating the micromechanics of granular soils subjected to cyclic loading using discrete element method

Joel Keishing

A dissertation submitted in partial fulfilment

for the degree of

Doctor of Philosophy

In the

Institute for Infrastructure and Environment

School of Engineering

The University of Edinburgh

2019

Declaration

This thesis entitled "*Investigating the micromechanics of granular soils subjected to cyclic loading using discrete element method*" is submitted to the University of Edinburgh for the degree of Doctor of Philosophy. I certify that this thesis is the result of my own work under the supervision of Dr. Kevin J Hanley. I have acknowledged all main sources of help and exercised reasonable care to ensure that the work is original and does not breach any law of copyright.

Publication based on this thesis:

1. Keishing, J. & Hanley, K. J. (2019). Improving constant-volume simulations of undrained behaviour in DEM. Submitted to Acta Geotechnica. (Under review)
2. Keishing, J. & Hanley, K. J. (2019). Energy dissipation in soil samples during cyclic triaxial simulations. Submitted to Computers and Geotechnics. (Under review)
3. Keishing, J. & Hanley, K. J. (2019). Investigating cyclic triaxial loading of sand using a Design of Experiments approach. UK-China PTF7 conference. (Presented).
4. Keishing, J. & Hanley, K. J. (2018). Incorporating the effect of pore pressure in undrained DEM simulations. GeoShanghai conference (Presented)
5. Keishing, J. & Hanley, K. J. (2016). Modifying the constant volume method for simulating undrained tests in DEM. GM3, UK. (Presented)

Joel Keishing

13 December 2019

Abstract

The soil experiences millions of load cycle from nature, i.e., earthquake or many geo-engineering structures are subjected to cyclic loading during normal operation, e.g., renewable offshore wind turbines are likely to experience millions of load cycles, with variations in cycle magnitude and frequency, during their service lives. These forces are transmitted to the soil which may cause unacceptable soil displacement and, in extreme cases, it may lead to soil liquefaction. This is a major concern to geotechnical engineers, therefore determination of soil response to cyclic loading has great importance.

This research investigates the undrained behaviour of sand subjected to monotonic and cyclic loading using DEM (Cundall and Strack, 1979). A series of constant-volume undrained simulations of sand subjected to monotonic loading at different initial stress ratio, confining pressure and void ratio were performed to gain the understanding of the monotonic behaviour of sand which is an essential precursor to the cyclic loading tests. One problem arises when shearing dense samples are the generation of unrealistically high stresses.

Four alternatives are hypothesised to address the shortcomings of the constant-volume method are explored, each of which has a physical basis: particle crushing, the presence of highly compressible air within the sample, or the reduction of stiffness due to particle surface asperities or non-spherical particle shapes. In situations where a significant amount of particle crushing occurs, it is important to incorporate this in the simulations so that stresses are not over-estimated. In the absence of particle crushing, the most effective method to achieve more realistic stress–strain responses is to reduce the particle shear modulus substantially. This approach has the added computational benefit of enabling an increase in the simulation time-step.

A Design of Experiments (DOE) approach was adopted to systematically investigate the behaviour of sand subjected to cyclic loading using DEM. Detailed simulations results are presented that related the influence of different parameters such as frequency, mean cyclic load, cyclic amplitude, confining pressure and void ratio on the dynamic properties of granular materials. Based on those DOE analyses, prediction of cyclic responses for randomly selected input parameters are presented. The void ratio was found to have the most significant effect on the shear modulus and

coordination number of the sample. The influence of frequency on cyclic response quantities was found to be insignificant.

In addition, energy terms were computed in a set of undrained cyclic triaxial discrete-element method simulations which form a parametric study of five factors: void ratio, initial mean effective stress, mean deviator stress, deviator stress amplitude and compressive/extensive initial loading. Void ratio is the only one of these factors which significantly affects the relationship between the excess pore water pressure and the unit energy. By increasing the void ratio or decreasing the initial mean effective stress, both the number of complete cycles and the energy dissipated per unit volume up to the onset of liquefaction, respectively denoted as N_l and δW_d, were reduced. Initial stress anisotropy reduces N_l but increases δW_d. Increasing the deviator stress amplitude also reduces N_l but has no significant effect on δW_d. All of these observed trends in N_l and δW_d match data from physical experiments, where available.

The preferred contact orientation for frictional dissipation is between 30° and 40° for these cyclic simulations. There is a greater heterogeneity for extension than for compression, regardless of whether the initial phase of loading is compressive or extensive. Immediately following a shear reversal, the boundary work decreases and there is a period of negligible frictional dissipation which lasts for around 0.04% axial strain.

If an energy-based model is being applied for liquefaction assessment of anisotropic samples, a significant improvement in the accuracy of the model may be achieved by including the mean deviator stress

Lay Summary

Over the past decades, many researchers have tried to understand the behaviour of soils under cyclic loading conditions. The soil adjacent to many engineering structures experiences millions of load cycles during the design life cycle of the structures. This situation can be arrived from nature, i.e., earthquake, wind, and or human activities such as high-speed train motion or the action of wind turbines. These forces are transmitted to the soil which may cause unacceptable soil displacement and, in extreme cases, it may lead to soil failure. Example, the extensive damage caused by a ground failure during the Alaska and Niigata earthquakes of 1964. This is a major concern to geotechnical engineers, therefore determination of soil response to cyclic loading has great importance.

Many researchers had conducted cyclic laboratory tests to studies the behaviour of soil response. These tests capture the macroscopic soil behaviour but give no insight into the governing micro-scale behaviour. Since soil is a complex granular and multi-phase material consisting of solid, liquid and gas, it is important to understand the dynamics governing particle-scale behaviour in order to interpret better the underlying causes of the observed macro-scale response. Numerical techniques, i.e., computer simulation are capable of providing information on particle-scale data, e.g., particle position, interparticle contact force, etc. which are difficult to obtain in physical experiments.

This thesis will address the following. Firstly, preliminary studies of sand behaviour by conducted monotonic loading simulations. Secondly, studies on the effects of cyclic loading on macro-micro behaviour of sand by adopted to systematically investigate approach, i.e., Design of Experiments (DOE). Based on those DOE analyses, prediction of cyclic responses for randomly selected input parameters are presented. The influence of various factors on energy terms under undrained cyclic computer simulations is presented: void ratio, frequency, initial sand strength, cyclic magnitude and compressive/extensive initial loading.

The influence of initial porosity of soil on cyclic response quantities was found to be most insignificant. Greater heterogeneity was found during extension than for compression, regardless of whether the initial phase of loading is compressive or extensive.

Acknowledgements

My foremost and greatest thanks should be given to my principal supervisor Dr Kevin John Hanley, who has been an inexhaustible source of ideas and inspiration for me in the past three and half years. His patience, prudence and enthusiasm for scientific truth have had a great impact on me. I also would like to express my deep gratitude to my second supervisors Dr Stefanos Papanicolopulos and internal reviewer Prof Jin Ooi for their constant encouragement and guidance, the freedom they offered to develop my own ideas is particularly appreciated.

I am in great debt to the University of Edinburgh for provided access to the HPC facility, Eddie and Archer. Without this facility, the project would have been prolonged. I would like to thank Academic Institute of Development for very useful training. A special thank to our IT department for their help and assistance. I also would like to thank our Granular Research Group for their help and encouragement. The list of names will be lengthy if I mention all of them. In particular, I would like to thank Dr JP Morrissey, Dr R Rangaragan, Dr Lige Wang, Dr Tim Najuch, Dr Xizhong Chen and Dr Zeynep Karatza for all their help, feedback and expertise in DEM.

Being enrolled in the PhD program the University of Edinburgh is fantastic as it doubled the number of friends. A special thanks to our following groups: IIE lunch group, football group, badminton group and weekend broad game group at the University of Edinburgh. Without their company the PhD life would have been dull and less joyful.

I am in debt to my parents who always give me the best.

Contents

List of Figures

List of Tables

Notation

a, b, c, d	Constants in energy-based models for liquefaction assessment
b	Intermediate stress ratio
C_c	Coefficient of curvature
C_u	Coefficient of uniformity
c_v	Coefficient of variation (standard deviation divided by the mean)
CV	Constant volume
CSL	Critical state line
CSR	Cyclic stress ratio
d	Local damping ratio
D	Damping ratio
D_{50}	Mean particle diameter
DEM	Discrete element method
e	Void ratio of a sample under constant-volume shearing
$E_f^{\beta-1}$, E_f^{β}	Total frictional dissipation which has occurred at time-steps $\beta - 1$ and β
$E_{f\_j}^{\beta-1}$, $E_{f\_j}^{\beta}$	Energy dissipated at contact j at time-steps $\beta - 1$ and β
E_{kr}, E_{kr}^0, E_{kr}^{β}	Rotational kinetic energy, energy at the start of shearing and at time-step β
E_{kt}, E_{kt}^0, E_{kt}^{β}	Translational kinetic energy, energy at the start of shearing and at time-step β

E_{sn}, E_{sn}^{0}, E_{sn}^{β}	Normal strain energy, energy at the start of shearing and at time-step β
E_{sn_j}	Normal component of strain energy at contact j
$E_{st}^{\beta-1}$, E_{st}^{β}	Tangential strain energy at time-steps $\beta - 1$ and β
$E_{st\_j}^{\beta-1}$, $E_{st\_j}^{\beta}$	Tangential component of strain energy at contact j at time-steps $\beta - 1$ and β
F_n	Normal component of the contact force
F_t	Shear/tangential component of the contact force
$F_{t\_o}^{\beta}$	Tangential force before applying Coulomb slip criterion
G	Particle shear modulus
G_s	Shear modulus of the entire sample
i	Identifier of a single particle in the system
I_i	Moment of inertia of particle i
I_{ss}	Initial stress state
IN	Inertial number
IR	Index of redundancy
ISL	Instability stat line
j	Identifier of a single Hertzian contact in the system
K_c	Anisotropic stress ratio $\sigma'_{z,0}/\sigma'_{x,0}$
K_f	Bulk modulus of pore fluid
k_t	Contact shear tangent stiffness
LAMMPS	Large-scale Atomic/Molecular Massively Parallel Simulator

m_i	Mass of particle i
$\boldsymbol{n}$	Unit branch vector
N	Number identifying any applied load cycle
$\boldsymbol{n}_p^j$	Unit contact normal for contact j
N_c	Number of interparticle contacts in the simulation
N_l	Number of complete load cycles until the onset of liquefaction
N_p	Number of particles in the simulation
p'	Mean effective stress
P_a	Absolute fluid pressure
p'_0	Initial mean effective stress after sample preparation
PB	Periodic boundary
PSD	Particle size distribution
PT	Phase transformation state
q	Deviator stress
q_{cyc}	Deviator stress amplitude
q_{mean}	Mean deviator stress
r_a, r_b	Sphere radii
r_g	$\sqrt{\frac{r_a r_b}{r_a + r_b}}$
r_i	Radius of particle i
S_r	Degree of saturation of the sample
t	Simulation time

T	Cycle period
V^p	Volume of particle p
$V_{particle}$	Total volume of the particles
V_{total}	Total bulk sample volume
V^β	Sample volume at time-step β
v_i	Translational speed of particle i
$W^{\beta-1}$, W^β	Total boundary work input between time-steps 0 and $\beta - 1$ or β
x, y, z	Reference Cartesian axes
α_n	Overlap between particles
β	Identifier of one time-step during shearing
$\delta E_{f\_j}^{\beta}$	Friction dissipated at contact j during time-step β
$\delta E_{st\_j}^{\beta}$	Increment of tangential component of strain energy at contact j during time-step β
δW	Increment of boundary work per unit volume
δW_d	Unit energy (energy dissipated per unit volume) up to the onset of liquefaction
$\delta \boldsymbol{\alpha}_t$	Increment of relative tangential displacement
$\delta\varepsilon_x$, $\delta\varepsilon_y$, $\delta\varepsilon_z$	Incremental normal strains
ΔE	Error term in the energy balance
Δu	Excess pore water pressure
u_r	Excess pore water pressure ratio
μ	Interparticle friction coefficient

μ_c	Interparticle friction coefficient during sample preparation
μ_s	Interparticle friction coefficient during shearing
υ	Particle Poisson's ratio
σ_{ij}	Average stress tensor
σ'_x, σ'_y, σ'_z	Effective normal stresses for the sample
σ'_1	Major principal effective normal stresses for the sample
σ'_2, σ'_3	Minor principal effective normal stresses for the sample
$\sigma'_{x,0}$	Minor principal effective normal stress (confining pressure, CP) after sample preparation
$\sigma'_{z,0}$	Major principal effective normal stress after sample preparation
Φ_{pq}	Second-order fabric tensor
ω_i	Rotational speed of particle i
Z	Coordination number
Z_m	Mechanical coordination number

Chapter 1 Introduction

1.1 Background and research objectives

Soil is a complex multi-phase, granular material consisting of solid, liquid and gas. The soil adjacent to many engineering structures experiences millions of load cycles during the design life cycle of the structures. This loading may be due to environmental factors such as seismic activity or storms, or human activities such as high-speed train motion or the action of wind turbines. These forces are transmitted to the soil which can cause unacceptable soil displacement and, in extreme cases, it may lead to soil liquefaction, e.g., the Alaska and Niigata earthquakes of 1964, the Loma Prieta earthquake of 1988, the Great Hanshin earthquake of 1995 which caused extensive damage. Fig. 1.1 presents characteristic numbers of cycles and cycle periods for various cyclic loading events, for example ranging from cycles with durations of hours for offshore tidal variations to several seconds for earthquakes. The shaded zone in Fig. 1.1 shows the space in which design documentation is available for cyclic loading. This figure also indicates the area where further research is needed (Andersen *et al*., 2013). Cyclic loading, irrespective of its origin, is a major concern to geotechnical engineers as they need to ensure safe, efficient engineering designs. Therefore, predicting the response of soil under the action of cyclic loading is of great importance.

Cyclic triaxial tests have been studied extensively in the context of seismic liquefaction resistance by many researchers including Seed and Idriss (1971); Ishihara *et al*. (1975) and Wichtmann *et al*. (2010). In recent years, with the expansion of the renewable offshore industry, understanding the soil around coastal structures such as wind turbines, breakwaters, foundations, slopes and embankments subjected to cyclic loads due to wind, waves, etc. has become increasingly essential to ensure efficient and safe structures (Lehane *et al*., 1993; Jardine and Standing, 2000; Tsuha *et al*., 2012). Comprehensive experiments at full scale, model scale and laboratory scale on dense marine Dunkerque sands were reported by Jardine and Standing (2000); Tsuha *et al*. (2012) and Aghakouchak (2015), respectively. Tests such as these capture the macroscopic soil behaviour but give no insight into the governing micro-scale behaviour. It is important to understand the dynamics governing micro-scale behaviour to be able to interpret the underlying causes of the observed macro-scale response. Numerical techniques are capable of providing this information on the dynamic changes occurring at the micro-scale.

Soil can fail under drained or undrained conditions depending on rate of loading, drainage length and coefficient of consolidation, i.e., rate at which the soil consolidation process proceed. Drained tests are conducted to investigate the soil behaviour when the fluids present in the soil are allowed to freely drain out when subjected to load. Undrained tests are conducted to study the behaviour of soil when the contained pore fluid does not have sufficient time to escape when subjected to loading, e.g., during an earthquake. To understand the behaviour of soil both drained and undrained behaviour should be checked. Due to time and resource constraints, the undrained behaviour of sand subjected to monotonic and cyclic loading will be investigated in this research.

This research has three objectives that will be met through the use of numerical simulations:

1. To validate a common assumption – that fully saturated soils can be simulated effectively by maintaining the sample's volume constant throughout a simulation.
2. To determine the influence of void ratio, frequency, mean deviator stress, deviator stress amplitude and confining pressure on sand behaviour under undrained cyclic triaxial conditions.
3. To understand the role of energy during undrained cyclic loading of a sand.

Discrete element method (DEM) simulations were chosen as the most suitable tool to achieve these objectives. Previous studies have shown that DEM captures many of the unique mechanical characteristics of soils and other granular materials (Cundall, 2001; Iwashita and Oda, 1998; O'Sullivan and Cui, 2009; Thornton, 2000). DEM provides particle-scale information, e.g., particle positions and interparticle contact forces, at each instant during a simulation. These data, which are difficult or even impossible to obtain in physical experiments, allow researchers to understand the evolution of the microstructure and the force transmission mechanism within a granular assembly.

1.2 Scope of the research

This research is restricted to the quasi-static behaviour of granular materials. All simulations were conducted with idealised perfectly spherical particles although, in a subset of simulations, the influence of particle shape is partially considered by

applying rolling and twisting resistances at the contacts between spherical particles. The particle size distribution used in this study does not correspond to a real sand. Because of this and the spherical shape, the aim is to achieve qualitative, rather than quantitative, agreement with physical experiments. All simulations are carried out using 3D periodic boundary conditions to eliminate boundary effects (Thornton, 2000). Therefore, there is no focus on soil–structure interaction in this thesis.

1.3 Organisation of the thesis

This thesis is organised into seven chapters.

Chapter 1: Introduction

This chapter gives an overview of the problem under investigation, the objectives and scope of this research and the overall layout of the work.

Chapter 2: Literature review

This chapter focuses on the numerical modelling of geotechnical triaxial tests using DEM. The servo-control schemes implemented in the open-source LAMMPS code for different geotechnical triaxial test conditions with periodic boundary conditions are presented. Macro- and micro-scale parameters are explained. Finally, prior research is discussed in which laboratory tests or DEM simulations have been used to explore the behaviour of sands under monotonic and cyclic loading.

Chapter 3: Undrained monotonic triaxial DEM simulations

This chapter presents results from a series of constant-volume undrained triaxial monotonic simulations. These were performed to gain an understanding of the monotonic behaviour of sand which is an essential precursor to the cyclic loading tests.

Chapter 4: Improving constant-volume simulations of undrained behaviour in DEM

Conventional constant-volume simulations are not able to quantitatively capture a real soil's undrained behaviour, particularly for dense samples. Several alternatives to the constant volume method were proposed to potentially mitigate these problems. These were explored through implementation in the open-source LAMMPS code.

Chapter 5: Evaluating the cyclic triaxial response of sand using Design of Experiments

A key challenge in DEM analyses is the computational expense: studying the influence of many different parameters such as the number of cycles, frequency, mean deviator stress, deviator stress amplitude, confining pressure and void ratio on the dynamic properties of granular materials could potentially be very costly. A Design of Experiments (DOE) approach was adopted to systematically investigate the behaviour of sand subjected to cyclic loading using DEM, and DOE analysis was used to predict the cyclic responses for randomly selected input parameters.

Chapter 6: Energy dissipation in soil samples during cyclic triaxial simulations

Energy terms were computed in a set of undrained cyclic triaxial DEM simulations which form a parametric study of five factors: void ratio, initial mean effective stress, mean deviator stress, deviator stress amplitude and compressive/extensive initial loading.

Chapter 7: Conclusion, remarks and recommendations

This chapter gives the conclusions of this research, final remarks and offers suggestions for future work.

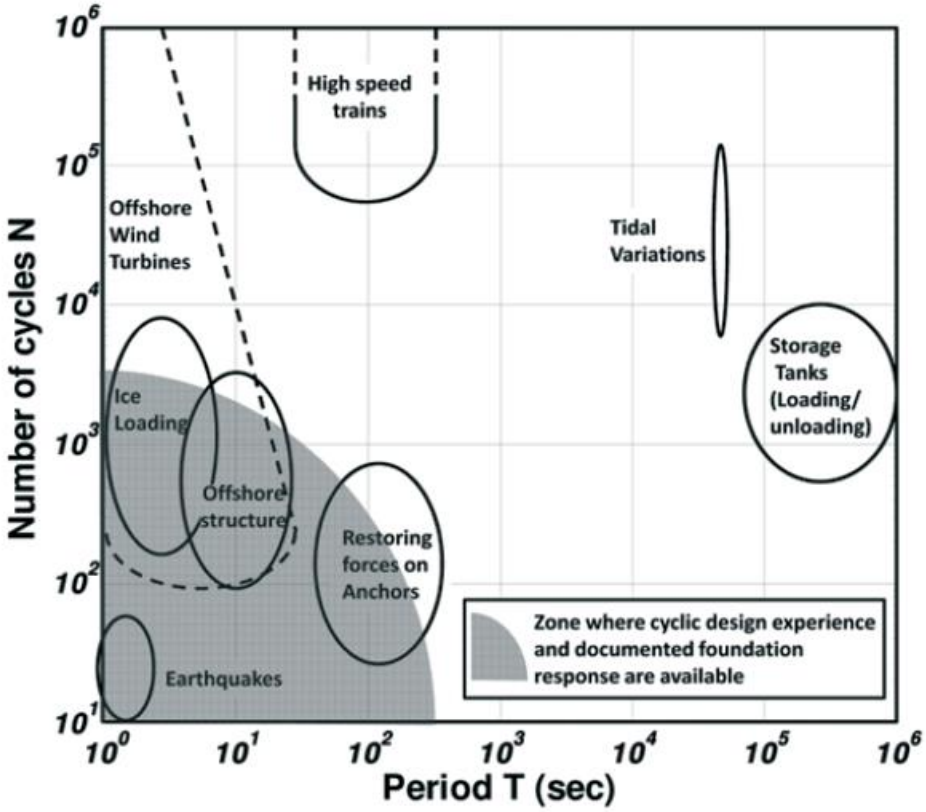

Figure 1.1: Characteristic numbers of cycles and cycle periods for common cyclic loading events (Andersen et al., 2013)

Chapter 2 Literature review

Firstly, this chapter presents a brief overview of the Discrete Element Method and the parameters that are most commonly used to quantify the behaviour of discrete granular systems. Secondly, a brief discussion of existing approaches for simulating triaxial loading conditions in DEM is presented. Finally, the fundamental behaviour of undrained sand samples subjected to monotonic and cyclic loads is described: a more detailed discussion of this subject is given in Chapters 3 and 5.

2.1 Discrete element method

The Discrete Element Method (DEM) (Cundall and Strack, 1979) simulates the mechanical behaviour of granular materials by monitoring the interaction and contact between the discrete particles. Fig. 2.1a shows the exponential increase in the number of DEM-related publications since its original formulation (O'Sullivan, 2014). Fig. 2.1b shows papers published only in the field of geomechanics indicates that DEM is widely accepted and used to study the behaviour of granular materials

DEM is an explicit numerical method in which the interactions and contacts between the discrete particles are monitored. The motion of a particle due to contact is calculated from integration of Newton's second law. Contact forces are calculated from interparticle overlaps. A simplified Hertz-Mindlin contact model (Itasca Consulting Group, 2007; Huang, 2014) combines the normal force calculated with Hertzian theory and tangential force calculated incrementally with no-slip Mindlin theory. For two overlapping elastic spheres with radii r_a and r_b, the normal component of the contact force, F_n, is given by:

$$F_n = \frac{4}{3}\frac{G}{1-\vartheta}\, r_g^{1/2}\delta_n^{3/2}\,\boldsymbol{n} \tag{2.1}$$

G is the shear modulus of both particles, ϑ is the Poisson ratio of the particles, $r_g = \frac{R_i R_j}{R_i + R_j}$ is the equivalent radius, δ_n is the interparticle overlap and $\boldsymbol{n}$ is the unit vector along the line joining the sphere centres. The tangential component of the contact force, F_t, is calculated incrementally as

$$F_t^{\beta} = F_t^{\beta-1} - k_t \Delta s \tag{2.2}$$

$$k_t = \frac{4G}{2-\vartheta}\, r_g^{1/2} \delta_n^{1/2} \tag{2.3}$$

$\beta - 1$ and β represent consecutive time-steps, k_t is the contact shear tangent stiffness and Δs is the increment of relative tangential displacement during time-step, β. A slip criterion is imposed to limit the shear force:

$$|F_t^{\beta}| \leq \mu |F_n| \tag{2.4}$$

In the real granular material contact situation, the energy is dissipated by different mechanisms such as interparticle friction and plastic deformation at the contacts (Barreto, 2009). Local damping is used to dissipate kinetic energy to reach quasi-static equilibrium.

$$|F_d| = d|F_u| sign(V) \tag{2.5}$$

F_d is a damping force/moment, F_u is the unbalanced force/moment applied to particles, V is the particles velocity and d is the local damping ratio. To understand the need for local damping, consider a free-falling ball bouncing on a horizontal wall. In the presence of local damping, the amplitude of the ball gradually decreases and eventually the ball becomes stationary. The simplified Hertz-Mindlin contact model was implemented by Dr Kevin Hanley (Huang, 2014) in the open-source LAMMPS code; this contact model was used to simulate all the monotonic and cyclic loading simulations in this thesis.

2.2 Macro and micro quantities in DEM simulations

The typical output of the DEM simulations consists of interparticle forces, particle positions and velocities, etc. However, to make use of this information in engineering situations, the output must be used to compute more typical macro-scale engineering quantities such as bulk stresses and strains (Section 2.2.1). Additional micro-scale quantities can also be computed from this output as described in Section 2.2.2

2.2.1 Macro-scale quantities

The void ratio, e, of a granular packing is the ratio of void volume (V_v) to the total volume of particles (V_p) in the sample:

$$e = \frac{V_v}{V_p} \tag{2.6}$$

The overlap is not considered while calculating the total volume of particles. The average stress tensor of a sample ensemble is calculated by (Potyondy & Cundall, 2004):

$$\sigma_{ij} = \frac{1}{V_{total}} \sum_{p=1}^{N_p} \sigma_{ij}^{p} V^{p} \tag{2.7}$$

V_{total} is the total volume of the sample, V^p is the volume of particle p and N_p is the number of particles in the sample. σ_{ij}^{p} is the average stress tensor for particle p, given by

$$\sigma_{ij}^{p} = -\frac{1}{V^p} \sum_{k=1}^{N_{k,p}} |x^k - x^p| \, \boldsymbol{n}^{k,p} F^k \tag{2.8}$$

x^k is the position of the contact point, x^p is the position of particle p's centroid, $\boldsymbol{n}^{k,p}$ is the unit-normal vector from the particle centroid to the contact location and F^k is the force acting at contact k. $N_{k,p}$ is the total number of contacts involving particle p. By considering porosity, n, the total volume of the sample is given as:

$$V_{total} = \frac{\sum_{p=1}^{N_p} V^p}{1 - n} \tag{2.9}$$

Substitute Eq. 2.8 and 2.9 into Eq. 2.7 to obtain the average stress tensor of a sample ensemble:

$$\sigma_{ij} = -\left(\frac{1 - n}{\sum_{p=1}^{N_p} V^p} \right) \sum_{p=1}^{N_p} \sum_{k=1}^{N_{k,p}} |x^k - x^p| \, \boldsymbol{n}^{k,p} F^k \tag{2.10}$$

The effective continuum normal and shear stresses, σ'_{xx}, σ'_{yy}, σ'_{zz} and τ'_{xx}, τ'_{yy}, τ'_{zz} respectively, of the sample are calculated using Eq. 2.10 (Potyondy and Cundall, 2004) where x, y and z represent the conventional Cartesian axes. The normal strains, ε_{xx}, ε_{yy}, ε_{zz}, are determined from the movements of the periodic boundaries (detail in section 3.2.1). The plane where there are no shear stresses is known as the

principal plane. The stresses acting on this plane are called the principal effective stresses. Typically the major principal effective stress is denoted as σ_1' and the minor principal effective stress is denoted as σ_3'. In 3D, the intermediate principal effective stress is denoted as σ_2'. In this study, σ_{xx}', σ_{yy}', σ_{zz}' are the principal effective stresses for all simulations due to the simulation setup, i.e., $\sigma_{xx}' = \sigma_3'$; $\sigma_{yy}' = \sigma_2'$; $\sigma_{zz}' = \sigma_1'$. For 3-dimensional triaxial simulations with uniform volume change in the radial direction, i.e., $\sigma_{xx}' = \sigma_{yy}'$, the mean effective stress, p' and deviator stress, q can be expressed in terms of principal effective stresses.

$$p' = \frac{\sigma_1' + 2\sigma_3'}{3} \tag{2.5}$$

$$q = \sigma_1' - \sigma_3' \tag{2.6}$$

The shear strain of the sample can be expressed in terms of principal effective strains.

$$\varepsilon_q = \frac{2}{3}(\varepsilon_1' - \varepsilon_3') \tag{2.7}$$

ε_1' and ε_3' are the major and minor principal effective strains, respectively.

The Mohr–Coulomb linear failure envelope (Taylor, 1948; Newland and Allely, 1957) is often used to describe the shear strength of sand. This envelope gives the relationship between shear strength at failure (τ_f) and the effective normal stress on the failure plane (σ_f') as

$$\tau_f = \sigma_f' tan\varphi' \tag{2.8}$$

$\varphi'$is the angle of shearing resistance. It is also known as the friction angle.

For triaxial stress conditions, Eq. 2.13 can be expressed as

$$\sigma_{1f}' = \sigma_{3f}' \left(\frac{1 + sin\varphi'}{1 - sin\varphi'}\right) \tag{2.9}$$

σ_{1f}' and σ_{3f}' are the major and minor effective principal stresses at the point of failure, respectively. The critical state soil mechanics (CSSM) framework, proposed by Roscoe *et al*. (1958) and documented by Schofield and Wroth (1968) is often used to

describe the critical state behavior of sand. Example, this framework relates the deviator stress q and mean effective stress p' at the critical state as

$$q = Mp' \tag{2.10}$$

M is a critical state parameter. For a triaxial stress state with $\sigma'_{xx} = \sigma'_{yy}$, Eq. 2.15 can also be expressed as Eq. 2.16:

$$\sigma'_1 = \sigma'_3 \left(\frac{3 + 2M}{3 - M}\right) \tag{2.11}$$

Morh-Coulomb is mainly used for drained conditions. For saturated soils (undrained), CSSM is the most popular model to study the behaviour of soils. Therefore, CSSM will be used in this research for analysis of soil behaviour.

2.2.2 Micro-scale quantities

The coordination number, Z is a scalar measure of fabric, i.e., internal topology, within a granular system, computed as

$$Z = \frac{2N_c}{N_p} \tag{2.12}$$

N_c is the number of interparticle contacts in the sample. The mechanical coordination number, Z_m, is computed similarly to Z, except those particles with zero or one interparticle contact are excluded from the calculation (Thornton, 2000).

$$Z_m = \frac{2N_c - N_1}{N_p - N_1 - N_0} \tag{2.13}$$

N_1 and N_0 are the numbers of particles with one or zero contacts, respectively. The critical coordination number, Z_c is 4 which indicates the number of contacts necessary to ensure stability. If $Z_m \geq Z_c$ then the system is stable.

The index of redundancy, IR, was proposed by Kruyt and Rothenburg (2009) to define the mechanical redundancy in a discrete system. It is defined as the ratio between the total number of governing constraints and the total number of degrees of freedom at the contacts. In a 3D system, IR is given by:

$$IR = \frac{N_c}{N_p}\left(\frac{3-2f_s}{6}\right) = Z\left(\frac{3-2f_s}{12}\right) \tag{2.14}$$

where f_s is the sliding fraction. If $IR \geq 1$, the system is mechanically stable; otherwise, the system is mechanically unstable (Kruyt and Rothenburg, 2009; Gong, 2008).

The second-order fabric tensor, φ_{pq}, was proposed by Satake (1982) to quantify the fabric anisotropy of granular assemblies.

$$\varphi_{pq} = \sum_{j=1}^{N_c} \boldsymbol{n}_p^j \boldsymbol{n}_q^j \tag{2.15}$$

$\boldsymbol{n}_p^j$ is the unit contact normal for contact j. The difference between the maximum and minimum eigenvalues of the second-order fabric tensor is defined as the deviatoric fabric, φ_d.

$$\varphi_d = \varphi_1 - \varphi_3 \tag{2.16}$$

$\varphi_1$and φ_3 are the maximum and minimum eigenvalues of the φ_{pq} tensor. This quantity allows us to understand the anisotropy that arises in the sample during shearing. The deviatoric fabric for a perfectly isotropic sample is zero.

2.3 Behaviour of sand under monotonic loading

2.3.1 Behaviour of sand under monotonic drained triaxial testing

Fig. 2.2 shows the typical drained test response for a loose sample A and a dense sample B subjected to monotonic loading. When a dense sample is sheared, initially it contracts, then very quickly begins to dilate. Conversely, if the sample is loose, it contracts upon shearing. After shearing to a relatively large strain, both dense and loose samples reach the same void ratio. At this so-called critical state (CS), the samples deform at constant stress and constant volume. Casagrande (1940) conducted drained tests at different confining pressures and found that the critical void ratio is uniquely related to the confining pressure. The locus of points drawn in critical state $e - p'$ space is termed the critical state line (CSL). The critical state line and specimen initial state in void ratio vs confining pressure space is usually referred as a state diagram. This diagram is used for identifying tendencies of volume change, i.e., contraction or dilation, during drained shearing.

2.3.2 Behaviour of sand under monotonic undrained triaxial testing

When the same initial samples are sheared under undrained conditions, the dense sample exhibits a negative pore water pressure while the loose sample exhibits a positive pore water pressure as observed by Casagrande (1940). Fig. 2.3 shows the typical undrained test response for loose sample A, medium-dense sample B and dense sample C subjected to monotonic loading. The loose sample A shows strain-softening behaviour and reaches a maximum deviator stress at a very small strain. This is followed by a large drop of deviator stress until it reaches a minimum value at a relatively small strain and thereafter remains constant. This type of behaviour is known as flow liquefaction. The pore pressure initially increases and continues to grow at a decreasing rate during the strain-softening stage until it reaches a stable constant value which is approximately equal to the initial confining pressure. The medium-dense sample B also shows strain softening: an initial peak value followed by a gradual reduction in deviator stress. However, upon reaching a minimum deviator stress, the sample begins to regain deviator stress when further strained and thereafter remains constant. The pore pressure increases at the beginning of the test until it reaches a peak value, followed by a gradual decrease as the sample begins to regain strength. After the maximum value of pore pressure has been reached, the specimen attempts to dilate, generating a reduction in the pore pressure. The minimum deviator stress is termed the phase transformation point, PTP, which coincides with the transition from contractive to dilative behaviour (Ishihara *et al*., 1975). This has been observed frequently by researchers such as Casto (1975); Mohamad and Dobry (1986); Been et al. (1991). The state corresponding to the stress and void ratio condition at the phase transformation point has been termed the quasi-steady state (QSS) by Alarcon and Leonards (1988). The dense sample C shows a strain-hardening response: as soon as the loading is applied, the deviator stress increases more sharply compared to tests A and B and thereafter remains constant. The pore water pressure exhibits an initial peak value followed by reduction in pore pressure as further straining is applied (Been and Jefferies, 1985; Ishihara *et al*., 1975; Mohamad and Dobry, 1986; Vaid and Chern, 1985). This continued deformation at constant stress has been termed steady state (SS) in undrained tests. The locus of points drawn in steady state $e - p'$ space is termed the steady state line (SSL).

Fig. 2.3 shows the typical loci of points and steady state line (SSL) drawn from these points in $e - p'$ space (Casagrande, 1940). According to Castro (1975) the state of stress at the steady state should be determined solely by the initial void ratio. This distance between initial void ratio and void ratio at the steady state was defined as the state parameter, ψ, by Been and Jefferies (1985):

$$\psi = e_{\mathrm{i}} - e_{ss} \tag{2.22}$$

e_{i} is the initial void ratio of a sample and e_{ss} is the void ratio at the steady state line.

From experiments conducted on Toyoura sand, both drained and undrained tests yield the same critical state line (Verdugo and Ishihara, 1996). However, there is experimental evidence that suggests that the CSL and the SSL may not be the same (Alarcon-Guzman, 1986; Yamamuro and Lade, 1998). This evidence suggests that the SSL is slightly below and roughly parallel to the CSL obtained from drained tests. However, more recently, many researchers such as Huang (2014), Keishing and Hanley (2019) have conducted simulations to show that drained and undrained tests yield the same critical state line, i.e., CSL = SSL. For consistency, CSL will be used to define critical state in this study for both drained and undrained situations.

Critical state, CS, is the particular state at which straining continues without a change in q, p'or e. The key relationships underpinning the critical state soil mechanics (CSSM) framework (Schofield and Worth, 1968) is given by $q = Mp'$. Where M is a critical state parameter that depends on the frictional coefficient between particles and particle shape (Huang *et al*., 2014a), the extent of particle crushing (Hanley *et al*., 2015) and other factors, and is specific to a sand. The sand is state-dependent, i.e., knowing the state parameter or how far the sand is from the CSL in $e - log(p')$ space can effectively describe strength and dilation behaviour of a sand (Been and Jefferies, 1985). Researchers (Been and Jefferies, 1985; Ishihara, 1993) have conducted experimental studies to investigate the dependency between the locus of the CSL in $e - log(p')$ space, the initial state and the loading conditions. Been *et al*. (1991) conducted triaxial tests on Erksak sand and showed that the CSL in $e - log(p')$ space is unique and independent of the initial states and the loading conditions as shown in Fig. 2.4a. Similarly, the uniqueness concept of CSL in $e - \log(p')$ space was reported by Murthy *et al*. (2007) and Yang and Wei (2012). The experimental report indicates that the initial anisotropy has no effect at large strain levels, resulting in a unique CSL (Been *et al*., 1991; Carrera *et al*., 2011; Ishihara, 1993) (See Fig. 2.4b, Fig. 2.5b and

Fig. 2.5a). They have confirmed that the CSL is unique and is independent of the initial states and loading conditions as shown in Fig. 2.6. The effect of anisotropy, quantified using the intermediate stress ratio, $b = \frac{\sigma_2' - \sigma_3'}{\sigma_1' - \sigma_3'}$, has been investigated by many researchers (Thornton, 2000; Thornton and Zhang, 2010; Barreto and O'Sullivan, 2012; Zhao and Guo, 2013; Huang *et al*., 2014b). They have shown that DEM can replicate the failure envelope proposed by Lade and Duncan (1975) for real sands. Huang *et al*. (2014b) revealed that there is a small dependence on b based on DEM simulations.

As discussed previously, void ratio and initial state influence the undrained behaviour of granular materials. However, many other factors also influence the undrained behaviour of granular materials such as initial anisotropy (Yimsiri and Soga, 2002), intermediate principal stress (Huang *et al*., 2014b; Uthayakumar and Vaid, 1998; Yoshimine *et al*., 1998; Oda, 1972), stress or strain paths (Yamada and Ishihara, 1983; Yoshimine *et al*., 1998; Vaid and Sivathayalan, 2000), degree of saturation (Lade and Pradel, 1990; Xia and Hu, 1991), fines content (Lade and Yamamuro, 1997; Yamamuro and Lade, 1998), particle shape (Vaid and Chern, 1985), boundary conditions (Finno *et al*., 1996; Yoshimine and Ishihara, 1998) and particle crushing (Hanley *et al*., 2015). The effects of some parameters on the undrained behaviour of granular materials subjected to monotonic loading are given in Table 2.1.

Table 2.1: Summary of factors affecting the monotonic response of granular materials under undrained conditions

Factors	Sand behaviour	References
Orientation of major principal stress, ∅	Stress–strain responses are affected, angle of shearing resistance decreases with increase in angle of principal stress (Fig. 2.7)	Oda (1972); Yoshimine *et al*. (1998); Uthayakumar and Vaid (1998)
Factors	Sand behaviour	References
Higher confining pressure	Higher stress value, however yields unique CSL.	Castro (1969)

Initial anisotropy	Stiffer than the isotropic sample during initial strain assuming the same void ratio, confining pressure and loading conditions, i.e., compression or extension. However, both yield the same, unique CSL.	Been *et al*. (1991); Ishihara, (1993); Yimsiri and Soga (2002); Murthy *et al*. (2007); Carrera *et al*. (2011);
Degree of saturation	Unstable behaviour at higher saturation degrees.	Lade and Pradel (1990)
Intermediate principal stress ratio, $b = \frac{\sigma'_y - \sigma'_x}{\sigma'_z - \sigma'_x}$	Has significantly different stress-strain responses. Angle of shearing resistance increases with increase in intermediate principal stress ratio (Fig. 2.8)	Oda (1972); Lade and Duncan (1973); Yoshimine *et al*. (1998); Uthayakumar and Vaid (1998); Barreto and O'Sullivan (2012); Huang *et al*. (2014b)
Strain rate	Significant effect in steepening the effective stress paths (Fig. 2.9). However, in the quasi static range (defined by inertial number), response is independent of strain rate.	Yamamuro and Lade (1998) Perez *et al*. (2016)

2.4 Behaviour of sand under cyclic undrained triaxial testing

When soil is loaded under undrained conditions, excess pore pressure is generated. The amount and nature of the pore pressure change depend on:

- the initial stress state of the soil
- the magnitude and number of load cycles applied
- the soil characteristics: grain size distribution, void ratio, degree of saturation, etc.

This excess pore pressure controls important soil responses such as liquefaction. Liquefaction has been defined as the complete loss of soil strength and stiffness by Castro (1969), as zero effective stress due to the cyclic loading by Seed and Idriss (1971), as the magnitude of cyclic stress ratio that is required to produce large deformation by Ishihara *et al*. (1975) or as the attainment of 5% axial strain in double amplitude or attainment of 5% peak axial strain in single amplitude by Mulilis *et al*. (1977) and Sze et.al (2013). Robertson *et al*. (1995) suggest the evaluation of liquefaction of soil under undrained shear. Flow liquefaction can occur during either monotonic or cyclic loading for a loose sand with soft hardening behaviour. Sand with strain hardening behaviour may cause cyclic liquefaction and cyclic mobility due to strain accumulation. Hyodo *et al*. (1994) made an attempt to correlate the undrained cyclic response to monotonic behaviour by conducting monotonic and cyclic undrained tests on Toyoura sand to study the cyclic failure behaviour. The resulting effective stress path is shown in Fig. 2.10 suggesting that flow deformation starts when the effective stress path intersects the phase transformation line (PTL) which lies between the critical state line (CSL) and instability line (ISL). The ISL is obtained by connecting the maximum deviator stress and the origin in $q - p'$ space under monotonic loading. This ISL is also known as the flow liquefaction lines, FLL (Lade, 1993). Huang *et al*. (2018) explored the link between the monotonic and cyclic undrained behaviour of sands using DEM and showed that DEM can capture the flow deformation of sands under both monotonic and cyclic undrained shearing. This flow deformation lies between the CSL and ISL, in a similar manner to experimental observations (Hyodo *et al*., 1994). Similarly, flow-type liquefaction was observed for a loose sample and cyclic mobility was observed for a dense sample. A brief review of the factors affecting the cyclic response of granular materials under undrained condition is shown in Table 2.2. More detailed discussion of these factors affecting cyclic response is presented in Chapter 5.

Table 2.2: Summary of factors affecting the cyclic response of granular materials under undrained conditions

Factors	Sand behaviour	References
Introduction of initial anisotropy	Reduces excess pore pressure generation. Contradictory: brings the initial effective stress states closer to the failure envelope	Seed *et al*. (1983) Konrad (1993)
Higher cyclic amplitude	Higher effective stress degradation rates	Dobry *et al*. (1982); Sitharam and Vinod (2010)
Frequency	No effect on the stress-strain response Contradictory: effect on the strain accumulation rate at higher loading frequency	Airey and Fahey (1991) Salvati and Anhdan (2008)
Confining pressure	Significant influence on the shear modulus of the sample.	Sitharam and Vinod (2010); Ishibashi and Zhang (1993)

Experimental tests have some inherent difficulties such as accuracy of measurements and reproducibility of initial sample preparation. These can be overcome by employing numerical methods such as DEM. Such methods can create an idealised virtual experimental environment with precise control of loading conditions and simulation parameters, and perfect reproducibility of a simulation. Maeda *et al*. (2010); Gu *et al*. (2014); Guo and Zhao (2013); Ng (2009); Sitharam and Vinod (2009); Yan and Dong (2011); Huang (2014), among others, carried out DEM simulations to investigate the CS behaviour of granular materials. Similarly, discrete element method (DEM) simulations were chosen as the most suitable tool to achieve the research objectives defined for this study.

2.5 Summary

This chapter offers a brief review on the numerical modelling of geotechnical triaxial tests using DEM. Macro- and micro-mechanics concepts frequently used in granular materials are presented. The later part of this chapter presents a brief literature review on laboratory tests and DEM simulation of the behaviour of sands under monotonic and cyclic loading. The effects of some parameters on the undrained behaviour of granular materials subjected to monotonic loading are reviewed in Table 2.2.

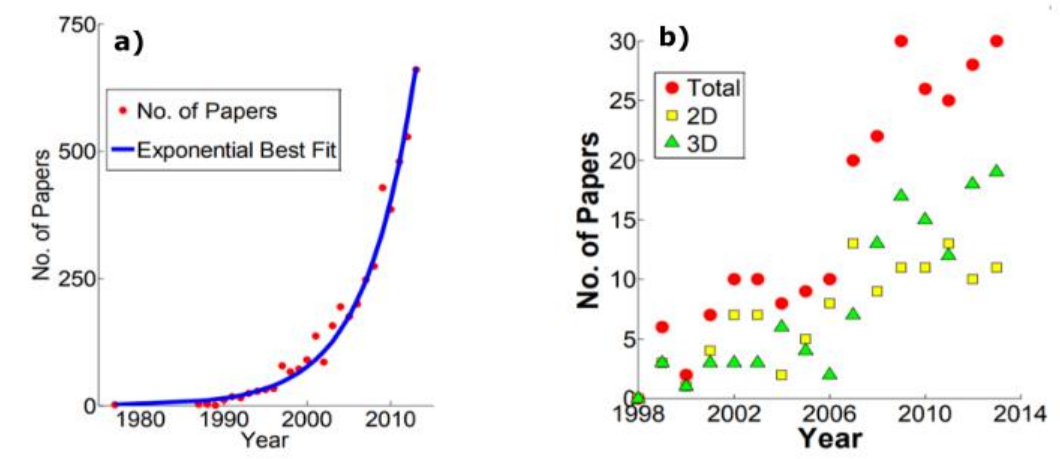

Figure 2.1: The growth in the number of publications using DEM (O'Sullivan, 2014): (a) all disciplines (b) geomechanics-related (data collected from 9 journals)

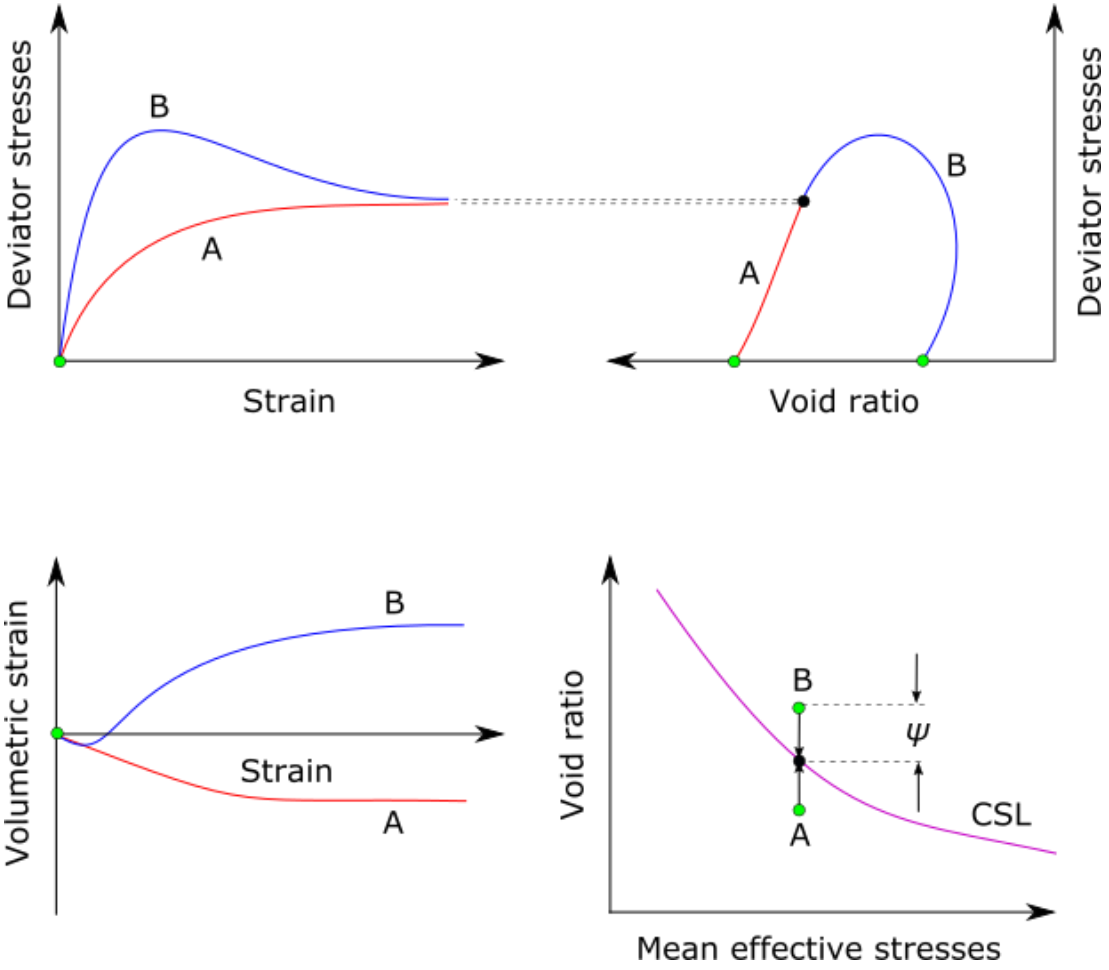

Figure 2.2: Typical drained test responses for monotonic loading (Casagrande, 1940)

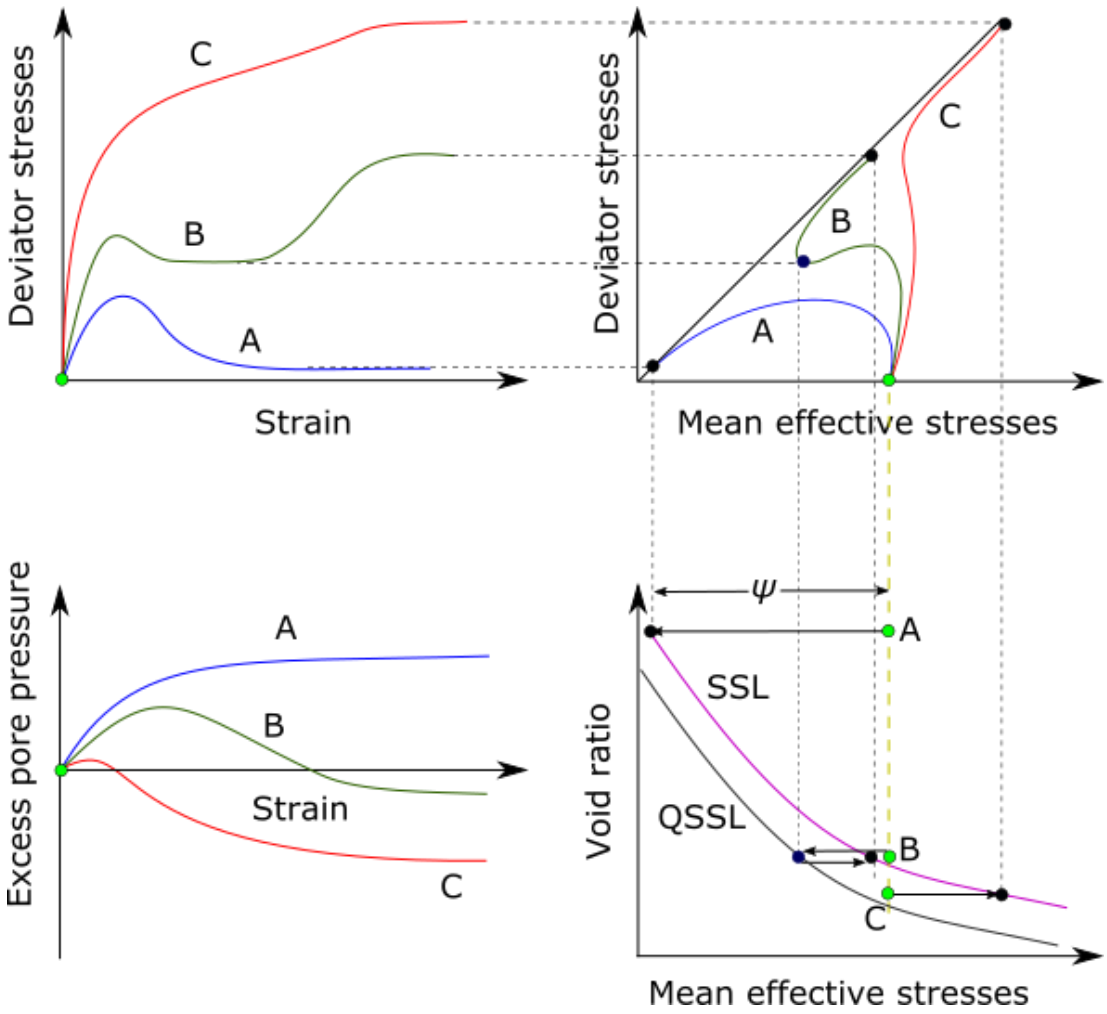

Figure 2.3: Typical undrained test response for monotonic loading (Casagrande, 1940)

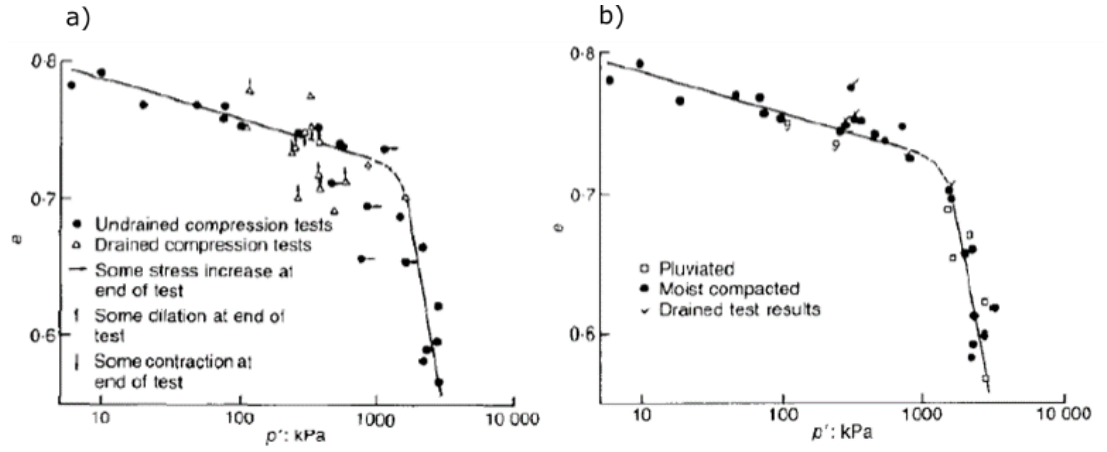

Figure 2.4: Critical state line plot in e-$log(p')$ space (Been et al., 1991): (a) drained vs undrained; (b) Inherent anisotropic

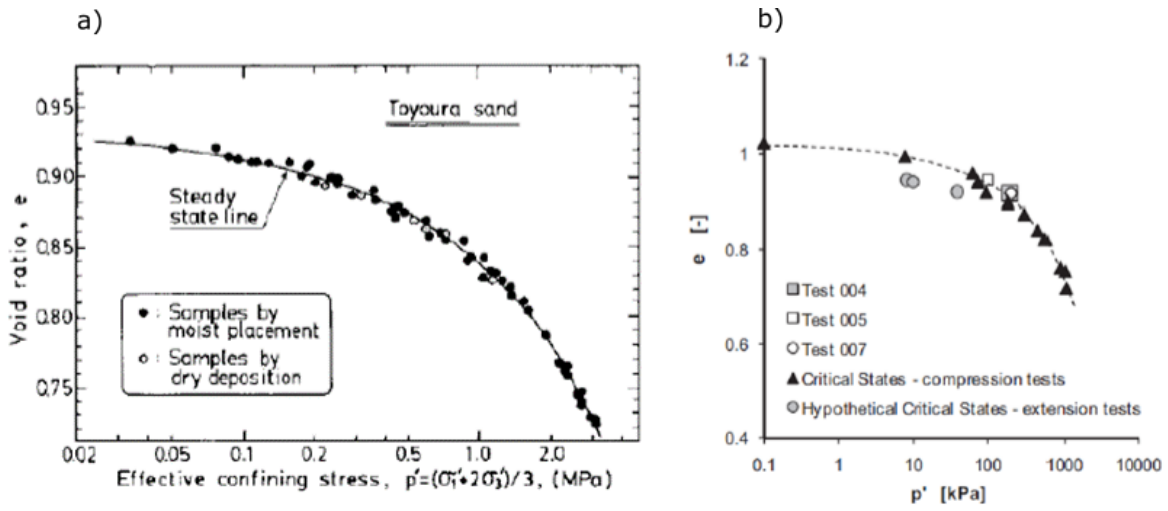

Figure 2.5: (a) CSL plot for anisotropic samples (Ishihara, 1993) and (b) CSL plot for anisotropic samples (Carrera et al., 2011)

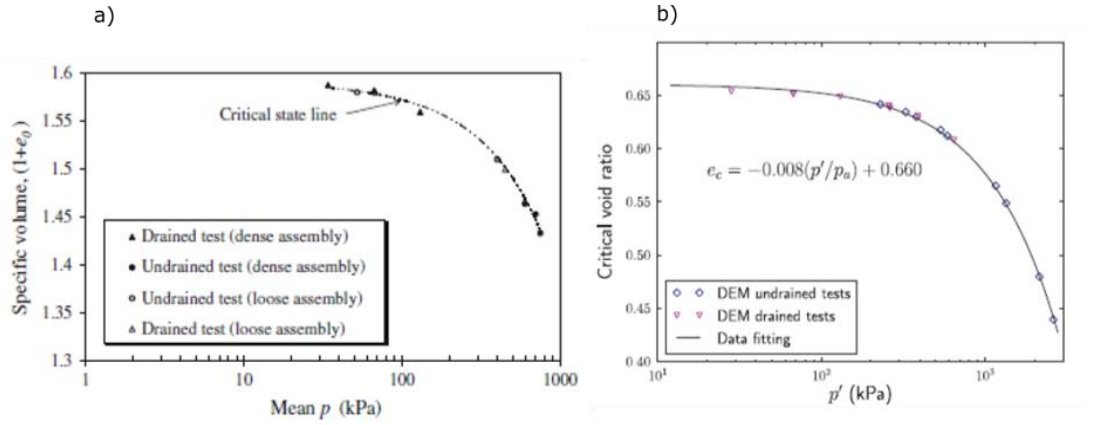

Figure 2.6: (a) Critical state line plot in v-$log(p')$ space (Sitharam and Vinod, 2009) and (b) Critical state line plot in e-$log(p')$ space (Guo and Zhao, 2013) under triaxial test using DEM simulations.

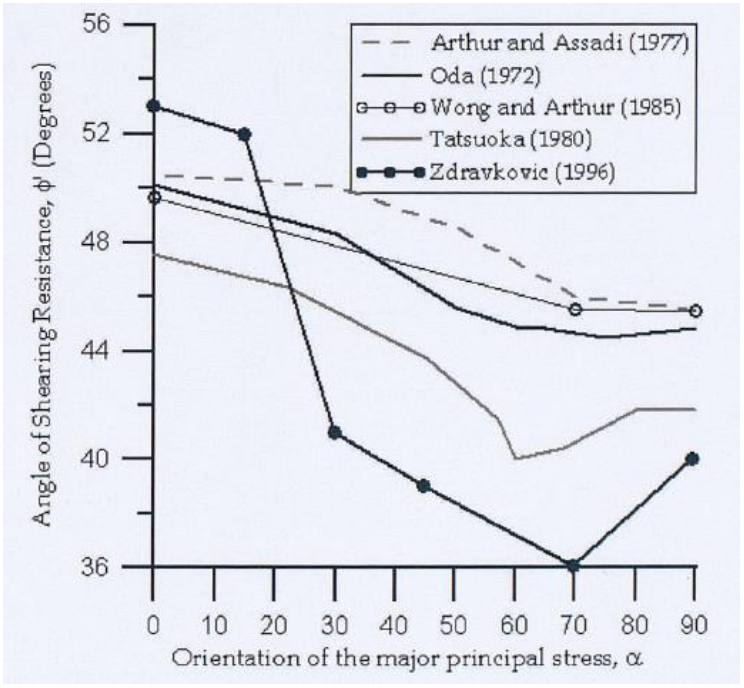

Figure 2.7: Effect of major principal effective stress orientation on angle of shearing resistance (taken from Barreto, 2009)

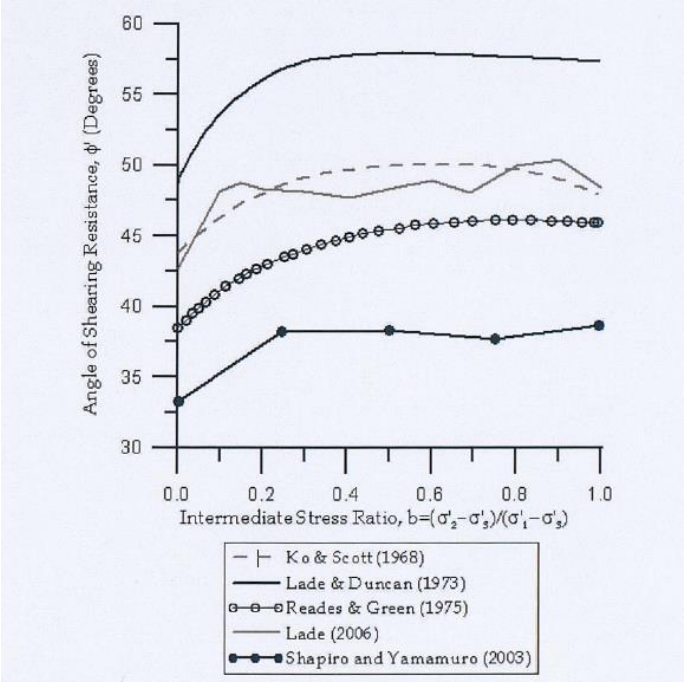

Figure 2.8: Effect of intermediate principal effective stress ratio on angle of shearing resistance (taken from Barreto, 2009)

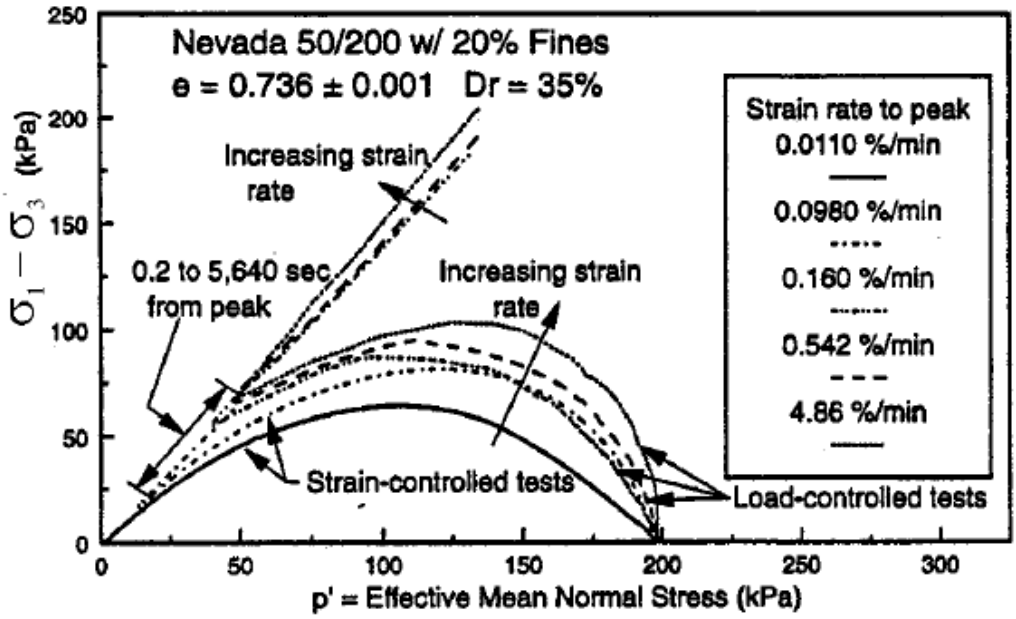

Figure 2.9: Effect of strain rate on the Nevada sand behaviour (Yamamuro and Lade, 1998)

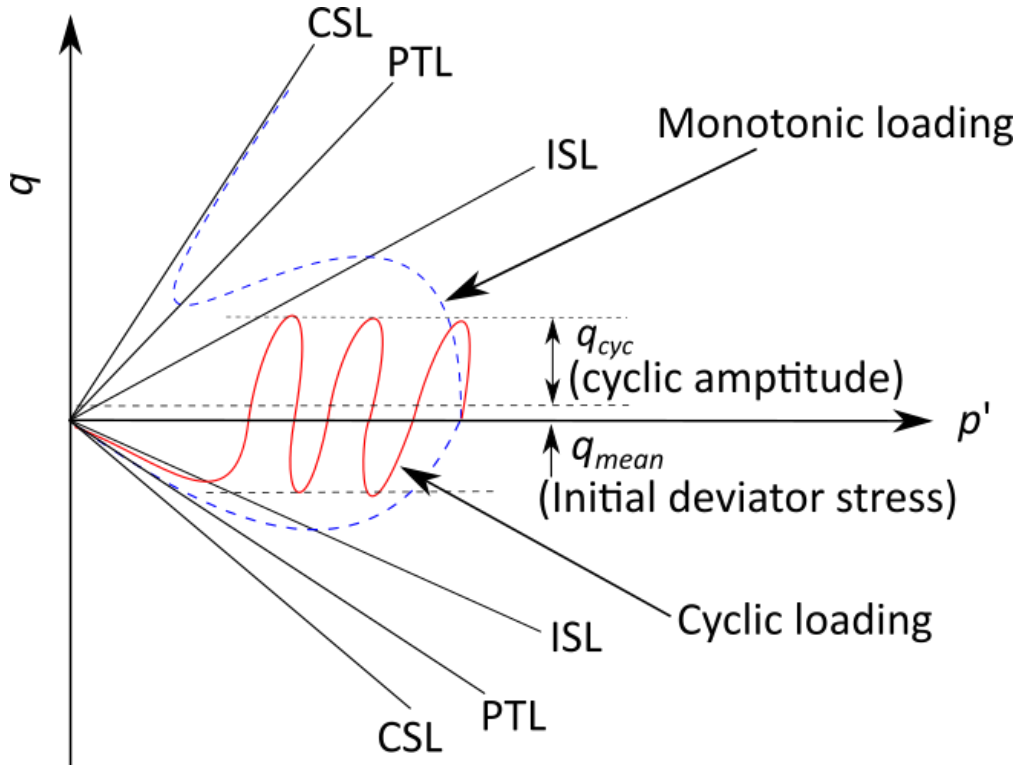

Figure 2.10: Schematic diagram for explaining the initiation of failure during cyclic loading (Hyodo et al., 1994)

Chapter 3 Undrained monotonic triaxial DEM simulations

It is important to understand the undrained static/monotonic strength of soil as it is a key influencer of the macro-scale response of loose/dense samples to loading. It also indicates the trigger mechanism for flow failure (Hyodo *et al*., 1994) and the origin of liquefaction (Mital and Andrade, 2016) during cyclic loading tests. Many researchers including Bishop and Eldin (1950), Ishihara *et al*. (1975) and Mohamad *et al*. (1986) have extensively studied the undrained behaviour of soil using laboratory testing. These tests enable us to understand the macro-scale stress–strain behaviour but cannot give any information on the dynamic changes occurring at the micro-scale that cause the observed macro-scale response. In recent years, DEM has become very popular in geomechanics research due to its ability to capture the macro-scale response of soil while enabling investigation at the micro-scale.

3.1 Introduction

Undrained tests are conducted to investigate the behaviour of soil from which the pore fluid does not have sufficient time to escape when subjected to load. To achieve this condition in laboratory triaxial tests, the drainage line is closed during shearing. Due to this, excess pore pressure is generated which may lead to phenomena such as liquefaction (Castro, 1969; Ishihara, 1993). Generally, there are two modelling approaches used by researchers to simulate undrained tests using DEM. The first approach involves coupling the DEM simulations of particles with a suitable CFD (computational fluid dynamics) code (Zhao and Shan, 2013; Liu *et al*., 2015). However, this complicates the simulations and increases their computational cost. The second approach is the 'constant-volume' (CV) approach, where the sample volume is maintained constant throughout shearing. CV simulations assume that the soil is fully saturated and water is incompressible. This approach has been widely adopted, e.g., Yimsiri and Soga (2010); Dubujet and Dedecker (1998) and Hanley *et al*. (2013). The constant-volume method has the advantage of computational simplicity. In a CV simulation, the excess pore water pressure is estimated as (Yimsiri and Soga, 2010):

$$\Delta u = \sigma'_{3,0} - \sigma'_3 \tag{3.1}$$

$\sigma'_{3,0}$ is the initial effective confining stress (at the start of shearing) and σ'_3 is the minor principal effective stress at every subsequent time step in the DEM simulation.

The main aim of this chapter is to investigate the undrained behaviour of sand subjected to monotonic loading using the CV DEM method. Gaining an understanding of the monotonic behaviour of sand is an essential precursor to the cyclic loading tests described in Chapters 5 and 6. A brief summary of triaxial simulations using DEM are presented in sections 3.2 to 3.6.

3.2 Triaxial simulations using LAMMPS

The open-source code LAMMPS (Plimpton, 1995) has an acronym which stands for Large-scale Atomic/Molecular Massively Parallel Simulator. It is parallelised using Message Passing Interface (MPI) and capable of running on both multi-core desktop machines as well as massively-parallel high-performance computers (HPC). It uses spatial-decomposition techniques while running on multiple processors: during a simulation, the simulation domain is divided into several subdomains as shown in Fig. 3.1a, each of which is assigned to a single processor (core). All calculations, i.e., contact detection, contact force calculation and the integration of motion of particles within an individual subdomain, are performed by the assigned processor. Information pertaining to particles near the boundary of two adjacent subdomains is communicated between assigned processors using MPI. However, this simulation time does not linearly decrease with increasing number of processors as shown in Fig. 3.1b (Huang, 2014; Munjiza, 2004). Increasing the number of processors leads to an increase in the interface communication cost between adjacent processors for the same problem. Therefore, the most effective way to take advantage of MPI is to run large simulations containing many particles. Due to the above advantages, access to the source code and demonstrated ability to capture the response of granular soils, LAMMPS was selected for this research. The remainder of this section describes periodic boundary conditions and the loading control schemes that have been implemented within the modified LAMMPS code by Dr Kevin Hanley (Huang, 2014) for simulating triaxial tests on soil elements.

3.2.1 Periodic boundaries

Using rigid-wall boundaries in DEM simulations has some disadvantages such as high porosities in the vicinity of the boundaries (Chan and Ng, 1986), and localisation of strain and contact forces in the area adjacent to the boundaries (Marketos and Bolton,

2010). Periodic boundary conditions assume the sample material is composed of infinitely repeating representative volume elements (RVEs) as shown in Fig. 3.2. This condition enables simulations free from boundary effects (Thornton, 2000). The periodic boundary condition follows the fundamental principle of mass conservation, i.e., a particle which protrudes from one side of a periodic boundary reappears on the opposite boundary with a continuous network of contact force calculation. To eliminate boundary effects (Huang *et al*., 2014c) and to ensure homogenous deformation (Cundall, 1988), periodic boundary conditions were adopted for this study. Many researchers such as Sitharam and Vinod (2009); Thornton (2000); Barreto and O'Sullivan (2012); Huang *et al*. (2014b); Hanley *et al*. (2015) have used this boundary condition to simulate triaxial tests.

3.2.2 Servo control

To perform triaxial simulations along different stress paths, the position of a stress-controlled periodic boundary is controlled by servo control.

$$\dot{\varepsilon} = -\frac{2 * \dot{\varepsilon}_{max}}{\sigma'_{target}}\left(\sigma'_{target} - \sigma'_{measured}\right) \tag{3.2}$$

$\dot{\varepsilon}$ is the strain rate, $g = \frac{2*\dot{\varepsilon}_{max}}{\sigma'_{target}}$ is the gain parameter which controls the speed of convergence between the user-defined σ'_{target} and the current effective stress $\sigma'_{measured}$. The gain parameter is typically determined through trial and error. $\dot{\varepsilon}_{max}$ is a user-defined maximum strain rate. This definition of the gain parameter implemented in LAMMPS (Huang, 2014) has several advantages. When $\sigma'_{measured} \leq 0.5\ \sigma'_{target}$, the boundaries move rapidly at the $\dot{\varepsilon}_{max}$ limit value. Due to this, the sample preparation, e.g., isotropic/anisotropic compression from a zero stress state, is faster than using a constant gain parameter which is sufficiently small to ensure stability at all times. When $\sigma'_{measured} > 0.5\ \sigma'_{target}$, the rate of compression/extension decreases according to the difference between $\sigma'_{measured}$ and σ'_{target}. $\dot{\varepsilon}$ approaches zero when $\sigma'_{measured} \approx \sigma'_{target}$. The gain parameter implementation is shown in Fig. 3.3 and below:

- $\sigma'_{measured} \leq 0.5\ \sigma'_{target} \rightarrow |\dot{\varepsilon}| \geq \dot{\varepsilon}_{max} \rightarrow |\dot{\varepsilon}|$ is limited to $\dot{\varepsilon}_{max}$
- $\sigma'_{measured} > 0.5\ \sigma'_{target} \rightarrow |\dot{\varepsilon}| < \dot{\varepsilon}_{max} \rightarrow |\dot{\varepsilon}|$ is less than $\dot{\varepsilon}_{max}$

Selection of the appropriate gain parameter is important. If g is too small, it takes a long time to reach the target stress and there is very large offset between the target stress and steady-state stress eventually attained. If g is too big, oscillations may result which affect the quality of the servo control and potentially cause instability if the oscillations increase in amplitude over time. In this triaxial compression study, three stress path loading conditions are used:

- Triaxial undrained compression. Compression in z-direction while $\sigma_x = \sigma_y$, sample volume constant and p' = variable.
- Triaxial drained compression. Compression in z-direction while $\sigma_x = \sigma_y$, sample volume not constant, and p' = variable.
- Triaxial constant p' compression. Compression in z-direction while $\sigma_x = \sigma_y$ and p' = constant

To reproduce these different triaxial stress path conditions, a different algorithm is required. These algorithms were implemented in the adapted version of LAMMPS used for this study through the 'fix multistress' command (Huang, 2014).

3.2.2.1 Constant-volume (CV) method for simulating undrained triaxial conditions

The CV loading condition in DEM simulations is often used to simulate undrained triaxial tests of fully-saturated soils. Lamei and Mirghasemi (2011) carried out CV DEM simulations and found the results to be consistent with fluid-coupled undrained simulations. The 'linkvolstress' option provided by the LAMMPS 'fix multistress' command is used to achieve constant-volume conditions. This maintains a constant sample volume and keeps the stresses in two specified directions equal. In the example, if the loading is applied in z-direction, the stresses in the x- and y-directions will be the same and the volume will be held constant. The servo-control algorithm implemented for maintaining a constant-volume during the simulation at each time-step is shown below, assuming an instantaneous strain rate of $\dot{\varepsilon}_z$ is applied in the z direction:

$$V_t = V_o\,(1 + \dot{\varepsilon}_x dt)\big(1 + \dot{\varepsilon}_y dt\big)(1 + \dot{\varepsilon}_z dt) = V_o \tag{3.3}$$

V_t is the volume of the sample at each time-step and V_o is the initial volume of the sample. Let $V = V_o\,(1 + \dot{\varepsilon}_z dt)$ so that the above Eq 3.3 becomes

$$(1 + \dot{\varepsilon}_x dt)\left(1 + \dot{\varepsilon}_y dt\right) = \frac{V_o}{V} \tag{3.4}$$

For identical lateral stress, i.e., $\sigma'_{x,t+\Delta t} = \sigma'_{y,t+\Delta t}$. Assuming stresses change in a linear manner related to the strain rate in the corresponding direction, i.e., $\sigma'_{i,t+\Delta t} \approx \sigma'_{i,t} + \frac{\sigma'_{i,t} - \sigma'_{i,t-\Delta t}}{\dot{\varepsilon}_{i,t-\Delta t}} \dot{\varepsilon}_{i,t}$ $(i = x, y, z)$ gives

$$\sigma'_{x,t} + \frac{\sigma'_{x,t} - \sigma'_{x,t-\Delta t}}{\dot{\varepsilon}_{x,t-\Delta t}} \dot{\varepsilon}_{x,t} = \sigma'_{y,t} + \frac{\sigma'_{y,t} - \sigma'_{y,t-\Delta t}}{\dot{\varepsilon}_{y,t-\Delta t}} \dot{\varepsilon}_{y,t} \tag{3.5}$$

Combining Eq. 3.4 and Eq. 3.5 and ignoring the second-order product of differentials, the strain rates in the lateral directions are

$$\dot{\varepsilon}_{x,t} = \frac{\left\{\frac{V_o - V}{Vdt}\right\}(\sigma'_{y,t} - \sigma'_{y,t-\Delta t}) - \dot{\varepsilon}_{y,t-\Delta t}(\sigma'_{x,t} - \sigma'_{y,t})}{\sigma'_{y,t} - \sigma'_{y,t-\Delta t} + \left\{\frac{\sigma'_{x,t} - \sigma'_{x,t-\Delta t}}{\dot{\varepsilon}_{x,t-\Delta t}}\right\}\dot{\varepsilon}_{y,t-\Delta t}} \tag{3.6}$$

$$\dot{\varepsilon}_{y,t} = \frac{V_o - V(1 + \dot{\varepsilon}_{x,t} dt)}{V(1 + \dot{\varepsilon}_{x,t} dt)dt} \tag{3.7}$$

This type of boundary condition has been used by many researchers such as Hanley *et al*. (2013); Huang (2014) to simulate constant-volume triaxial tests.

3.2.2.2 Constant confining stress for simulating drained triaxial conditions

To achieve drained loading conditions, the movement in the lateral direction of the periodic cell is controlled by:

$$\dot{\varepsilon}_{i,t} = -\frac{2 * \ maximum\ strain\ rate}{\sigma'_{i,target}}\left(\sigma'_{i,target} - \sigma'_{i,measured}\right) \tag{3.8}$$

$\dot{\varepsilon}_{i,t}$ is the strain rate of boundaries normal to the i th axis at the current time-step, t.

3.2.2.3 Constant effective stress, p' for simulating drained triaxial conditions

Similar to 'linkvolstress', the 'constantp' option in the LAMMPS 'fix multistress' command is used to maintain a constant mean effective stress, p', during the simulation while keeping the stresses in two specified directions equal. Assuming a strain-controlled applied load in the z direction, the target stresses for the next time-step are estimated at each time-step:

$$p' = \frac{1}{3}\left(\sigma'_x + \sigma'_y + \sigma'_z\right) \rightarrow \sigma'_x = \sigma'_y = \frac{1}{2}(3p' - \sigma'_z) \quad (3.9)$$

Since time-steps are small, the change in σ'_z due to the load applied in the z direction from t to $t + \Delta t$ is approximately equal to the change from $t - \Delta t$ to t, and thus at $t + \Delta t$ can be estimated by:

$$\sigma'_{z,t+\Delta t} = \sigma'_{z,t} + \left(\sigma'_{z,t} - \sigma'_{z,t-\Delta t}\right) \quad (3.10)$$

Therefore, the target stresses in the x and y directions at $t + \Delta t$ can be obtained by Eq. 3.11:

$$\sigma'_{x,t+\Delta t} = \sigma'_{y,t+\Delta t} = \frac{1}{2}\left(3p' - \sigma'_{z,t+\Delta t}\right) \quad (3.11)$$

The servo-control equations are provided above (3.2–3.11); for further detail, the reader is directed to Huang (2014). The above servo-control algorithm has been used by Huang (2014) and Hanley *et al*. (2015), among others, to study the behaviour of granular materials under triaxial test conditions. The above servo-control algorithm was selected for this research.

3.3 Selection of DEM parameters for simulating sand specimens

As documented by O'Sullivan (2014), the computational cost limits the number of particles used in DEM simulations. Fig. 3.4 indicates that around 10,000 particles are commonly used in 3D DEM simulations. For laboratory testing, ASTM (2011) suggests that the diameter of a cylindrical specimen should not be smaller than 33 mm and larger than 6 times the largest particle diameter for triaxial compression tests. According to Head (1994) the thickness of the specimen should not be less than 10 times the maximum particle diameter for shear box tests. In Chapter 3, the selection of domain size and the number of particles used in these DEM simulations for this research are presented.

Table 3.1: Summary of DEM parameters used by researchers for simulating sand specimens in 3D using spherical particles and a Hertz-Mindlin contact model

References	Coeff. of friction, μ_s	Contact model parameters	No. of particles	Boundary conditions
Barreto & O'Sullivan (2012)	0.3-0.5	G = 28.68 GPa ϑ = 0.22	4000	periodic
Ng (2009)	0.5	G = 29 GPa ϑ = 0.15	1,170-3,000	rigid
Hanley *et al*. (2013)	0.5	G = 29 GPa ϑ = 0.2	11781-43906	periodic
Huang *et al*. (2014b)	0.25	G = 29 GPa ϑ = 0.12	20164	periodic
Yimsiri & Soga (2011)	1.0	G = 29 GPa ϑ = 0.2	3,500-3,900	rigid
Thornton (2000)	0.3	G = 26.92 GPa ϑ = 0.3	3620	periodic

The range of friction coefficient values for quartz sand was 0.12 < μ < 0.35 from the particle–particle friction tests conducted by Senetakis *et al*. (2013). Many researchers used different values of μ for quartz sand in DEM simulations as shown in Table 2.1. In this study, μ_s = 0.25 was selected for shearing, based on Huang *et al*. (2014a). Huang *et al*. (2014a) has shown that the DEM stress-strain response becomes unphysical if μ_s ≥ 0.5.

For monotonic loading conditions, the strain rate, $\dot{\varepsilon}_z$, was fixed at 1/s in the z direction to ensure an inertia number less than the limiting value of 7.9 x 10^{-5} proposed for quasi-static behaviour (Perez *et al*., 2016). The inertia number, IN, is calculated using Eq. 3.12:

$$IN = \frac{\dot{\varepsilon}_z d}{\sqrt{P/\rho}} \tag{3.12}$$

d is the mean diameter of particles, P is the pressure and ρ is the particle density. For cyclic loading conditions, the strain rates change constantly in these stress-controlled simulations. However, the inertia number was maintained below the limit proposed by Perez *et al*. (2016) up to the onset of liquefaction.

3.4 DEM sample preparation

Cubic granular specimens of 10 × 10 × 10 mm^3 were created which contained 28,309 spheres as shown in Fig. 3.5a. The grading used was not representative of any specific sand; particle diameters varied between 0.1 mm and 1 mm (D_{50} = 0.516 mm), with C_u = 3.004 and C_c = 0.573 indicating a poorly graded sand as shown in Fig. 3.5b. The sample preparation approach described by Hanley *et al*. (2014) was adopted as summarised in Fig. 3.6. In stage 1, the particles were placed randomly within the periodic cells without initial overlaps using a MATLAB code. Stage 2: the initial particle positions were imported to LAMMPS before each sample was compressed by moving the boundaries under stress control to achieve a stable desired stress state. Different interparticle friction coefficients were used during sample preparation to achieve a range of void ratios. Then the prepared samples were sheared monotonically or cyclically as shown in Fig. 2.6. DEM parameters for quartz sand selection and the undrained behaviour of sand subjected to monotonic loading using the CV DEM method are described in sections 3.5 and 3.6.

3.5 Selection of DEM parameters for quartz sand

Before the monotonic triaxial constant-volume (CV) DEM simulations were conducted, a preliminary parametric study was conducted to confirm the ability of the simulations to capture the typical characteristics of monotonic loading of sand, and to identify a suitable local damping coefficient, coefficient of friction and strain rate for the remaining simulations. Sample preparation was carried out according to the procedure described in section 3.4. Nine dense cuboidal samples were created using μ_c = 0.00 with the particle size distribution shown in Fig. 3.5b and with varying DEM parameters as shown in Table 3.2. All simulations were run using a simplified Hertz-Mindlin (smooth) contact model as described in Chapter 2 (section 2.1), with a shear modulus G = 29 GPa, particle density ρ = 2675 kg /m^3 and Poisson's ratio ϑ = 0.2 which represent physically realistic values for quartz.

Table 3.2: Summary of nine CV DEM samples with varying parameters for simulating sand specimens in 3D using spherical particles and a Hertz-Mindlin contact model

Simulations	No. of particles	During shearing		
		Coefficient of friction, μ	Local damping coefficient, d	Strain rate, s^{-1}
S1	**12439**	0.25	0.2	1
S2	**28309**	0.25	0.2	1
S3	**56564**	0.25	0.2	1
S4	28309	**0.05**	0.2	1
S5	28309	**0.5**	0.2	1
S6	28309	0.25	**0.1**	1
S7	28309	0.25	**0.3**	1
S8	28309	0.25	0.2	**0.5**
S9	28309	0.25	0.2	**1.5**

The time-steps used in DEM simulations are very small to ensure numerical stability. This, along with the necessity to calculate the forces between contacting particles and update their positions and velocities makes DEM simulations computationally expensive. This limits the number of particles used in DEM simulations. The DEM study conducted by Huang (2014) on small and large PB assemblies (10,624 and 20,164 particles, respectively) indicates that the stress–strain responses are insensitive to sample size within this range. The sensitivity of the macro–micro behaviour of sand using PB samples to the sample size was also investigated in this study. Fig. 3.7 shows the response of sand after isotropic compression (μ_c = 0) under a confining pressure (CP) of 150 kPa with an inter-particle friction coefficient μ_s = 0.25 during shearing of three PB samples (S1-S3) containing different numbers of particles. The small PB sample contained 12,439 particles, medium PB sample contained 28,309 particles and the large PB sample was comprised of 56,564

particles. Fig. 3.7a and Fig. 3.7b confirm that the stress–strain response of PB samples is not significantly different when the number of particles contained in the sample changes. However, looking at micro-scale behaviour, Z_m, all three samples are closer to each other, however the small sample is approached to lesser Z during initial shearing which can make unstable for a loose sample as shown in Fig. 3.8a. Therefore, to ensure statistically reliable particle-scale results at affordable computational cost, medium PB samples containing 28,309 particles were used throughout this research work.

According to Senetakis *et al*. (2013) that the range of friction coefficient values for quartz sand was $0.12 < \mu < 0.35$ from particle–particle friction tests. Many researchers used different values of μ for quartz sand in DEM simulations was shown in Chapter 2 (Table 3.1). The sensitivity of the micro- and macro-scale responses of sand using PB samples to interparticle coefficient of friction was also examined in this study. Fig. 3.9 shows the macro-scale response of sand for three PB samples (S2, S4 and S5) with different interparticle coefficients of friction, i.e., 0.25, 0.05 and 0.5 (Table 3.2). Fig. 3.9a and Fig. 3.9b show that the stress–strain response and initial peak strength of PB samples are increased with the increase of interparticle friction coefficient. A similar result was obtained by Barreto and O'Sullivan (2012), Kruyt and Rothenburg (2006) and Yang *et al*. (2012). Fig. 3.10a and Fig. 3.10b show that Z and IR were decreased with the increase of interparticle coefficient of friction. Similar results was observed by Huang *et al*. (2014a) and Barreto and O'Sullivan (2012). Huang *et al*. (2014a) show that the DEM stress–strain response becomes unphysical if $\mu_s \geq 0.5$. Therefore, based on Huang *et al*. (2014a) and Senetakis *et al*. (2013), $\mu_s = 0.25$ was selected for shearing for the remainder of the simulations in this thesis.

Local damping, controlled by a local damping coefficient d, is used for dissipating energy so that the system can reach a stable state. Fig. 3.11 shows the influence of local damping coefficient on the macro-scale behaviour of sand using PB samples (S2, S6 and S7) with varying d = 0.2, 0.1, 0.3 in CV triaxial simulations. Fig. 3.11a and Fig. 3.11b confirm that the stress–strain response of PB samples is not significantly different with different local damping coefficients and there is no effect on simulation time by changing the damping ratio. Similarly, the micro-scale behaviour is also insensitive to local damping as shown in Fig. 3.12a and Fig. 3.12b. Similar insensitivity of the stress–strain response was reported by Huang (2014). This insensitivity to local damping is explained more in Chapter 6.

The influence of strain rate on the behaviour of sand using PB samples (S2, S8 and S9) with a varying strain rate of 1.0, 0.5 and 1.5 s^{-1} in CV triaxial simulations is shown in Fig. 3.13 and Fig. 3.14. The quasi-static condition was defined with the Eq. 2.32. For all simulations, these strain rates ensured an inertia number less than 6.8×10^{-5} throughout shearing: lower than the limiting value of 7.9×10^{-5} proposed for quasi-static behaviour by Perez *et al*. (2016). Fig. 3.13 and Fig. 3.14 confirm an insensitivity to the strain rate. A strain rate of 1 s^{-1} was selected for shearing in this research work.

3.6 CV triaxial monotonic loading DEM simulations: a parametric study

3.6.1 DEM sample preparation

A monotonic triaxial constant-volume (CV) DEM simulation parametric study was conducted to gain an understanding of monotonic behaviour of sand which is essential for the cyclic loading tests. This study helped in selecting the parameters for the cyclic loading tests. The sample preparation procedure described in section 3.4 was applied. Twenty seven cuboidal samples were created which contained 28,309 spheres with radii varying between 0.1 mm and 1 mm as shown in Table 3.3: nine samples (D1-D9) are dense samples created using μ_c = 0.00 with initial stress state, $I_{ss} = \frac{\sigma'_{3,0-} p'_0}{p'_0}$ of 0.00, 0.30 and 0.55; nine samples (MD1-MD9) are medium-dense samples created using μ_c = 0.08 with I_{ss} of 0.00, 0.16 and 0.30 and nine samples (L1-L9) are loose samples created using μ_c = 0.16 with I_{ss} of 0.00, 0.10 and 0.19. In this table, the friction coefficient were increased for some samples, i.e., D2, D3, D9, MD3 and L3 from the based value, i.e., 0.00, 0.08 and 0.16 to generate desired initial stress state, I_{ss} and it is denoted with an asterisk as shown in Table 3.3.

Table 3.3: Summary of the twenty seven samples prepared for these CV simulations: the friction coefficient increased for some samples are denoted with an asterisk

Simulation ID	*Coefficient of friction,* μ_c	*Minor principal effective stress,* $\sigma'_{3,0} = \sigma'_{2,0}$ (kPa)	*Major Principal effective stress,* $\sigma'_{1,0}$ (kPa)	*Void ratio,* e
D1 or S2	0.00	150	150	0.3940
D2	0.00/0.05*	150	200	0.3939

Simulation ID	*Coefficient of friction,* μ_c	*Minor principal effective stress,* $\sigma'_{3,0} = \sigma'_{2,0}$ (kPa)	*Major Principal effective stress,* $\sigma'_{1,0}$ (kPa)	*Void ratio,* e
D3	0.00/0.06*	150	250	0.3960
D4	0.00	300	300	0.3926
D5	0.00	300	350	0.3902
D6	0.00	300	400	0.3882
D7	0.00	500	500	0.3912
D8	0.00	500	550	0.3898
D9	0.00/0.01*	500	600	0.3866
MD1	0.08	150	150	0.4395
MD2	0.08	150	200	0.4321
MD3	0.08/0.22*	150	250	0.4393
MD4	0.08	300	300	0.4392
MD5	0.08	300	350	0.4361
MD6	0.08	300	400	0.4323
MD7	0.08	500	500	0.4383
MD8	0.08	500	550	0.4373
MD9	0.08	500	600	0.4348
L1	0.16	150	150	0.4601
L2	0.16	150	200	0.4523

Simulation ID	*Coefficient of friction,* μ_c	*Minor principal effective stress,* $\sigma'_{3,0} = \sigma'_{2,0}$ (kPa)	*Major Principal effective stress,* $\sigma'_{1,0}$ (kPa)	*Void ratio,* e
L3	0.16/0.18*	150	250	0.4481
L4	0.16	300	300	0.4598
L5	0.16	300	350	0.4590
L6	0.16	300	400	0.4527
L7	0.16	500	500	0.4597
L8	0.16	500	550	0.4594
L9	0.16	500	600	0.4579

This friction coefficient was increased to 0.25, based on Huang *et al*. (2014a), before shearing each sample at a fixed strain rate of 1/s. This strain rate ensured an inertia number less than 6.8×10^{-5} throughout shearing: lower than the limiting value of 7.9×10^{-5} proposed for quasi-static behaviour by Perez *et al*. (2016). All simulations were run using a simplified Hertz-Mindlin (smooth) contact model (Itasca Consulting Group, 2007), with a shear modulus of 29 GPa. This shear modulus represented a physically realistic value for quartz. The particle density and Poisson's ratio were set at 2675 kg /m^3 and 0.2, respectively. The local damping coefficient was chosen as 0.2. Gravity was not considered and particle crushing was not permitted in these simulations. To obtain a CSL, three supplementary triaxial drained simulations were run at $\sigma'_{3,0}$ of 150, 300 and 500 kPa and two constant p' simulations were run at 40 and 47 MPa.

3.6.2 Results and discussion

Macro-scale

A summary at critical state of all twenty seven CV triaxial shearing simulations is shown in Appendix Table A.1. The macro-scale responses are presented in Fig. 3.15-3.21 for three different initial packing values of ~ 0.39 (dense, D), ~ 0.43 (medium-

dense, MD) and ~ 0.46 (loose, L). The effective stress, p', generated at 25% axial strain reached 95.25 MPa for D1 (for D1-D9, MD1-MD9 and L1-L9, p', values are presented in Appendix Table A.1) as shown in Fig. 3.15a. These extremely high stresses generated in CV simulations for dense samples were also observed by Hanley *et al*. (2013). Stresses of this magnitude would lead to considerable particle crushing in reality (Hanley *et al*., 2015) which was not permitted in these simulations. The shear modulus of the soil samples is extremely high: 312 MPa at 1 x 10^{-3}% strain for the dense sample, D1. The high stresses generated during shearing may be caused by this initial unrealistically stiff response of Hertzian spheres using the particle shear modulus of quartz. With a void ratio of ~ 0.43, the $p'$of each sample was reduced by around 81% at 25% axial strain compared to the samples with a void ratio of ~ 0.39, e.g., comparing D1 at 95.25 MPa and MD1 at 17.99 MPa. Six samples with a void ratio of ~ 0.46 liquefied: L1, L4, L5, L7, L8 and L9. The post-liquefied responses are not considered in this study. The remaining three loose samples, L2, L3 and L6, had p' values at 25% axial strain which were reduced by around 94-99% compared to those samples at a void ratio of ~ 0.39. Similarly, for the void ratio of ~ 0.39, the deviator stress, q, at 25% axial strain reached 68.78 MPa for D1 (D1-D9, MD1-MD9 and L1-L9 values are presented in Appendix Table A.1) as shown in Fig. 3.16a. These values of q reduce by around 70-80% by increasing the void ratio to ~ 0.43. For the non-liquefied loose samples, L2, L3 and L6, q at 25% axial strain was reduced by 90-99% compared to samples with a void ratio of ~ 0.39. Increasing I_{ss} leads to a small reduction in initial void ratio and the generation of higher p' and q for the same $\sigma'_{3,0}$. Increasing $\sigma'_{3,0}$ tends to increase p' and q.

Six samples (L1, L4, L5, L7, L8, L9) show a very loose sample characteristic: liquefied under small strain. Two samples (L2, L6) show loose sample characteristic: quasi-steady state, QSS, a state at which sand samples reach a minimum q before it increases and thereafter attains a constant value at the critical state (Fig 3.16c and Fig 3.16d). The existence of these characteristics has been reported by many researchers (Murthy *et al*, 2007; Castro, 1969; Been and Jefferies, 1985; Ishihara *et al*., 1975). D and MD samples show a very dense sample characteristic: initially increased p' until it reaches *CS* state, after which p' remains constant as shown in Fig. 3.17. Fig. 3.17c shows samples L2 and L6, which initially decreased in p' to the PT state and subsequently increased until a constant value of p' was reached at the CS. This initial reduction in p' at the PT state increased with increasing e value; a

similar experimental observation was made by Wanatowski (2007). The slope of the flow liquefaction lines, FLL, which connect the origin and IS point in $q - p'$ space (Lade, 1993) decrease with increasing e as shown in Fig. 3.17c, suggesting a higher liquefaction resistance with decreasing e as expected.

All simulations reached a critical state before 25% axial strain except the six loose samples L1, L4, L5, L7, L8 and L9 which liquefied at small strain. The non-liquefied simulations attained a similar angle of shear resistance, ASR, and stress ratio, $M = q/p'$, of around 18.7° and 0.72 respectively as shown in Fig. 3.18 and Fig. 3.19, regardless of void ratio, confining pressure or initial stress state. Fig. 3.18a and 3.19a shows behaviour characteristic of dense samples: the angle of shear resistance and the stress ratio increased abruptly to a high initial peak value upon initial shearing and dropped thereafter to a constant value at the critical state. Fig. 3.19b shows behaviour characteristic of medium-dense samples: the stress ratio increased to a peak value lesser than dense sample upon initial shearing and dropped thereafter to a constant value at the critical state. Fig. 3.19c shows no initial peak value upon shearing of the loose samples though a constant value is attained at the critical state. These characteristics were also reported for laboratory experiments by Castro (1969); Been and Jefferies (1985); Ishihara *et al*. (1975). As the stress ratios at critical state are very similar for all simulations (Fig. 3.19), all points are collinear on Fig. 3.20: the critical state line in $q - p'$space. Fig. 3.21 shows that the CSL in $e - log(p')$ space is unique and independent of the initial state and the loading conditions. Similar observations were reported by Murthy *et al*. (2007); Maeda *et al*. (2010); Gu *et al.* (2014); Zhao and Guo (2013); Ng (2009); Sitharam and Vinod (2009); Yan and Dong (2011) and Yang and Wei (2012). The initial peak value and CS value of angle of shear resistance and stress ratio are much lower than values obtained in physical tests. The main reason is the simulated particles are smooth spheres which can rotate freely whereas, in a real system, interparticle movements are much more inhibited because of interlocking (Huang *et al.*, 2017). The mean interparticle overlap, O_p, normalized by mean particle radius is shown on Appendix Table A.1 at the critical state. This is important to quantify because of the fundamental assumption of point contact in DEM (Potyondy and Cundall, 2004). The mean interparticle overlaps were below 4% in all cases. However, the largest overlap exceeded 20%. As the void ratio increases, the mean interparticle overlap decreased.

Micro-scale

The coordination number, Z, is a scalar measure of fabric, i.e., internal topology, within a granular system. It is computed as $Z = \frac{2N_c}{N_p}$ (see detail in Chapter 2, Section 2.2.2). Fig. 3.22a for the dense samples shows that Z decreases immediately upon shearing until it reaches a minimum value of ~4.2 at 0.5% axial strain. Afterwards, Z increases and a stable value of around 5 is reached at critical state. Fig. 3.22b for the medium-dense samples is similar in appearance: Z decreases immediately upon loading to reach a minimum value of ~3.6 at 0.5% axial strain, followed by a gain of Z until a stable value between 4 and 4.2 is reached at critical state. Fig. 3.22c shows for six samples, L1, L4, L5, L7, L8, L9, Z decreases immediately upon shearing to zero at 0.5% axial strain. L2 and L3 lack an initial minimum value upon shearing and continue to grow until reaching a constant value around 3.5 at the critical state. L6 initially has a decreasing Z but attains a similar critical state value around 3.5. Samples with lower void ratio showed slightly higher Z values at critical state. The mechanical coordination number, Z_m, is computed similarly to Z, except those particles with zero or one interparticle contact are excluded from the calculation (Thornton, 2000). Fig. 3.23 shows that the trends in Z_m are the same as those in Z reported above.

The deviatoric fabric, φ_d, is the difference between the maximum and minimum eigenvalues of the second-order fabric tensor defined by Satake (1982) (see detail in Chapter 2, Section 2.2.2). It is widely used to quantify the fabric anisotropy of granular assemblies. Fig. 3.24 shows the variation of deviatoric fabric with axial strain for all simulations considered. φ_d is almost zero at the start of shearing of each isotropic sample. Fig. 3.24a, for the dense samples, shows that φ_d increases sharply to a maximum value of around 0.08 at 2.5% axial strain before decreasing to a stable value between 0.04 and 0.05 at critical state. For medium-dense samples (Fig. 3.24b), φ_d rises gradually to a peak value of around 0.06 at 5% axial strain before decreasing to a stable constant value of around 0.05 at critical state. Increasing I_{ss} leads to an increase in the initial peak value of φ_d but the same CS values are attained. These results agree with experiments tests (Been *et al*., 1991; Carrera *et al*., 2011; Ishihara, 1993) which show that the initial anisotropy has no effect at large strain levels, resulting in a unique CSL. Fig. 3.24c shows that, for the loose samples L2, L3 and L6, there is no initial peak upon shearing and a constant value between 0.05 and 0.06 is

attained at the critical state. Samples with lower void ratios show slightly higher φ_d values at peak.

The index of redundancy, IR, was proposed by Kruyt and Rothenburg (2009) to define the mechanical redundancy in a discrete system. It is defined, $IR = Z\left(\frac{3-2f_s}{12}\right)$ where f_s is the sliding fraction (see detail in Chapter 2, section 2.2.2). IR decreases immediately upon initial shearing of the dense samples (D1-D9) until it reaches a minimum value around 0.8; this is followed by an increase in IR until a stable maximum constant value of ~1 is attained at critical state as shown in Fig. 3.25a. Similarly, for medium-dense samples (MD1-MD9), IR decreases immediately to around 0.7, followed by a gain of IR until it attains a stable maximum constant value between 0.8 and 0.85 at critical state as shown in Fig. 3.25b. The three non-liquefying loose samples, (i.e., L2, L3, L6) show an initial minimum value of IR = 0.72 upon shearing before a constant value around 0.78 is attained at the critical state as shown in Fig. 3.25c. Samples with lower void ratio showed slightly higher IR values at critical state. This is expected as void ratio decreases cause Z to increase as shown in Fig. 3.22, which leads to higher IR. Fig. 3.26 shows the sliding fraction, f_s, against axial strain. Samples with lower void ratios have higher f_s values than samples with higher void ratios.

3.7 Considering rotational resistance

The peak and critical-state ASR and M observed in DEM simulations using smooth spherical particles are much lower than for a real sand, even with the use of high coefficients of friction (Huang *et al*., 2014a; Yang *et al*., 2012; Thornton, 2000). Freely rotating smooth spheres are unable to capture the effect of surface asperities and non-spherical particle shapes whereas, in a real system, interparticle movements are much more prone to particles interlocking due to asperities and non-spherical overall particle shape that prevent free rotation (Huang *et al*., 2017). The rotational resistance model used in this simulation is similar to the model proposed by Jiang *et al.* (2005) and is described by Huang *et al*. (2017). The rotational resistance implemented in LAMMPS (Huang, 2014) is decomposed into two components of moment: a rolling moment, M_r, opposing the rotational motion around axes in the contact plane and a twisting moment, M_t, counteracting the rotational motion about the contact normal. This model can be illustrated by considering two rolling gears. The rough nature of

particle surfaces that produces interlocking can be presented by gears' teeth and the contact force at the teeth induces a rolling moment relative to both particles in contact.

$$M_{r,i} = \overline{k_n} I_i \theta_{r,i} \;\&\; M_{r,i} \leq \kappa f_n R_r (i = x, y) \tag{3.13}$$

$$M_{t,i} = \overline{k_s} J_z \theta_{t,i} \;\&\; M_{t,i} \leq \mu \kappa f_n R_r (i = z) \tag{3.14}$$

$I_i = \frac{\pi}{4} (\delta B)^4$ is the area moment of inertia of a circular area with respect to the contact plane in the i[th] axis direction and $J_z = \frac{\pi}{2} (\delta B)^4$ is the polar area moment of inertia with respect to the contact normal in the z axis direction. B is the radius of the contact plane and δ is a shape parameter accounting for the unsmooth nature of the contact surface. κ is a strength index which relates the compressive strength of asperities to the normal contact force. $\theta_{r,i}$ and $\theta_{t,i}$ are the relative rolling and twisting angles, respectively.

Two rotational resistance model parameters needed to be chosen. δ was set at 0.5 (Huang *et al*., 2017). One isotropic sample was created using our standard sample preparation approach (details in Section 3.4) with κ = 0.0, i.e., no rotational resistance. κ was increased to a value of 0.1, 0.3 or 0.5 prior to triaxial shearing. All of the other parameters were fixed at the values for D1 as shown in Table 3.4.

Table 3.4: Summary of four CV monotonic undrained simulations with/without a rotational resistance model running with simplified Hertz-Mindlin contact model and periodic boundaries for sand specimens using LAMMPS

Simulation ID	With/without rolling friction	Void ratio, e	Initial mean effective stress, p'_0 (kPa)	κ
D1	No rolling friction	0.3940	150	-
DR1	With rolling friction	0.3929	150	0.1
DR2	With rolling friction	0.3929	150	0.3
DR3	With rolling friction	0.3929	150	0.5

These simulation results at critical state are summarised in Appendix Table A.2. The stress–strain responses for four CV simulations with and without rotational resistance are presented in Fig. 3.27. The effective stress p' generated at 25% axial strain reached 95.25 MPa for D1 without rotational resistance as shown in Fig. 3.25a. With rotational resistance, the effective stress of the sample at 25% axial strain increased by around 23% compared with no rotational resistance. Similarly, without rotational resistance, the deviator stress q at 25% axial strain reached 68.78 MPa for D1 (Fig. 3.27b), which increased by around 70% when rotational resistance was added. Increase of the deviator stress q due to the addition of rotational resistance was also observed by Huang *et al*. (2017). Increasing κ has no significant effect on q and slightly decreases p'. However, the drained DEM simulation conducted by Huang *et al*. (2017) revealed that increasing κ leads to an increase in q. The main reason for this disparity may be sample density, i.e., particles are not freely moveable in a very dense sample. Nonetheless, adding rotational resistance does not solve the high-stress-generation issue in CV simulations of dense samples.

All simulations with rotational resistance reached a critical state before 25% axial strain, attaining a similar angle of shear resistance, ASR, and stress ratio, $M = q/p'$, of around 25.36° and 0.99 respectively (values for DR1). By comparison, D1 reached a critical state ASR= 18.7° and M= 0.72 as shown in Fig. 3.28. The angle of shear resistance and stress ratio at critical state with rotational resistance is much higher than without rotational resistance and closer to physical test values. A similar result was obtained by Huang *et al*. (2017). Fig. 3.29 shows that Z decreases fractionally with rotational resistance but this difference is small, particularly at critical state.

3.8 Conclusion

This chapter presents a brief review on the numerical modelling of geotechnical triaxial tests using LAMMPS (open-source DEM/MD code). The servo-control schemes for different geotechnical triaxial test conditions with periodic boundaries using the open-source LAMMPS code (Plimpton, 1995) and how the DEM samples are prepared for triaxial tests are presented.

This chapter presents results from a series of constant-volume (CV) undrained triaxial monotonic simulations. These were performed to gain an understanding of the monotonic behaviour of sand which is an essential precursor to the cyclic loading tests. Constant-volume (CV) simulations assume that the soil is fully saturated and

water is incompressible. The CV method has the advantage of computational simplicity. However, the stresses generated during shearing a dense sample are unrealistically high. This may be caused by an initial unrealistically stiff response of Hertzian spheres using the particle shear modulus of quartz. With rotational resistance in DEM simulations, the initial peak value, angle of shear resistance value and stress ratio value at CSL are closer to physical tests. However, the stresses generated during shearing are higher than simulations without rotational resistance.

These problems mean that an alternative to the constant-volume method should be sought which retains the method's computational efficiency but without the unphysicality for dense soils. Chapter 4 will discuss a computationally efficient and physically justifiable alternative to the conventional constant-volume method using perfect spheres in DEM.

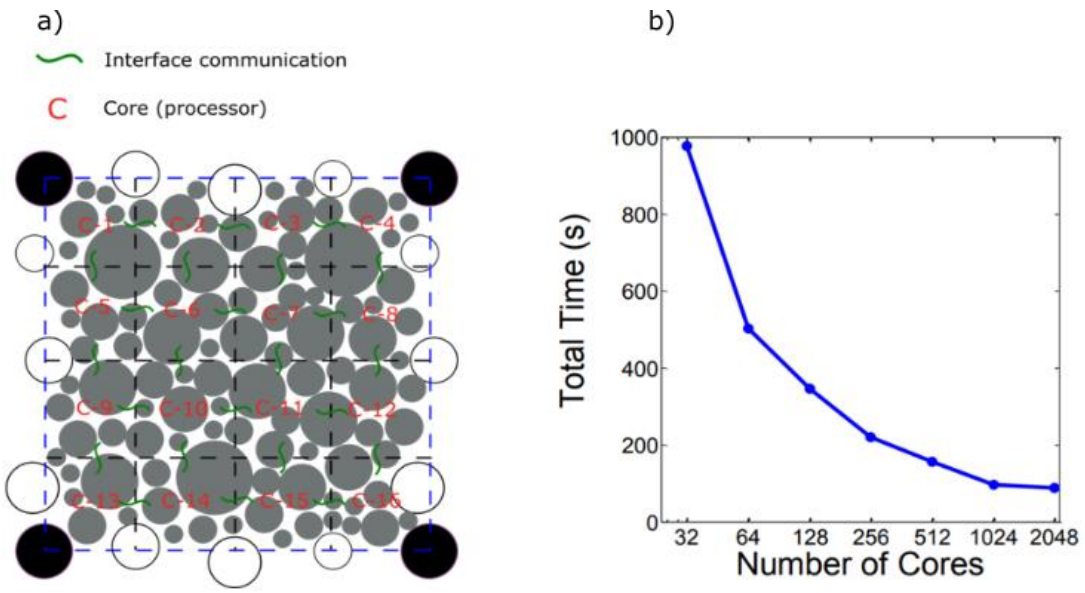

Figure 3.1: a) Schematic of domain partition (C denotes core) into 16 subdomains in 2D space (Munjiza, 2004) (b) Scaling test results for a triaxial compression DEM simulation consisting of 125,000 uniform spheres in a face-centred-cubic assembly, run for 100,000 time steps on HECToR Phase 3 using LAMMPS by Dr Kevin Hanley (Huang, 2014)

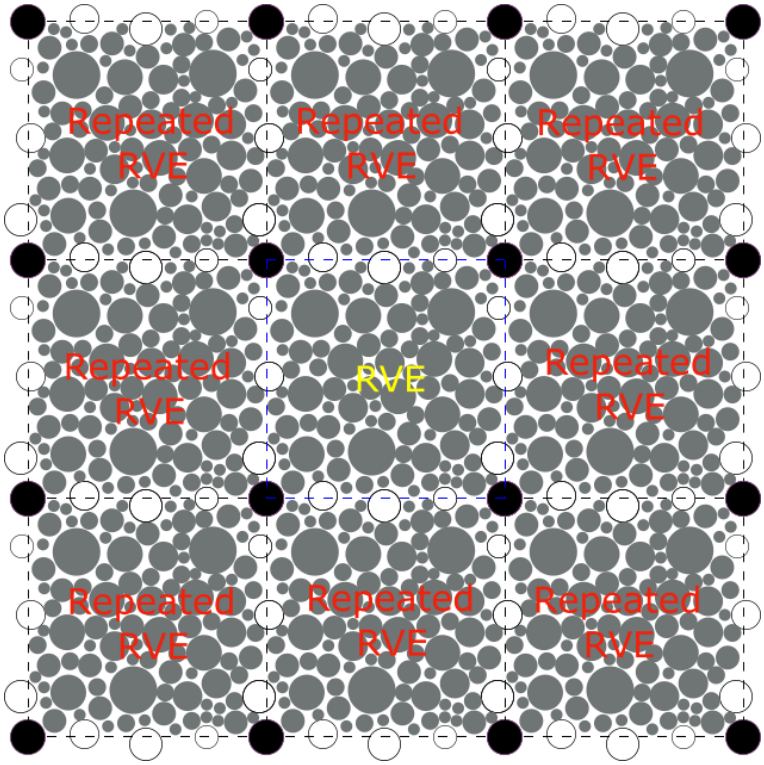

Figure 3.2: Illustration of periodic boundaries in 2D space

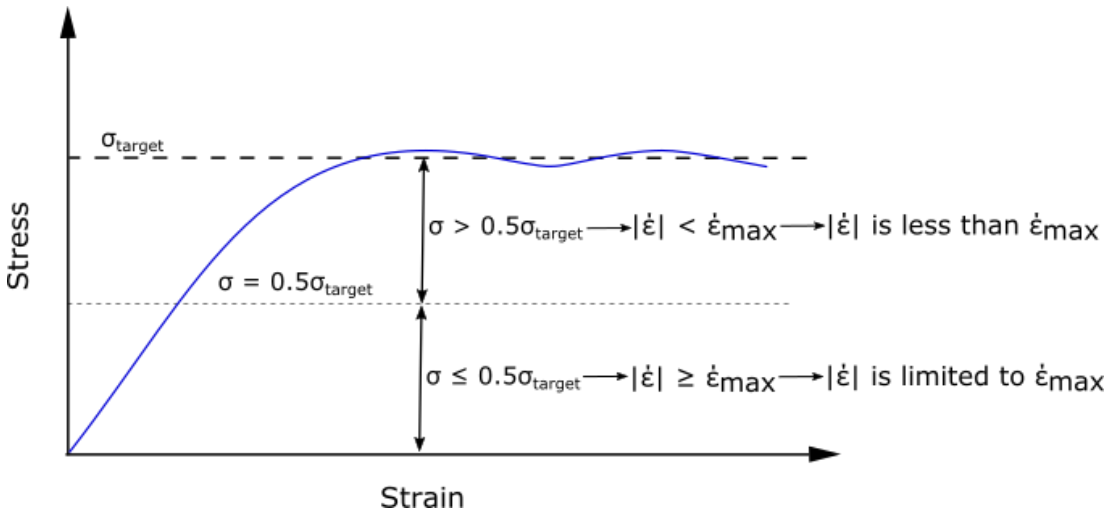

Figure 3.3: Schematic illustrating gain parameter implementation

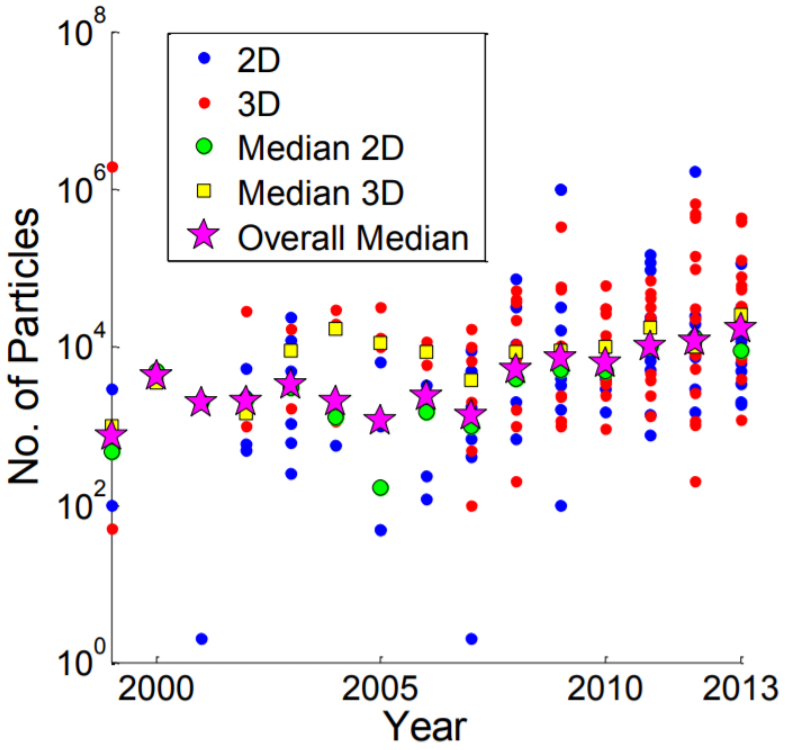

Figure 3.4: Number of particles used in published DEM simulations (O'Sullivan, 2014)

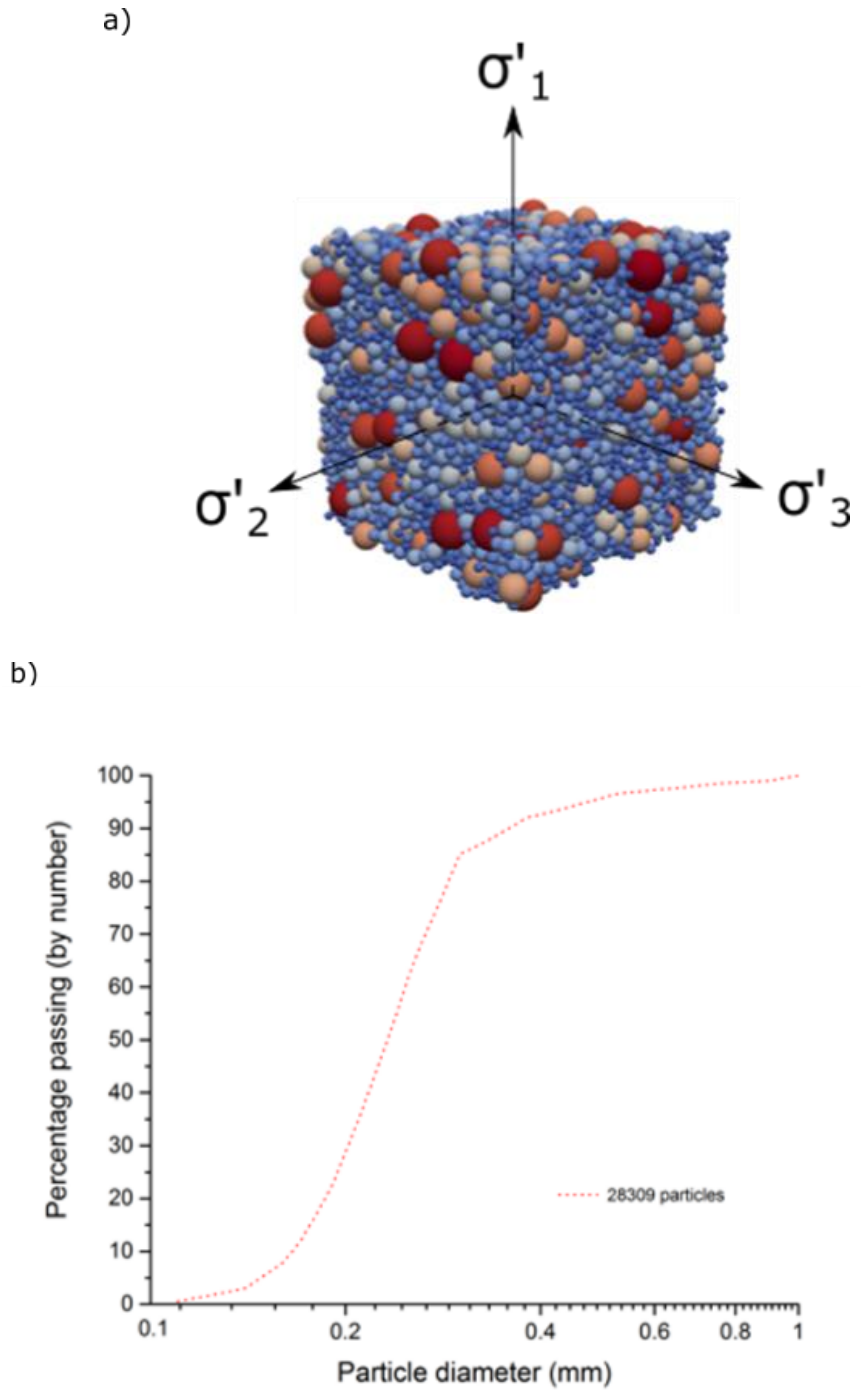

Figure 3.5: a) Assembly of particles and b) particle size distribution (PSD) used in this study

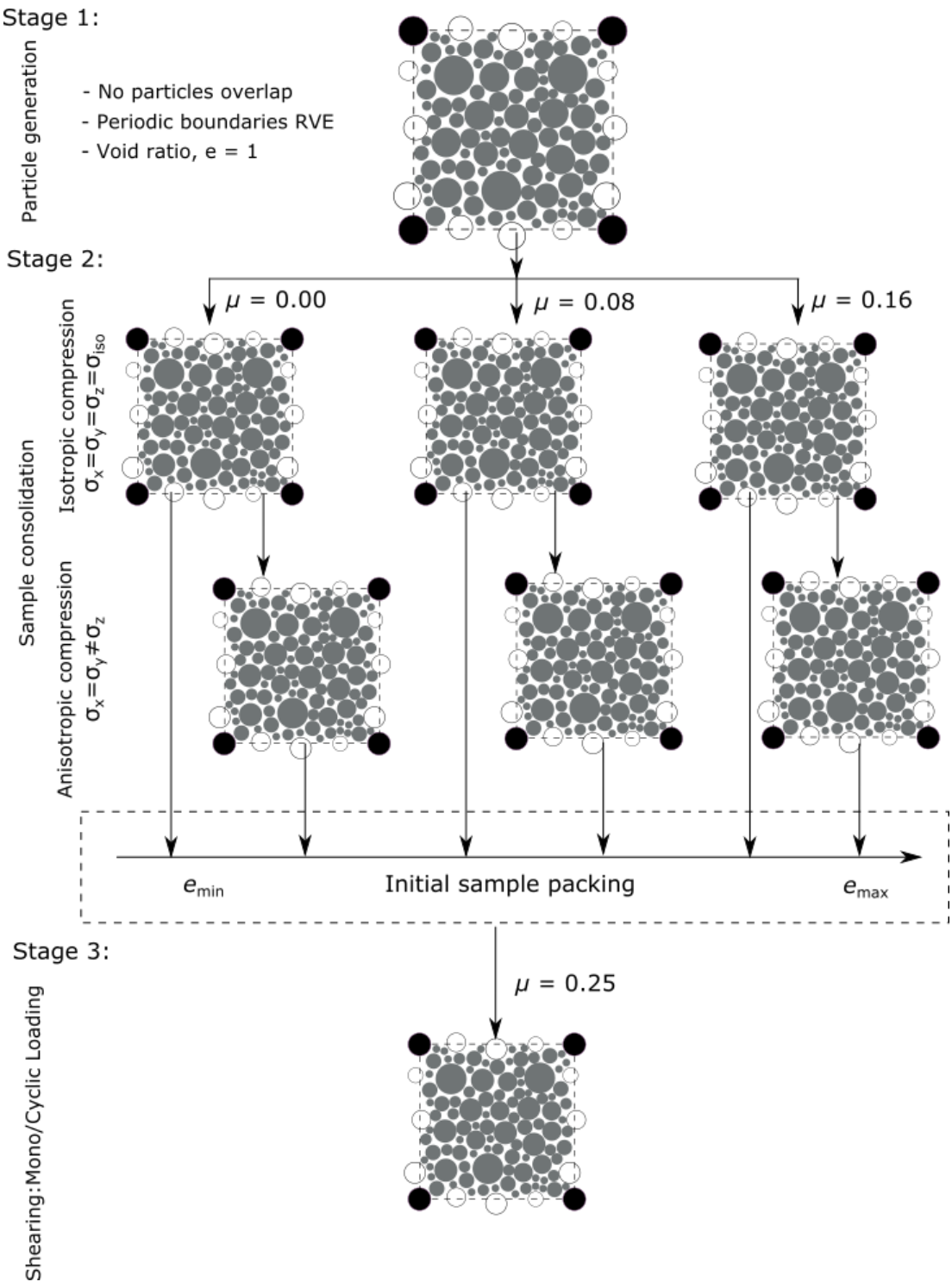

Figure 3.6: Sample preparation procedure used in this study

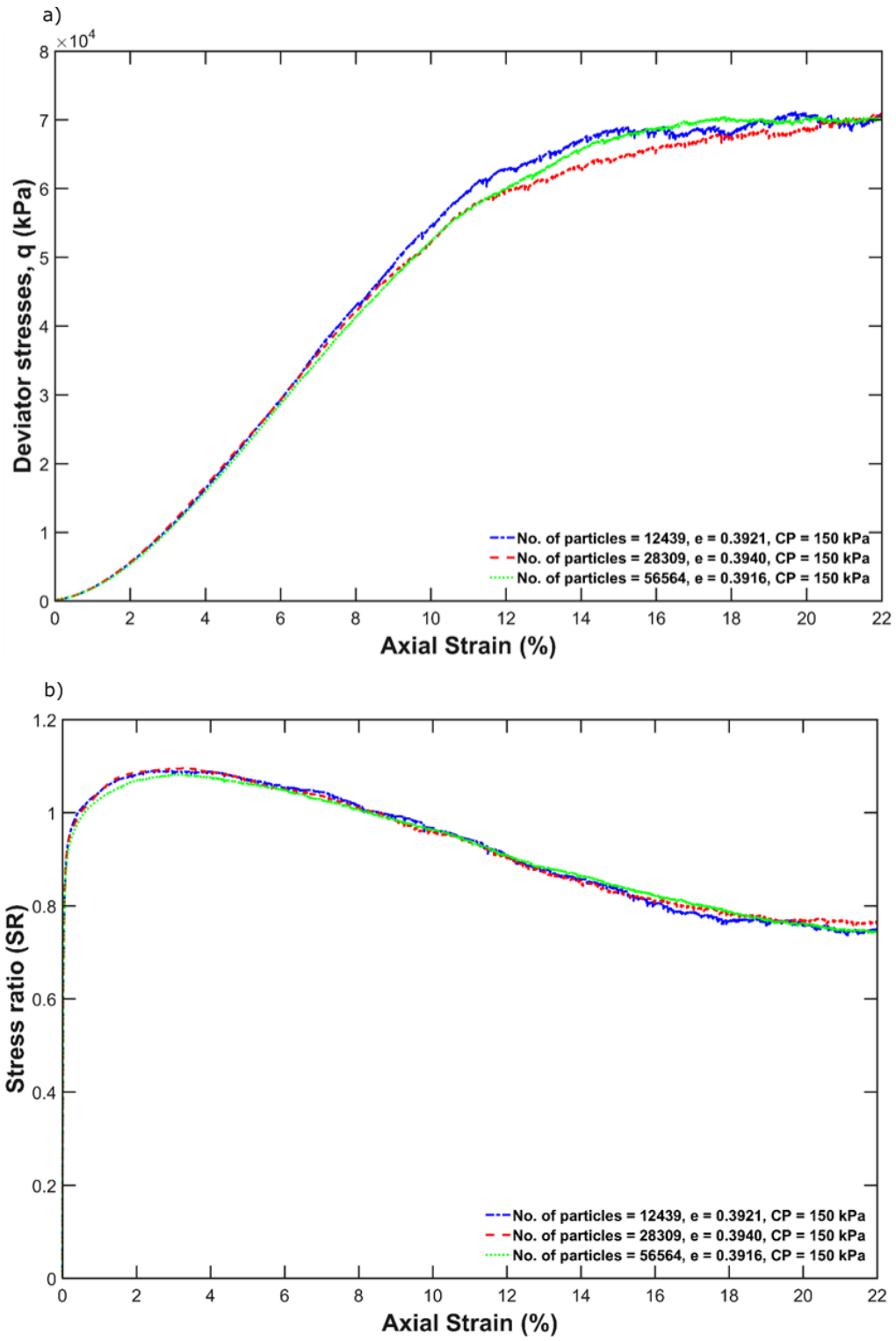

Figure 3.7: CV triaxial simulations (S1-S3) with varying numbers of particles for dense samples under fixed confining pressure, CP=150 kPa: a) Deviator stresses in kPa, against axial strain (%); b) Stress ratio against axial strain (%)

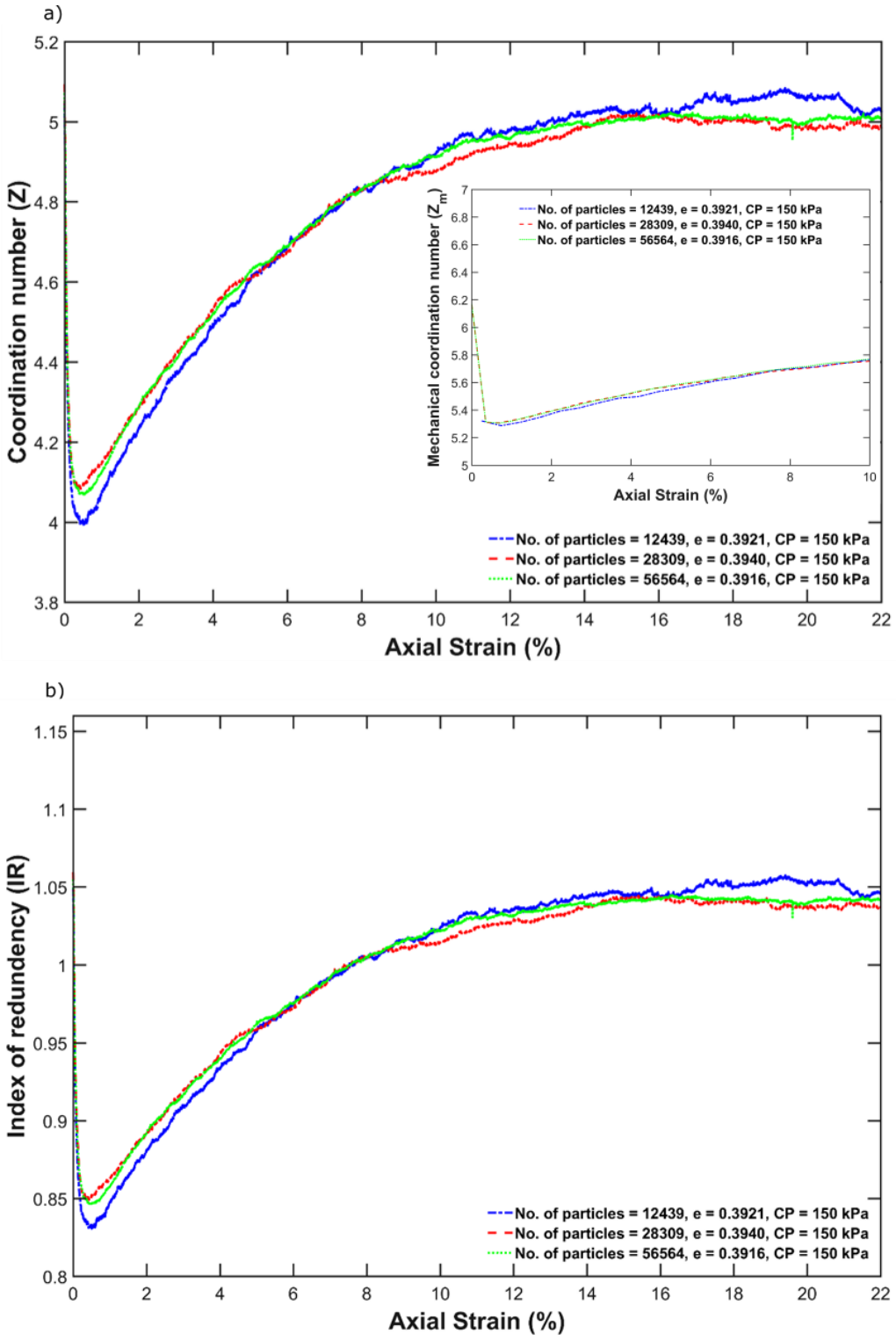

Figure 3.8: CV triaxial simulations (S1-S3) with varying numbers of particles for dense samples under fixed confining pressure, CP=150 kPa: a) Coordination number against axial strain (%) and b) Index of redundancy against axial strain (%).

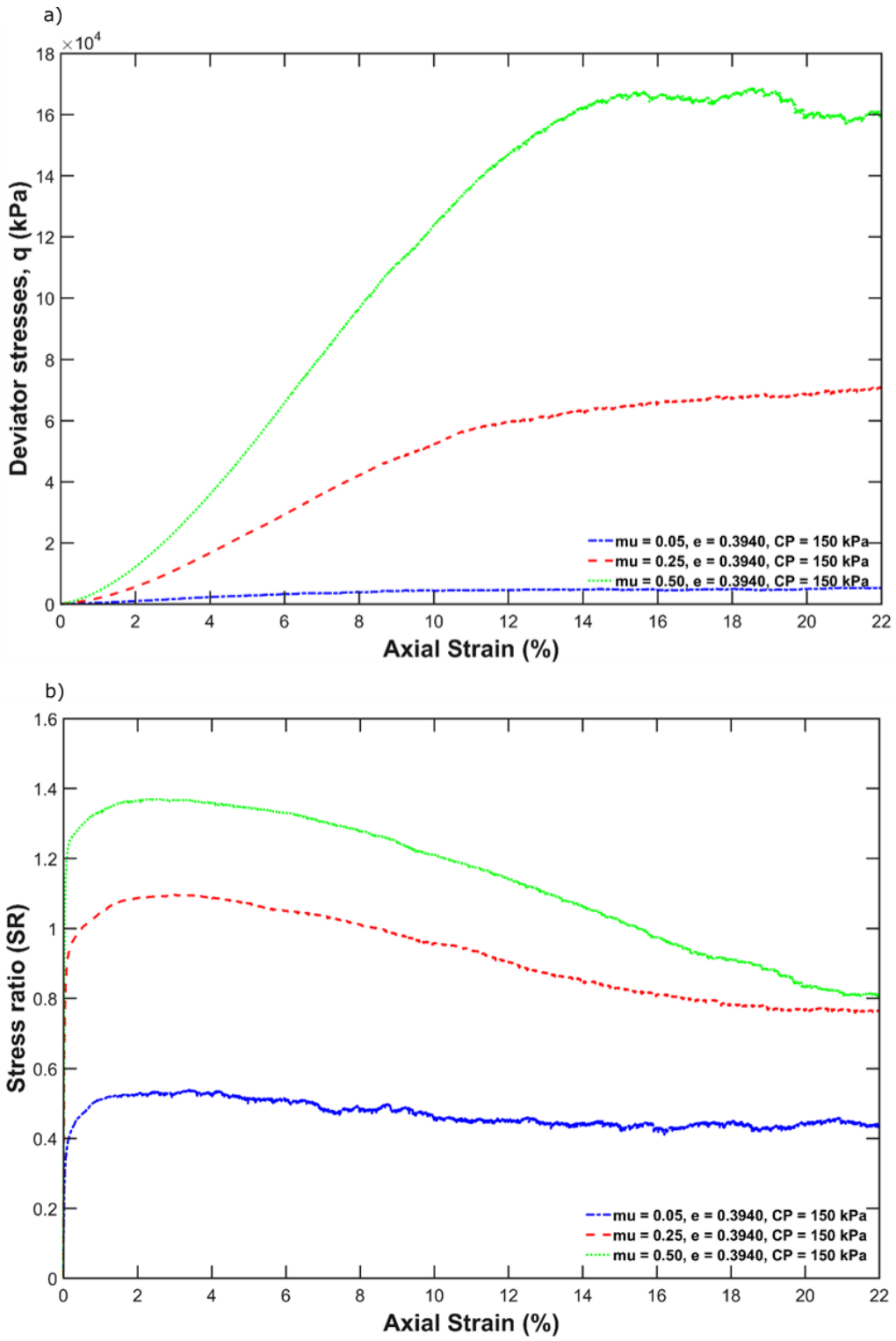

Figure 3.9: CV triaxial simulations (S2, S4 and S5) with varying interparticle coefficient of friction for a dense sand sample with a fixed void ratio, e= 0.3940 and confining pressure, CP=150 kPa: a) Deviator stresses in kPa, against axial strain (%) and b) Stress ratio against axial strain (%).

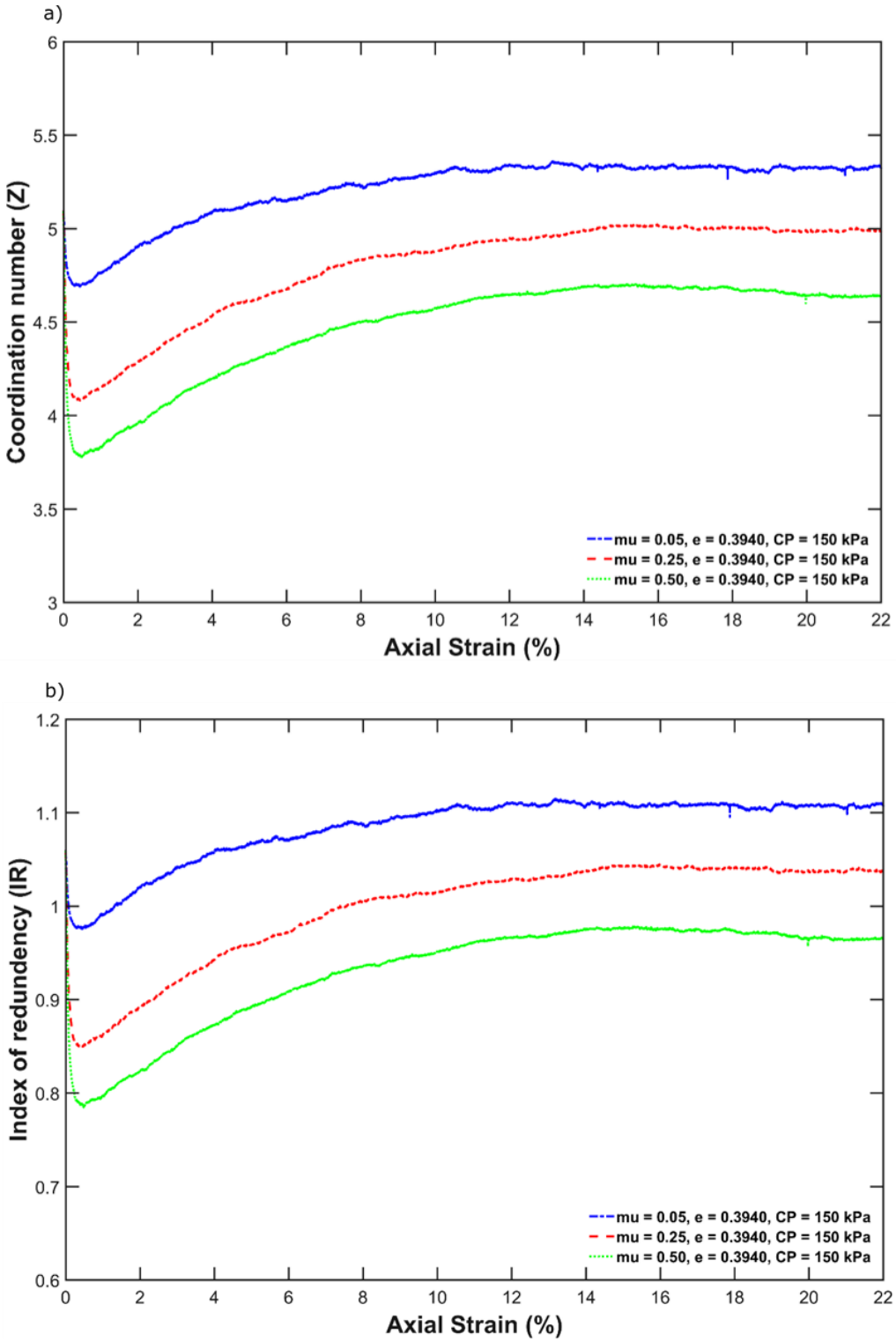

Figure 3.10: CV triaxial simulations (S2, S4 and S5) with varying interparticle coefficient of friction for a dense sand sample with a fixed void ratio, e= 0.3940 and confining pressure, CP=150 kPa: a) Coordination number against axial strain (%) and b) Index of redundancy against axial strain (%).

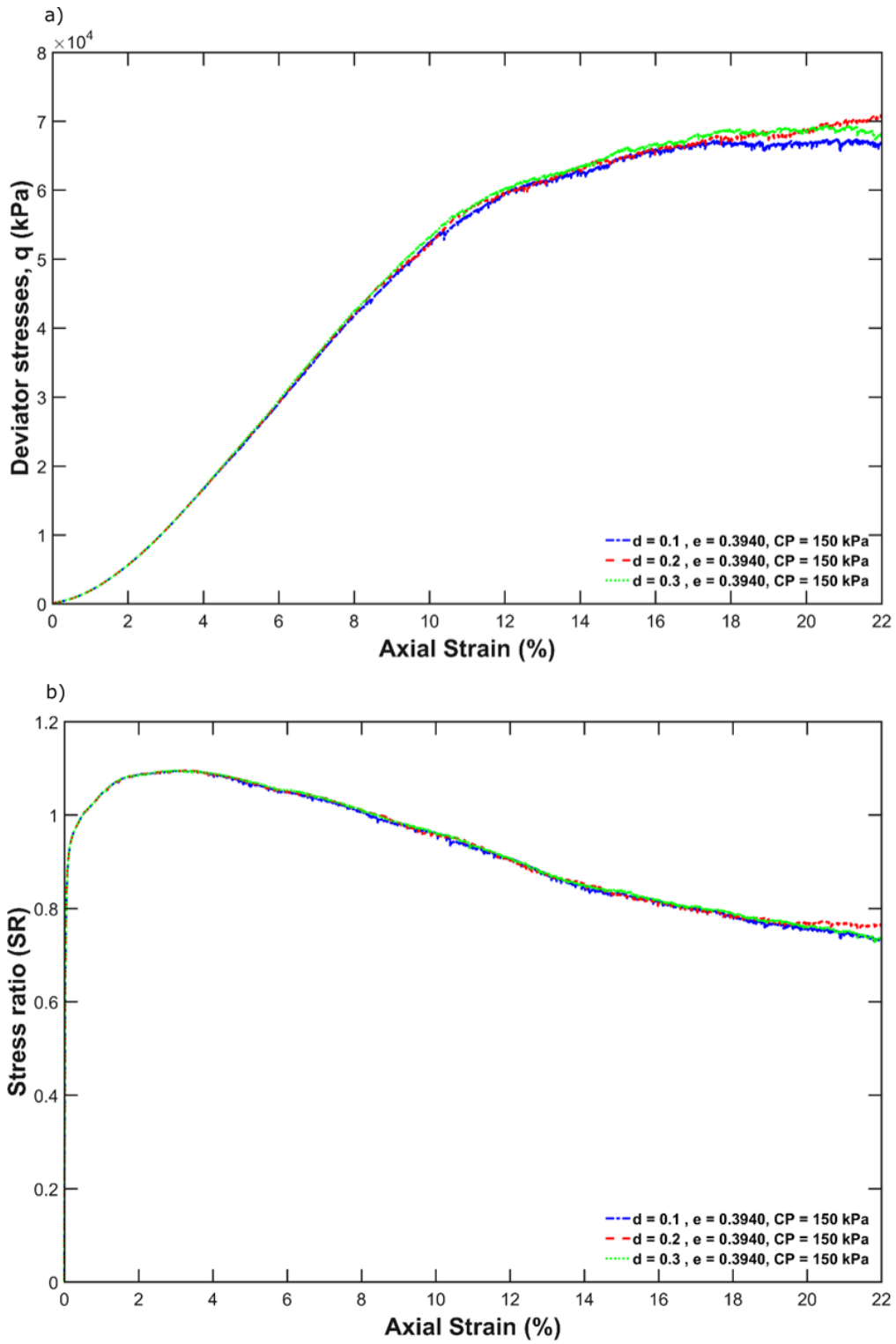

Figure 3.11: CV triaxial simulations (S2, S6 and S7) with varying local damping coefficient, d, for a dense sand sample of void ratio, e= 0.3940 under fixed confining pressure, CP=150 kPa: a) Deviator stresses in kPa, against axial strain (%) and b) Stress ratio against axial strain (%).

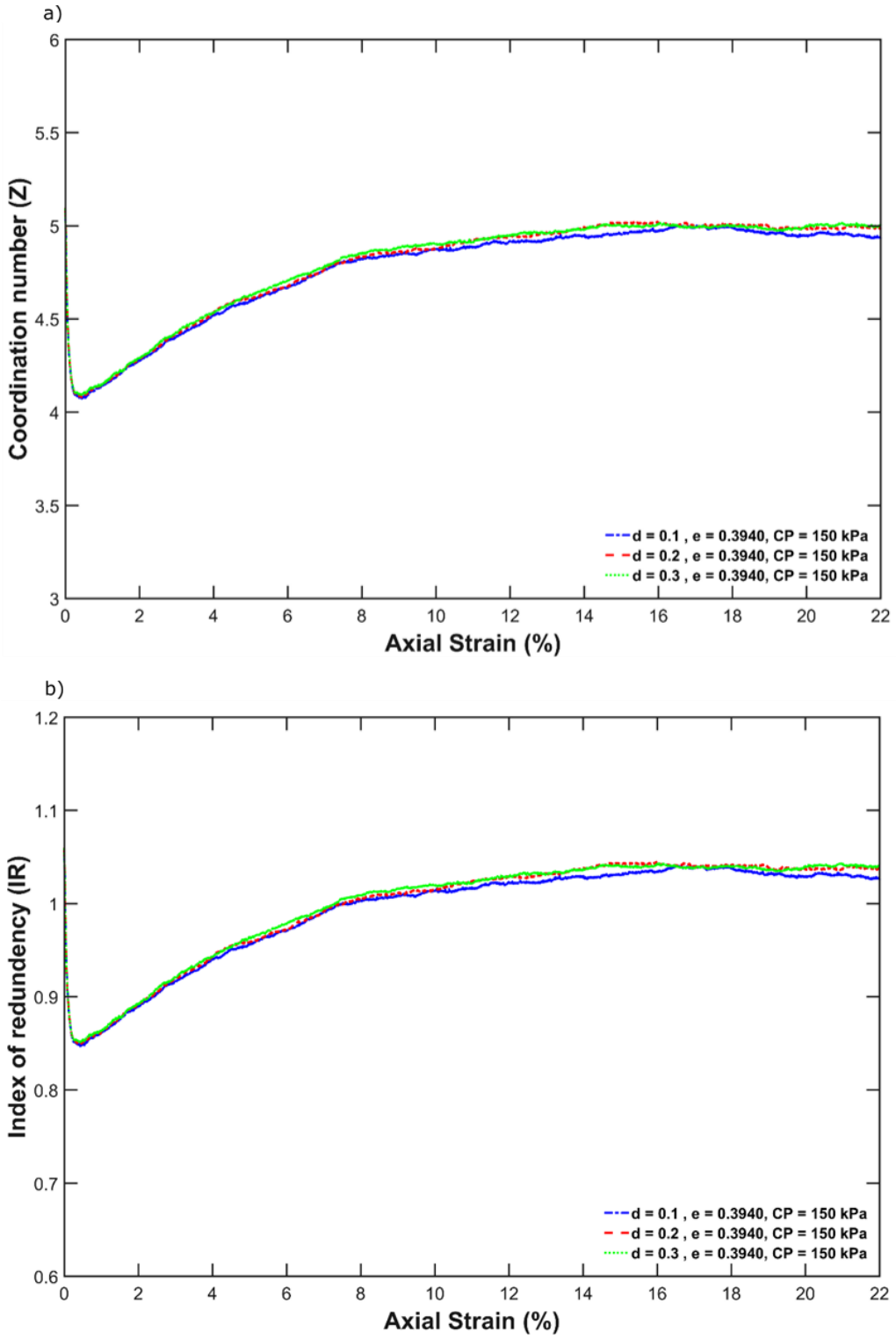

Figure 3.12: CV triaxial simulations (S2, S6 and S7) with varying local damping coefficient, d, for a dense sand sample of void ratio, e= 0.3940 under fixed confining pressure, CP=150 kPa: a) Coordination number against axial strain (%) and b) Index of redundancy against axial strain (%).

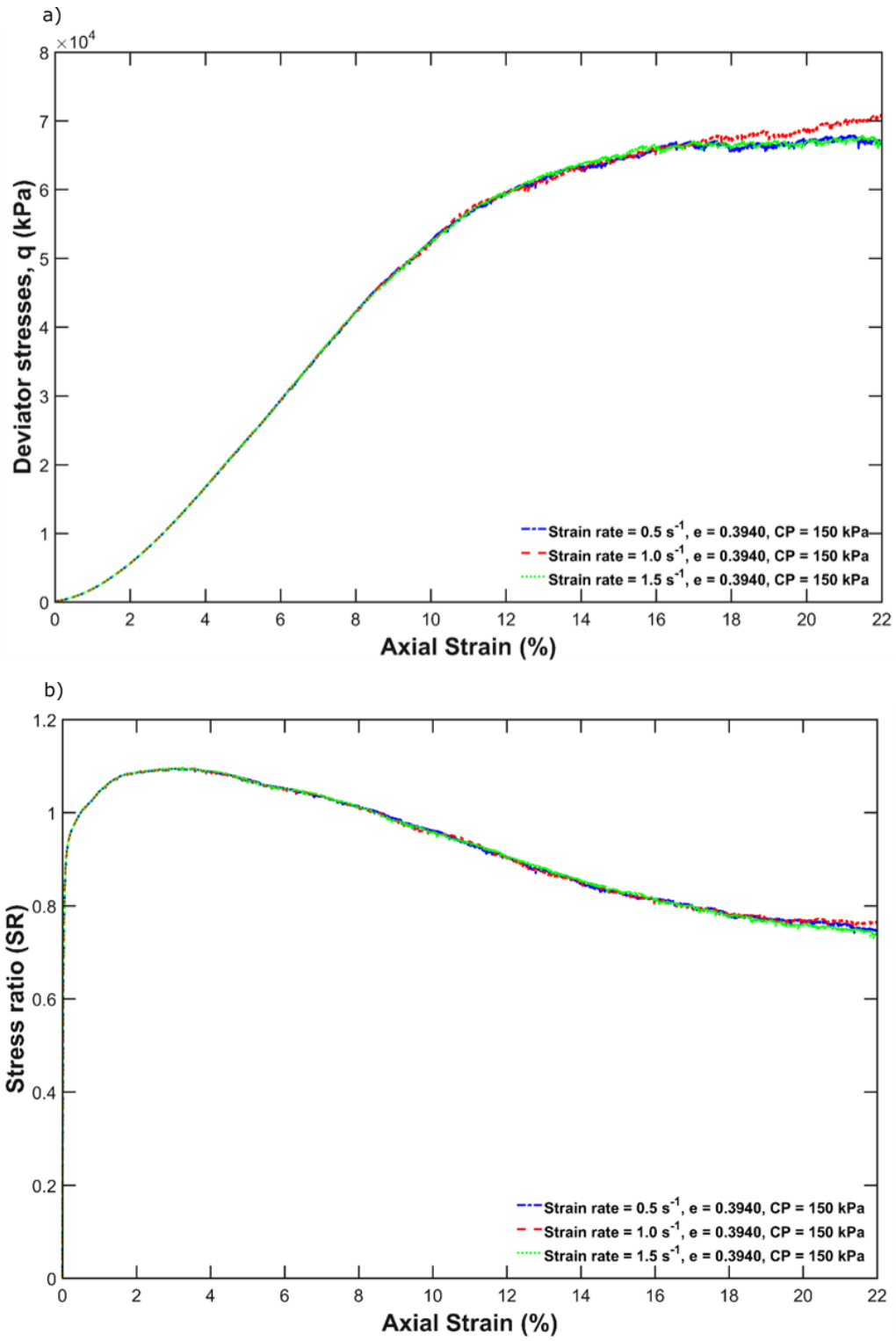

Figure 3.13: CV triaxial simulations (S2, S8 and S9) with varying strain rate for a dense sand sample of void ratio, e= 0.3940 under fixed confining pressure, CP=150 kPa: a) Deviator stresses in kPa, against axial strain (%) and b) Stress ratio against axial strain (%).

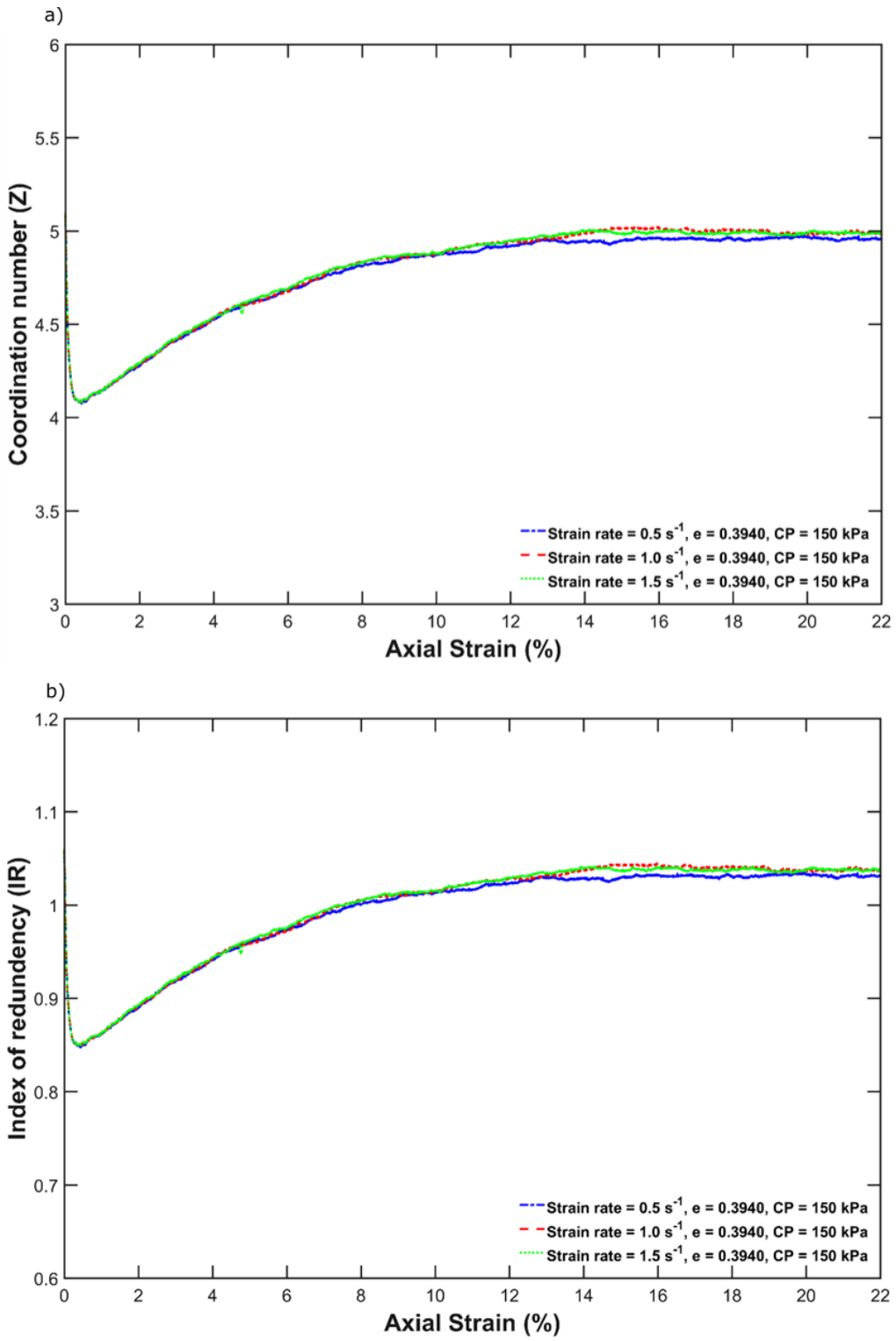

Figure 3.14: CV triaxial simulations (S2, S8 and S9) with varying strain rate for a dense sand sample of void ratio, e= 0.3940 under fixed confining pressure, CP=150 kPa: a) Coordination number against axial strain (%) and b) Index of redundancy against axial strain (%).

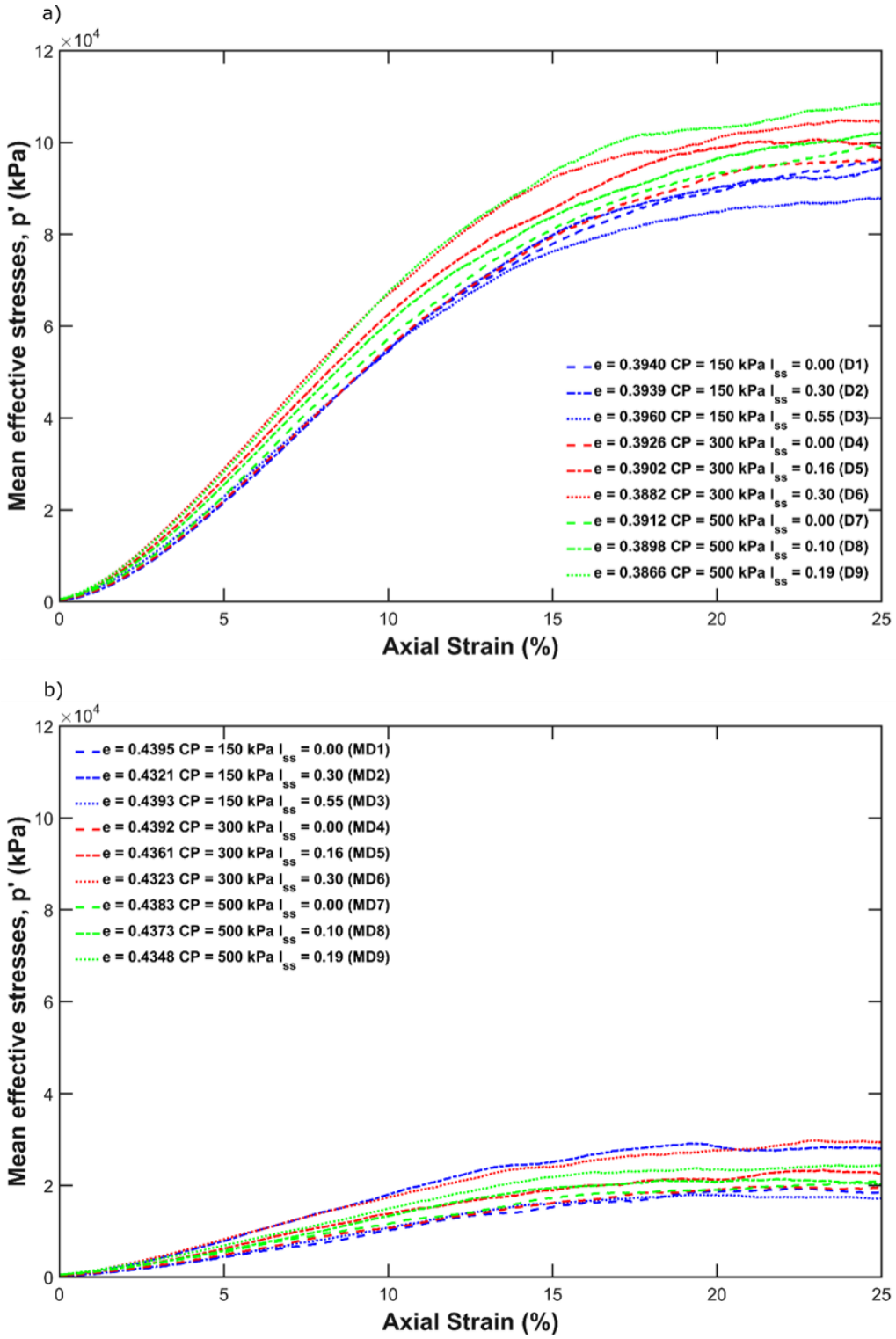
a)
×10^4
Mean effective stresses, p' (kPa)
Axial Strain (%)
e = 0.3940 CP = 150 kPa I_ss = 0.00 (D1)
e = 0.3939 CP = 150 kPa I_ss = 0.30 (D2)
e = 0.3960 CP = 150 kPa I_ss = 0.55 (D3)
e = 0.3926 CP = 300 kPa I_ss = 0.00 (D4)
e = 0.3902 CP = 300 kPa I_ss = 0.16 (D5)
e = 0.3882 CP = 300 kPa I_ss = 0.30 (D6)
e = 0.3912 CP = 500 kPa I_ss = 0.00 (D7)
e = 0.3898 CP = 500 kPa I_ss = 0.10 (D8)
e = 0.3866 CP = 500 kPa I_ss = 0.19 (D9)
b)
×10^4
Mean effective stresses, p' (kPa)
Axial Strain (%)
e = 0.4395 CP = 150 kPa I_ss = 0.00 (MD1)
e = 0.4321 CP = 150 kPa I_ss = 0.30 (MD2)
e = 0.4393 CP = 150 kPa I_ss = 0.55 (MD3)
e = 0.4392 CP = 300 kPa I_ss = 0.00 (MD4)
e = 0.4361 CP = 300 kPa I_ss = 0.16 (MD5)
e = 0.4323 CP = 300 kPa I_ss = 0.30 (MD6)
e = 0.4383 CP = 500 kPa I_ss = 0.00 (MD7)
e = 0.4373 CP = 500 kPa I_ss = 0.10 (MD8)
e = 0.4348 CP = 500 kPa I_ss = 0.19 (MD9)

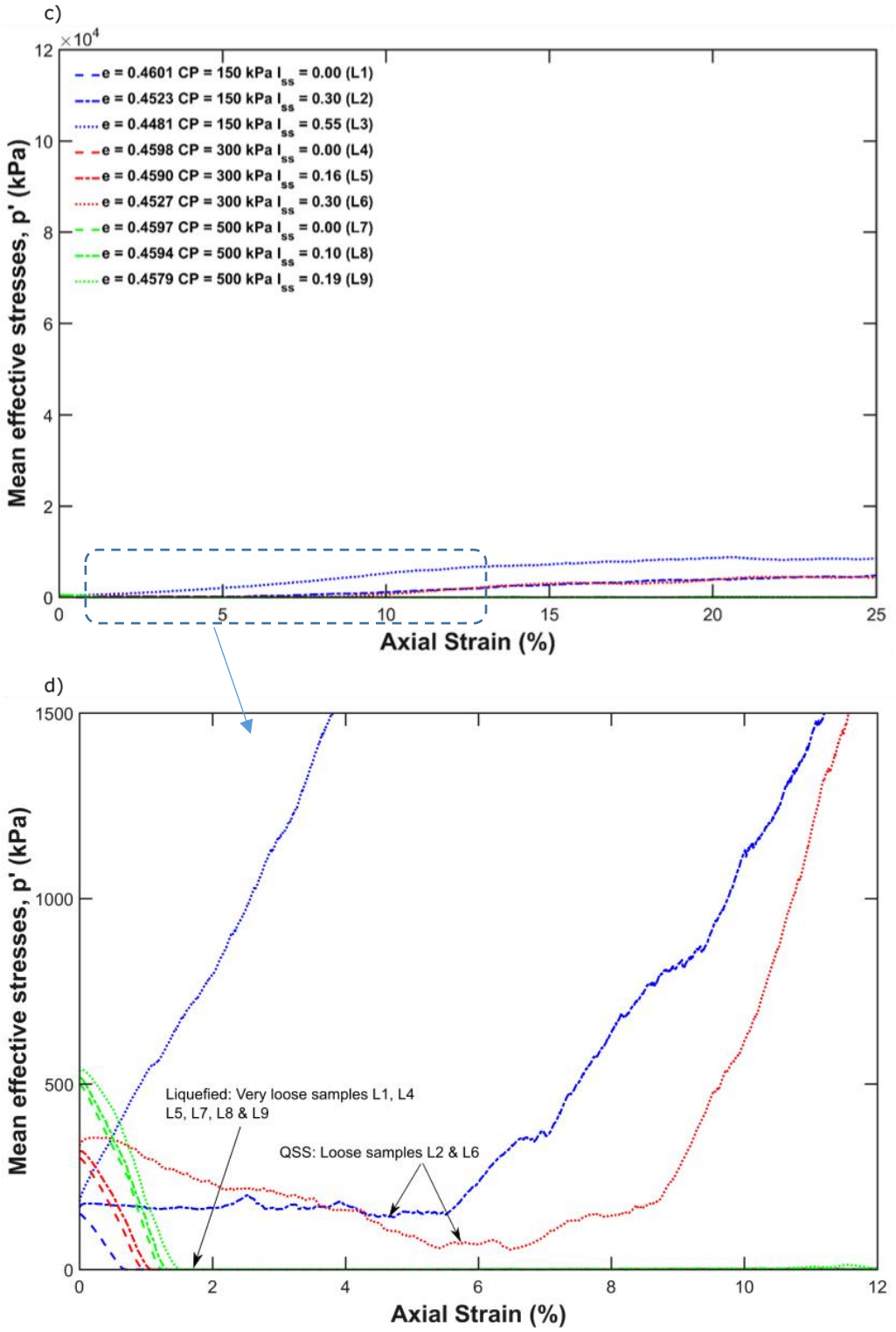

Figure 3.15: Mean effective stresses in kPa, against axial strain (%) for the 27 CV triaxial simulations. a) dense samples, D1-D9; b) medium-dense samples, MD1-MD9; c) loose samples, L1-L9 and d) zoom view of loose samples, L1-L9.

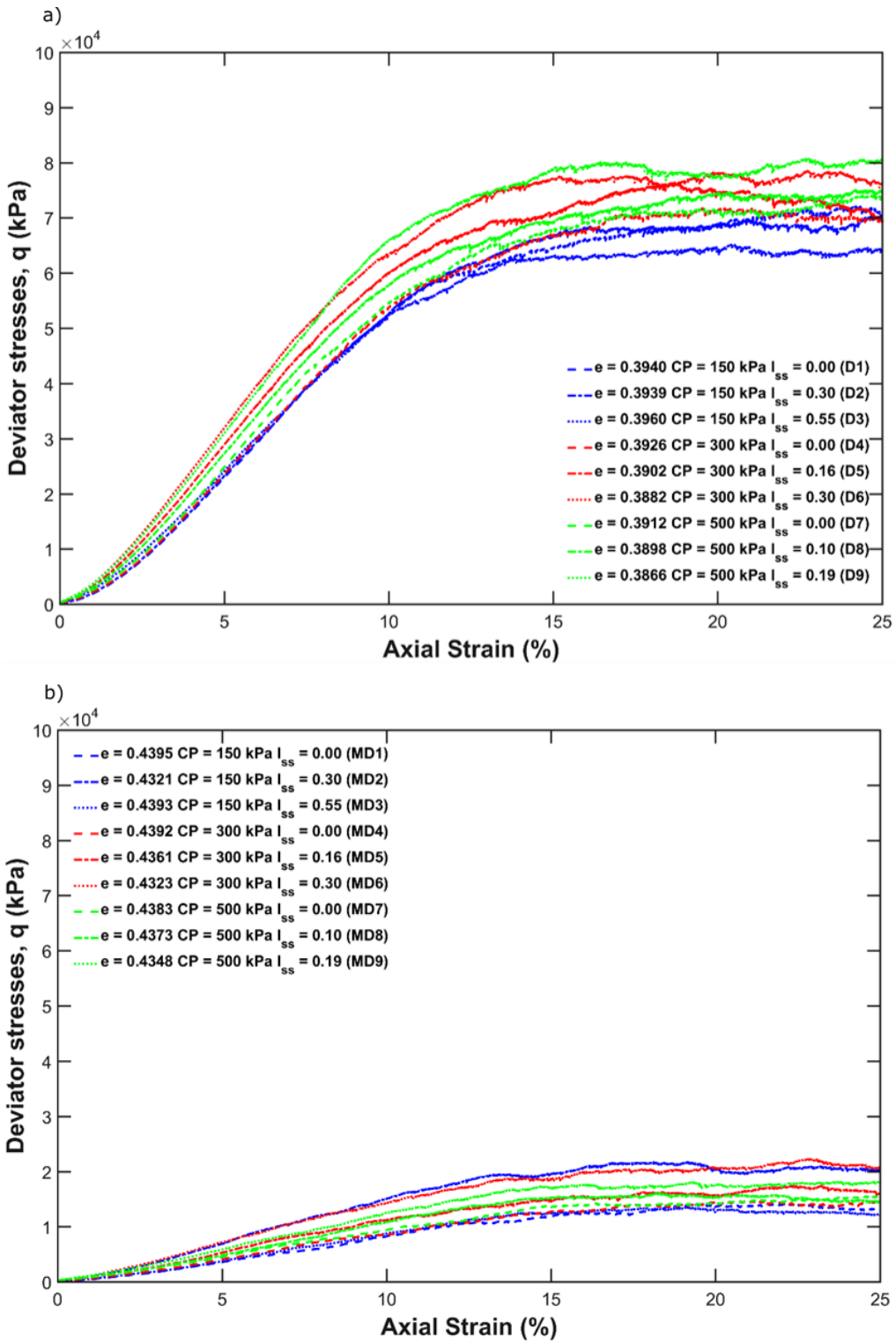
a)
×10^4
Deviator stresses, q (kPa)
Axial Strain (%)
e = 0.3940 CP = 150 kPa I_ss = 0.00 (D1)
e = 0.3939 CP = 150 kPa I_ss = 0.30 (D2)
e = 0.3960 CP = 150 kPa I_ss = 0.55 (D3)
e = 0.3926 CP = 300 kPa I_ss = 0.00 (D4)
e = 0.3902 CP = 300 kPa I_ss = 0.16 (D5)
e = 0.3882 CP = 300 kPa I_ss = 0.30 (D6)
e = 0.3912 CP = 500 kPa I_ss = 0.00 (D7)
e = 0.3898 CP = 500 kPa I_ss = 0.10 (D8)
e = 0.3866 CP = 500 kPa I_ss = 0.19 (D9)
b)
×10^4
Deviator stresses, q (kPa)
Axial Strain (%)
e = 0.4395 CP = 150 kPa I_ss = 0.00 (MD1)
e = 0.4321 CP = 150 kPa I_ss = 0.30 (MD2)
e = 0.4393 CP = 150 kPa I_ss = 0.55 (MD3)
e = 0.4392 CP = 300 kPa I_ss = 0.00 (MD4)
e = 0.4361 CP = 300 kPa I_ss = 0.16 (MD5)
e = 0.4323 CP = 300 kPa I_ss = 0.30 (MD6)
e = 0.4383 CP = 500 kPa I_ss = 0.00 (MD7)
e = 0.4373 CP = 500 kPa I_ss = 0.10 (MD8)
e = 0.4348 CP = 500 kPa I_ss = 0.19 (MD9)

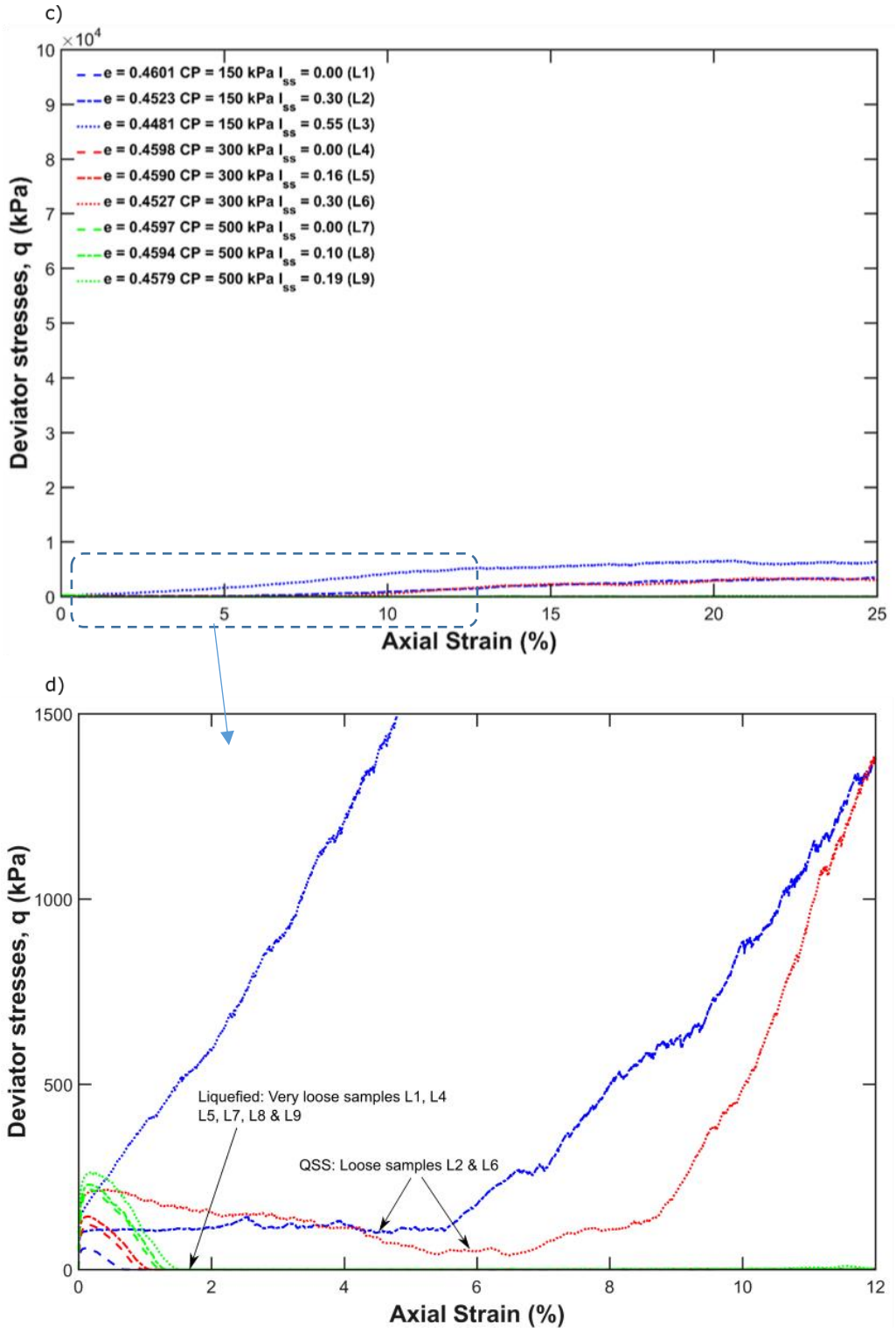

Figure 3.16: Deviator stresses in kPa, against axial strain (%) for the 27 CV triaxial simulations. a) dense samples, D1-D9; b) medium-dense samples, MD1-MD9; c) loose samples, L1-L9 and d) zoom view of loose samples, L1-L9.

a)

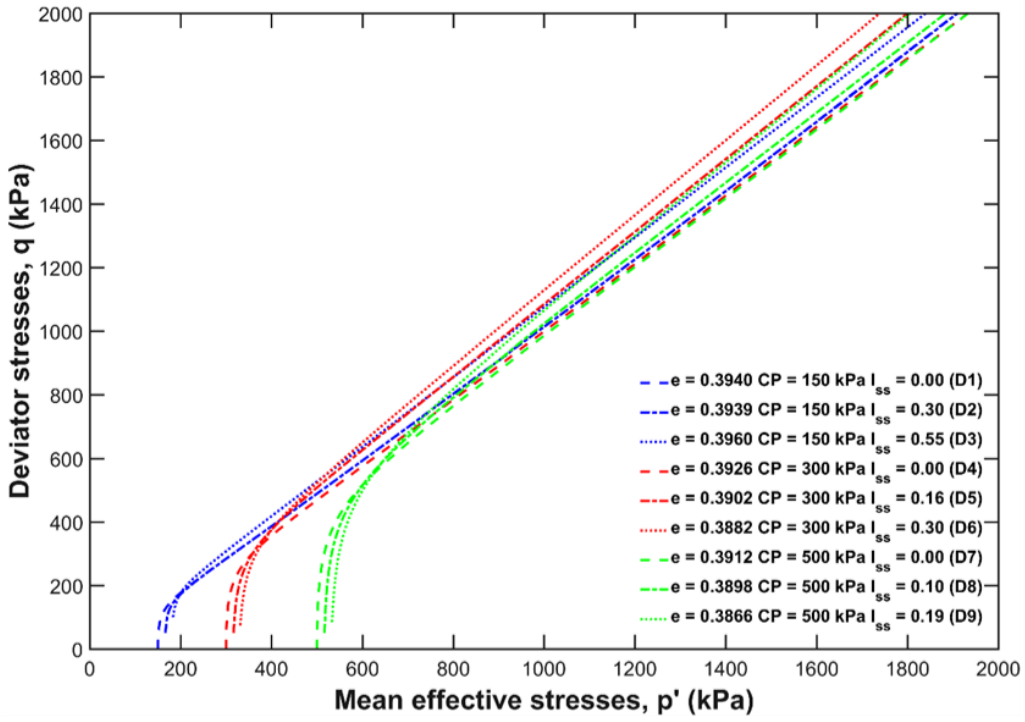
Deviator stresses, q (kPa)
Mean effective stresses, p' (kPa)
e = 0.3940 CP = 150 kPa I_ss = 0.00 (D1)
e = 0.3939 CP = 150 kPa I_ss = 0.30 (D2)
e = 0.3960 CP = 150 kPa I_ss = 0.55 (D3)
e = 0.3926 CP = 300 kPa I_ss = 0.00 (D4)
e = 0.3902 CP = 300 kPa I_ss = 0.16 (D5)
e = 0.3882 CP = 300 kPa I_ss = 0.30 (D6)
e = 0.3912 CP = 500 kPa I_ss = 0.00 (D7)
e = 0.3898 CP = 500 kPa I_ss = 0.10 (D8)
e = 0.3866 CP = 500 kPa I_ss = 0.19 (D9)

b)

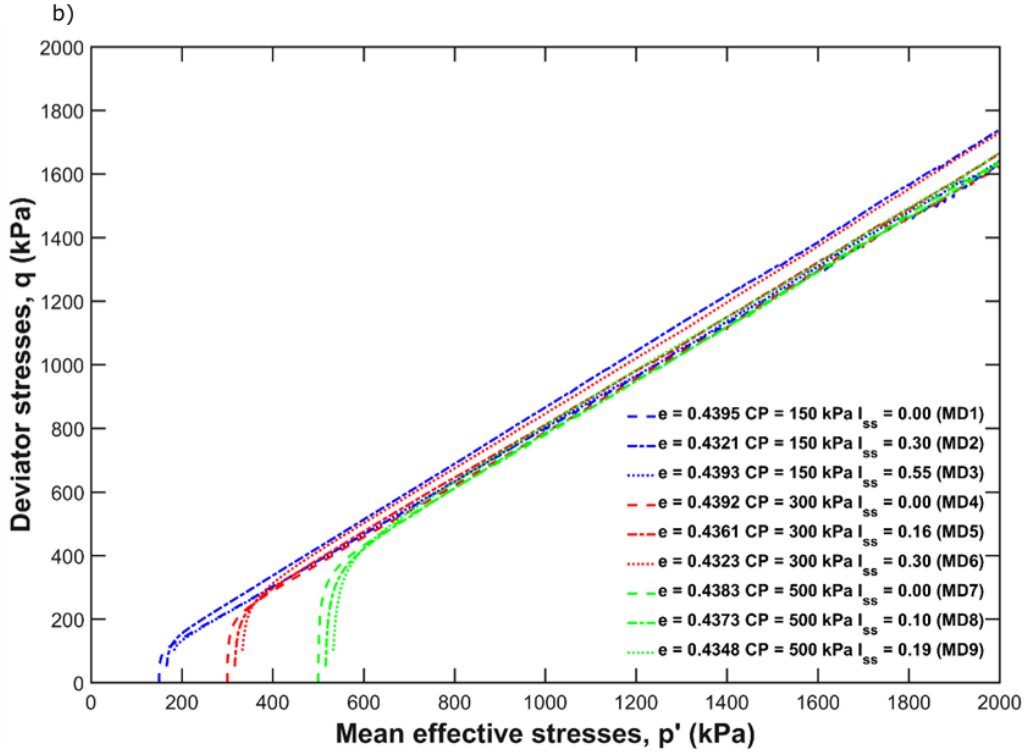
Deviator stresses, q (kPa)
Mean effective stresses, p' (kPa)
e = 0.4395 CP = 150 kPa I_ss = 0.00 (MD1)
e = 0.4321 CP = 150 kPa I_ss = 0.30 (MD2)
e = 0.4393 CP = 150 kPa I_ss = 0.55 (MD3)
e = 0.4392 CP = 300 kPa I_ss = 0.00 (MD4)
e = 0.4361 CP = 300 kPa I_ss = 0.16 (MD5)
e = 0.4323 CP = 300 kPa I_ss = 0.30 (MD6)
e = 0.4383 CP = 500 kPa I_ss = 0.00 (MD7)
e = 0.4373 CP = 500 kPa I_ss = 0.10 (MD8)
e = 0.4348 CP = 500 kPa I_ss = 0.19 (MD9)

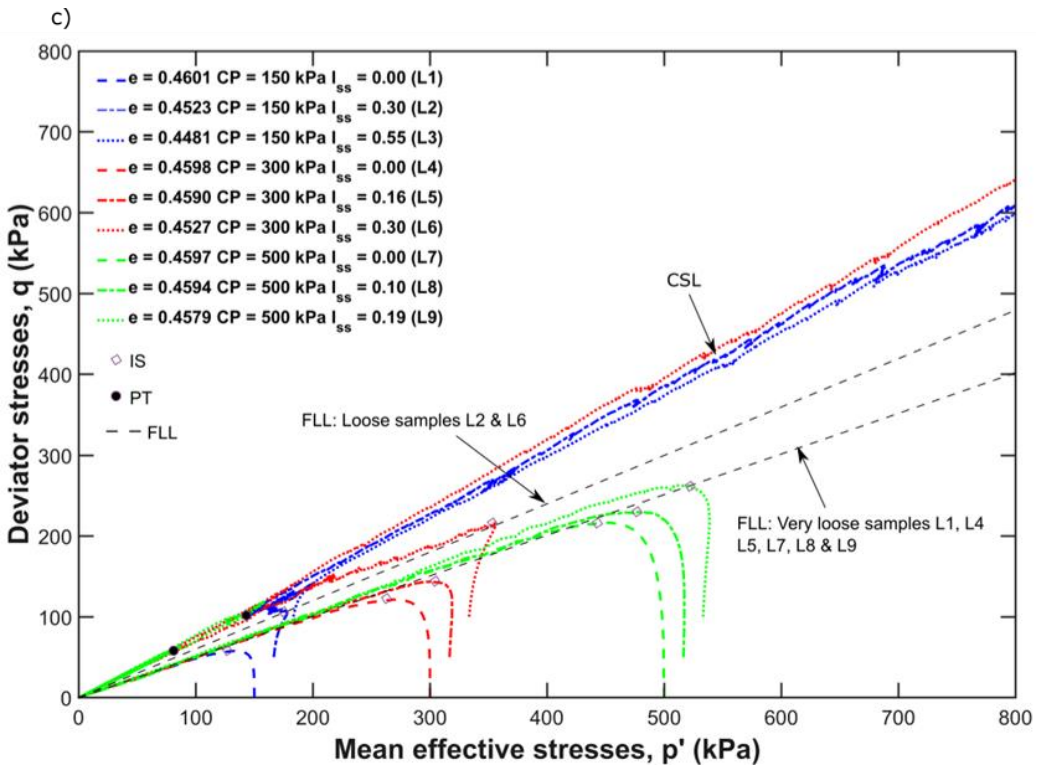

Figure 3.17: q-p' plot for the 27 CV triaxial simulations at initial shearing. a) dense samples, D1-D9; b) medium-dense samples, MD1-MD9 and c) loose samples, L1-L9.

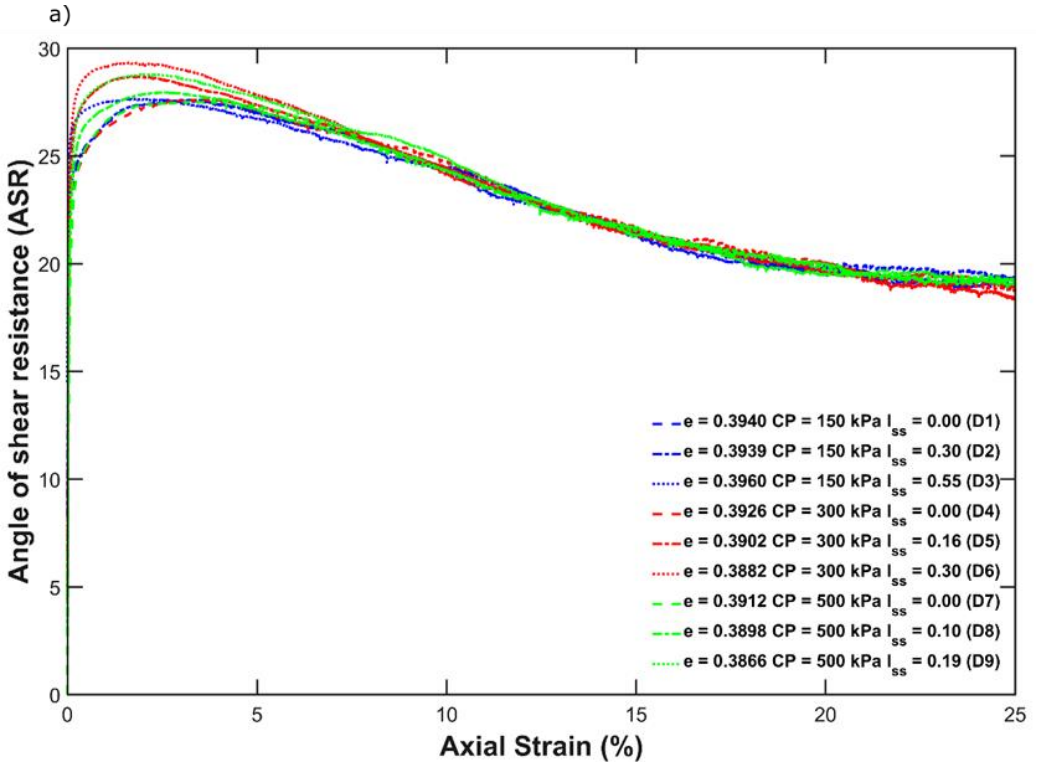

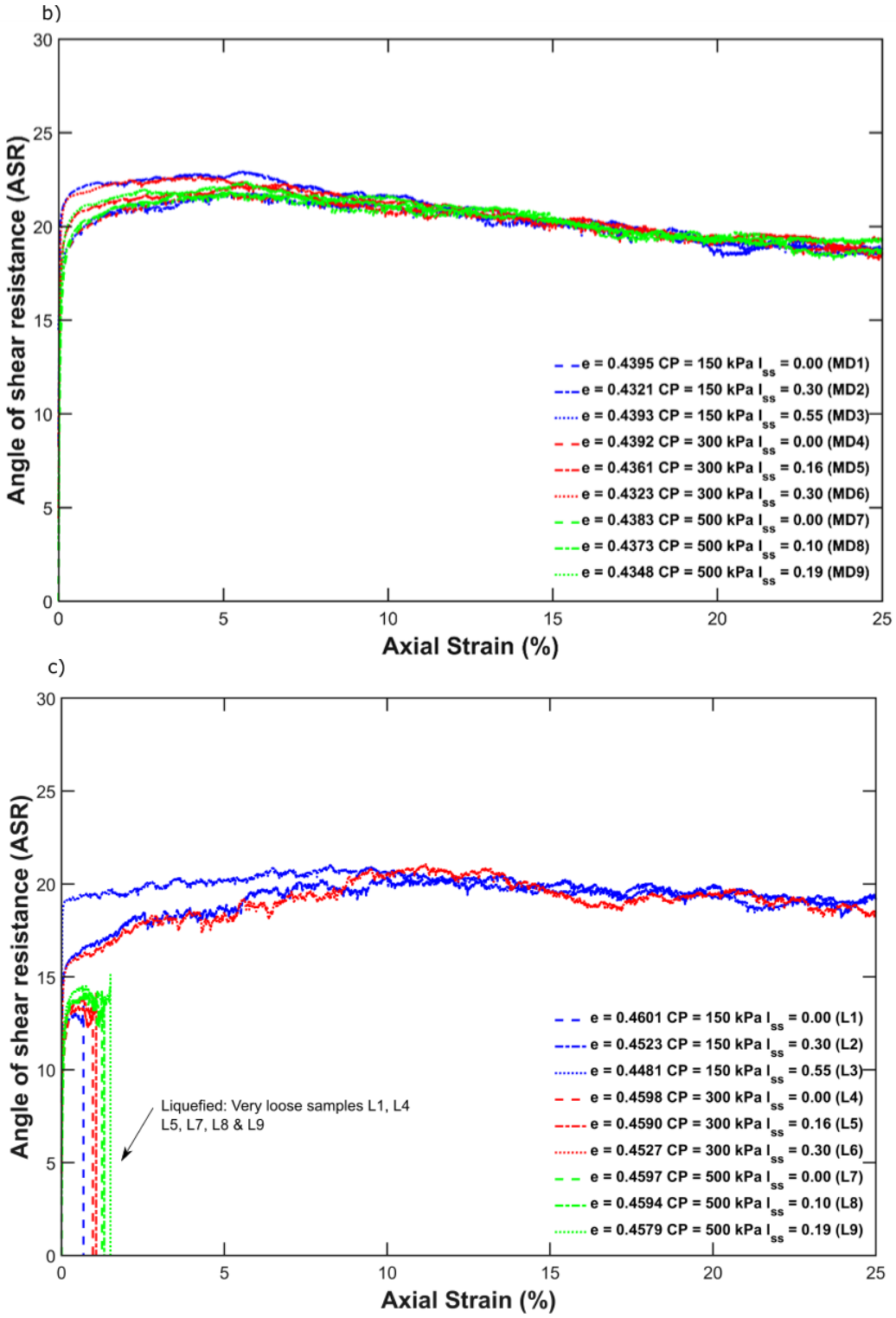

Figure 3.18: Angle of shearing resistance, ASR, in degree, against axial strain (%) for the 27 CV triaxial simulations. a) dense samples, D1-D9; b) medium-dense samples, MD1-MD9 and c) loose samples, L1-L9

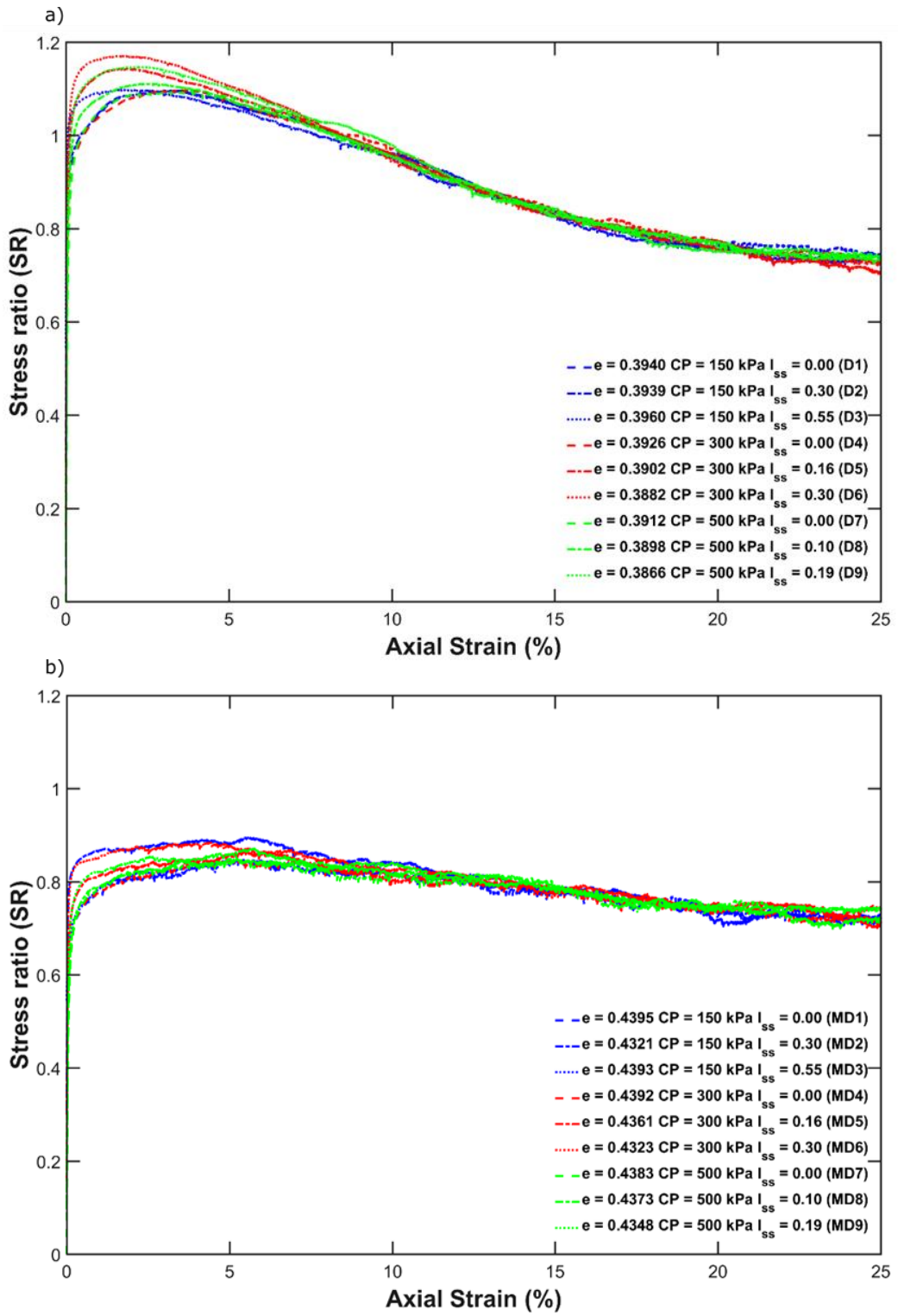
a)
Stress ratio (SR)
Axial Strain (%)
e = 0.3940 CP = 150 kPa I_ss = 0.00 (D1)
e = 0.3939 CP = 150 kPa I_ss = 0.30 (D2)
e = 0.3960 CP = 150 kPa I_ss = 0.55 (D3)
e = 0.3926 CP = 300 kPa I_ss = 0.00 (D4)
e = 0.3902 CP = 300 kPa I_ss = 0.16 (D5)
e = 0.3882 CP = 300 kPa I_ss = 0.30 (D6)
e = 0.3912 CP = 500 kPa I_ss = 0.00 (D7)
e = 0.3898 CP = 500 kPa I_ss = 0.10 (D8)
e = 0.3866 CP = 500 kPa I_ss = 0.19 (D9)
b)
Stress ratio (SR)
Axial Strain (%)
e = 0.4395 CP = 150 kPa I_ss = 0.00 (MD1)
e = 0.4321 CP = 150 kPa I_ss = 0.30 (MD2)
e = 0.4393 CP = 150 kPa I_ss = 0.55 (MD3)
e = 0.4392 CP = 300 kPa I_ss = 0.00 (MD4)
e = 0.4361 CP = 300 kPa I_ss = 0.16 (MD5)
e = 0.4323 CP = 300 kPa I_ss = 0.30 (MD6)
e = 0.4383 CP = 500 kPa I_ss = 0.00 (MD7)
e = 0.4373 CP = 500 kPa I_ss = 0.10 (MD8)
e = 0.4348 CP = 500 kPa I_ss = 0.19 (MD9)

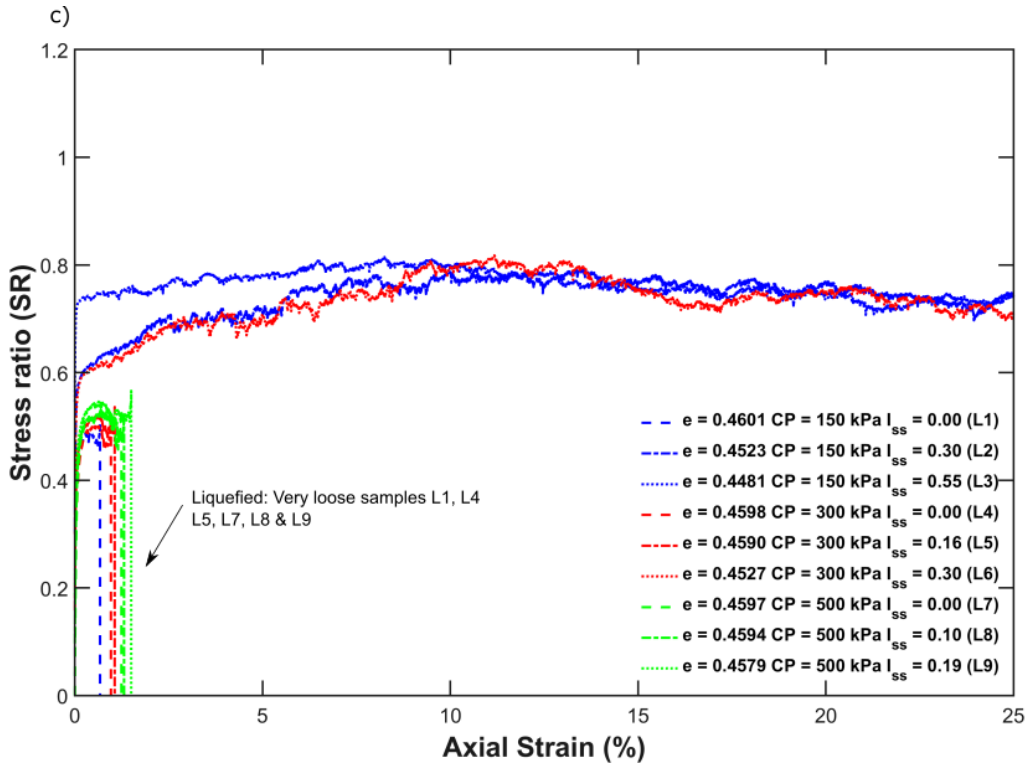

Figure 3.19: Stress ratio against axial strain (%) for the 27 CV triaxial simulations. a) dense samples, D1-D9; b) medium-dense samples, MD1-MD9 and c) loose samples, L1-L9.

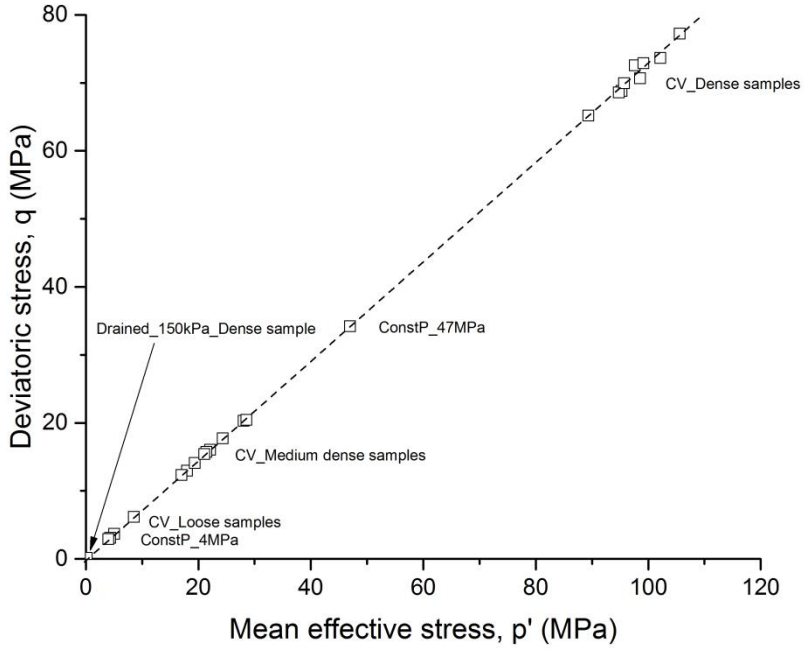

Figure 3.20: Plot of CSL for the 27 CV triaxial simulations in q-p' space.

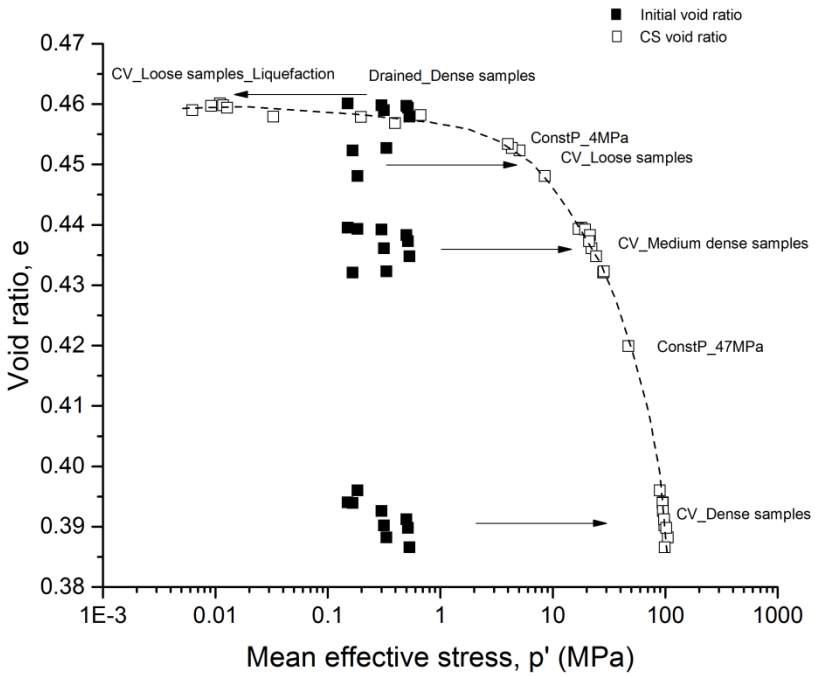

Figure 3.21: Plot of CSL for the 27 CV triaxial simulations in e-log(p') space.

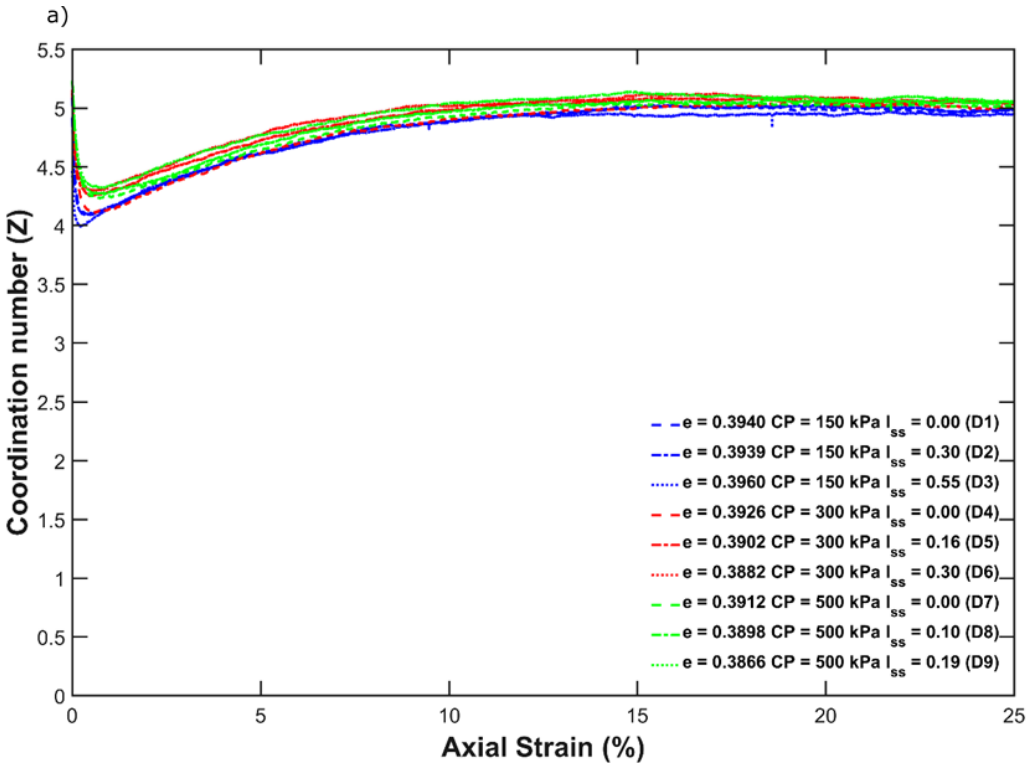

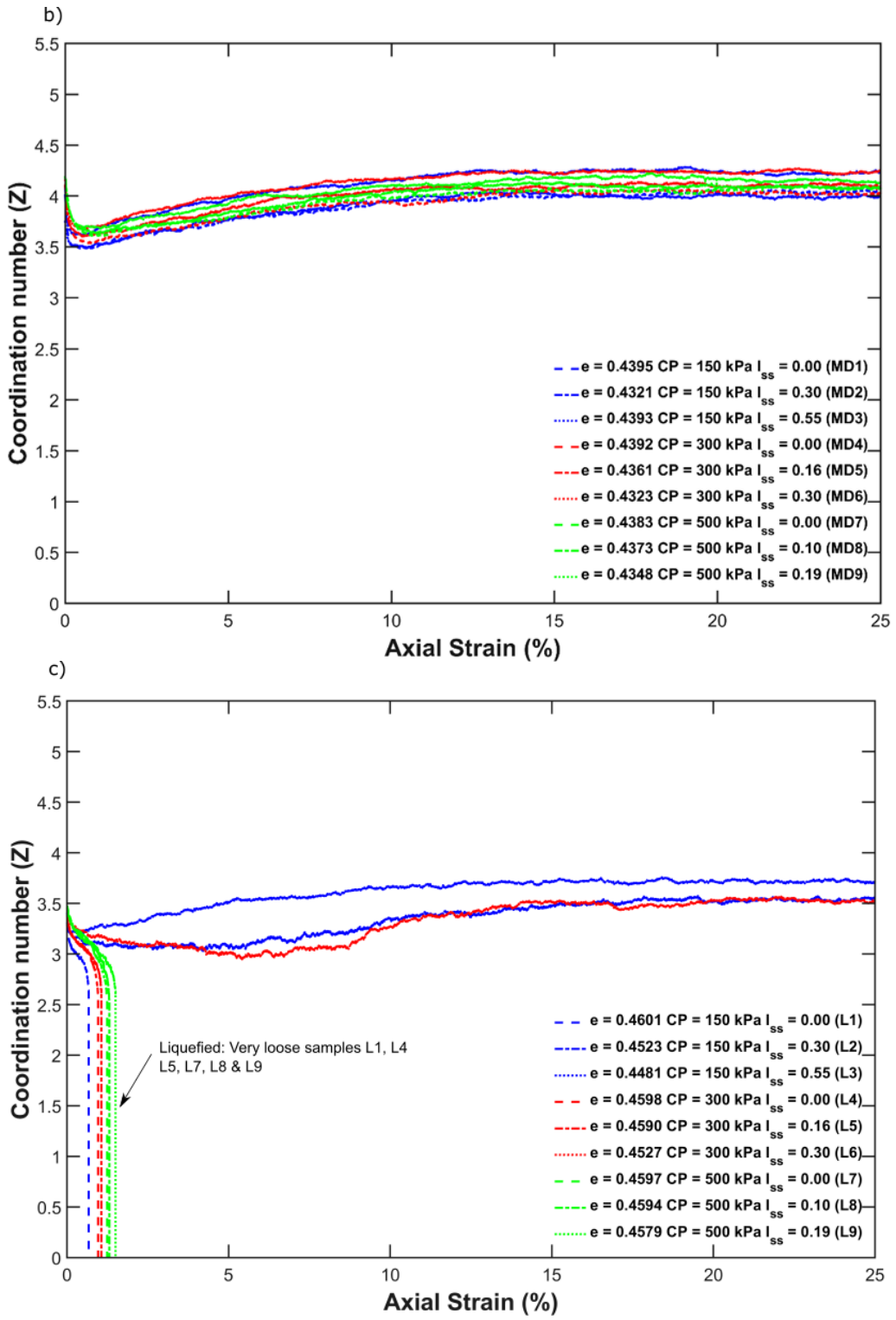

Figure 3.22: Coordination number, Z, against axial strain (%) for the 27 CV triaxial simulations. a) dense samples, D1-D9; b) medium-dense samples, MD1-MD9 and c) loose samples, L1-L9

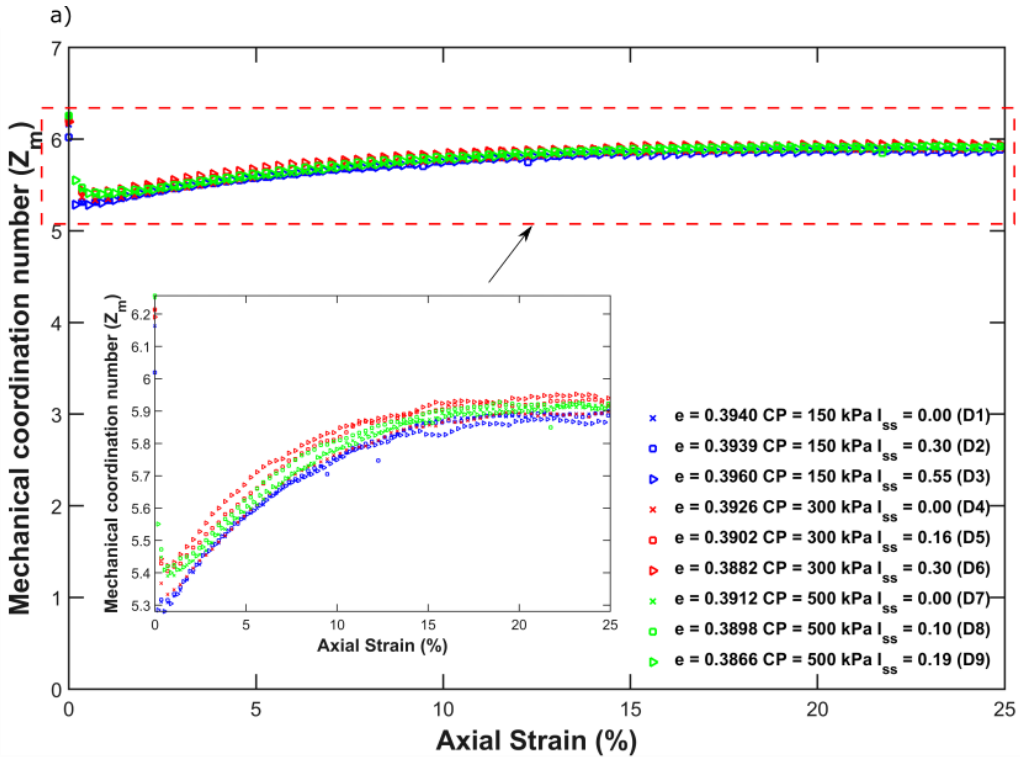
a)
Mechanical coordination number (Z_m)
Axial Strain (%)
Mechanical coordination number (Z_m)
Axial Strain (%)
e = 0.3940 CP = 150 kPa I_{ss} = 0.00 (D1)
e = 0.3939 CP = 150 kPa I_{ss} = 0.30 (D2)
e = 0.3960 CP = 150 kPa I_{ss} = 0.55 (D3)
e = 0.3926 CP = 300 kPa I_{ss} = 0.00 (D4)
e = 0.3902 CP = 300 kPa I_{ss} = 0.16 (D5)
e = 0.3882 CP = 300 kPa I_{ss} = 0.30 (D6)
e = 0.3912 CP = 500 kPa I_{ss} = 0.00 (D7)
e = 0.3898 CP = 500 kPa I_{ss} = 0.10 (D8)
e = 0.3866 CP = 500 kPa I_{ss} = 0.19 (D9)

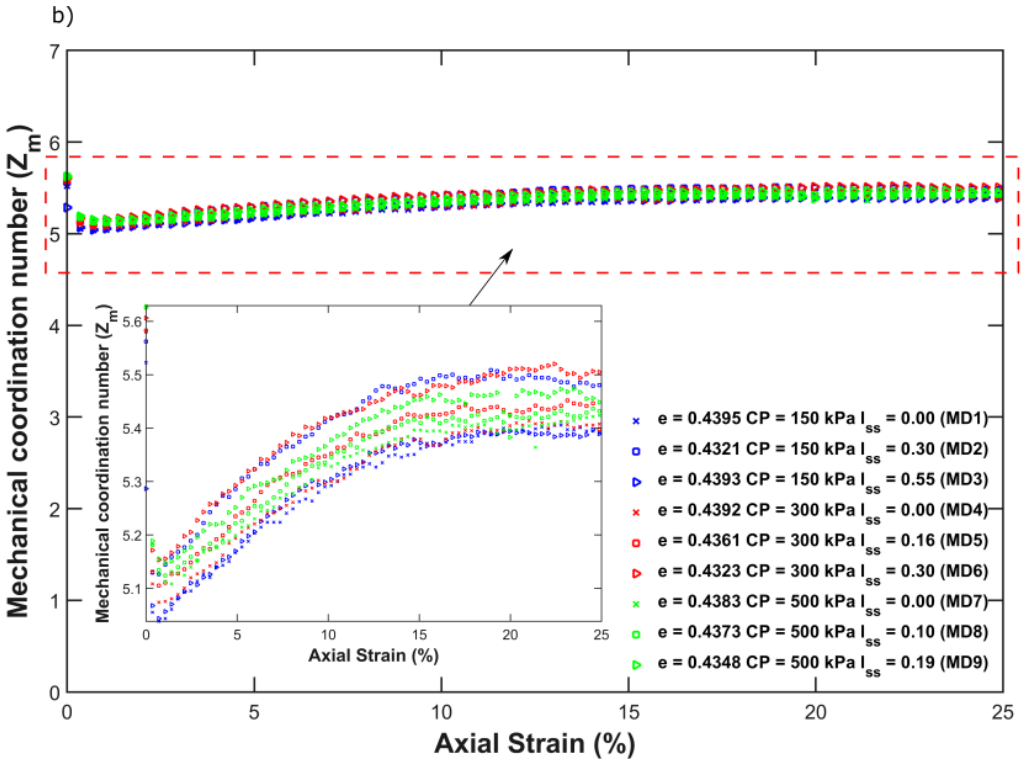
b)
Mechanical coordination number (Z_m)
Axial Strain (%)
Mechanical coordination number (Z_m)
Axial Strain (%)
e = 0.4395 CP = 150 kPa I_{ss} = 0.00 (MD1)
e = 0.4321 CP = 150 kPa I_{ss} = 0.30 (MD2)
e = 0.4393 CP = 150 kPa I_{ss} = 0.55 (MD3)
e = 0.4392 CP = 300 kPa I_{ss} = 0.00 (MD4)
e = 0.4361 CP = 300 kPa I_{ss} = 0.16 (MD5)
e = 0.4323 CP = 300 kPa I_{ss} = 0.30 (MD6)
e = 0.4383 CP = 500 kPa I_{ss} = 0.00 (MD7)
e = 0.4373 CP = 500 kPa I_{ss} = 0.10 (MD8)
e = 0.4348 CP = 500 kPa I_{ss} = 0.19 (MD9)

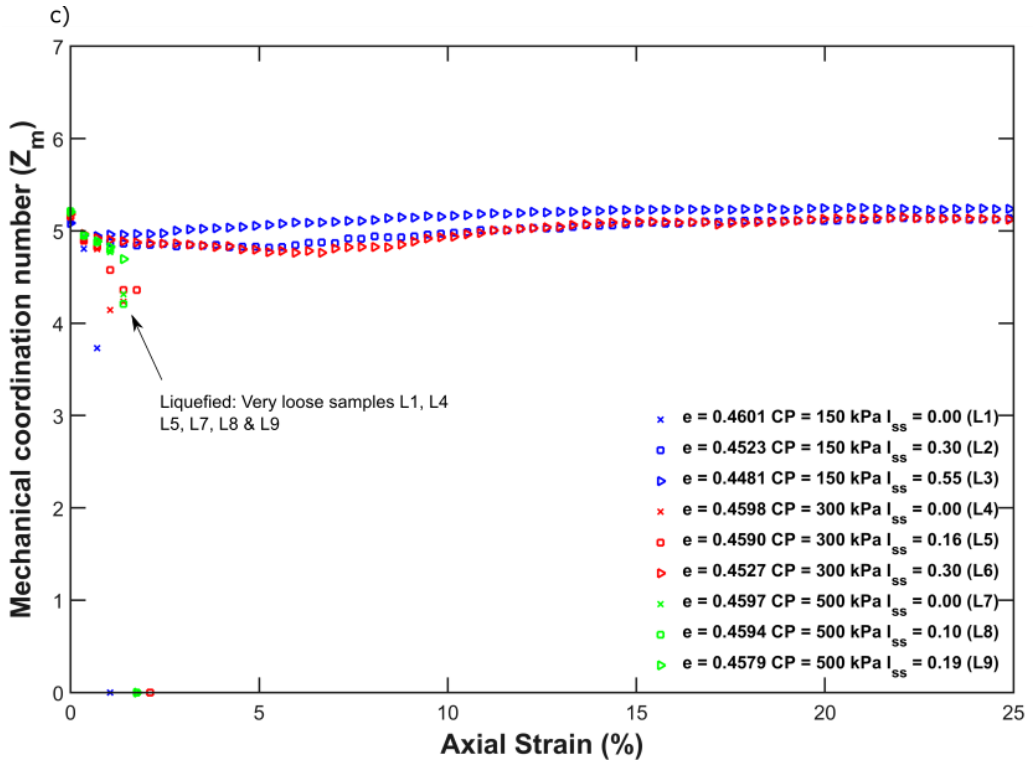

Figure 3.23: Mechanical coordination number, Z_m, against axial strain (%) for the 27 CV triaxial simulations. a) dense samples, D1-D9; b) medium-dense samples, MD1-MD9 and c) loose samples, L1-L9

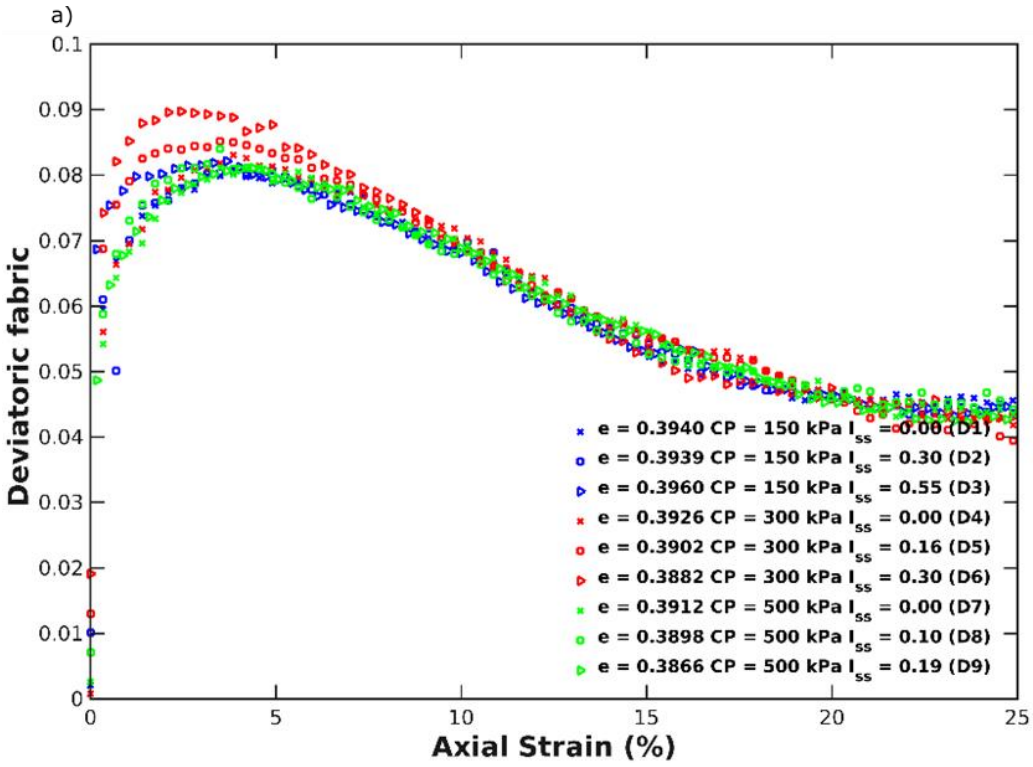

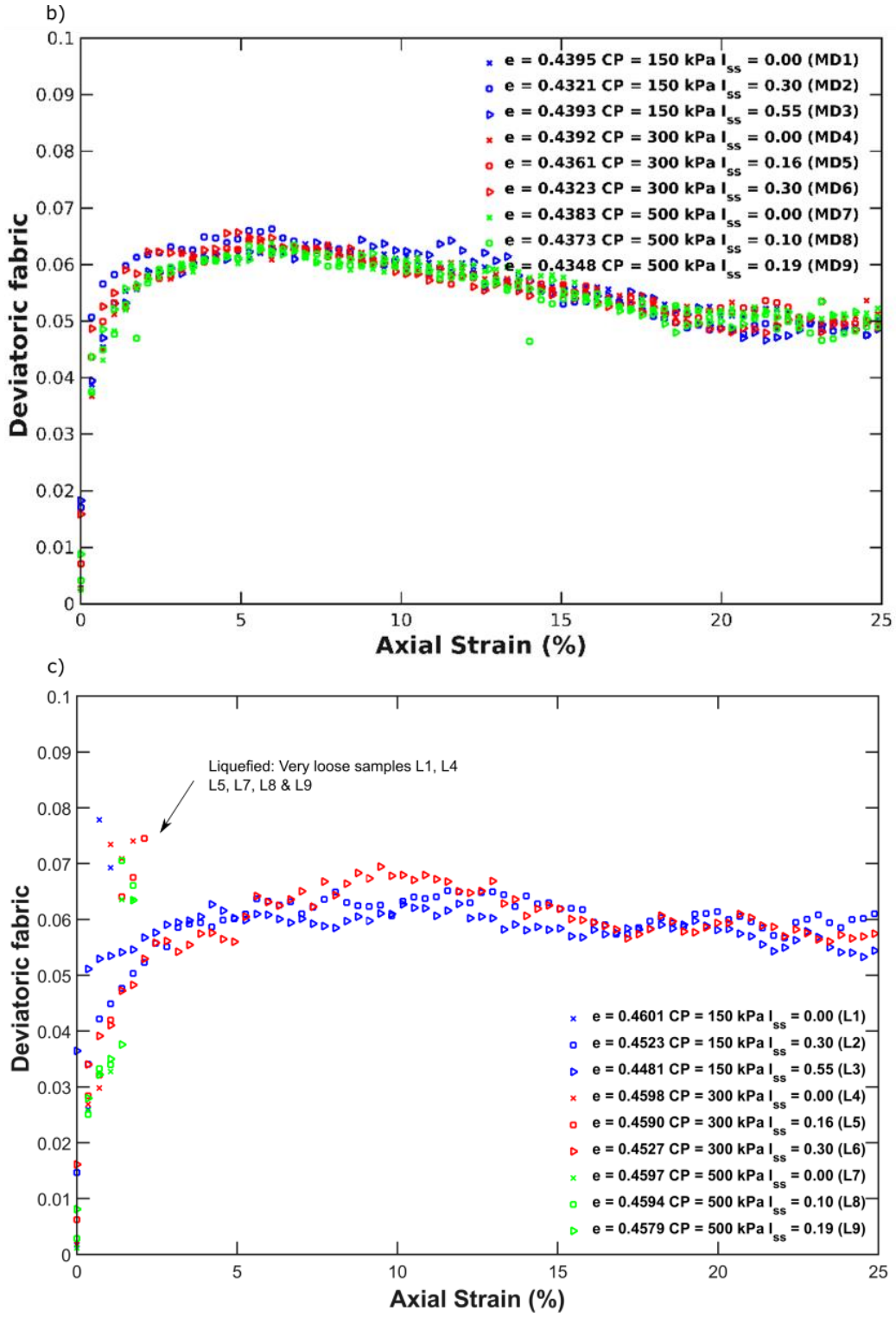

Figure 3.24: Deviatoric fabric against axial strain (%) for the 27 CV triaxial simulations. a) dense samples, D1-D9; b) medium-dense samples, MD1-MD9 and c) loose samples, L1-L9

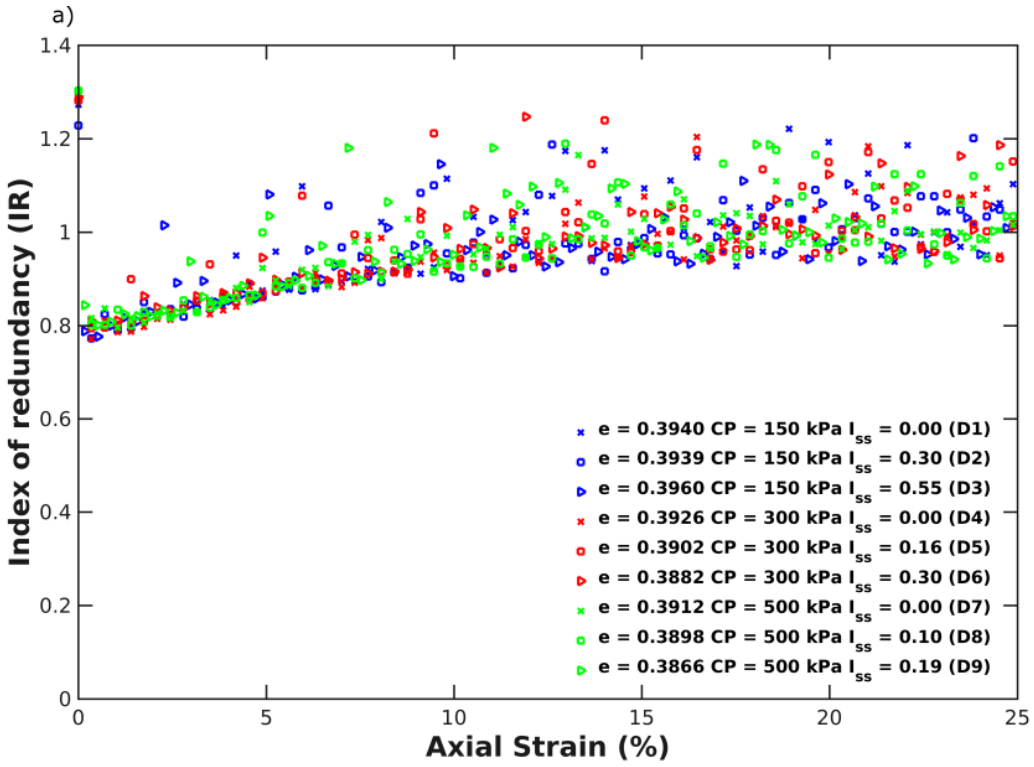
a)
Index of redundancy (IR)
Axial Strain (%)
e = 0.3940 CP = 150 kPa I_ss = 0.00 (D1)
e = 0.3939 CP = 150 kPa I_ss = 0.30 (D2)
e = 0.3960 CP = 150 kPa I_ss = 0.55 (D3)
e = 0.3926 CP = 300 kPa I_ss = 0.00 (D4)
e = 0.3902 CP = 300 kPa I_ss = 0.16 (D5)
e = 0.3882 CP = 300 kPa I_ss = 0.30 (D6)
e = 0.3912 CP = 500 kPa I_ss = 0.00 (D7)
e = 0.3898 CP = 500 kPa I_ss = 0.10 (D8)
e = 0.3866 CP = 500 kPa I_ss = 0.19 (D9)

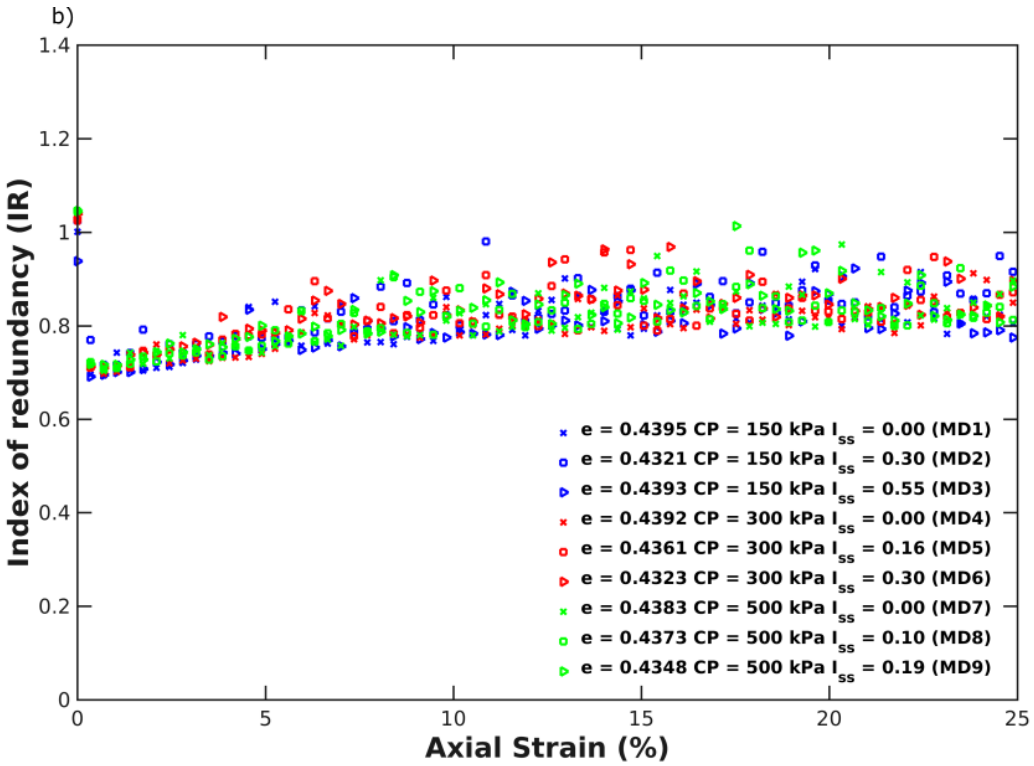
b)
Index of redundancy (IR)
Axial Strain (%)
e = 0.4395 CP = 150 kPa I_ss = 0.00 (MD1)
e = 0.4321 CP = 150 kPa I_ss = 0.30 (MD2)
e = 0.4393 CP = 150 kPa I_ss = 0.55 (MD3)
e = 0.4392 CP = 300 kPa I_ss = 0.00 (MD4)
e = 0.4361 CP = 300 kPa I_ss = 0.16 (MD5)
e = 0.4323 CP = 300 kPa I_ss = 0.30 (MD6)
e = 0.4383 CP = 500 kPa I_ss = 0.00 (MD7)
e = 0.4373 CP = 500 kPa I_ss = 0.10 (MD8)
e = 0.4348 CP = 500 kPa I_ss = 0.19 (MD9)

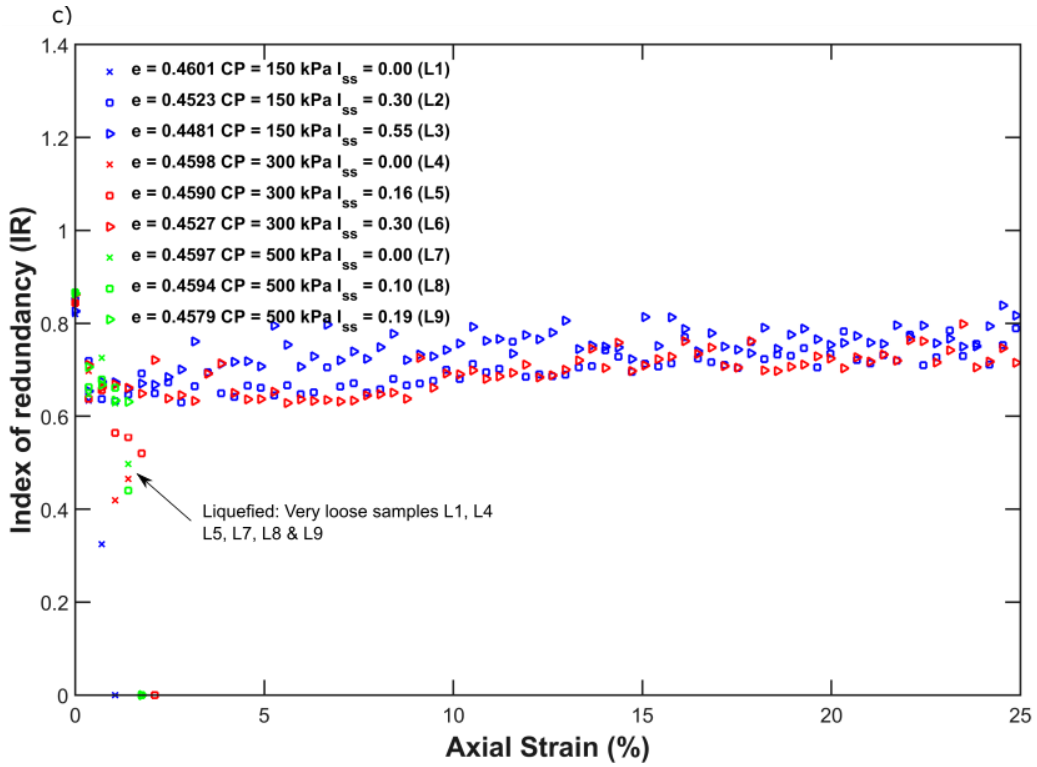

Figure 3.25: Index of redundancy, IR against axial strain (%) for the 27 CV triaxial simulations. a) dense samples, D1-D9; b) medium-dense samples, MD1-MD9 and c) loose samples, L1-L9

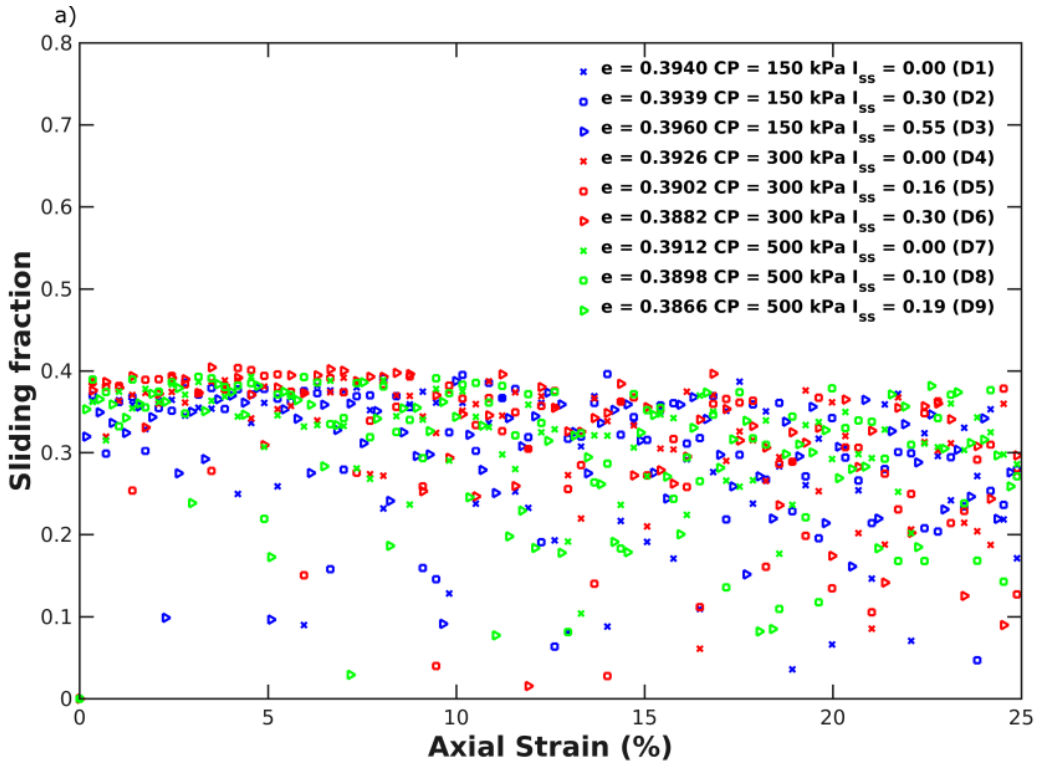

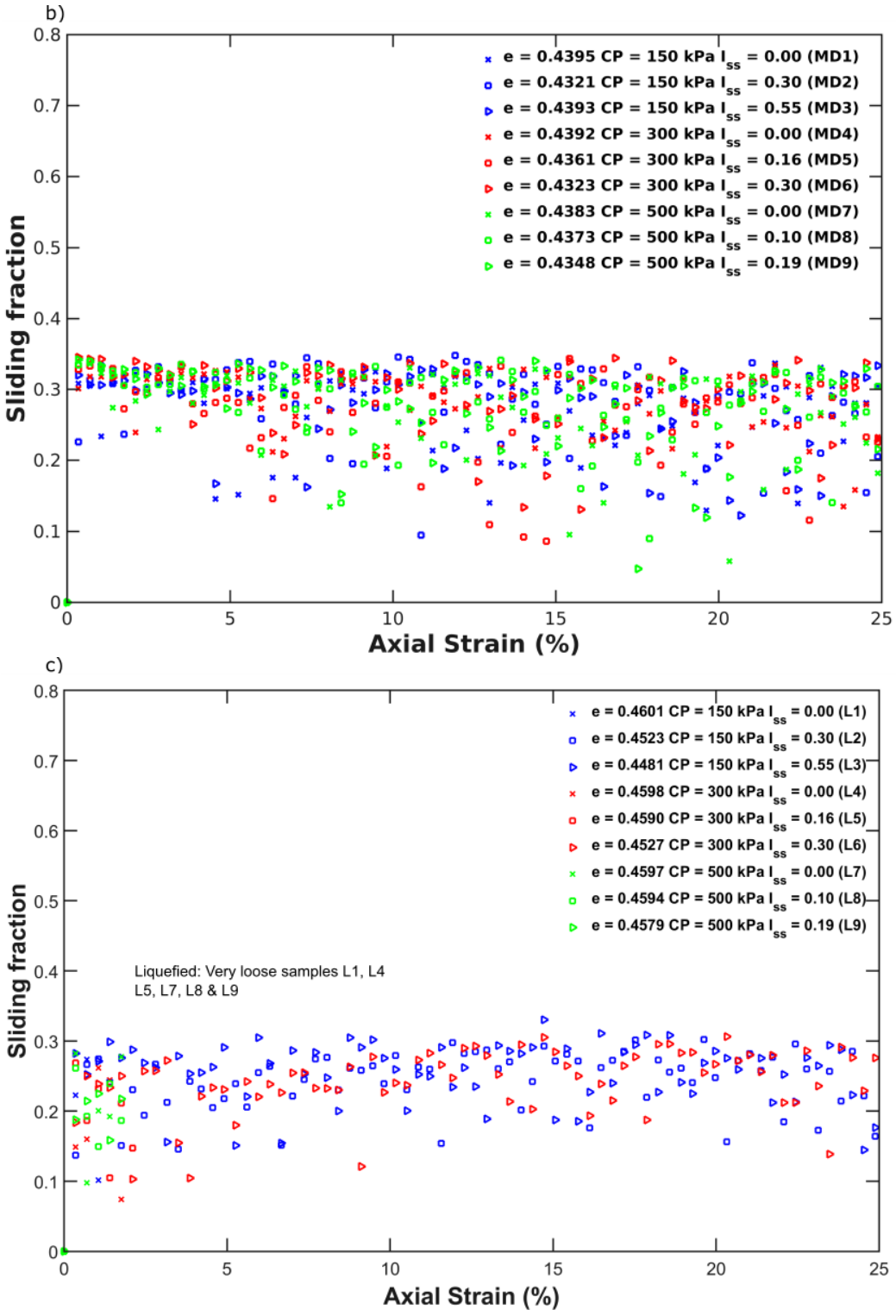

Figure 3.26: Sliding fraction, against axial strain (%) for the 27 CV triaxial simulations. a) dense samples, D1-D9; b) medium-dense samples, MD1-MD9 and c) loose samples, L1-L9

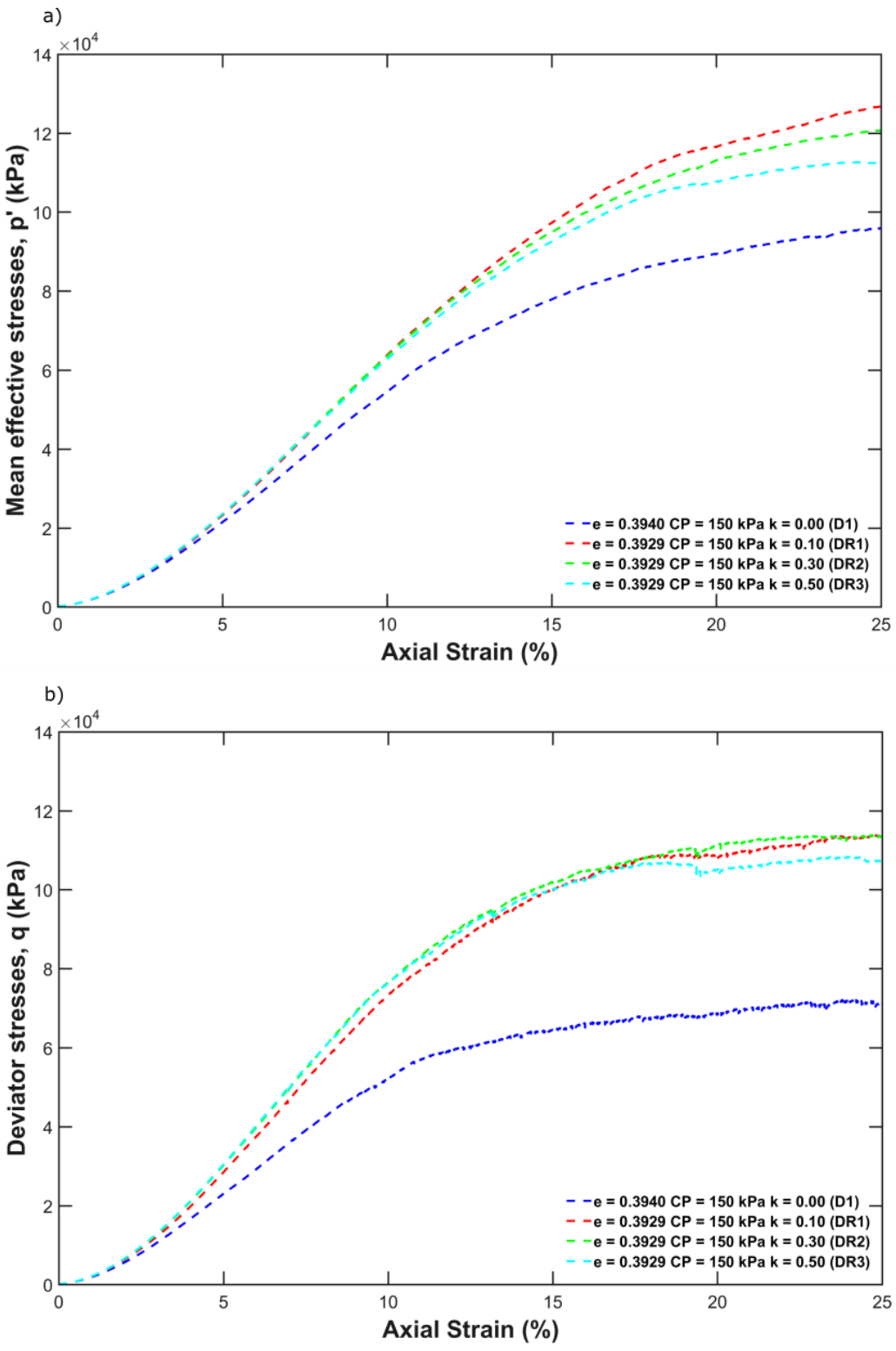

Figure 3.27: The plot for the 4 CV triaxial simulations, 3 with a rotational resistance model and 1 without: a) Mean effective stresses response in kPa, against axial strain (%) and b) Deviator stresses in kPa, against axial strain (%)

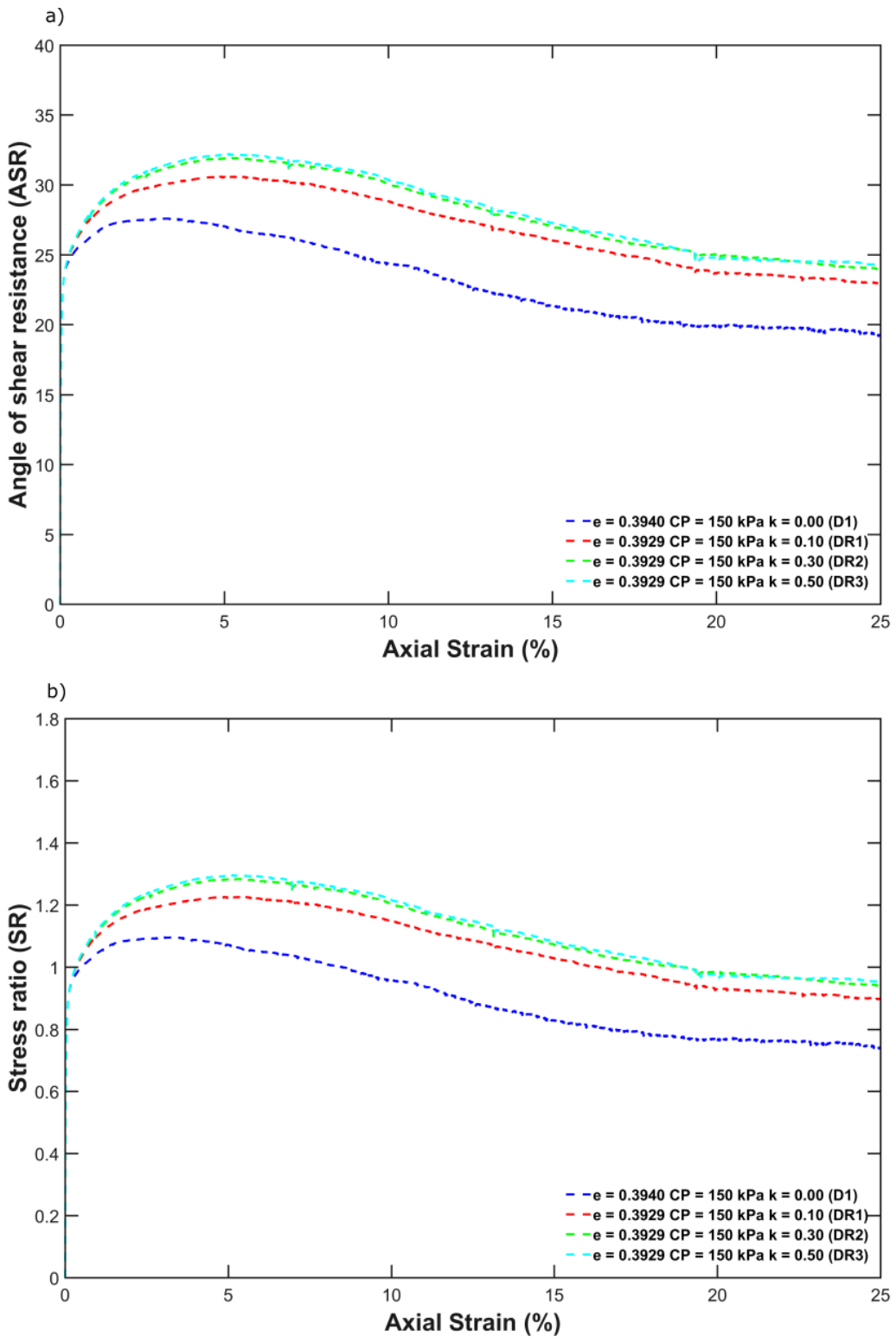

Figure 3.28: The plot for the 4 CV triaxial simulations, 3 with a rotational resistance model and 1 without: a) angle of shearing response in degree, against axial strain (%) and b) stress ratio, against axial strain (%)

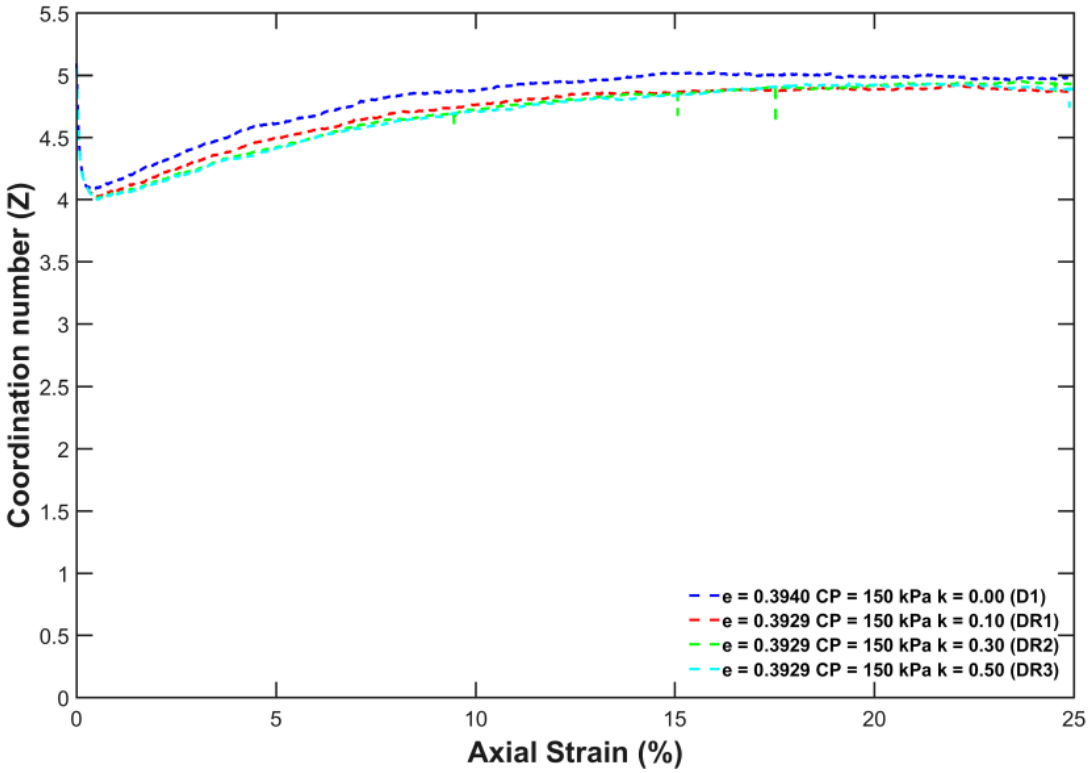

Figure 3.29: Coordination number, Z, against axial strain (%) for the 4 CV triaxial simulations: 3 with rotational resistance and 1 without

Chapter 4 Improving constant-volume simulations of undrained behaviour in DEM

In order to simulate undrained conditions using the discrete element method, a constant sample volume is often assumed. There are well-recognised problems with these constant-volume triaxial simulations, particularly of dense samples, which inhibit quantitative comparison with laboratory experiments. In this chapter, four possible explanations for these problems with conventional constant-volume simulations of ideal spherical particles are explored, each of which has a physical basis: particle crushing, the presence of highly compressible air within the sample, or the reduction of stiffness due to particle surface asperities or non-spherical particle shapes. These options are explored independently and in combination through implementation in the open-source LAMMPS code. In situations where a significant amount of particle crushing occurs, it is important to incorporate this in the simulations so that stresses are not over-estimated. There is experimental evidence that irregular particles have lower Young's moduli than the Hertzian spheres often used in DEM. In the absence of particle crushing, the most effective method to achieve more realistic stress–strain responses is to reduce the particle shear modulus substantially. This approach has the added computational benefit of enabling an increase in the simulation time-step.

4.1 Introduction

Soil is a complex multi-phase material consisting of solid, liquid and gas. Undrained tests permit the behaviour of soil to be investigated from which the pore fluid does not have sufficient time to escape when subjected to load. Excess pore pressure is generated during shearing under undrained conditions. This excess pore pressure controls important soil responses such as liquefaction: the complete loss of soil strength and stiffness (Castro, 1969; Ishihara *et al*., 1990). Many researchers, e.g., Bishop (1950); Bishop (1973) and Mohamad (1986), have studied undrained soil behaviour using laboratory testing. These tests enable us to understand the macro-scale responses of soil such as the stress-strain behaviour but cannot give any information on the dynamic changes occurring at the micro-scale that cause the observed macro-scale response. In recent years, the discrete element method (DEM) (Cundall and Strack, 1979) has become very popular in geomechanics research due

to its ability to capture the macro-scale response of soil while enabling investigation at the micro-scale (O'Sullivan, 2014). Generally there are two modeling approaches used by researchers to simulate undrained tests using DEM. The first approach involves coupling the DEM code with a suitable fluid-solving code, often computational fluid dynamics (Zhao and Shan, 2013; Liu *et al*., 2015). However, this adds complications to the simulation and increases the computational cost.

In the alternative 'constant-volume' approach, the sample volume is maintained constant throughout shearing and the excess pore water pressure is estimated as Eq. 3.1,where $\sigma'_{3,0}$ is the initial confining effective stress at the start of shearing and σ'_3 is the minor principal effective stress at every subsequent time-step in the DEM simulation. Constant-volume (CV) simulations assume that the soil is fully saturated and water is incompressible. This approach has been widely adopted, e.g., Yimsiri and Soga (2010) and Dubujet and Dedecker (1988). The constant-volume method has the advantage of computational simplicity. However, some problems arise when shearing dense samples, stemming from the generation of unrealistically high stresses as described in Chapter 3. Indeed, stresses > 10 MPa are often generated in CV simulations which invalidate the underlying assumption of the incompressibility of water, e.g., the volume of water compressed to 10 MPa is reduced by 0.5%, given a bulk modulus of 2.2 GPa (Hanley *et al*., 2013). The assumption of point contact in DEM (Potyondy and Cundall, 2004) is also violated, e.g., overlaps reached almost 20% (normalised by mean diameter) by the end of the simulations presented by Hanley *et al*. (2013). Other challenges include the failure of the simulations to capture the volume changes observed during undrained laboratory shearing (Newland and Allely, 1959; Schofield and Wroth, 1968; Castro and Poulos, 1977).

These problems mean that an alternative to the constant-volume method should be sought which retains the method's computational efficiency but without the unphysicality for dense soils. The aim of this chapter is to establish a computationally efficient and physically justifiable alternative to the conventional constant-volume method using perfect spheres in DEM. Four alternatives are hypothesised according to physical phenomena to address the shortcomings of the constant-volume method described above:

1. Particle crushing causes a reduction of the stresses upon shearing.

2. Air greatly increases compressibility of the pore fluid, causing some changes of sample volume to occur.
3. Particle surface asperities reduce the initial contact stiffness.
4. Adopting Hertzian spheres to represent non-spherical particles gives an overly stiff response. This can be corrected by reducing the particle shear modulus by a factor obtainable from uniaxial compression of single particles.

These options are explored independently and in combination through implementation in the open-source LAMMPS code (Plimpton, 1995). Based on this study, recommendations are made to improve quantitative agreement with laboratory data.

4.2 Theoretical background

4.2.1 Influence of particle crushing

Particle crushing often occurs during shearing or compression of real sands (Luzzani and MR, 2002; Altuhafi and Coop, 2011). DEM simulations of triaxial shearing have shown that particle crushing causes the peak stresses to reduce, the volumetric response to become more contractive and the position of the critical state line to shift in $e - log(p')$ space (Bolton *et al*., 2008; de Bono and McDowell, 2014; Hanley *et al*., 2015). Even though it can have significant effects, particle crushing is often disregarded in DEM simulations for two reasons: (i) the necessity to simulate fine particles post-crushing is very computationally expensive; (ii) the assumptions that are made for reasons of computational tractability can be unphysical, e.g., accepting the loss of solid volume from the simulation, imposing a comminution limit or predefining highly idealised fragment size distributions (i.e. minimum size of particles allowable after particles crushing occurs). The crushing model adopted for this study is described in detail in Hanley *et al*. (2015); in summary, a particle is deemed to fail when any contact force acting on the particle exceeds a predefined crushing force. This is shown in the flowchart in Fig 4.1. These crushing forces are experimentally measured from uniaxial compression of single particles (Nakata *et al*., 1999). Upon failure, the particle's radius is reduced so that contact is lost with all surrounding particles and its crushing force is increased. Fine particles are inserted into the void space to conserve solid volume. Particles can no longer fail once a comminution limit has been reached.

4.2.2 Influence of air: bulk modulus of water–air mixtures

The pore fluid is not directly simulated in this research. Instead, the compressibility of the pore fluid is captured by allowing the total volume of the periodic cell to vary based on the theory presented in this section. One cause of unrealistically high stresses may be the assumption of perfect saturation; in physical experiments, samples contain a small fraction of air. Before shearing begins, a *B*-test is usually performed to approximate the degree of saturation of the soil. When *B* = 1 or 100%, the soil is fully saturated. Typically *B* = 90–95% during a physical undrained triaxial test, meaning that 5–10% of air is present in the soil sample even though it may still be considered fully saturated. Since air is highly compressible, the presence of a small percentage of air is likely to be influential. Even though the pore fluid is not directly simulated, some of its properties can be estimated by subtraction, e.g., its volume must equal the total cell volume minus the solid particle volume.

The increment of pore pressure Δu is the difference between the increments of total stress Δp and mean effective stress $\Delta p'$:

$$\Delta u = \Delta p - \Delta p' \tag{4.1}$$

The mean effective stress and deviator stress can be expressed in terms of principal effective stresses. Since the volume change is uniform in the radial direction, i.e., $\Delta\sigma_2' = \Delta\sigma_3'$:

$$\Delta p' = \frac{\Delta\sigma_1' + 2\Delta\sigma_3'}{3} \tag{4.2}$$

$$\Delta q = \Delta\sigma_1' - \Delta\sigma_3' \tag{4.3}$$

For an undrained triaxial compression test where the intermediate stress ratio $= \frac{\sigma_2' - \sigma_3'}{\sigma_1' - \sigma_3'} = 0$, the loading path is equal to $\Delta p = {}^{\Delta q}/_{3}$. Therefore,

$$\Delta u = \left(\frac{\Delta\sigma_1' - \Delta\sigma_3'}{3}\right) - \left(\frac{\Delta\sigma_1' + 2\Delta\sigma_3'}{3}\right)$$

$$\Delta u = -\Delta\sigma_3' \tag{4.4}$$

This change in the minor principal effective stress can be computed from the interparticle contact force data in DEM. Eq. 4.5 is the definition of the bulk modulus, assuming that the soil particles are incompressible:

$$K_f = -V_{total}\eta \left(\frac{\Delta u}{\Delta V_{total}}\right) \tag{4.5}$$

$V_{total}\eta$, the product of porosity and sample volume, is the volume occupied by pore fluid, K_f is the bulk modulus of the pore fluid and ΔV_{total} is the volume change of the soil sample, i.e., the volume change of the pore fluid. Reorganising Eq. 4.5 we get:

$$\Delta V_{total} = -\frac{\Delta u}{K_f}\left(V_{current} - V_p\right) \tag{4.6}$$

$V_{current}$ is the total sample volume updated at every time-step during the simulation and V_p is the fixed volume of the solid particles within the soil sample. The minus sign in Eq. 4.6 indicates that the sample volume is allowed to expand when Δu is negative (or $\Delta\sigma_3'$ is positive) during shearing. Conversely, a positive Δu in Eq. 4.6 leads to sample contraction, capturing compression of the entrained air that takes place in the physical test.

Knowing the bulk modulus of the pore fluid, K_f, the volume change at every time-step may be calculated from Eq. 4.6. K_f is given by Yang (2005) and (Yang and Sato, 2000):

$$\frac{1}{K_f} = \frac{1}{K_w} + \frac{(1 - S_r)}{P_a} \tag{4.7}$$

K_w is the bulk modulus of water, S_r is the degree of saturation of the soil sample and P_a is the absolute fluid pressure: the sum of atmospheric pressure and excess pore pressure. The assumption being made is that the degree of saturation is high, the pore fluid is homogenous and the air exists in the pore water in the form of well distributed bubbles (Yang and Sato, 2000). Dissolution of air into water at high pressure has been neglected. Fig. 4.2 shows the variation of K_f with P_a according to Eq. 4.7, taking K_w as 2.2 GPa. When the degree of saturation is 100%, the bulk modulus of the pore fluid is equal to the bulk modulus of water. K_f is substantially

reduced by the presence of a small percentage of air at low to moderate pressures relevant to laboratory soil testing.

4.2.3 Influence of particle surface asperities: rough-surface contact model

Another explanation for the unrealistically high computed stresses is the perfectly smooth nature of the interparticle contact. The presence of surface asperities on real particles reduces the contact stiffness compared to smooth spheres during the initial phase of loading. The influence of surface asperities at interparticle contacts is discussed by Greenwood *et al*. (1984); Yimsiri and Soga (2000); Yang *et al*. (2016). With the increase of surface asperities, the shear wave velocity decreases which cause the initial shear modulus of the sample to reduce (Otsubo *et al.*, 2016). In this research, a DEM contact model developed by Otsubo *et al*. (2016) was adopted which includes crushing of asperities. This model was selected as it is capable of capturing the dynamic response of granular materials (Otsubo *et al.*, 2016) and was readily available in LAMMPS. This contact model was an extension of a previous model developed based on single-particle compression tests which includes surface roughness, S_q, and hardness (Cavarretta *et al*., 2012). Otsubo *et al*.'s model (Otsubo *et al*., 2016) includes three regimes: asperities dominating, a transitional regime and Hertzian contact. δ_{T1} and δ_{T2} are the threshold contact displacements at the threshold normal interparticle contact force, $N = N_{T1}$ and N_{T2}, respectively, as shown in Fig. 4.3. At interparticle contact overlaps less than δ_{T1}, the contact response is dominated by crushing of surface asperities. This is controlled by two constants, δ_1 and δ_2, which may be experimentally measured..

4.2.4 Influence of using Hertzian spheres to represent non-spherical particles

The presence of asperities on the surface of the particle is expected to reduce the initial contact stiffness. However, experimental data for uniaxial compression of individual particles (Cavarretta, 2009; Cavarretta *et al*., 2010) suggest that the overall particle shape may have a much more significant effect on the load–deformation response. For an irregular silica gravel particle, the experimentally measured Young's modulus was found to be 20 times less than the Young's modulus of an equivalent sphere calculated from Hertzian mechanics (Cavarretta and O'sullivan, 2012).

This experimental result must be reconciled with other experiments (Yang and Luo, 2015) which show that increasing the particles' angularity while keeping all other inputs constant gives a stronger bulk stress–strain response. The simple addition of rotational resistance, to include some degree of shape irregularity, has a similar effect in DEM simulations (Huang et al., 2017). The reason for this apparent inconsistency is that non-spherical particles do not behave according to Hertzian mechanics of spheres, the adoption of which gives an overly stiff response. In the absence of a better understanding of contact mechanics for non-spherical particle shapes, the contact forces and stiffnesses calculated using Hertzian mechanics of spheres can be corrected by reducing the Young's modulus of the particle (which is, in reality, an irregular sand grain). This reduction could be calibrated to obtain the correct stiffness for an individual particle under uniaxial compression. The reduction in the stiffness of the bulk sample is purely a result of reducing the stiffness of each individual particle comprising the sample. The results in (Cavarretta and O'sullivan, 2012) imply that the bulk stiffness of an assembly of irregular particles would be substantially lower than for perfect Hertzian spheres composed of the same material.

4.3 Code implementation

All of the simulations were run using a version of open-source, MPI-parallelised LAMMPS code (Plimpton, 1995). The approaches by which the four hypotheses described in Sections 4.2.1–4.2.4 were implemented in LAMMPS are discussed in Sections 4.3.1–4.3.4, respectively.

4.3.1 Influence of particle crushing

The particle crushing model described in Section 4.2.1 was developed by Hanley *et al*. (2015). The implementation of this model in LAMMPS was carried out as part of Hanley *et al*. (2015); the reader is referred to that paper for details.

4.3.2 Influence of air: bulk modulus of water–air mixtures

The flowchart in Fig. 4.4 shows the implementation of the equations described in Section 4.2.2 in LAMMPS. Implementation of the bulk modulus method in LAMMPS involved extending one existing .cpp file and its header file which enable control of stresses on an periodically bounded assembly. The bulk modulus method is largely coded in one function which contains around 40 lines of code excluding comments and spaces. In addition, the usual functions needed to be extended to save values of internal variables to/from restart files, enable the user to specify input parameters

through the script. In summary, this version of LAMMPS contains a servo-control algorithm for periodically bounded samples which requires the computation of principal effective stresses from interparticle contact forces. $\Delta\sigma_3'$ is found as the change in minor principal effective stress between successive time-steps. This is equal to the negative change in the excess pore water pressure, $-\Delta u$, i.e., Eq. 4.4. Δu is accumulated and is added to atmospheric pressure, P_{atm}, to find P_a, the absolute pore fluid pressure.

Two limits were imposed in the implementation of the equations described in Section 4.2.2. The first limit was imposed on P_a to avoid the attainment of low pressures which would cause fluid vaporization in reality, and beyond that, the attainment of non-physical negative pressures. A limit of $P_a \geq 0.25P_{atm}$ was imposed. This predefined limit is the lowest permissible absolute pressure. The upper bound on P_a is the confining pressure, σ_3, at which the effective stress terms become zero. P_a is used to calculate the bulk modulus of the pore fluid, K_f, using Eq. 4.7. The volume change of the sample on that time-step is given by Eq. 4.6, assuming a discontinuous jump from time-step t to the time-step $t + \Delta t$. If the time-step Δt were divided into infinitely many smaller time increments, the required volume change would be half of that given by Eq. 4.6. This halved volume increment corresponding to a continuous time scenario was implemented in the code. The derivation is given in Appendix B.

The second limit was imposed on absolute volumetric strain on each time-step of 2.3 x 10^{-9}. This value was determined through trial and error so that the absolute volumetric strain during shearing did not exceed the volume of air present in the pore fluid (5% of the pore fluid). Without this condition, huge values of ΔV could be achieved in single time-step when very stiff particles are used and hence $\Delta\sigma_3'$ could be unreasonably large. This would lead to instability of the proportional servo-controller. Volumetric strains beyond the limit are stored until the following time-step. The stored volumetric strain term is multiplied by a dissipation factor of 0.9999 to prevent the accrual of huge stored strains and ensure that critical state is eventually reached. Using K_f and Δu, the volume change is calculated at every time-step using Eq. 4.6.

4.3.3 Influence of particle surface asperities: rough-surface contact model

The rough-surface contact model described in Section 4.2.3 was developed by Otsubo *et al*. (2016). The implementation of the model in LAMMPS was carried out as part of Otsubo *et al*. (2016); the reader is referred to that paper for details.

4.3.4 Influence of using Hertzian spheres to represent non-spherical particles

The Young's modulus of an irregular silica gravel particle measured experimentally by Cavarretta and O'Sullivan (2012) was 20 times lower than that of an equivalent Hertzian sphere. In this research using Hertzian spheres, the shear modulus of the individual particles, *G*, was reduced by a factor of 20 to compensate for this known disparity between experimental data and the Hertzian predictions for spheres.

An added benefit of this approach is an increase in the stable simulation time-step. For the nonlinear Hertzian contact model, the critical time-step based on the Rayleigh wave velocity for the system has the relationship $\Delta t_c \propto G^{-0.5}$ (Thornton and Randall, 1988). Thus, reducing G by a factor of 20 increases the time-step by a factor of $\sqrt{20} \approx 4.5$, substantially reducing a simulation's run-time without compromising its stability.

4.4 DEM model preparation and simulation plan

Cubic granular specimens of 10 × 10 × 10 mm^3 were created which contained 28,309 spheres with diameters varying between 0.1 mm and 1 mm as shown in Fig. 4.5. A non-uniform particle size distribution was used to avoid crystallization that would arise during shearing of uniformly sizee particles. To eliminate boundary effects (Huang *et al*., 2014c) and to ensure homogenous deformation (Cundall, 1988), periodic boundary conditions were adopted for this study. The particles were placed randomly within these periodic cells without initial overlaps using a MATLAB code. The initial particle positions were imported to LAMMPS before each sample was isotropically compressed by moving the boundaries under stress control to achieve a specified confining pressure of 150 kPa. The friction coefficient was set to zero during the sample preparation process to generate dense samples. This friction coefficient was increased to 0.25, based on (Huang *et al*., 2014a), before shearing each sample at a fixed strain rate of 1 s^{-1}. This strain rate ensured an inertia number less than 3.6×10^{-5} throughout shearing: lower than the limiting value of 7.9×10^{-5} proposed for quasi-static behaviour (Parez *et al*., 2016). Eight triaxial shearing simulations are the

principal focus of this study: four using the constant-volume method and four using the bulk modulus method. Each subset of four simulations consisted of simulations with the simplified Hertz-Mindlin (smooth) (Itasca Consulting Group, 2007) and rough-surface (Otsubo *et al*., 2016) contact models, with shear moduli of 29 GPa or 1.46 GPa. These shear moduli, G, respectively represented a physically realistic value for quartz and a reduced value to capture irregularity of the particle shape based on Cavarretta and O'Sullivan (2012). The particle density and Poisson's ratio were set at 2675 kg /m^3 and 0.2, respectively. The local damping coefficient was chosen as 0.2. The bulk modulus of water, K_w, was 2.2 GPa and the degree of saturation, S_r, of the soil sample was 0.95. Atmospheric pressure was set at 0.1 MPa. The surface roughness, S_q, was set at 0.5 x 10^{-6} m for the rough-surface contact model: similar to that of an LBSA sand grain (Cavarretta, 2009). Values of $\delta_1 = 0.82S_q$ and $\delta_2 = 1.24S_q$ were used in these simulations, based on experimental data (Greenwood *et al*., 1984 and Yimisiri and Soga, 2000). Gravity was not considered and particle crushing was not permitted in these eight simulations.

It is already well known that particle crushing reduces the peak stresses in a triaxial test, e.g., Hanley *et al*. (2015). Only one simulation was run in which particle crushing was considered. This simulation used the constant-volume method, simplified Hertz-Mindlin contact model and G = 29 GPa. The parameters of the crushing model were a Weibull modulus of 4.2, a limiting comminution radius of 50 μm, and a characteristic stress (σ_0) of 760 MPa at which 37% of the particles of characteristic diameter 1.29 mm survive. A linear trendline of the form $P_s(d) = a\left(\frac{\sigma}{\sigma_{0,d}}\right) + b$ relating the probability of survival for particles of diameter *d* to a stress σ was assumed, based on the statistics in Nakata *et al*. (1999) for a quartzitic Aio sand. These parameters were identical to those in Hanley *et al*. (2015), except a larger σ_0 value was used in this study to limit the amount of crushing that occurred. To obtain a critical state line, three supplementary triaxial drained simulations were run at confining pressures of 150, 300 and 500 kPa and two constant p' simulations were run at 40 and 47 MPa.

4.5 Results and discussion

4.5.1 Macro-scale

Consider firstly the one simulation which includes particle crushing. This is compared to the equivalent simulation in which crushing is ignored on Fig. 4.5. Without crushing, the mean effective stress, p', is 28.72 MPa at 15% axial strain. The inclusion of

particle crushing reduced p' by 63% at the same strain. However, this p' is much higher than in a laboratory test conducted by Kuwano (1999), who obtained p' = 1.46 MPa at 15% axial strain for the same sand with a confining pressure of 400 kPa. This experimental data are also shown in Fig. 4.6. The stresses generated can be calibrated using (σ_0 – 760) MPa for this simulation – as an adjustable parameter (selected through trial and error considered the amount particle crushing and simulation time). Using this parameter, a significant amount of crushing occurred; the number of particles increased to 52898 (28309 particles before shearing) when the sample was sheared to 15% axial strain. The change in particle size distribution (PSD) is shown in Fig. 4.7. Reducing σ_0 induces more particle crushing and hence reduces p'. Hanley *et al*. (2015) used σ_0 = 38 MPa and obtained a huge amount of breakage at high confining pressures in drained simulations.

In situations where a considerable amount of particle crushing occurs, it is important to consider this in the simulations to correctly capture the bulk behaviour. However, particle crushing does not fully explain the disparity between undrained laboratory tests and constant-volume DEM simulations. The amount of crushing that would be required to quantitatively match the stress–strain behaviour for a dense sample would be far more than observed in laboratory tests of sands (and would be unachievable with the type of crushing model proposed by Hanley *et al.* (2015). Furthermore, undrained tests on dry spherical glass beads conducted by Cui *et al*. (2017) observed a maximum deviator stress of 440 kPa for a confining pressure of 200 kPa and no particle crushing occurred. This indicates that particle crushing is not the only reason for high stresses in constant-volume simulations.

Considering separately the eight simulations without crushing, all simulations reached a critical state before 25% axial strain, attaining a similar stress ratio, q/p', of around 0.72 as shown in Fig. 4.8, regardless of simulation method, contact model or particle stiffness. These plots show behaviour characteristic of dense samples: the stress ratio increased abruptly to a peak value upon initial shearing and dropped thereafter to a constant value at the critical state (Newland and Allely, 1959). Fig. 4.9 shows the variation of mean effective stress, p', and deviator stress, q, with axial strain where these quantities are defined by Eq. 4.3. Using the constant-volume method with a Hertzian contact model and particle shear modulus of 29 GPa, the stresses generated at critical state were 95.18 MPa and 68.14 MPa for p' and q, respectively: similar in magnitude to the stresses reported by Hanley *et al*. (2013). Changing to a rough-

surface contact model allowing for asperity crushing reduced the stresses to 80.72 MPa and 58.42 MPa, respectively: a reduction of around 15%. Switching from constant volume to the bulk modulus method was more effective, leading to a reduction of 56% (41.87 MPa and 29.89 MPa). The most effective method to achieve more physically realistic stresses was reducing the shear modulus from 29 GPa to 1.46 GPa, which captures the effect of irregular, non-spherical particle shapes when Hertzian mechanics are adopted. This yielded a reduction of 94%, to p' = 5.28 MPa and q = 3.83 MPa, compared to using the shear modulus of quartz. A 20-fold reduction of G reduced the stresses to around one-twentieth of their former values. In combination, using the bulk modulus method with a rough-surface contact model and G = 1.46 GPa led to the lowest stress state among these eight simulations of p' = 3.58 MPa and q = 2.55 MPa at critical state. These results are quantitatively similar to experimental results (Been *et al*., 1991).

The shear modulus of the bulk soil sample is computed as $\frac{1}{3}$ of the slope of a plot of deviator stress against triaxial shear strain. As shown in Fig. 4.10, the shear modulus of the soil samples using a smooth Hertzian contact model with a particle shear modulus of 29 GPa were extremely high: 311 MPa initially at 1 x 10^{-3}% strain. By considering the particle surface asperities, the shear modulus of the soil sample was considerably reduced (by 64% initially) compared to smooth Hertzian model. The high stresses generated during shearing may be caused by this initial unrealistically stiff response of Hertzian spheres using the particle shear modulus of quartz. Using a reduced particle shear modulus of 1.46 GPa, the initial stiffness of the sample was reduced by around 85% compared to using the shear modulus of quartz particles.

The variation of volumetric strain with axial strain during shearing is plotted on Fig. 4.11. The four simulations using the constant-volume method do not permit any volumetric strain throughout shearing. When the bulk modulus method is used, the samples contract slightly during initial shearing and then dilate until critical state is attained. This expansion of each sample's volume reflects the expansion of the air, principally, within the pore fluid as negative pore pressures develop. According to Boyle's law, the volume increases as the pressure of gas decreases within a closed system. In this implementation, it is noted that the maximum dilation achieved is smaller than indicated by Boyle's law at the limiting pressure of $0.25P_{atm}$. This is due to the volumetric strain limit imposed on each time-step during shearing, which restricted the sample dilation to 1–2% at critical state. This is similar to the volume of

air within each sample: at $S_r = 0.95$, 5% of air is present in the pore fluid which corresponds to around 1.5% of the total volume of each sand sample. As stresses increase to a maximum of p' = 95.18 MPa for a Hertzian contact model with G = 29 GPa, dilation also increases.

Fig. 4.12a shows that the adoption of any of the proposed alternatives to the constant-volume method, i.e., the bulk modulus method, the rough-surface contact model to capture crushing of surface asperities, or the reduced particle shear modulus to to correct for the use of Hertzian spheres to simulate non-spherical particles, all lead to a downward shift of the critical state line in *e*–log(p') space. Particle crushing at high p' causes a similar shift of the critical state line (Hanley *et al*., 2015). As the stress ratios at critical state are very similar for all simulations (Fig. 4.7), all points are collinear on Fig. 4.12b: the critical state line in $q - p'$ space. The slope of this line, *M* = 0.72, is equivalent to a critical state angle of shearing resistance of 18.8°. This similar slope and angle of shearing resistance indicate that the CSL is unique and independent of the initial state and the loading conditions. This angle is much lower than values obtained in physical tests. The main reason for this disparity is the simulated particles are spherical and can rotate freely whereas, in a real system, interparticle movements are much more inhibited because of interlocking, both at the particle level and at the contact level where interlocking of asperities prevents free rotation.

The mean interparticle overlap normalised by mean particle radius is shown on Fig.4. 13 as shearing proceeds. Regardless of contact model used, the mean overlaps were below 5% in all cases. However, the largest overlap exceeded 20%. As the particle shear modulus was reduced from 29 GPa to 1.46 GPa, the mean overlap increased slightly but remained below 5%. This is important to quantify because of the fundamental assumption of point contact in DEM (Potyondy and Cundall, 2004). The contact area, and hence the interparticle overlap, is significantly larger for the rough-surface contact model than for the smooth Hertzian contact model which agrees with Greenwood and Tripp (1967). Because the stresses are lower when the presence of air is considered (bulk modulus method), this method leads to reduced interparticle overlaps compared to the conventional constant-volume method.

4.5.2 Micro-scale

The coordination number, $Z = \frac{2N_c}{N_p}$, is a scalar measure of fabric, i.e., internal topology, within a granular system. In all cases, Z decreases immediately upon shearing and attains a constant value of 4.2–5.0 at critical state (Fig. 4.14). The bulk modulus method consistently gives a substantial reduction in coordination number compared to the equivalent constant volume simulations. This is expected as dilation is associated with a reduction in contact density within a granular assembly. The rough-surface contact model gives a slightly higher coordination number than the smooth Hertzian model. Reducing G also increases Z. Both of these methods lead to higher mean interparticle overlaps Fig. 4.13, which is expected to give a small increase in N_c. The mechanical coordination number, Z_m, is computed similarly to Z, except those particles with zero or one interparticle contact are excluded from the calculation (Thornton, 2000). The trends in Z_m on Fig. 4.14 broadly match those for Z; however, the range of Z_m values at critical state of 5.4–5.7 is narrower than the range of Z values. These results quantitatively agree with Huang *et al*. (2014a). The deviatoric fabric, $\varphi_d = \varphi_1 - \varphi_3$, is the difference between the maximum and minimum eigenvalues of the second-order fabric tensor defined by Satake (1982). It is widely used to quantify the fabric anisotropy of granular assemblies. Fig. 4.15 shows the variation of deviatoric fabric with axial strain for all simulations considered. φ_d is almost zero at the start of shearing of each isotropic sample. φ_d attains a maximum value of around 0.08 at 5% axial strain before decreasing to a stable value between 0.04 and 0.05 at critical state. For same particle shear modulus, the bulk modulus method simulations showed slightly higher φ_d values at peak and critical state than the constant-volume simulations. These results also quantitatively agree with Huang *et al*. (2014a). Reducing G decreases φ_d. The reason may be due to small increase in N_c.

4.6 Conclusions

This chapter was introduced with the aim of establishing a computationally efficient and physically justifiable alternative to the constant-volume method with ideal spherical particles. Four alternatives were hypothesised, each of which has a physical justification: that particle crushing substantially reduces the peak stresses upon shearing, that air greatly increases compressibility of the pore fluid, causing some changes of sample volume to occur; that particle surface asperities reduce the initial

contact stiffness; and that non-spherical particle shapes reduce the sample stiffness when Hertzian mechanics for spheres are adopted for the calculation of contact forces. All of these hypotheses were explored, both independently and in combination, using triaxial compression simulations run using the LAMMPS code.

When the conventional constant-volume method was used with a Hertzian contact model and particle shear modulus of 29 GPa, p' exceeded 95 MPa at critical state, highlighting one of the main problems with this approach. When particle crushing was considered, the stresses were substantially reduced. In principle, the parameters controlling the degree of crushing which occurs could be calibrated to give the desired macro-scale response. However, the amount of crushing that would be required to give the correct stress–strain response would be unrealistically high for a dense sample if a constant-volume simulation with smooth spheres were chosen for the DEM. The computational expense of such a simulation would also be prohibitive.

The most effective method to achieve more realistic stresses was reducing the shear modulus by a factor of 20 (p' = 5.28 MPa at critical state). This captured the effect of irregular particle shape when Hertzian mechanics are adopted, based on experimental measurements of the Young's modulus of an irregular silica gravel particle (Cavarretta and O'Sullivan, 2012). This method is also computationally beneficial as the reduced shear modulus allows the simulation time-step to be increased by a factor of approximately 4.5. Furthermore, this method reduces the small-strain stiffness of the sample to more realistic values. Adopting a rough-surface contact model (capturing the effect of asperity crushing) or switching to the bulk modulus method (enabling changes of sample volume) were both less effective and more computationally expensive than reducing G. All simulations attained similar stress ratios at critical state of around 0.72 while the deviatoric fabric was almost unaffected.

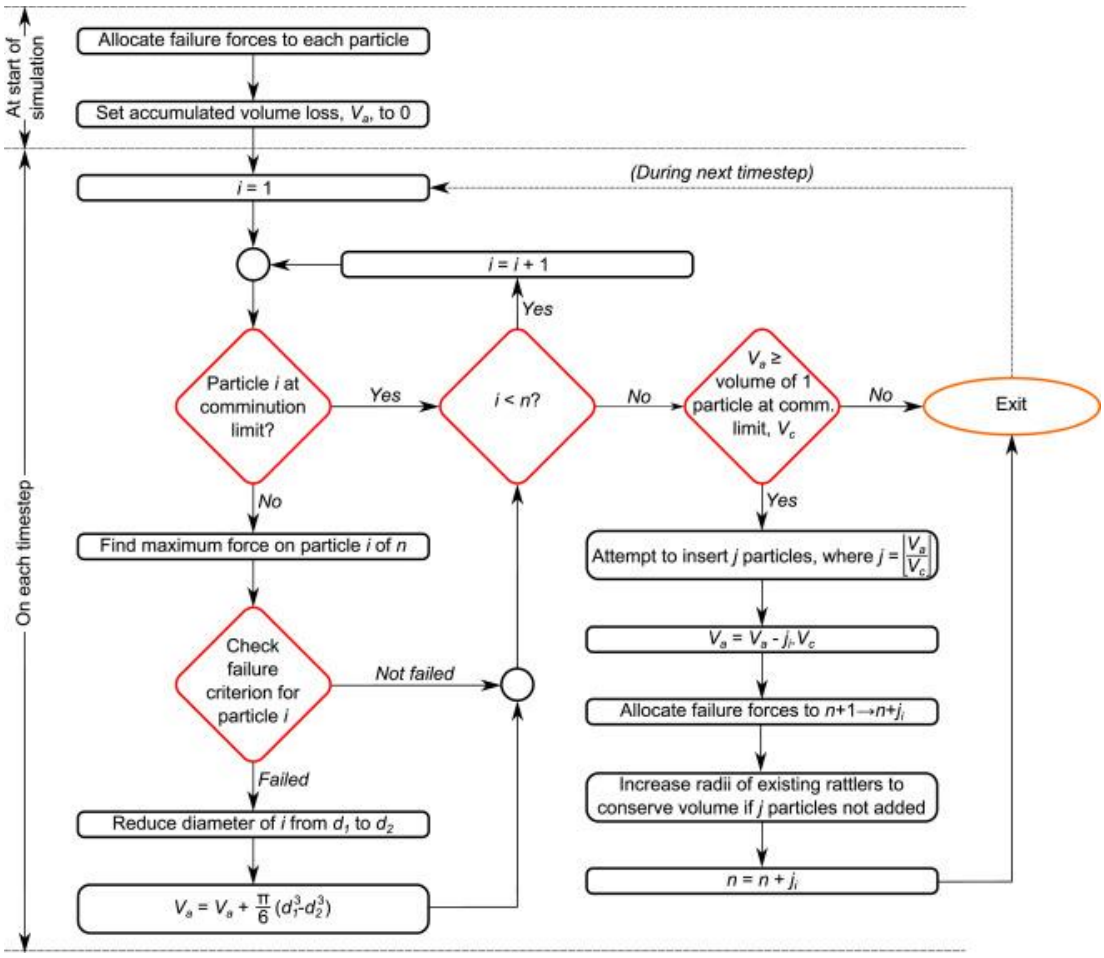

Figure 4.1: Crushing model flowchart implemented in a DEM code. (Hanley et al. 2015)

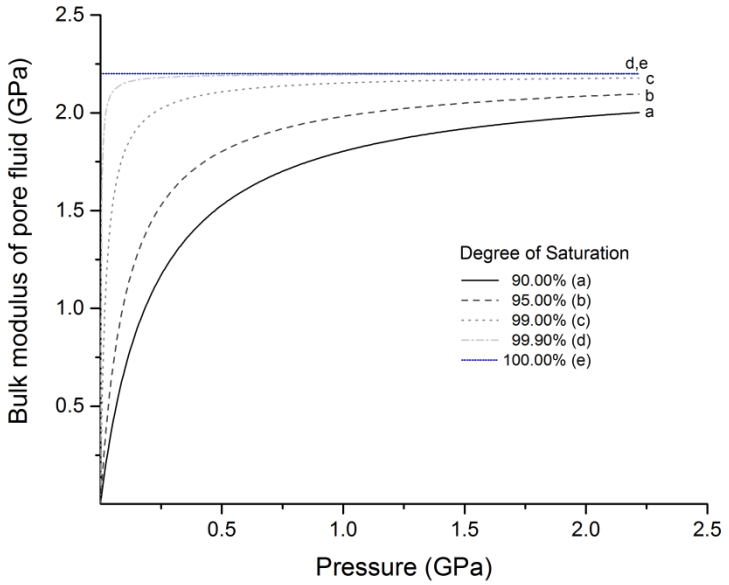

Figure 4.2: Bulk modulus of pore fluid against absolute fluid pressure, both in GPa, calculated from Eq. 7 for a range of degrees of saturation from 90% to 100% (fully saturated).

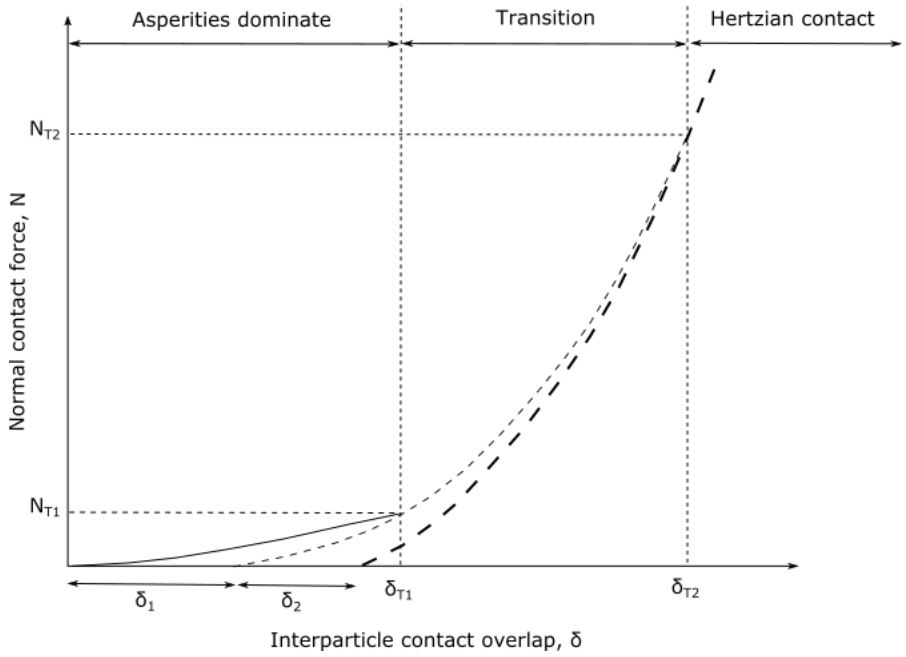

Figure 4.3: Schematic of the rough-surface contact model used in this study, based on Otsubo et al. (2016).

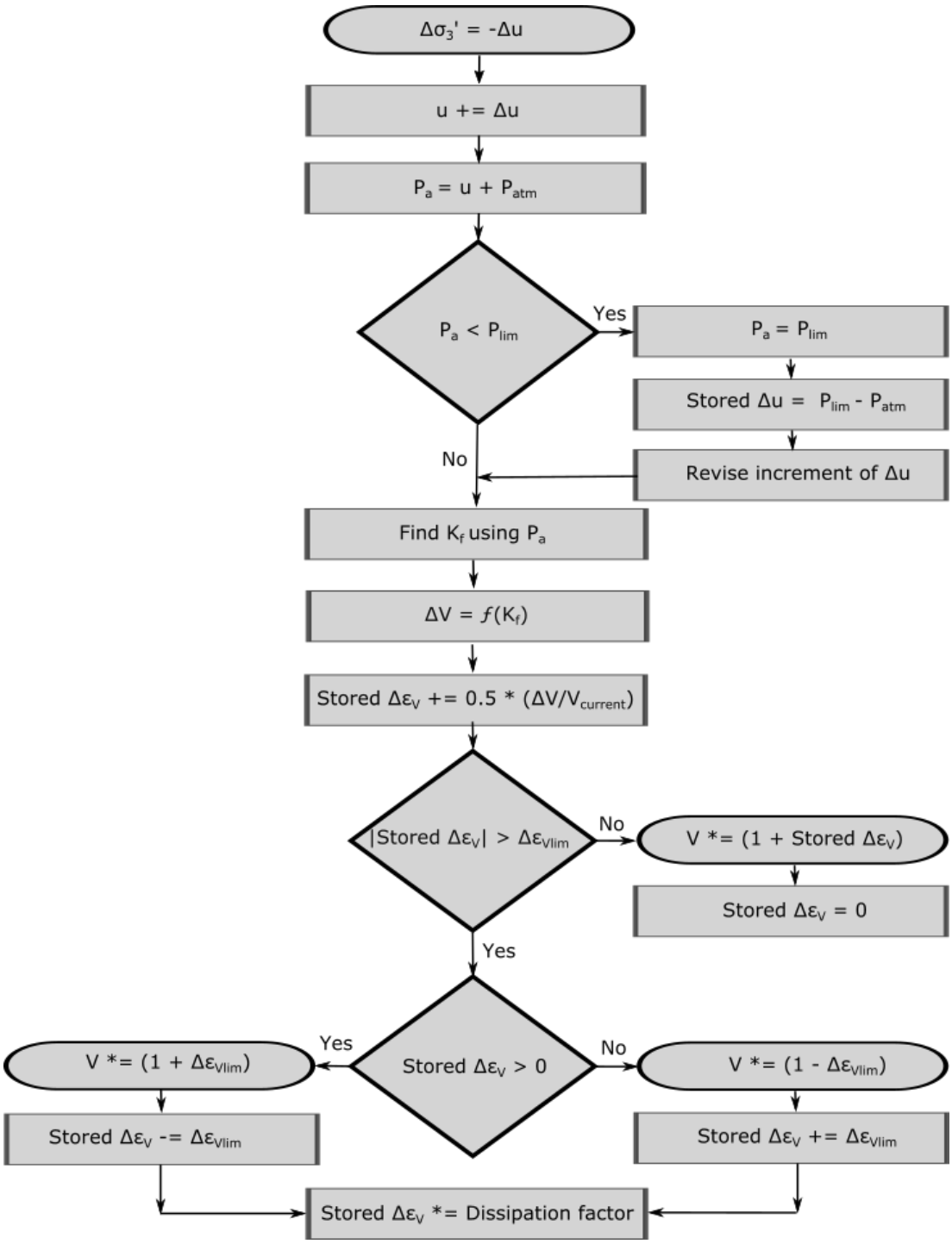

Figure 4.4: Flowchart showing the implementation of the bulk modulus method in a DEM code.

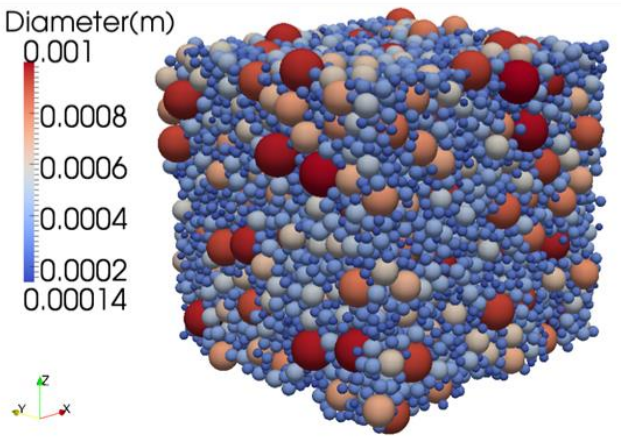

Figure 4.5: Assembly of particles used in this study.

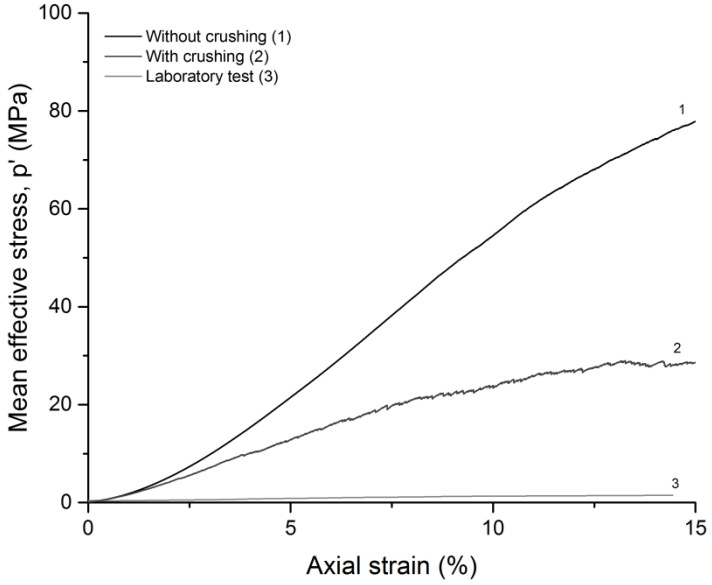

Figure 4.6: Mean effective stress (MPa) against axial strain (%) for the constant-volume triaxial simulations with and without crushing compared with data from an undrained triaxial laboratory test for a confining pressure of 400 kPa (Kuwano, 1999).

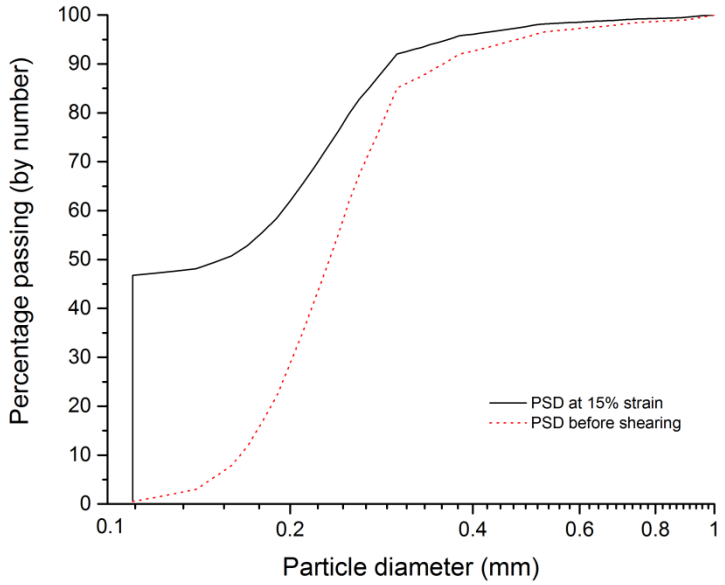

Figure 4.7: Comparison of particle size distributions by number before shearing and at 15% strain for the constant-volume triaxial simulation where particle crushing is considered.

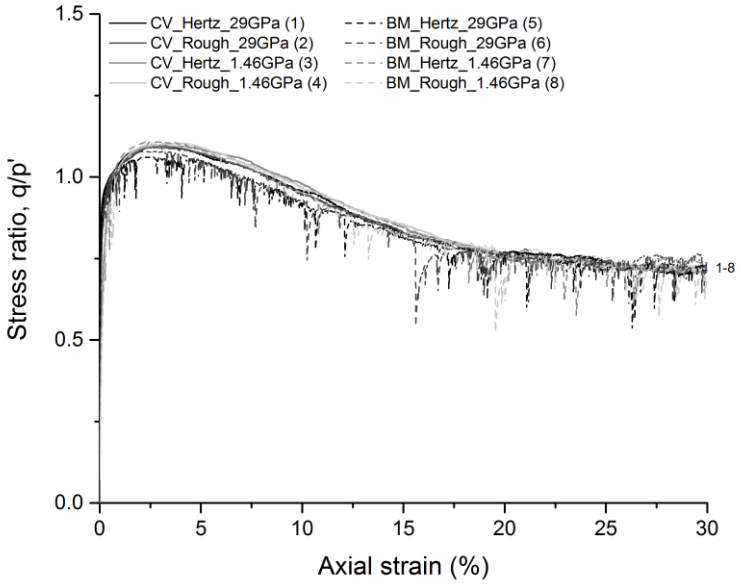

Figure 4.8: Plot of stress ratio against axial strain (%) for triaxial shearing of dense samples using the constant volume (CV) and bulk modulus (BM) methods, smooth Hertz-Mindlin and rough-surface contact models, and particle shear moduli of 29 GPa or 1.64 GPa. The numbers 1–8 denote different combinations of these variables. Particle crushing is not considered.

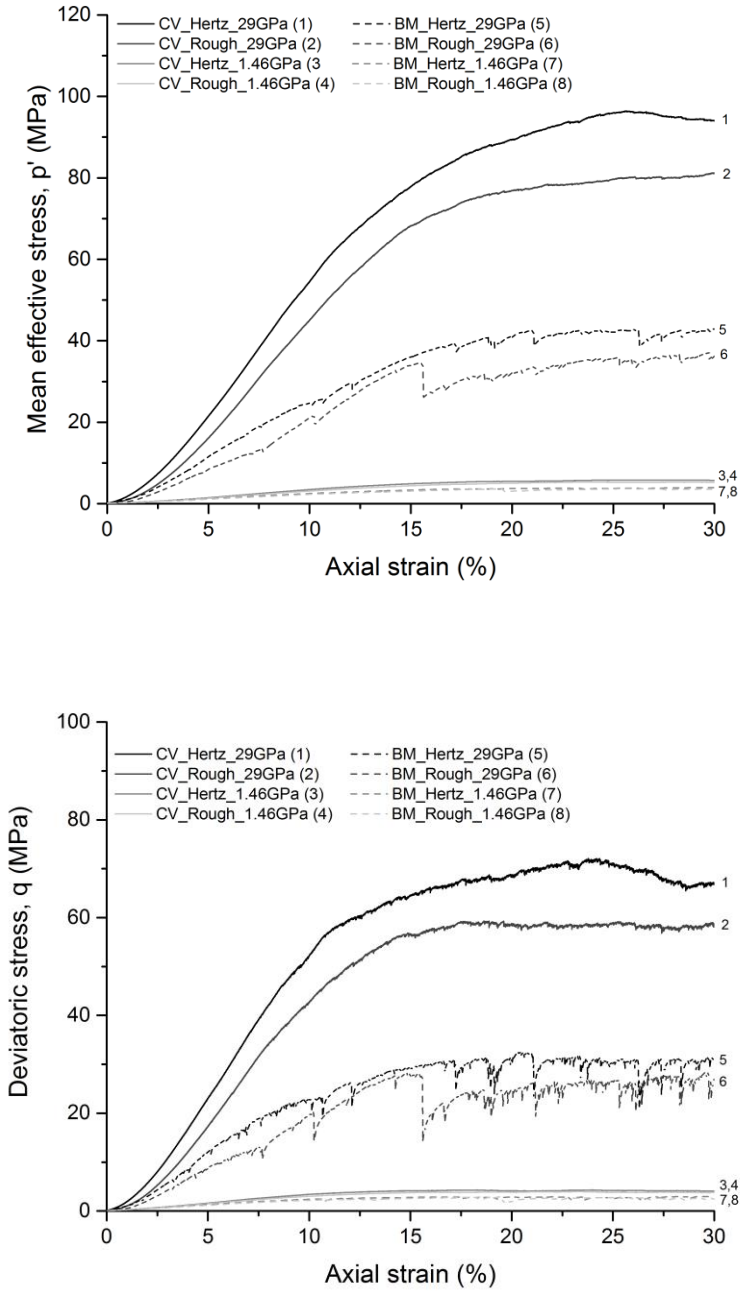

Figure 4.9: Mean effective stress (a) and deviator stress (b), both in MPa, against axial strain (%) for the eight triaxial simulations without crushing.

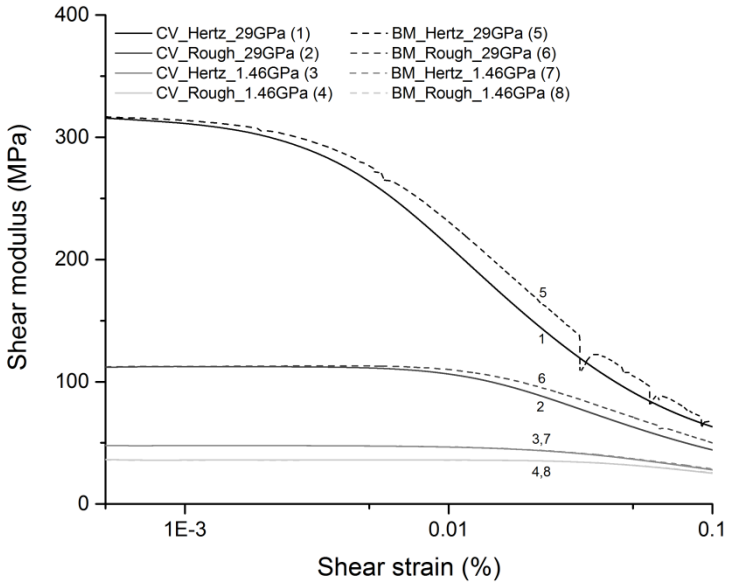

Figure 4.10: Degradation of shear modulus (MPa) against triaxial shear strain (%) for the eight simulations without crushing considered.

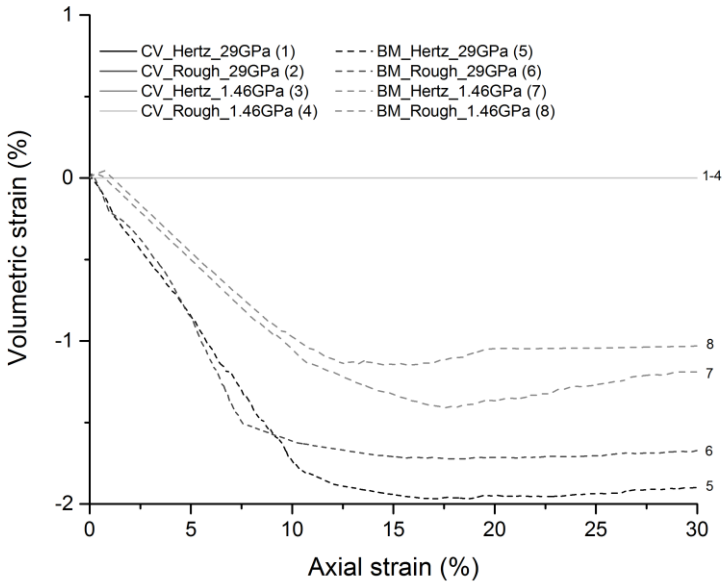

Figure 4.11: Volumetric strain (%) vs axial strain (%) for the triaxial simulations of 28309-sphere samples denoted as 1–8 in the caption of Fig. 5. Negative volumetric strains indicate dilation.

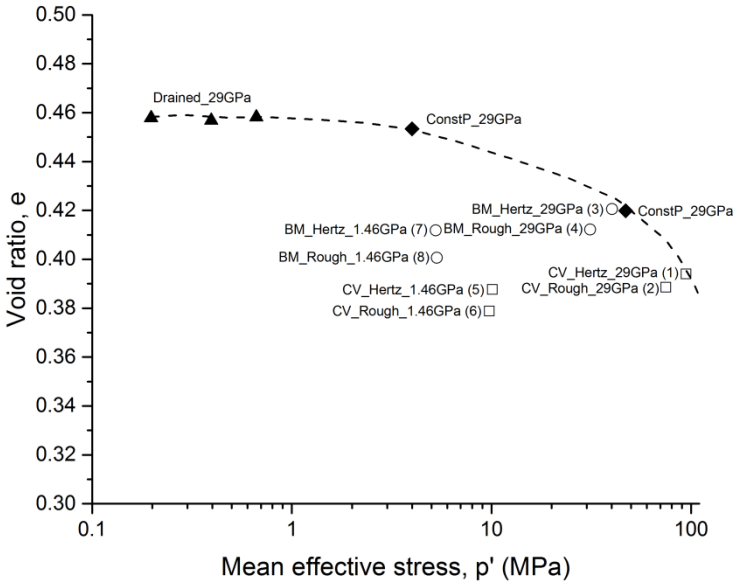

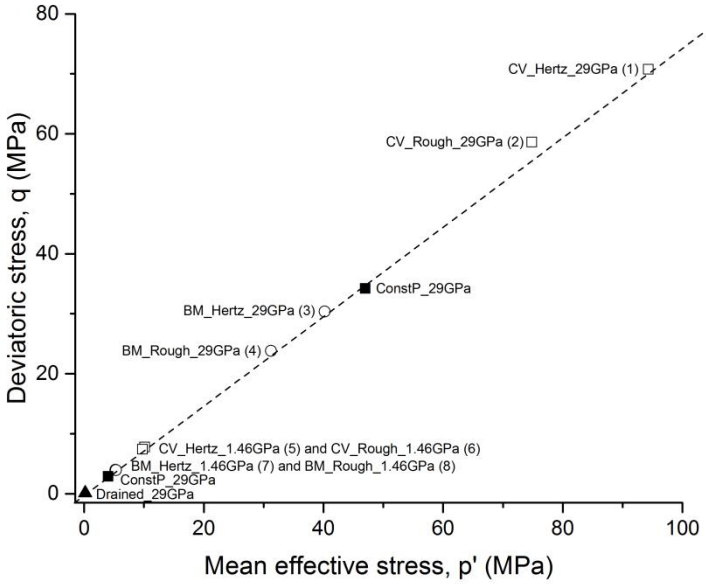

Figure 4.12: Critical state line in (a) e–log(p') and (b) q–p' spaces for a range of constant volume, constant mean effective stress and constant minor principal effective stress (drained) using G = 29 GPa and a Hertzian contact model. Points beneath this line are for simulations using the bulk modulus method, a rough surface contact model and/or a reduced G of 1.46 GPa.

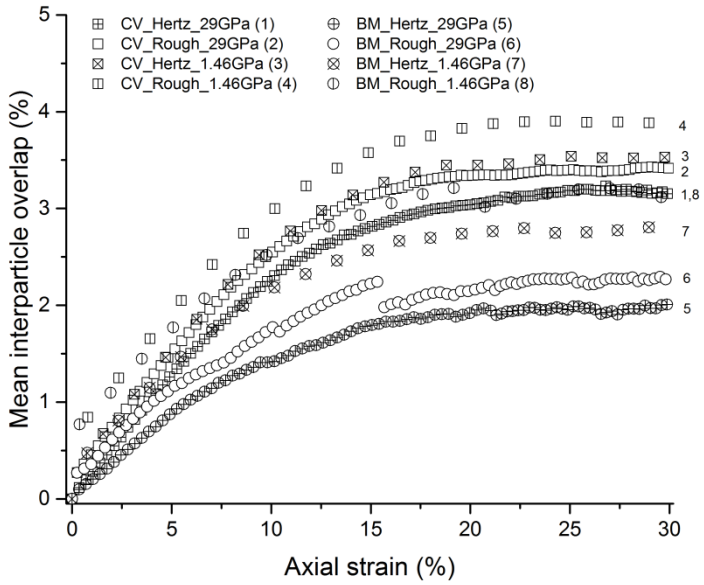

Figure 4.13: Mean interparticle overlap against axial strain, both in %, for the simulations described in the caption of Fig. 4.5.

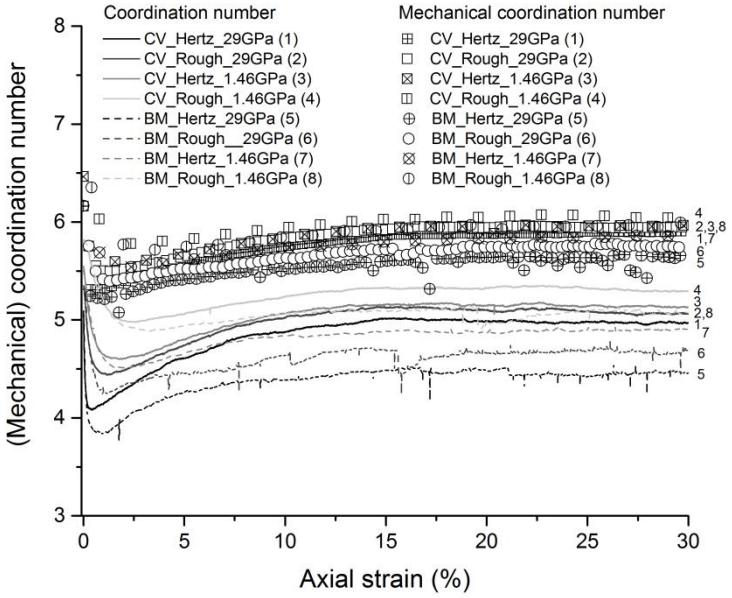

Figure 4.14: Plots of coordination number (Z) vs axial strain (%) and mechanical coordination number vs axial strain (%) for undrained triaxial simulations conducted using a dense sample containing 28309 uncrushable spheres.

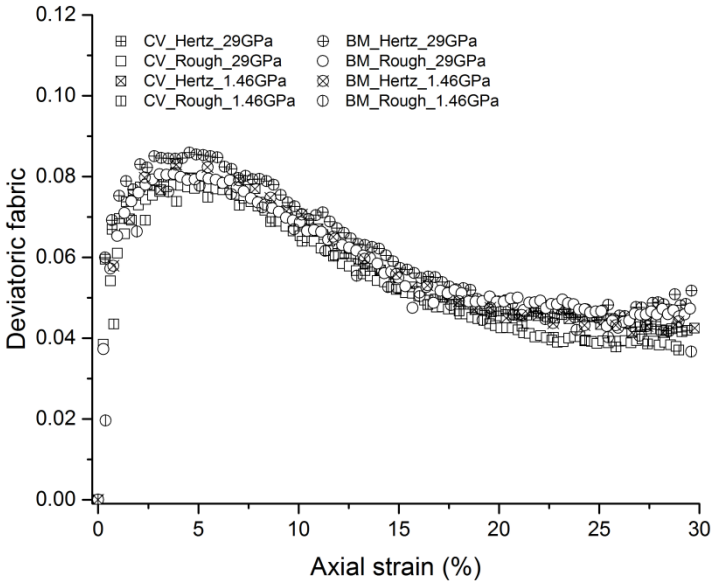

Figure 4.15: Deviatoric fabric against percentage axial strain for the eight simulations considered without crushing.

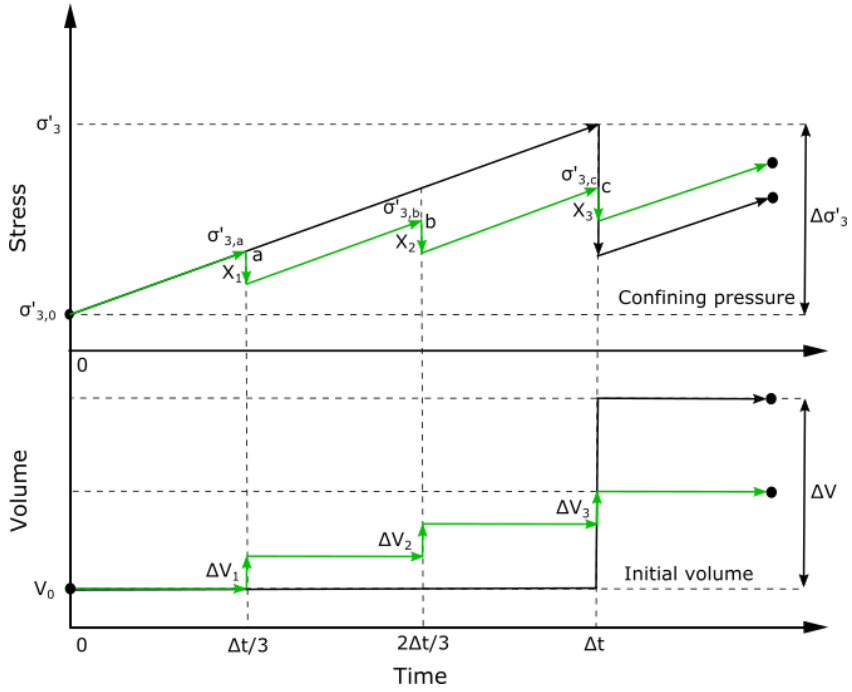

Figure 4.16: Schematic of the volume increment for a continuous time scenario implemented in the code.

Chapter 5 Evaluating the cyclic triaxial response of sand using Design of Experiments

Many geo-engineering structures are subjected to cyclic loading during normal operation, e.g., renewable offshore wind turbines are likely to experience millions of load cycles, with variations in cycle magnitude and frequency, during their service lives. These forces are transmitted to the soil which may cause unacceptable soil displacement and, in extreme cases, it may lead to soil liquefaction. These failure features have been studied in field tests (Jardine and Standing, 2000), model tests (Tsuha *et al*., 2012) and soil element laboratory tests. These tests capture the macroscopic soil behavior but give no insight into the governing micro-scale behaviour. Numerical techniques are capable of providing information on the dynamic changes occurring at the micro-scale that cause the observed macro-scale response.

5.1 Introduction

The soil adjacent to many engineering structures experiences millions of load cycles during the design life cycle of the structures. Such loading may be due to environmental factors such as seismic activity or storms, or human activities such as high-speed train motion or the action of wind turbines. Fig. 1.1 presents characteristic numbers of cycles and cycle periods for various cyclic loading events and also indicates the space in which design documentation is available for cyclic loading (shaded zone) and the area where further research is needed (Andersen *et al*., 2013). Researchers have conducted physical tests such as triaxial, hollow cylinder or shear box tests, or numerical experiments based on the discrete element method and the finite element method to understand the soil response due to cyclic loading. Cyclic triaxial tests have been studied extensively in the context of seismic liquefaction resistance by many researchers such as Seed and Idriss (1971) and Ishihara *et al*. (1975). In recent years, with the expansion of the renewable offshore industry, understanding the soil around coastal structures such as wind turbines, breakwaters, foundations, slopes and embankments subjected to cyclic loads due to wind, waves, etc. has become increasingly essential to ensure efficient and safe structures (Tsuha *et al*., 2012; Jardine and Standing, 2000; Lehane *et al*., 1993). Comprehensive experiments at full scale, model scale and laboratory scale on dense marine Dunkerque sands were reported by Jardine and Standing (2000), Tsuha *et al*. (2012)

and Aghakouchak (2015), respectively. These tests proved that low-level cyclic amplitudes could lead to an improvement in effective stress with little strain accumulation over large cycles, whereas high-level cyclic amplitudes led to heavy losses in effective stress and failure within few cycles.

It is important to understand the dynamics governing micro-scale behaviour to be able to interpret the underlying causes of the observed macro-scale response. To understand the evolution of microstructure, researchers have used many different techniques, both experimental (e.g., X-ray tomography, shear wave velocity measurement) and numerical (e.g., discrete element method). DEM has previously been used to investigate the mechanical behaviour of soil under cyclic loading (Sitharam and Vinod, 2010; Kuhn *et al*., 2014; Huang *et al*., 2018). DEM is capable of providing information on the dynamic changes occurring at the micro-scale; however, a key challenge in DEM analyses is the computational expense: studying the influence of many different parameters such as number of cycles, period, mean cyclic load, cyclic load amplitude, confining pressure and void ratio on the dynamic properties of granular materials could potentially be very costly.

The aim of this chapter is to establish a way to investigate the behaviour of sand subjected to cyclic loading using a Design of Experiments approach to address the shortcomings mentioned above. There are three main parts in this study. Firstly, preliminary studies of sand behaviour were conducted, using undrained triaxial cyclic loading simulations with the constant volume method. Secondly, a Design of Experiments (DOE) approach was adopted to systematically investigate the behaviour of sand subjected to cyclic loading using DEM. Thirdly, the above DOE analysis was used to predict the cyclic responses for randomly selected input parameters. This study will help in interpreting the causes of macro- and micro-mechanical responses in sand samples under cyclic loading at acceptable computational cost. Reducing the shear modulus by a factor of 20 is used as it achieves more realistic stresses and is computationally beneficial as the reduced shear modulus allows the simulation time-step to be increased as presented in chapter 4.

5.1.1 Cyclic loads:

Cyclic loads can arise in nature from the action of waves, tides, wind or earthquakes, in addition to anthropogenic sources such as machinery operation or railways. In most

cases, cyclic loads are often composed of a succession of irregular-amplitude cycles that are distributed randomly in time. However, the cyclic field, laboratory-model and soil-element tests that are conducted to explore cyclic loading effects are usually restricted to tests that can be conducted within limited time-frames and at cyclic rates that allow suitable control, precision and data capture rates. The most common practice is to apply sinusoidal regular cycles which can be defined by the number of cycles (*N*), period (T), mean cyclic load (q_{mean}), and cyclic load amplitude (q_{cyc}) as shown in Fig. 5.1. The cyclic deviator stress is given by

$$q = q_{mean} + q_{cyc} sin\left(\frac{2\pi t}{T}\right) \tag{5.1}$$

where T is the cyclic period and t is the elapsed simulation time. Regular cyclic loading can be either symmetrical, i.e., an initially isotropic soil sample where q_{mean} is zero, or non-symmetrical, i.e., an anisotropic soil sample (q_{mean} not equal to zero) which often arises when the dead-weight of the structure is considered. The initial stress state (α) condition is defined by the ratio of q_{mean} and mean effective stress, p_0' (Yang and Sze 2011).

$$\alpha = \left(\frac{q_{mean}}{p_0'}\right) \tag{5.2}$$

$$q_{mean} = \sigma_{1,0}' - \sigma_{3,0}' \tag{5.3}$$

where $\sigma_{1,0}'$ is the major principal consolidation effective stress and $\sigma_{3,0}'$ is the major principal consolidation effective stress. Triaxial cyclic loading on anisotropic soil samples consolidated under $\sigma_{1,0}'$ and $\sigma_{3,0}'$ with an initial q_{mean} has been carried out by many researchers (Seed and Lee, 1966; Hyodo *et al*., 1994; Yang and Sze, 2011). One-way loading (no reversal stress) occurs when $q_{cyc} \leq q_{mean}$ while two-way loading occurs when $q_{cyc} > q_{mean}$.

5.1.2 Cyclic loading response

The dynamic cyclic loading response of soils is mostly analysed using two standards:

1. ASTM D3999-11: Determination of the Modulus and Damping Properties of Soils Using Cyclic Triaxial Apparatus (D3999-11, 2013).
2. ASTM D5311-11: Load Controlled Cyclic Triaxial Strength of Soil (D5311-11, 2013).

Most of the research on offshore foundations focused on the behaviour of effective stress drifting and cyclic stress ratio (CSR) of the sand that leads to liquefaction during undrained cyclic loading. Under high amplitude cycles, liquefaction occurs through effective stress drifting in undrained tests. For the triaxial test, effective stress drifting is calculated as ratio of change in mean effective stress and initial mean effective stress before shearing:

$$ESR = \frac{\Delta p'}{p'_0} = \frac{p' - p'_0}{p'_0} \tag{5.4}$$

The cyclic stress ratio, CSR, is given by

$$CSR = \frac{q_{cyc}}{p'_0} \tag{5.5}$$

where p'_o is the initial mean effective stress before shearing.

Shear modulus and damping ratio parameters are used by many researchers for analysing the cyclic response. Shear modulus, G_s , is calculated by Eq. 5.7:

$$E = \frac{q_{cyc}}{\varepsilon} \tag{5.6}$$

$$G_s = \frac{E}{2(1+\vartheta)} \tag{5.7}$$

E, the Young's modulus, is the slope of the q_{cyc} and corresponding strain ε in a hysteresis loop. ϑ is the Poisson's ratio of the sand sample: 0.5 for the saturated undrained condition. During the cyclic triaxial test, a hysteresis loop similar to one shown in Fig. 5.2 is obtained by plotting deviator stress versus axial strain. This represents the amount of energy dissipated during the load cycle. Damping ratio, D, is a measure of energy dissipated to the maximum elastic strain energy and may be computed from the area of the hysteresis loop using Eq. 5.8:

$$D = \frac{A_L}{4\pi A_T} \tag{5.8}$$

A_L is the area enclosed by the hysteresis loop. The area enclosed by the hysteresis loop is calculated using the Masing rule, i.e., the tangent of the hysteresis loop at the reversal points of the unloading and reloading should be identical to initial cyclic loop (Matasovic and Vucetic, 1993). A_T is the area of the shaded triangle on Fig. 5.2. It is

the area of the triangle defined by maximum q_{cyc} and corresponding strain ε. The rule followed for determination of G_s and D at any strain from the hysteresis loop is restricted to maximum closure, i.e., 0.00254 mm between two successive peaks (D3999-11, 2013).

It is noted that researchers have used different approaches to calculate damping ratio, e.g., Lee and Hartmann (1998) used the entire loading cycle work done instead of that during half a cycle (approximated by the triangular area bounded by the secant modulus). Assimaki *et al*. (2000) proposed four parameters ($\mu_o', \omega, C_b, \omega_s$) model to predict the shear moduli and damping values of granular material subjected to cyclic shearing with is derived from the MIT-S1 soil model (Pestana, 1994). In Eq. 5.9, shear stress, $\tau(\gamma_c)$ is dependent on the previously mentioned parameters. The model formulation is given by Assimaki *et al*. (2000):

$$G(\gamma_c) = \frac{\tau(\gamma_c)}{\gamma_c} \tag{5.9}$$

$$D(\gamma_c) = \frac{1}{2\pi}\frac{\Delta E}{G(\gamma_c)\gamma_c^2} \tag{5.10}$$

Khouri (1984) and Ishibashi and Zhang (1993) proposed an equation to predict D for sand as:

$$D = 0.333\left[0.586\left(\frac{G}{G_{max}}\right)^2 - 1.547\left(\frac{G}{G_{max}}\right) + 1\right] \tag{5.11}$$

The maximum damping ratio, D_{max}, is defined as 33.3% for very high strain where $\frac{G}{G_{max}}$ approaches zero for sand. This value is used by many researchers such as Hardin and Drnevich (1972) and Sherif *et al*. (1977) for sand. Therefore in this study, the onset of liquefaction is defined as the attainment of 33.3% in damping ratio and this value is used in the DOE analysis.

As shearing continues, excess pore pressure builds up which reduces the effective stress of the soil sample. To quantify the pore pressure generation during shearing, the excess pore pressure ratio is used. It is the ratio of pore pressure change during shearing to consolidation effective stress applied before shearing. Therefore, when u_r =1, the pore pressure generated during cyclic shearing is equal to the initial minor principal stress, $\sigma_{3,0}'$, of the sample.

$$u_r = \frac{\Delta u}{\sigma'_{3,0}} \tag{5.12}$$

In a constant-volume simulation, the excess pore water pressure is estimated as $\Delta u = \sigma'_{3,0} - \sigma'_3$ (Yimsiri and Soga 2010). Where σ'_3 is the minor principal effective stress at every subsequent time-step in the DEM simulation. Sections 5.1.3 and 5.1.4 offer a brief review on the behaviour of sands under cyclic loading.

5.1.3 Cyclic failure

Soil is a complex multi-phase material consisting of solid and pore fluid (liquid and gas in the general case). Under undrained tests, the pore fluid does not have sufficient time to escape from the soil sample when subjected to load. Due to this, excess pore pressure is generated. This excess pore pressure controls important soil responses such as liquefaction: the complete loss of soil strength and stiffness (Castro, 1969). Researchers defined liquefaction as a loss of strength, i.e., zero effective stress due to the cyclic loading (Seed and Idriss, 1971) or by the magnitude of cyclic stress ratio that is required to produce large deformation (Ishihara *et al*., 1975). To understand this failure condition, the common failure criterion adopted is the attainment of 5% axial strain in double amplitude or attainment of 5% peak axial strain in single amplitude (Mulilis *et al*., 1977; Sze and Yang, 2013). Robertson *et al*. (1995) suggest the evaluation of liquefaction of soil under undrained shear as shown in Fig. 5.3. Flow liquefaction can occur during either monotonic or cyclic loading for a loose sand with strain hardening behaviour. Sand with strain hardening behaviour may cause cyclic liquefaction and cyclic mobility due to strain accumulation. Stress reversal where the static stress is less than the cyclic stress as shown in Fig. 5.4 under undrained cyclic loading causes cyclic liquefaction when the effective stress reaches zero. Stress reversal where the static stress is larger than the cyclic stress as shown in Fig. 5.5 under undrained cyclic loading causes cyclic mobility but the effective stress never reaches zero. Many researchers such as Hyodo *et al*. (1994); Huang *et al*. (2018); made an attempt to correlate the undrained cyclic response to monotonic behaviour by conducting monotonic and cyclic undrained tests to study the cyclic failure behaviour. The results suggest that flow deformation starts when the effective stress path intersects the phase transformation line (PTL) which lies between the critical state line (CSL) and instability line (ISL). Flow-type liquefaction was observed for a loose sample and cyclic mobility was observed for a dense sample (Hyodo et al. (1994).

Many researchers such as Jardine and Standing (2000), Tsuha *et al*. (2012) and Aghakouchak (2015) conducted cyclic tests to investigate the potential for effective stress drift and total stiffness degradation and liquefaction of a sand for offshore applications and identified three modes of behaviour: stable (S) where the strain accumulation is below 0.4 mm over 500 cycles throughout the tests; metastable (MS) where strain accumulates at moderate rates until a certain cycle and after that accelerates more sharply; and unstable (US) where permanent displacements (≈0.5 mm/cycle) develop in the first few cycles.

5.1.4 Factors affecting cyclic response

The rates at which permanent strains accumulate in drained tests or effective stresses degrade in undrained tests depend on several factors including:

1. The cyclic loading parameters such as amplitude or frequency
2. The void ratio of the sample
3. Effective stress ratio, stress history, and preloading prior to cycling

- Effect of cyclic amplitude (q_{cyc}) on cyclic response behaviour:

Seed and Idriss (1971), Dobry *et al*. (1982) and Hsu and Vucetic (2004), among others, have investigated the effect of cyclic stress amplitude, considered to be the most influential parameter for strain accumulation in drained tests and effective stress degradation rates in undrained tests. Aghakouchak (2015) investigated the effect of cyclic stress amplitude (described using cyclic stress ratio CSR parameter defined as $\frac{q_{cyc}}{p'_o}$) on Dunkerque sands under cyclic undrained triaxial tests. He concluded that a low CSR of ~0.25 and below could lead to an improvement in effective stress and little strain accumulation during a large number of cycles, whereas a higher CSR ~0.35 and above led to heavy losses in effective stress as illustrated in Fig. 5.6 and 5.7. Dobry *et al*. (1982) reported that higher strain levels lead to high effective stress degradation rates in undrained tests and high accumulated volumetric strains in drained tests. Sitharam and Vinod (2010) studied the effect of cyclic strain amplitude level on a granular sample undergoing cyclic undrained triaxial tests using DEM and found that higher strain amplitude leads to an increase in hysteresis loop area.

- Effect of Initial anisotropy (q_{mean}) on cyclic response behaviour:

Most triaxial cyclic tests on soil are performed under isotropic confining pressures. However, in nature the soil experiences anisotropic stress conditions due to the ground condition or adjacency to loaded structures. The effects of initial anisotropy on cyclic resistance have been debated. Seed *et al*. (1983) pointed out that existence of initial anisotropy reduces excess pore pressure in undrained tests and decreases strain accumulation in drained tests. Konrad (1993) argued that anisotropy brings the initial effective stress states closer to the failure envelope, leading to failure under smaller cyclic loads. DEM cyclic undrained simulations on anisotropically compressed assemblies show an influence on the shear modulus of the sample, especially at low values of shear strain below 10^{-1} %; however, at larger shear strains (bigger than 10^{-1} %), anisotropy has an insignificant influence on the shear modulus and damping ratio is not influenced much by the anisotropy (Sitharam and Vinod, 2010).

- Effect of loading frequency on cyclic response behaviour:

Salvati and Anhdan (2008) conducted cyclic triaxial tests on dense Monterey sand with loading frequencies of 0.1 and 1.5 Hz under different confining pressures. They reported that the strain accumulation rates appeared greater under the higher loading frequency in the initial cycles, then dropped and followed similar trends as cycling continued. Airey and Fahey (1991) reported results from cyclic triaxial tests on marine silica sand with frequencies between 0.05 to 10 Hz and q_{cyc} of 100 kPa under confining pressures of 300 to 500 kPa. They found no effect on the stress-strain response. Therefore, in general, the conclusion is that loading frequency does not have much influence on the cyclic response.

- Effect of void ratio on cyclic response behaviour:

Wichtmann (2005) reports, based on drained cyclic tests conducted at varying void ratios that strain accumulation decreases as relative density rises. Sitharam and Vinod (2010) conducted a DEM undrained cyclic triaxial test at a confining pressure of 100 kPa with different values of initial void ratio. They observed that initial void ratio has a significant influence on the shear modulus of the sample, especially at low values of shear strain below 10^{-1}%; however, beyond a shear strain of 10^{-1}%, initial void ratio has an insignificant influence on shear modulus. A similar result was observed experimentally by Ishihara (1996).

- Effect of confining pressure on cyclic response behaviour:

Sitharam and Vinod (2010) conducted undrained cyclic triaxial simulations for different confining pressures and showed that confining pressure has a significant influence on the shear modulus of the sample at low values of shear strain below 1%. Increasingthe confining pressure for the same void ratio decreases the cyclic resistance to liquefaction. However it depends on cyclic stress ratio at that given confining pressure (Seed, 1990; Suazo et al., 2016).

5.1.5 Design of experiments: Taguchi

DEM techniques are capable of providing information on the dynamic changes occurring at the micro-scale that cause the observed macro-scale response. However, a key challenge in DEM analyses is the computational expense: simultaneously studying the influence of many different parameters such as the number of cycles, cyclic amplitude, loading frequency, confining pressure, void ratio and initial anisotropy on the dynamic properties of granular materials could potentially be very costly. Design of experiments (DOE) approaches have become very popular in industrial practice as a tool to achieve robust quality design and to minimise costs (Taguchi, 1987). DOE entails a systematic investigation of system variables that influence the key overall responses of the system. Once the system variables that affect the overall responses have been identified, and changes in system variables have been related to changes in each response, robust predictions can be made. When computational or experimental resources are limited, it allows for getting the most information from relatively few experimental tests. Some of the DOE methods are factorial, Plackett–Burman design, response surface and Taguchi method. Yoon (2007) used Plackett–Burman design to calibrate DEM micro-scale parameters related to the uniaxial compression of bonded rock particles. DOE methods were used to calibrate DEM models of a mixer and a hopper based on experimental measurements of torque and discharge flow rate, respectively (Favier *et al*., 2010). Johnstone and Ooi (2010) used DOE methods to find the DEM model parameters based on experimental measurements of flow in a rotating drum device and mechanical response during a confined compression test. Hanley (2011) applied the Taguchi method to study the discrete element model parameters of a single bonded agglomerate.

Taguchi DOE methods were first introduced by Genichi Taguchi, a Japanese researcher who applied a set of statistical methods to quality management. He is widely regarded as pioneering the modern quality-by-design approach (Ross and Ross, 1988). The Taguchi design method is widely used in industrial practice as a valuable tool to achieve robust quality design and minimise costs by establishing an optimum process with consistency in performance (Taguchi, 1987). A Taguchi design is an orthogonal array defining an experiment that requires only a fraction of the number of full-factorial combinations. An orthogonal array means the design is balanced so all the factors are weighted equally, thus allowing the influence of each factor to be assessed independently. The Taguchi method views the design/process as a three-phase design (Ross and Ross, 1988, p .168):

- System design
- Parameter design
- Tolerance design

System design involves identifying design parameters which may have the greatest influence on the response and suitable settings for the parameters selected. The parameters selected are the factors in the design, and the settings of the factors are referred to as levels. The output results to be analysed are referred as responses, e.g., damping ratio or shear modulus. The parameter design phase finds the optimum levels for each factor from those tested in the system design. The tolerance design phase improves quality by tightening the tolerance on the process at a minimal cost. Taguchi designs are denoted as L_N where N is the number of experiments to be run. The selection of a suitable orthogonal array depends on the number of factors and levels to be tested (Ross and Ross, 1988, p.74). The standard table representing the L_{27} orthogonal array is shown in Appendix C.1 (Table C.1). Each column in the orthogonal array represents a factor and each row represents an experiment with that particular combination of factor levels.

The main advantage of the Taguchi approach is the use of orthogonal arrays minimises the amount of experimental data to be gathered, e.g., if the full factorial design were used to assess 13 factors for three levels, it would necessitate 3^{13} (1594323) experiments. The L_{27} array requires only 27 experiments: a small fraction of the full factorial design. Taguchi designs are primarily intended to study the main effects of factors. However, the DOE with orthogonal arrays generates very intricate

confounding. This means effects of the factors and of interactions are mixed; a column may contain the effect of partial or full interactions, in addition to the effect of a factor, e.g., the interaction between the factors in columns 1 and 2 is distributed between columns 3 and 4 for any three-level array as shown in Appendix C.1 (Table C.1). If factors are allocated to columns 1, 2 and 3 of this array, it would become impossible to distinguish between the effect of the factor in column 3 and the partial interactive effect due to the factors in columns 1 and 2, both of which are contained in column 3. Taguchi designs use a triangular table for assigning the factors to array columns in a way that avoids confounding. The standard triangular table for the L_{27} is shown in Appendix C.2.

5.1.5.1 Analysis of Variance (ANOVA)

Analysis of variance (ANOVA) was first introduced by Sir Ronald Fisher in the 1930s as a way to interpret the results of agricultural experiments (Ross and Ross, 1988). It is a statistical method used to analyse the response variability attributed to each factor or interaction collected from a Design of Experiments. The Taguchi method uses Analysis of Variance (ANOVA) for interpreting experimental data and to make statistically based decisions (Ross and Ross, 1988), (Taguchi, 1987). In the two-way ANOVA, the total sum of squares (SS_T) for two factors is decomposed into (Ross and Ross, 1988, p 48):

$$SS_T = SS_A + SS_B + SS_{A*B} - SS_E \tag{5.13}$$

where SS_A is the variation due to factor *A,* SS_B is the variation due to factor *B,* SS_{A*B} is the variation due to the interaction between factors *A* and *B,* SS_E is the variation due to error*.*

The total sum of squares, SS_T, is a quantity that measures the total variation or deviation of the data and it is calculated by the given equation:

$$SS_T = \sum_{i=1}^{n_p} (y_i - \bar{y})^2 \tag{5.14}$$

where n_p is the total number of data points and $\bar{y}$ is the global mean of the data.

The sum of squares due to factor *A,* SS_A, is the portion of the total sum of squares that may be attributed to variations in factor *A*.

$$SS_A = SS_T - \sum_{k=1}^{n_A} \left(\sum_{i=1}^{n_p/n_A} \left(y_{i|k} - \overline{y_k} \right)^2 \right) \tag{5.15}$$

n_A is the number of levels of factor A and $y_{i|k}$ is the subset of data points in which factor A was tested at level *k*. $\overline{y_k}$ is the mean of this data subset.

The sum of squares of the error, SS_E, is the portion of the total sum of squares that is not accounted for by any of the factors or explicitly calculated interactions, where n_f is the number of factors.

$$SS_E = SS_T - \sum_{j=1}^{n_f} SS_j - SS_{AxB} \tag{5.16}$$

The sum of squares due to the variation of interaction factors *A* and *B* (SS_{A*B}) is given by:

$$SS_{AxB} = SS_T - SS_A - SS_B - \sum_{l=1}^{n_A} \left[\sum_{\substack{k=1 \\ k \neq l}}^{n_B} \left(\sum_{i=1}^{n_p/(n_A x n_B)} \left(y_{i|lk} - \overline{y_{lk}} \right)^2 \right) \right] \tag{5.17}$$

n_A and n_B are the numbers of levels of factors A and B, respectively. $y_{i|lk}$ is the subset of data points in which factor A is at level l and factor B is at level k. $\overline{y_{lk}}$ is the mean of this data subset. A brief summary of the basic ANOVA equations are provided above (5.13–5.17); for further detail, the reader is directed to Ross and Ross (1988) and Hanley (2011).

For completing the ANOVA calculations and to check for significance, variances (V) are calculated by dividing a sum of squares by the appropriate number of degrees of freedom. A degree of freedom, DF, is the amount of information available to allow estimation of the value of the unknown parameters and its variation. Four different degrees of freedom are defined as:

$$DF_{Total} = n_p - 1 \tag{5.18}$$

$$DF_{factor_j} = n_j - 1 \tag{5.19}$$

$$DF_{interaction\_factor_j} = \prod_{1}^{i=2} DF_{factor_j} \tag{5.20}$$

$$DF_{Error} = DF_{Total} - \sum_{j=1}^{n_f} DF_{factor_j} - \sum_{i=1}^{n_i} DF_{interaction\_factor_j} \tag{5.21}$$

n_j is the number of levels of factor j, n_f is the number of factors and n_i is the number of explicitly calculated interactions between two factors (interactions between more than two factors are neglected). For example, if a factor has three levels, the degrees of freedom of that factor is equal to *2*.

Once the experiments and calculations above have been completed, the main effects and interactions can be tested for statistical significance using the *p-value*. Statistical significance can be determined by dividing variances, V_j, for each factor (or interaction) j by the variance of the error, V_e, and comparing the result to the f-distribution value for the specified confidence level. The p-value is the probability of getting an f-distribution value greater than or equal to the f-statistic value indicating that the hypothesis is true. The significance level (α) tells us the acceptable level of risk for the given confidence level (CL). It is given by:

$$\alpha = 1 - \left(\frac{CL}{100}\right) \tag{5.22}$$

For example, if the confidence level is chosen as 95%, then α = 0.05. The *p-value* is used to determine whether or not a factor is significant by comparing against α value. If the *p-value* is lower than α value, i.e., $p < 0.05$, then the factor is significant.

5.2 DEM sample preparation for cyclic CV simulations.

A cubic granular specimen of 10 × 10 × 10 mm^3 containing 28,309 spheres with radii varying between 0.1 mm and 1 mm was created. The particles were placed randomly within the periodic cell without initial overlaps using a MATLAB code (Hanley *et al*., 2014). Periodic boundary conditions were adopted to eliminate boundary effects (Huang *et al*., 2014c) and to ensure homogenous deformation (Cundall, 1988). The initial particle positions were imported to LAMMPS and 7 samples were created for parametric study as shown in Table 5.1 and 27 samples were created for DOE as shown in Table 5.3 by moving the boundaries under stress control. by moving the

boundaries under stress control. The particle shear modulus, G, was set to 1.46 GPa (see chapter 4 section 4). The particle density and Poisson's ratio were set at 2675 kg/m^3 and 0.2, respectively. Gravity and particle crushing were not considered in this study. A simplified Hertz-Mindlin smooth particle contact model was used. During cyclic loading, the friction coefficient was increased to 0.25 from the values used during sample preparation. All of the simulations were run using a modified version of the LAMMPS (Plimpton, 1995) software.

5.3 Undrained cyclic DEM simulations: a preliminary parametric study

Before the cyclic triaxial constant-volume (CV) DEM simulation were conducted according to the DOE, a preliminary parametric study was conducted to assess the ability of the simulations to capture the typical characteristics of cyclic loading of sand, for choosing a suitable local damping coefficient and to help in selecting the levels of each factor for DOE study. A parametric study was conducted under fixed $\sigma'_{3,0}$ = 300 kPa and loading frequency, f = 6 Hz with varying e = 0.39, 0.42 and 0.45 and q_{cyc} = 40, 80 and 120 kPa. Seven CV triaxial cyclic DEM simulations as shown in Table 5.1 were simulated.

Table 5.1: A preliminary parametric study was conducted before L27 DOE study.

Isotropic		Cyclic shearing	
Confining pressure, $\sigma'_{3,0}$ (kPa)	Void ratio, e	Local damping, d	Deviator stress amplitude, q_{cyc} (kPa)
300	0.42	0.1	80
300	0.42	0.0	80
300	0.42	0.2	80
300	0.42	0.1	40
300	0.42	0.1	120
300	0.39	0.1	120

300	0.45	0.1	120

The main purpose of using local damping in LAMMPS is to expedite the kinetic energy dissipation to reach quasi-static equilibrium. Fig. 5.8 shows the effect of local damping on three undrained cyclic simulations. There is no significant difference in macro- or micro-scale results such as mean effective stress and coordination number by using local damping coefficients of 0, 0.1 or 0.2. The main reason for the similarity may be due to the quasi-static cyclic loading condition. There is no significant change in simulation calculation time by using different local damping coefficients. Fig. 5.9 shows the shear modulus (G_s) of the bulk sample from the start of loading until the maximum deviator stress in a single loading cycle. The shear modulus remains constant up to an axial strain of 0.01%, beyond which the shear modulus started to decrease characteristically of soil: soil behaves purely elastically when the shear strain is below 0.01 % and thereafter becomes elasto-plastic (Ishihara, 1996). At higher q_{cyc} values, the shear modulus of the sample tends to reduce more; for example, for q_{cyc} = 120 kPa, SM reduces to 37 MPa compared to q_{cyc} = 80 kPa (SM = 43 MPa). The damping ratio (D) is determined from the area of the hysteresis loop on a plot of *q* against axial strain. Fig. 5.10a shows these hysteresis loops for three simulations in which only q_{cyc} was varied. Higher q_{cyc} values lead to higher D; the increasing size of hysteresis loop with q_{cyc} was previously reported by Sitharam and Vinod (2010). Fig. 5.10b shows that higher q_{cyc} values tend to decrease p' and promote a migration toward a critical state line, a result well known in the literature, e.g., Sitharam and Vinod (2010). This result indicates that higher CSR lead to a degradation in p'; this was also observed during experimental cyclic triaxial tests (Aghakouchak, 2015). Fig. 5.11a shows that mean effective stress ratio, $ESR = \frac{\Delta p'}{p'_0} = \frac{p' - p'_0}{p'_0}$ against the number of cycles. Higher q_{cyc} values lead to a degradation in ESR; a similar observation was made by Aghakouchak (2015). To quantify the change in pore pressure during shearing, the excess pore pressure ratio, $u_r = \frac{\Delta u}{\sigma'_{3,0}}$ is often used. In DEM constant-volume simulations, Δu is calculated using Eq. 3.1 (chapter 3). Fig. 5.11b shows that higher q_{cyc} tends to increase u_r, a result well known from the literature, e.g., Huang *et al*. (2018). Fig. 5.12 shows that higher q_{cyc} leads to decreasing coordination number Z.

Fig. 5.13 shows $q - p'$ for three simulations for fixed q_{cyc} = 120 kPa in which only void ratio (e) was varied. Higher *e* values lead to migrating p' toward a critical state line, M = 0.73 (from monotonic CV simulation) and lesser e values lead to migrating p' away from a critical state line. Similar observations were made in a physical test conducted by Aghakouchak (2015). This preliminary parametric study indicated the capability of the simulation to capture the typical characteristics of cyclic loading of sand, enabled choosing a suitable local damping coefficient for the simulation and helped in selecting the levels of each factor for DOE study.

5.4 Experimental design for cyclic triaxial DEM simulations

Five factors were varied in these experiments while keeping the other factors constant during these cyclic simulations. The five factors (q_{cyc}, q_{mean}, frequency, void ratio and confining pressure), each tested at three levels, are shown in Table 5.2. Three levels were chosen for each factor to capture the intermediate effect on responses and to discover any potential non-linearity in the variation of a response with a factor. The levels of each factor were selected to achieve desirable CSR, a medium dense sample and to ensure an inertia number less than 3.6×10^{-5}: lower than the limiting value of 7.9×10^{-5} proposed for quasi-static behaviour (Perez *et al*., 2016).

Table 5.2: Factors and levels for L_{27} experimental design.

Factors	Unit	Levels			Column
		1	2	3	
q_{cyc}	kPa	40	80	120	1
q_{mean}	kPa	0	50	100	2
Frequency, f	Hz	2	4	6	5
Void ratio, e		0.39	0.42	0.45	8
Initial confining pressure	kPa	150	300	500	9

In order to study the complete factorial for these 5 factors with 3 levels, 3^5 = 243 simulations would be required. Using the orthogonal Taguchi L_{27} DOE, only 27 simulations are needed if an L_{27} design array containing 13 columns were selected for these experiments as shown in Appendix C.1 (Table C.1).

As the interactions between the three-level factors are distributed between two columns, columns 3, 4, 6 and 7 are left vacant to avoid confounding with two interactions of interest to study. Interaction (I) between q_{cyc} and q_{mean} is contained in columns 3 and 4, and interaction (II) between q_{cyc} and frequency is contained in columns 6 and 7, according to the triangular table in Appendix C.2 (Table C.2). These interaction factors were chosen based on physical cyclic phenomena such as q_{cyc} (amplitude), q_{mean} (one-way or two-way loading) and frequency. The number of degrees of freedom remaining is allotted for interactive effects. There are many DOE methods available. However the Taguchi L_{27} method was selected due to its aforementioned advantages.

27 samples were created to satisfy the combinations required of the L_{27} as shown in Table 5.3 by moving the boundaries under stress control.

Table 5.3: L_{27} array showing the columns used after assigning all factors to the array.

Row	Column				
	q_{cyc} (kPa)	q_{mean} (kPa)	Frequency (Hz)	Void ratio (e)	$\sigma'_{3,0}$ (kPa)
1	40	0	2	0.39	150
2	40	0	4	0.42	300
3	40	0	6	0.45	500
4	40	50	2	0.42	300
5	40	50	4	0.45	500
6	40	50	6	0.39	150
7	40	100	2	0.45	500

Row	Column				
	q_{cyc} (kPa)	q_{mean} (kPa)	Frequency (Hz)	Void ratio (e)	$\sigma'_{3,0}$ (kPa)
12	80	0	6	0.45	150
8	40	100	4	0.39	150
9	40	100	6	0.42	300
10	80	0	2	0.39	300
11	80	0	4	0.42	500
13	80	50	2	0.42	500
14	80	50	4	0.45	150
15	80	50	6	0.39	300
16	80	100	2	0.45	150
17	80	100	4	0.39	300
18	80	100	6	0.42	500
19	120	0	2	0.39	500
20	120	0	4	0.42	150
21	120	0	6	0.45	300
22	120	50	2	0.42	150
23	120	50	4	0.45	300
24	120	50	6	0.39	500
25	120	100	2	0.45	300

26	120	100	4	0.39	500
27	120	100	6	0.42	150

5.5 Results and discussion of DOE cyclic triaxial DEM simulations

All 27 cyclic simulations were run for 10 cycles or until the onset of liquefaction, whichever occurred sooner. The DEM simulation results obtained for four responses (ESR, Z, G_s, D) are provided in Appendix C Tables (C.5-C.9). In these tables, one-way cyclic loading simulations where $q_{cyc} < q_{mean}$ are denoted with an asterisk. Those simulations for which liquefaction occurred during the 10 cycles are denoted by 'L' and the number of cycles when liquefaction occurred. In this study, the onset of liquefaction is defined as attainment of 5% axial strain in double amplitude or attainment of 5% peak axial strain in single amplitude or $p' \approx 0$. At liquefaction, ESR = 100%, Z = 0, G_s = 0 and D = 33.3% are used in ANOVA analysis.

Six simulations liquefied before reaching 10 cycles. Liquefaction occurred with CSR > 0.36 for e = 0.45 and with *CSR* > 0.72 for e = 0.42 before reaching 10 cycles. However, for e = 0.45 with one-way loading (no reversal of stress) with CSR = 0.43, liquefaction didn't occur within 10 cycles. No liquefaction occurred for e = 0.38 within 10 cycles, even with CSR = 0.58. The DOE gives a rough indication of three modes of sand behaviour (*stable, metastable* and *unstable*) under different q_{cyc} applied to samples with different void ratios. Higher q_{cyc} leads to increasing D, which means the sample is dissipating more energy; similar results were reported by Sitharam and Vinod (2010). With the introduction of anisotropic q_{mean} , p_0' increases as does the G_s of the sample. Accumulation of strain in a single load cycle may be relatively small but the cumulative effect over a large number of cycles can be significant and lead to liquefaction. Table C.3 and Table C.4 shows the comparison between the response at the first and ninth complete load cycle for ESR, Z, G_s and D. As 6 simulations liquefied before reaching 10 cycles, the first load cycle responses were used for ANOVA study. The main effects and interactions were analysed for these four responses at the end of the first cycle.

Table 5.4 shows the mean to means response, i.e, mean of all of the means of several subsamples of D, G_s, ESR, Z obtained from an ANOVA statistical analysis after one complete load cycle. The statistical significance (α) was measured with the *p-value*, as described in Section 5.1.5.1; a confidence level of 95% was chosen for analysis. For visualisation of results, the statistically-significant effects are denoted in bold and with an asterisk. The data were analysed using Minitab (version 17). Fig. 5.14 shows the main effects plots for four responses (ESR, Z, G_s, D) obtained from this ANOVA analysis. Fig. 5.14a shows that selecting e =0.39 (very dense sample) tends to increase ESR whereas selecting $\sigma'_{3,0}$ = 150 kPa tends to reduce it. The increase of e leading to a degradation in ESR was also observed during experimental cyclic triaxial tests conducted by Aghakouchak (2015). However, e and $\sigma'_{3,0}$ had no statistically significant effect on ESR at the 95% level ($p < 0.05$) in the ANOVA analysis as shown in Table 5.4 and the sum of squares error, SS_E, accounted for more than 25% of SS_T for ESR as shown in Fig. 5.16. Fig. 5.14b shows that selecting a higher void ratio, i.e., e =0.45, leads to a reduction in Z on average and selecting lower $\sigma'_{3,0}$ = 150 kPa leads to a reduction. Both have a statistically significant effect on Z as shown in Table 5.4. The reason for this reduction in Z is that particles are more free to move inside the loose sample than the dense sample. The void ratio, e accounted for more than 49% of SS_T for Z and SS_E is around 11% of SS_T for Z as shown in Fig. 5.15.

Table 5.4: ANOVA table for mean to mean responses. DF is the number of degrees of freedom, SS the sum of squares associated to each element of the table and p the p-value calculated with the respective variances. Statistically-significant effects at a 95% confidence level are denoted in bold and with an asterisk

Factor	DF	Mean effective stress ratio (ESR)		Coordination Number (Z)	
		SS	p	SS	p
q_{cyc}	2	2481.7	0.179	3.5434	0.182
q_{mean}	2	673.1	0.580	0.6934	0.673
Frequency, f	2	688.5	0.573	1.2918	0.493

Void ratio, e	2	3656.1	0.097	27.7783	**0.001***
Confining pressure, $\sigma'_{3,0}$	2	2987.1	0.136	11.6581	**0.018***
$q_{cyc} * q_{mean}$	4	1541.7	0.631	2.3235	0.615
$q_{cyc} * f$	4	1529.0	0.635	1.9447	0.684
Error	8	4609.4		6.6720	
Total	26	18166.7		55.9053	

Factor	DF	Shear Modulus (G_s)		Damping ratio (D)	
		SS	p	SS	p
q_{cyc}	2	1.33E+09	**0.000***	0.042154	**0.034***
q_{mean}	2	1.17E+07	0.654	0.026371	0.088
Frequency, f	2	2.08E+07	0.484	0.013023	0.251
Void ratio, e	2	5.91E+09	**0.000***	0.027786	0.080
Confining pressure, $\sigma'_{3,0}$	2	8.52E+09	**0.000***	0.091113	**0.004***
$q_{cyc} * q_{mean}$	4	5.81E+07	0.414	0.019030	0.379
$q_{cyc} * f$	4	3.44E+07	0.638	0.009487	0.672
Error	8	1.04E+08		0.031533	
Total	26	1.59E+10		0.260497	

Fig. 5.14c shows that selecting q_{cyc} = 40 kPa and e = 0.38 tends to increase G_s whereas selecting $\sigma'_{3,0}$ = 150 kPa tends to reduce it. q_{cyc} , e and $\sigma'_{3,0}$ had a statistically significant effect on G_s as shown in Table 5.4 and accounted for more than 8%, 37 % and 53% of SS_T for G_s , respectively. SS_E is around 0.9% of SS_T for SM as shown in Fig. 5.15. Fig. 5.14d shows that selecting q_{cyc} = 40 kPa tends to reduce D and selecting $\sigma'_{3,0}$ = 150 kPa tends to increase it. q_{cyc} and $\sigma'_{3,0}$ had a statistically significant effect on D as shown in Table 5.4 and accounted for more than 33% and 17% of SS_T for D respectively. SS_E is around 12% of SS_T for D as shown in Fig. 5.15. Frequency and q_{mean} had no statistically significant effect on ESR, Z, G_s and D.

5.5.1 Prediction

The prediction is made from the regression equation generated from the ANOVA table. To assess the predictive ability of the Taguchi method, eight similar undrained triaxial cyclic DEM simulations with randomly selected combinations of factor levels (not in the L_{27} design array) were simulated as shown in Table 5.5. The same four simulation responses, CSR, coordination number, damping ratio and shear modulus at the end of one load cycle, were compared with the ANOVA predictions based on the L_{27} design responses.

Table 5.5: Randomly selected parameter values used for response prediction

Run	q_{cyc} (kPa)	q_{mean} (kPa)	Freq. Hz	Void ratio, e	$\sigma'_{3,0}$ (kPa)
1	80	100	6	0.42	150
2	40	50	4	0.45	150
3	80	0	2	0.38	150
4	120	100	6	0.42	300
5	40	50	6	0.45	300
6	120	0	4	0.38	300
7	120	100	4	0.42	500
8	80	50	2	0.45	500

Fig. 5.16 shows the four responses, i.e., ESR, Z, G_s, D obtained from DEM simulation vs model predictions from an ANOVA statistical analysis at one complete load cycle. The correlation between the model predicted values and simulation response for ESR, Z, G_s and D are 42.97%, 89.75%, 93.93%, and 56.64%, respectively.

5.5.2 Varying amplitude cycle analysis

Many researchers such as Ishihara and Yasuda (1972), Ishihara and Nagase (1988) and Tatsuoka *et al*. (1986) studied the effect of cyclic loading with varying amplitudes. Seed and Idriss (1971) replaced the random cyclic loading with equivalent regular cycles of constant amplitude to estimate the risk of liquefaction. Wichtmann *et al*. (2010) applied Miner's rule to study the strain accumulation in sand under drained cyclic loading. Miner's rule is used for fatigue analysis under reversal loading. It is expressed as $\sum_{i=1}^{n} \frac{N_i}{N_{fi}} = 1$, where N_i is the number of load cycles applied and N_{fi} is the number of cycles to failure (onset of liquefaction in this context). Many researchers such as Wang (1989); Azeiteiro *et al*. (2017) and Kuhn *et al*. (2014) found that the pore pressure depends on the sequence of varying amplitudes applied during cyclic test.

Eight varying amplitude cyclic loading DEM simulations with 3 stages running with different sequences of low, medium and high q_{cyc} were carried out using $\sigma'_{3,0}$ = 300 kPa and f = 6 Hz as shown in Table 5.6. Each stage runs for 5 cycles with same q_{cyc}. There are three sequences in complete cyclic simulation, e.g., Run 1: sequence of q_{cyc} = 40 kPa, 80 kPa and 120 kPa is shown in Fig. 5.17. The four standard simulation responses (Effective stress ratio, pore pressure ratio, axial strain and coordination number) were analysed.

Fig. 5.18a plots the pore pressure ratio (u_r) vs number of cycles (N) for these eight simulations. The sequence with larger q_{cyc} at stage-3 cycle (i.e., 40-80-120 kPa or 80-40-120 kPa) was found to produce more u_r for both e= 0.39 and 0.42 than the sequence starting with smaller q_{cyc} at the stage-3 cycle (i.e., 120-40-80 kPa or 120-80-40 kPa). A similar trend was observed by Kuhn *et al*. (2014). Run 1 and Run 3, Run 2 and Run 5 & Run 4 and Run 6 have same u_r at the end of 15 cycles. Higher e

value leads to higher u_r for the same sequence of load cycles for both increasing and decreasing order sequences, i.e., for (Run 1 and Run 7) and for (Run 6 and Run 8).

Table 5.6: Eight distinct sequences of varying amplitude simulations

Run	Void ratio (e)	Stage-1	Stage-2	Stage-3
		q_{cyc} (kPa) (1 to 5 cycles)	q_{cyc} (kPa) (6 to 10 cycles)	q_{cyc} (kPa) (11 to 15 cycles)
1	0.39	40	80	120
2	0.39	40	120	80
3	0.39	80	40	120
4	0.39	80	120	40
5	0.39	120	40	80
6	0.39	120	80	40
7	0.42	40	80	120
8	0.42	120	80	40

Fig. 5.18b plots the mean effective stress ratio ($\frac{\Delta p'}{p'_o}$) vs number of cycles (N). An mean effective stress ratio, $\frac{\Delta p'}{p'_o} = \frac{p' - p'_o}{p'_o} = -1$ means p' = 0. A negative sign indicates effective stress degradation. The larger q_{cyc} was found to produce more positive $\frac{\Delta p'}{p'_o}$ response than the smaller q_{cyc} for e = 0.39 and produce more negative $\frac{\Delta p'}{p'_o}$ response than the smaller q_{cyc} for e = 0.42. A similar result was observed by Aghakouchak (2015) for a triaxial test conducted on medium dense sand. Fig. 5.19 shows the evolution of axial strain (%) vs N. However, at the third sequence of 10-15 cycles the axial strain is approximately similar for same q_{cyc} loading sequence for the very dense sample, i.e., e = 0.38. However, for e = 0.42, the axial strain is different for the same

q_{cyc}. Higher q_{cyc} values lead to reduce Z and Z_m. Similarly there is not significantly differenced in cyclic responses at the end of 15 cycles with varying q_{cyc} loading sequence for same initial void ratio as shown in Fig. 5.20a, Fig. 5.20b and Table 5.7. The above reason may be due to particles being more free to move inside the loose sample than the dense sample. A similar result was observed by Wichtmann *et al*. (2010): no significant change in stresses due to changing the cyclic amplitude. Larger void ratio causes larger strain. Niemunis *et al*. (2006) also observed the same strain accumulation resulting from a different sequence of cyclic amplitudes.

Table 5.7: Summary of eight responses at the end of 15 cycles

Void ratio (e)	q_{cyc} (kPa) (1-5)	q_{cyc} (kPa) (6-10)	q_{cyc} (kPa) (11-15)	End of 15 cycles			
				Axial strain (%)	u_r	ESR	Z
0.39	40	80	120	0.0608	0.1058	0.0051	5.649
0.39	40	120	80	0.0329	0.0718	0.0021	5.673
0.39	80	40	120	0.0608	0.1058	0.0051	5.647
0.39	80	120	40	0.0115	0.0361	0.00085	5.679
0.39	120	40	80	0.0329	0.0718	0.0021	5.674
0.39	120	80	40	0.0108	0.0361	0.00084	5.682
0.42	40	80	120	0.0759	0.1277	-0.0169	4.673
0.42	120	80	40	0.0075	0.0588	-0.0218	4.692

As the final values are not much influenced by the cyclic loading sequence for a very dense sample, a DOE prediction technique could be used to predict the varying amplitude cyclic responses. The sum of the decay (change from the original state) caused by the uniform cyclic load at the particular number of cycles is approximately similar to the decay caused by the varying amplitude cyclic loading. For example, the sum of mean effective stress decay for uniform cycle loading of q_{cyc} = 40 kPa, 80 kPa

and 120 kPa at 5 cycles is 0.0003 + 0.003 + 0.025 = 0.0283 kPa and the mean effective stress decay for the varying amplitude cyclic loading of q_{cyc} = 40 kPa, 80 kPa and 120 kPa at the end of 15 cycles is 0.022 kPa. This similarity of decay may be due to smooth spherical cohesiveness elastic particles consideration and no particle crushing in the simulation.

5.6 Conclusion

This chapter highlighted the capability of the discrete element method to simulate the cyclic response behaviour of sand samples with different cyclic parameters such as q_{cyc}, q_{mean}, and frequency. Unlike in experiments, in these numerical simulations, sample preparation, repeatability and reproducibility are assured. Micromechanical analysis showed that Z decreases with an increase in axial strain and the number of load cycles. The void ratio *e* was found to have the most significant effect on G_s and Z. With the introducing of anisotropy q_{cyc} value in the sample, leads to increase ESR. However, the influence of frequency on cyclic response quantities was found to be insignificant.

Four responses, i.e., ESR, Z, G_s, D, obtained from DEM simulation vs model predictions from an ANOVA statistical analysis at one complete load cycle were correlated. The correlations for ESR, Z, G_s and D are 42.97%, 89.75%, 93.93%, and 56.64%, respectively.

From the eight varying amplitude cyclic loading DEM simulations, the sequence with larger q_{cyc} at stage-3 cycle was found to produce more u_r for both e = 0.39 and 0.42 than the sequence starting with smaller q_{cyc} at the stage-3 cycle. The larger q_{cyc} was found to produce more positive ESR response than the smaller q_{cyc} for e = 0.39 and produce more negative ESR response than the smaller q_{cyc} for e = 0.42.

In this chapter, the Taguchi method was introduced to simulate cycle loading using discrete element models. Taguchi approach has many advantages one such is that orthogonal arrays are used to minimise the amount of data required but the main disadvantage is confounding due to the use of orthogonal arrays. However, this can be mitigated by careful allocation of factors to columns of the array to avoid confounding effect. L_{27} Taguchi design approach is used in this study.

The Taguchi method is certainly suitable to studies the DEM cyclic responses and to identify the main effects and the interactive effects. There is a good prediction between DEM simulation responses for shear modulus and coordination number with the results obtained from ANOVA predictions.

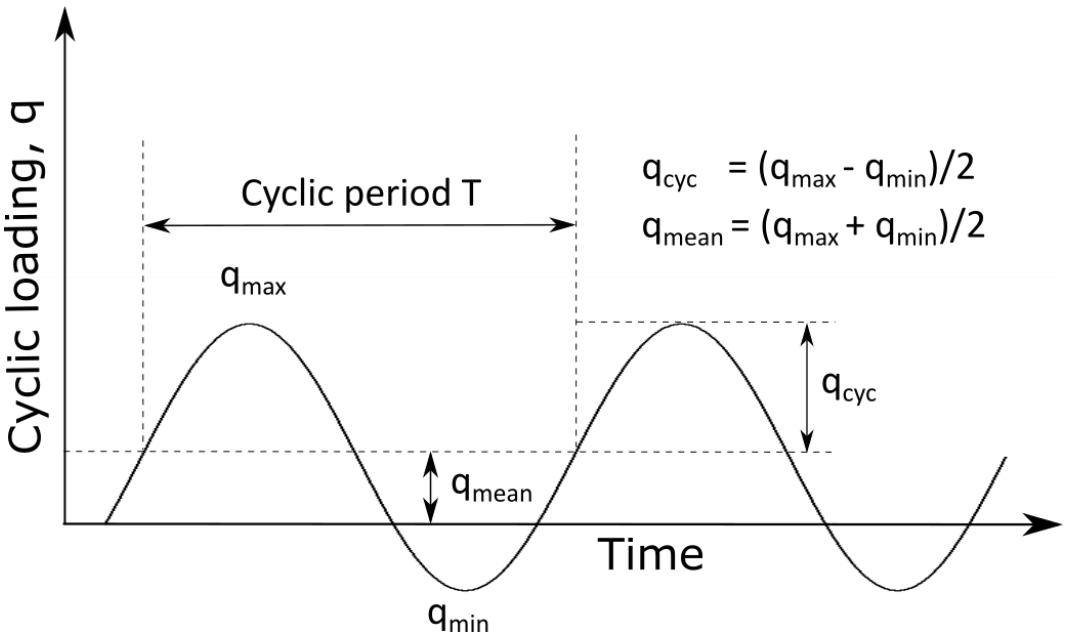

Figure 5.1: Schematic diagram of cyclic loading

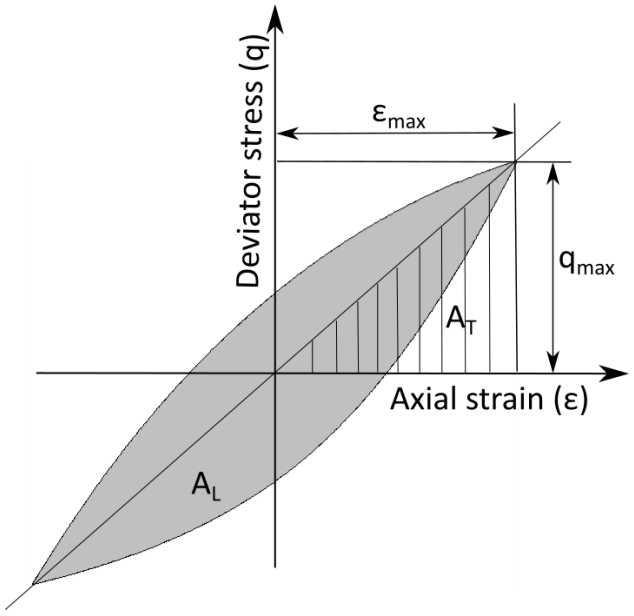

Figure 5.2: Schematic of a hysteresis loop for computing the damping ratio

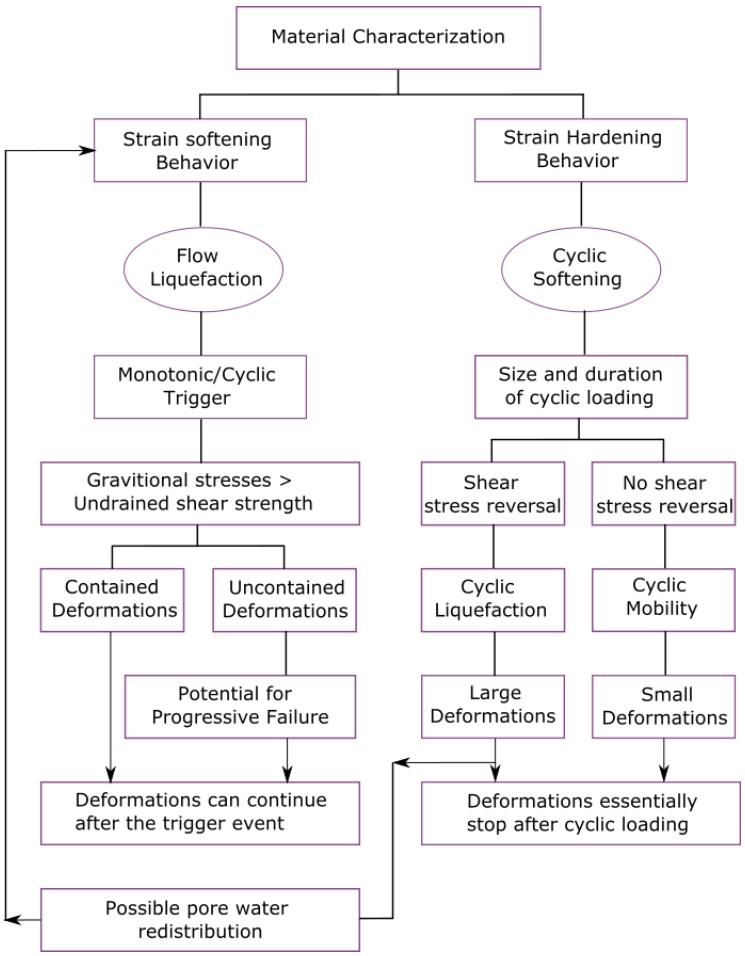

Figure 5.3: Schematic flow chart for evaluation of soil liquefaction (Robertson et al., 1995)

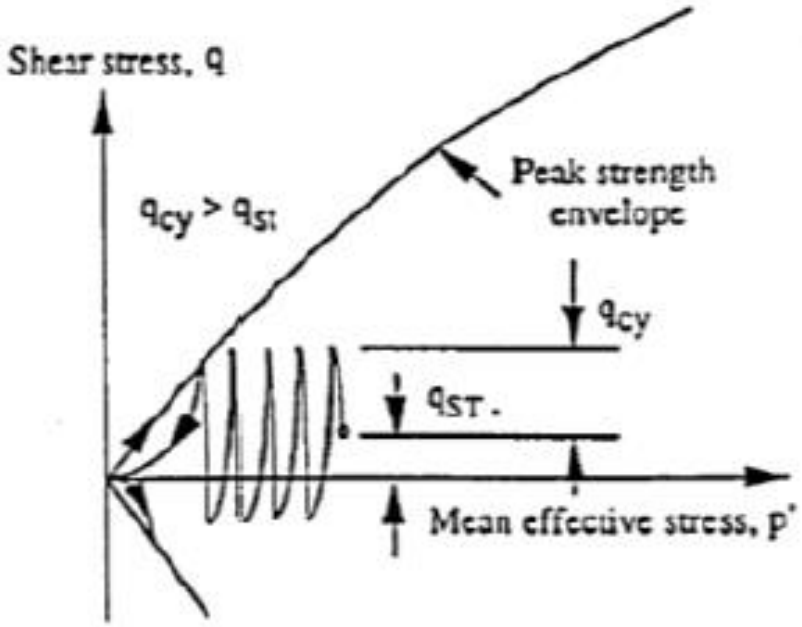

Figure 5.4: Schematic diagram of cyclic liquefaction (Prearo et al., 2015)

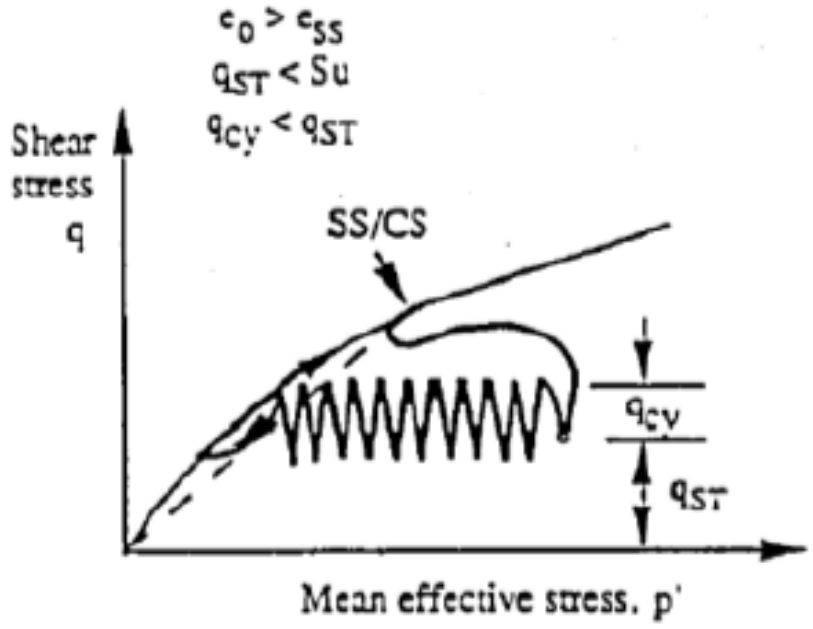

Figure 5.5: Schematic diagram of cyclic mobility (Prearo et al, 2015)

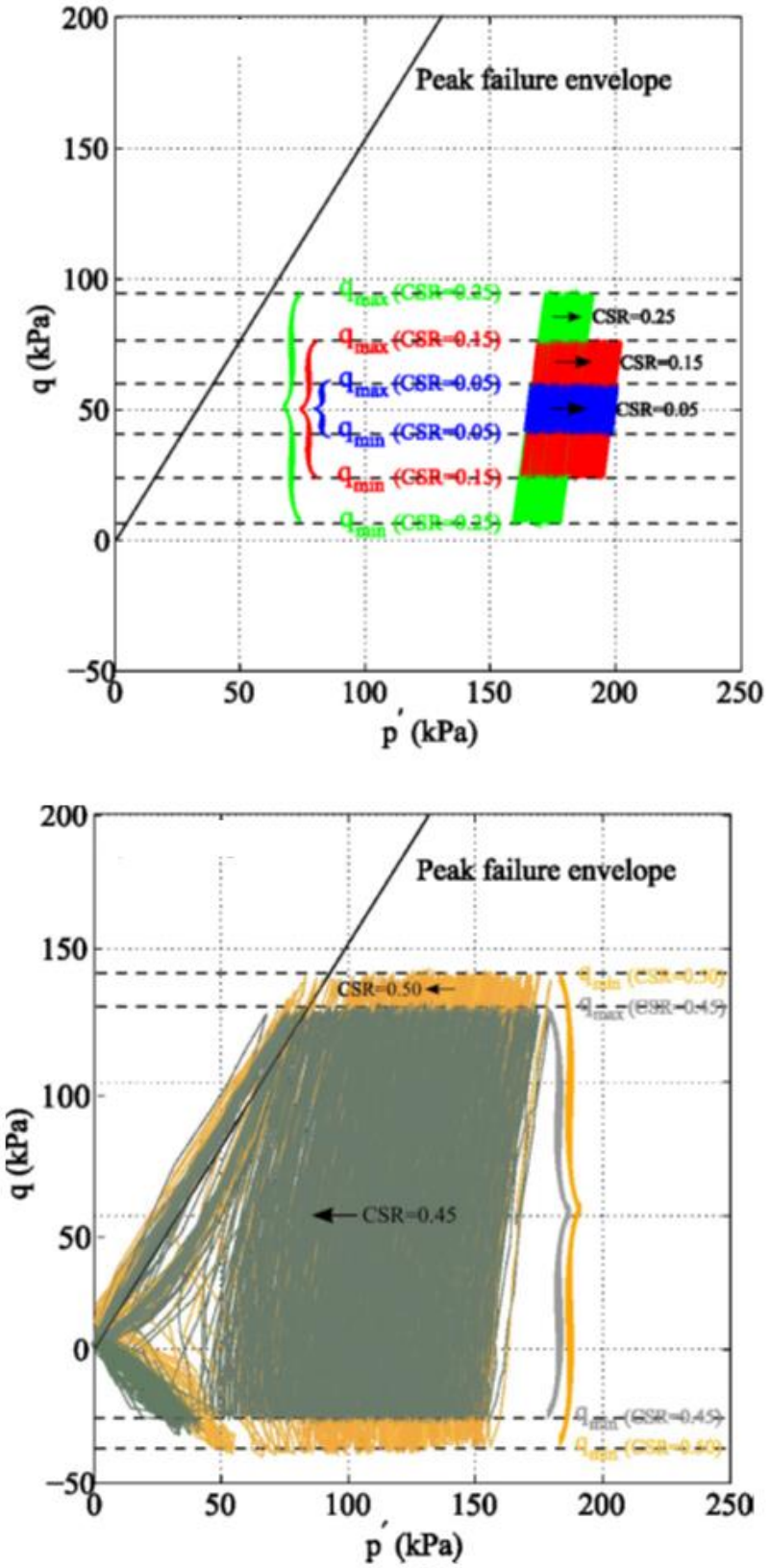

Figure 5.6: Stress paths followed in q-p′space for undrained triaxial tests a) CSR levels below 0.40 and b) CSR levels above 0.40 for Dunkerque sand specimens (Aghakouchak, 2015).

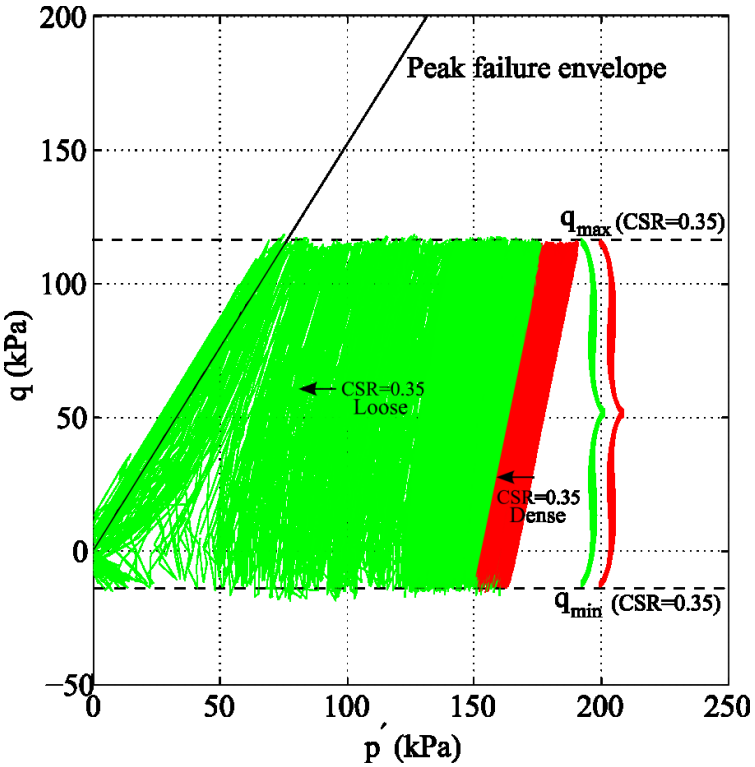

Figure 5.7: Stress paths followed in q-p' space for undrained triaxial tests with a CSR level of 0.35 for loose and dense Dunkerque sand specimens (Aghakouchak, 2015).

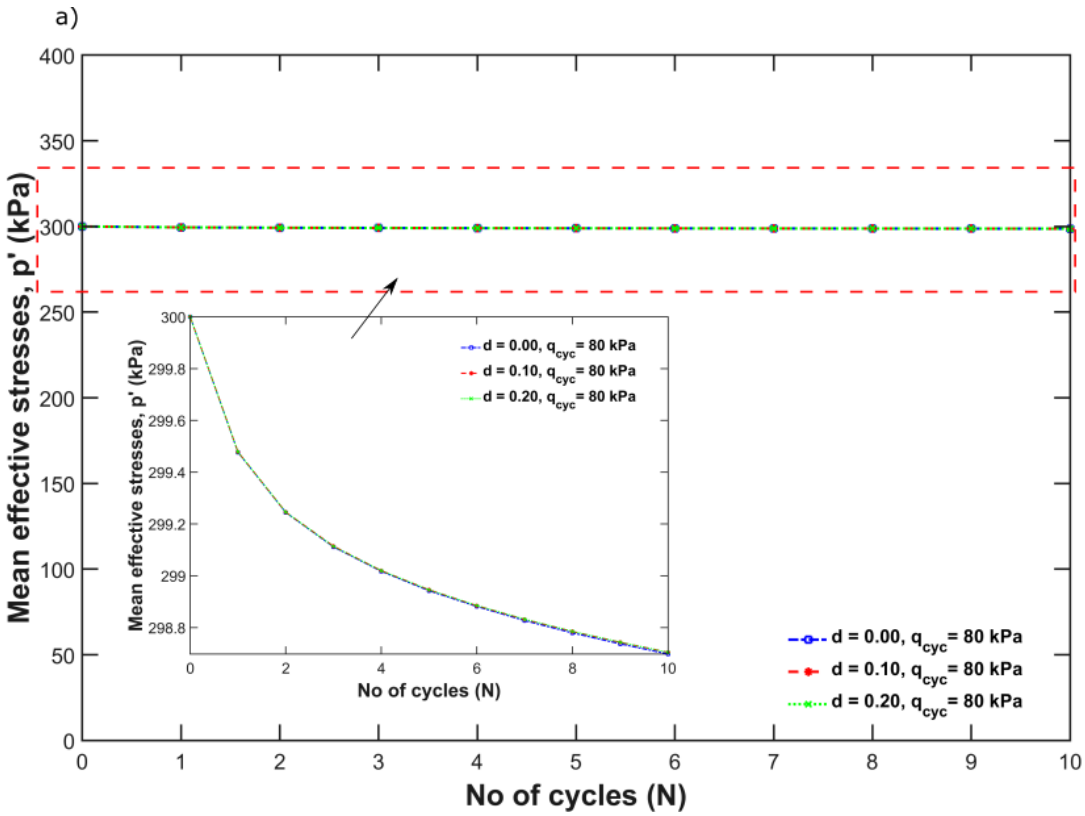

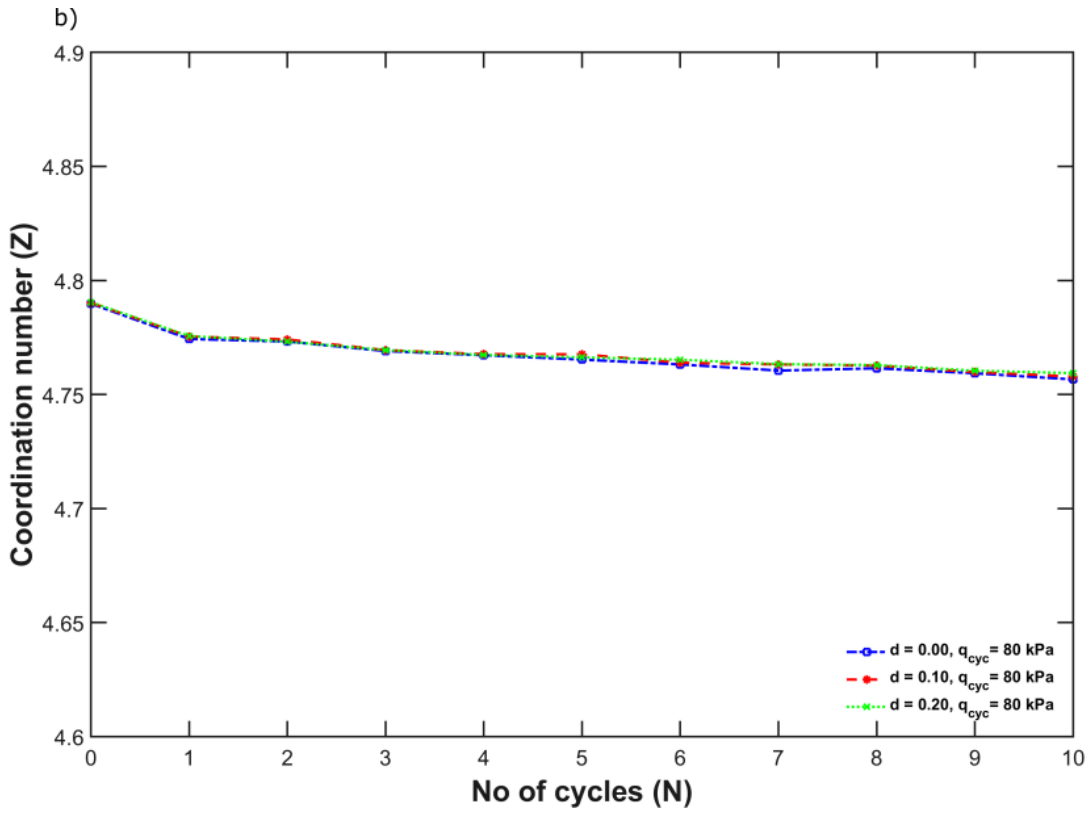

Figure 5.8: Effect of local damping on undrained cyclic triaxial tests under initially isotropic conditions, σ'$_{3,0}$ = 300 kPa, e = 0.42 and q_{cyc} = 80 kPa a) mean effective stresses vs no of cycles and b) coordination number vs no of cycles.

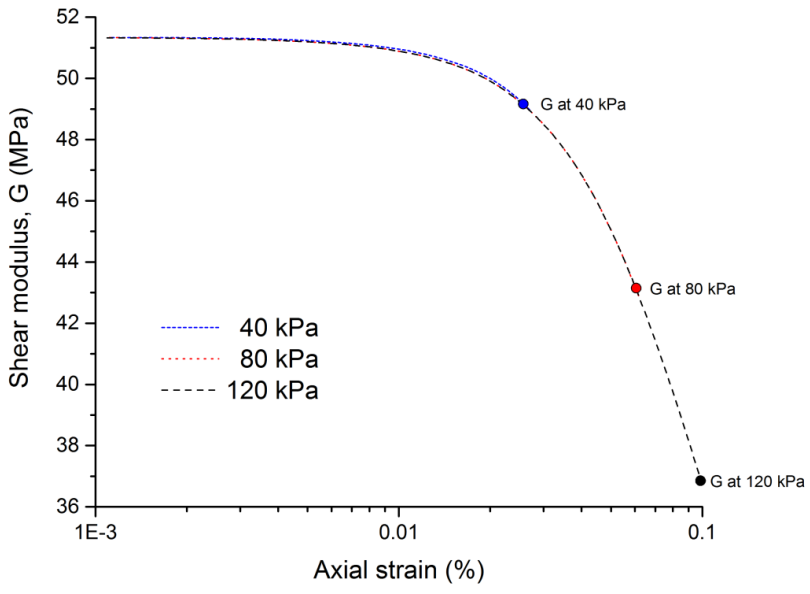

Figure 5.9: Plot of shear modulus vs axial strain for cyclic undrained triaxial tests at an isotropic σ'$_{3,0}$ = 300 kPa and e = 0.42 with varying q_{cyc} = 40 kPa, 80 kPa and 120 kPa.

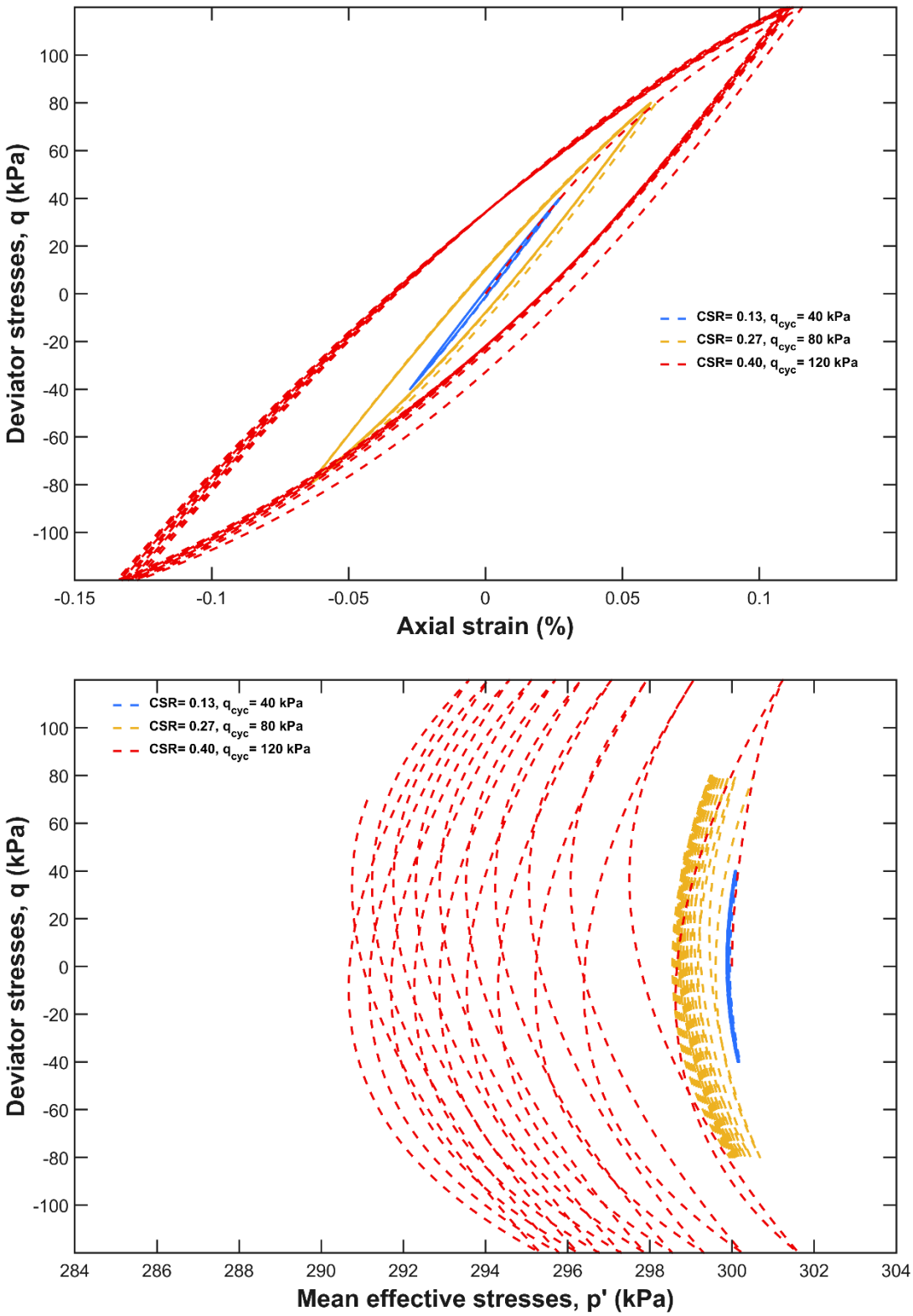

Figure 5.10: Isotropic cyclic undrained triaxial simulations at $\sigma'_{3,0}$ = 300 kPa and e = 0.42 with varying q_{cyc} = 40 kPa, 80 kPa and 120 kPa; a) deviator stresses (kPa) vs axial strain (%); b) deviator stresses (kPa) vs mean effective stresses (kPa)

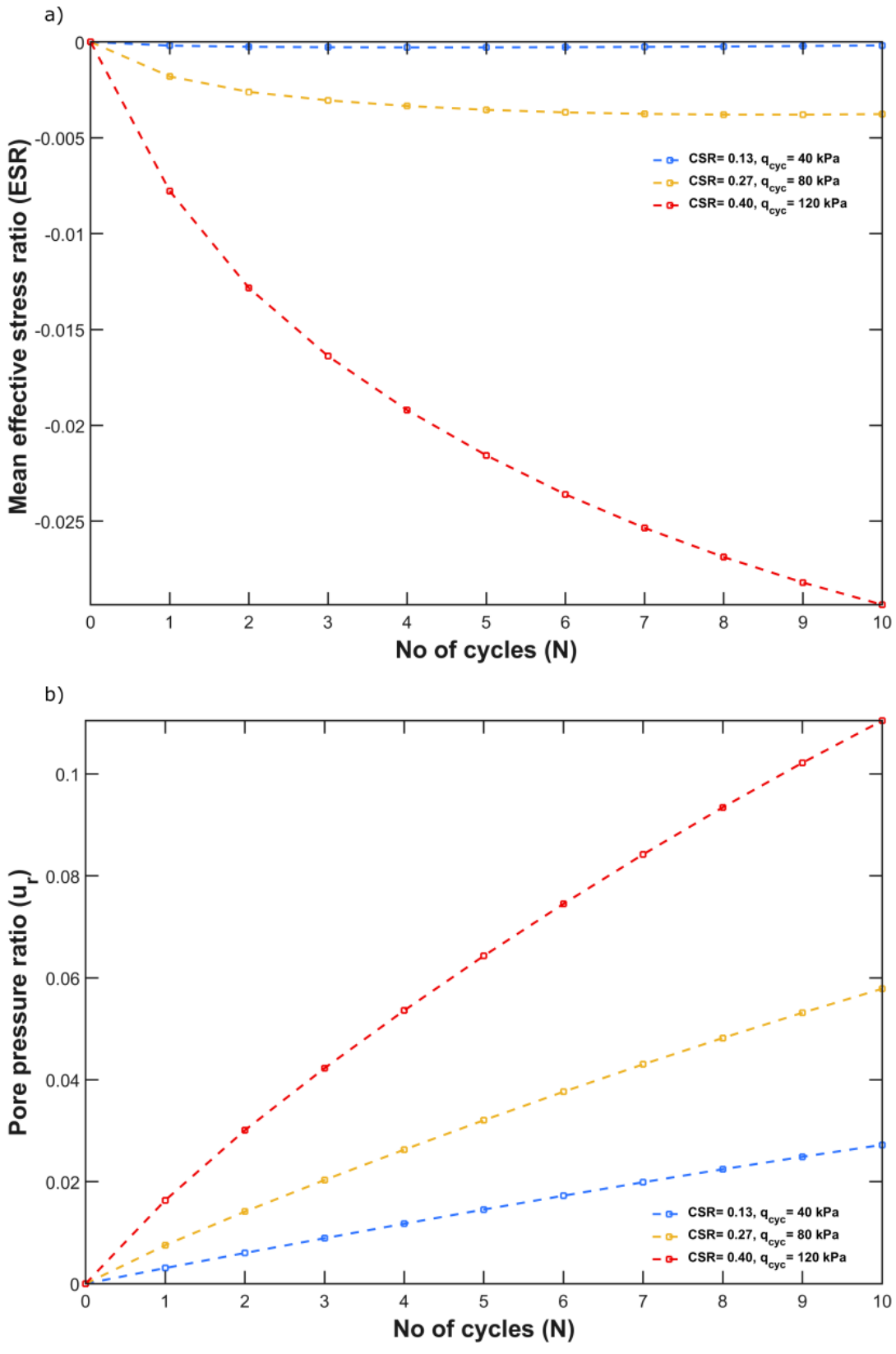

Figure 5.11: Isotropic cyclic undrained triaxial simulations at $\sigma'_{3,0}$ = 300 kPa and e = 0.42 with varying q_{cyc} = 40 kPa, 80 kPa and 120 kPa; a) mean effective stress ratio vs loading cycles (N); b) pore pressure ratio vs loading cycles (N)

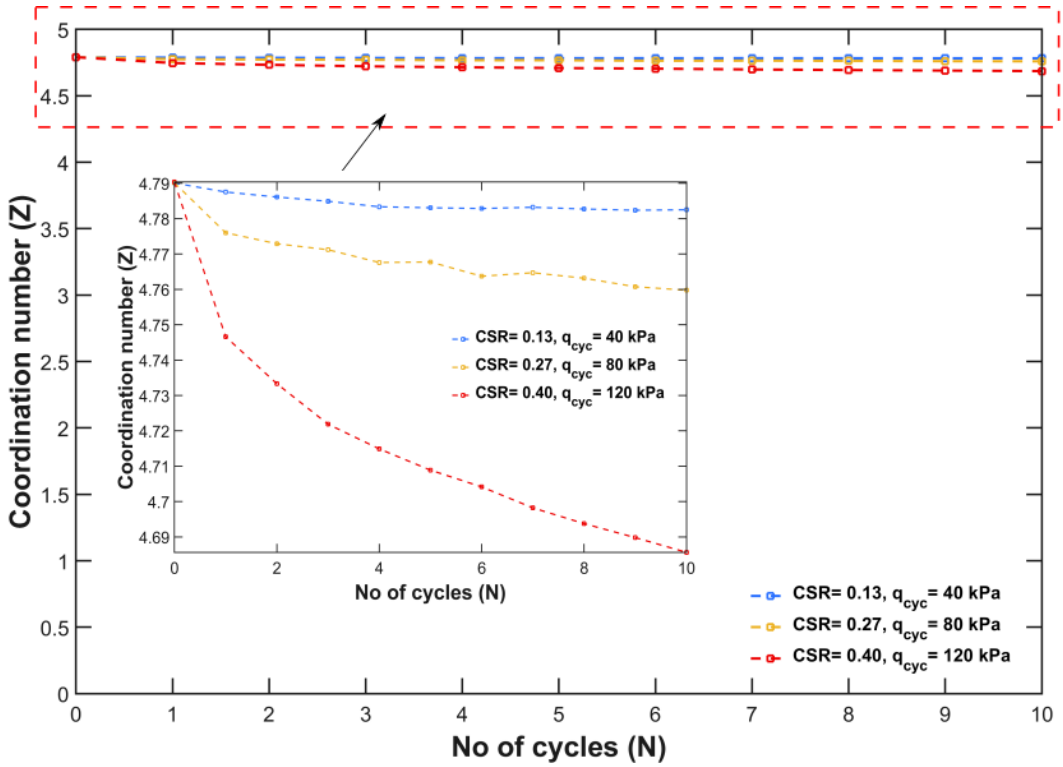

Figure 5.12: Plot of coordination number (Z) with no of cycles for cyclic undrained triaxial tests at an isotropic $\sigma'_{3,0}$ = 300 kPa and e = 0.42 with varying q_{cyc} = 40 kPa, 80 kPa and 120 kPa.

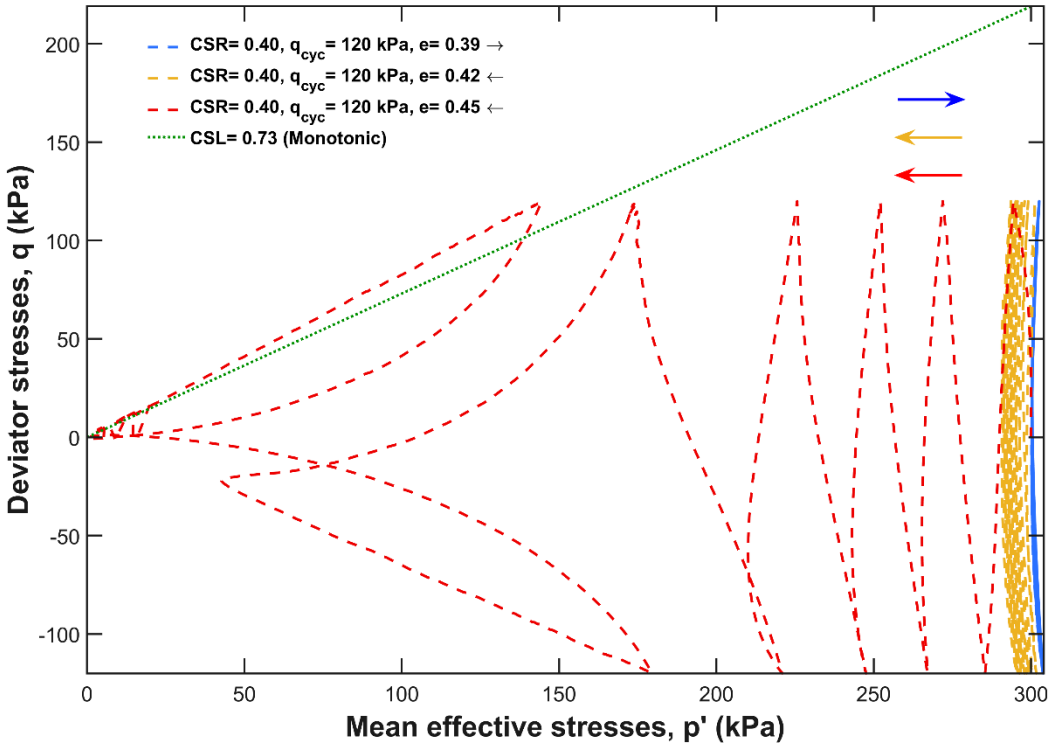

Figure 5.13: Stress paths followed in q-p'space for undrained triaxial tests at an isotropic $\sigma'_{3,0}$ = 300 kPa and q_{cyc} = 120 kPa with varying e=0.39, 0.42 and 0.45.

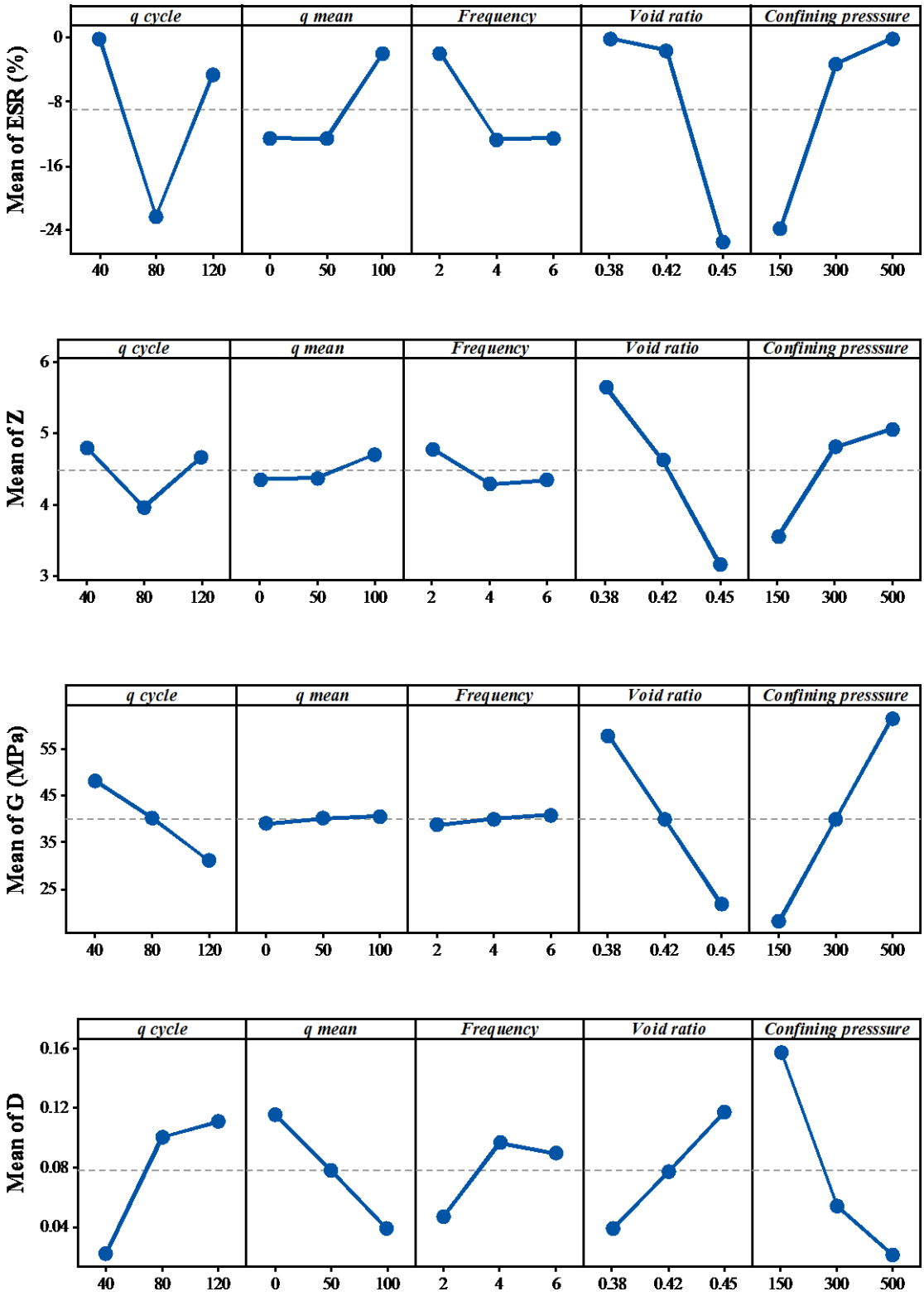

Figure 5.14: ANOVA main effect plots for four responses for the undrained triaxial cyclic simulations at one complete load cycle: a) Mean effective stress ratio, ESR; b) coordination number, Z; c) shear modulus, G (MPa); and d) damping ratio, D.

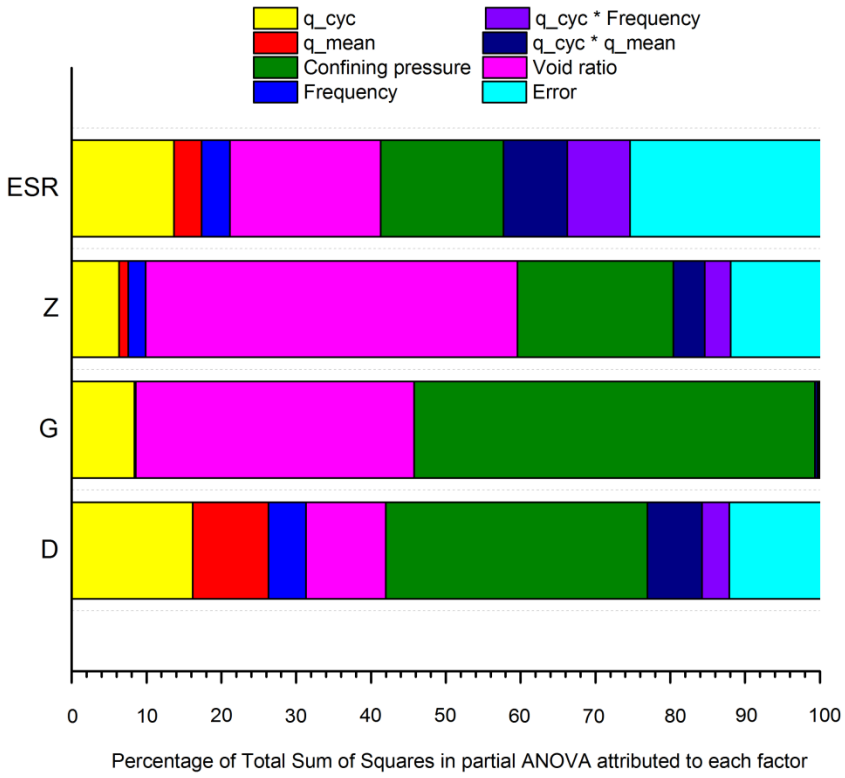

Figure 5.15: Stacked bar plot showing the distribution of SS_T for partial ANOVA means analysis as percentages allotted to each factor.

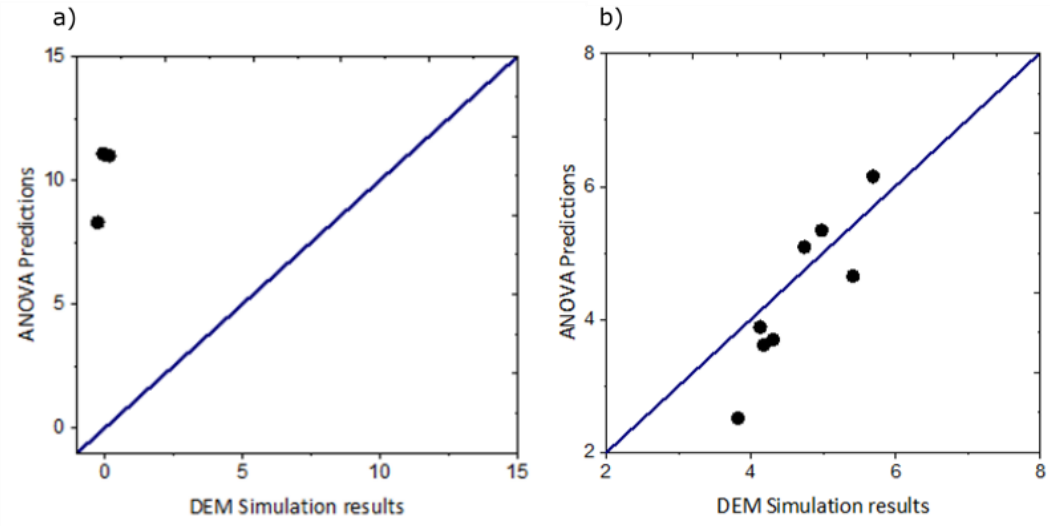

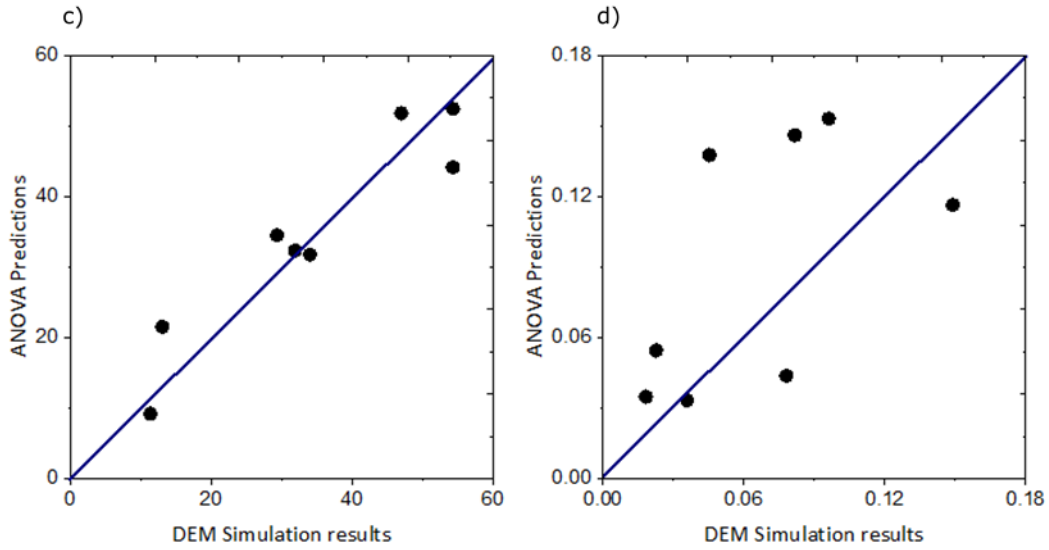

Figure 5.16: Plots of model predictions versus simulation results for four responses for the undrained triaxial cyclic simulations at one complete load cycle: a) ESR; b) coordination number; c) shear modulus (MPa); and d) damping ratio

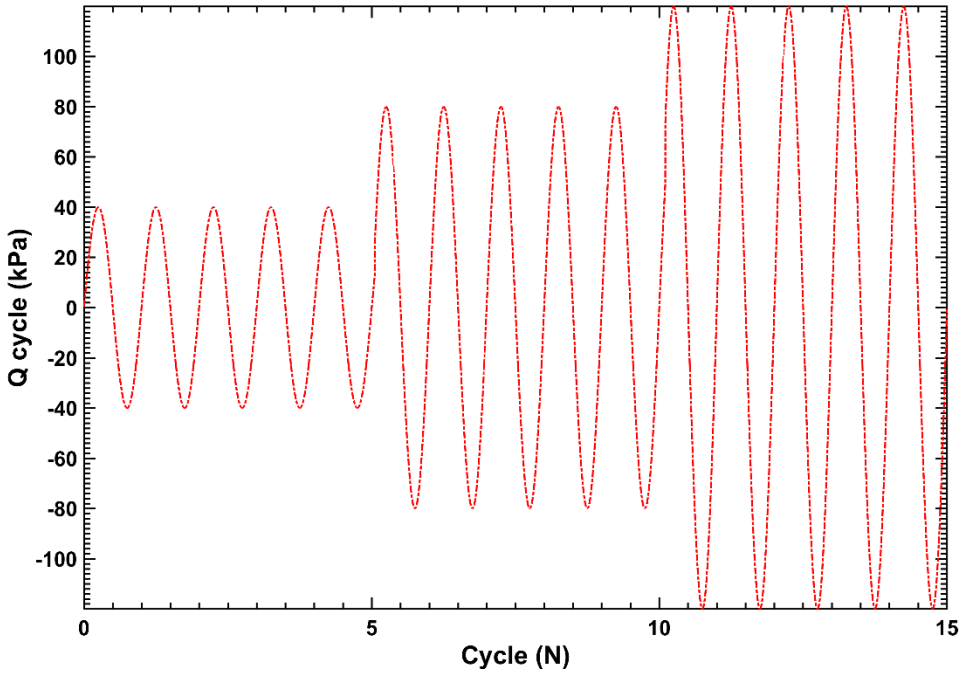

Figure 5.17: Plot of one varying amplitude simulation against the number of cycles for a cyclic undrained triaxial test with q_{cyc} of 40 kPa, 80 kPa and 120 kPa in that order

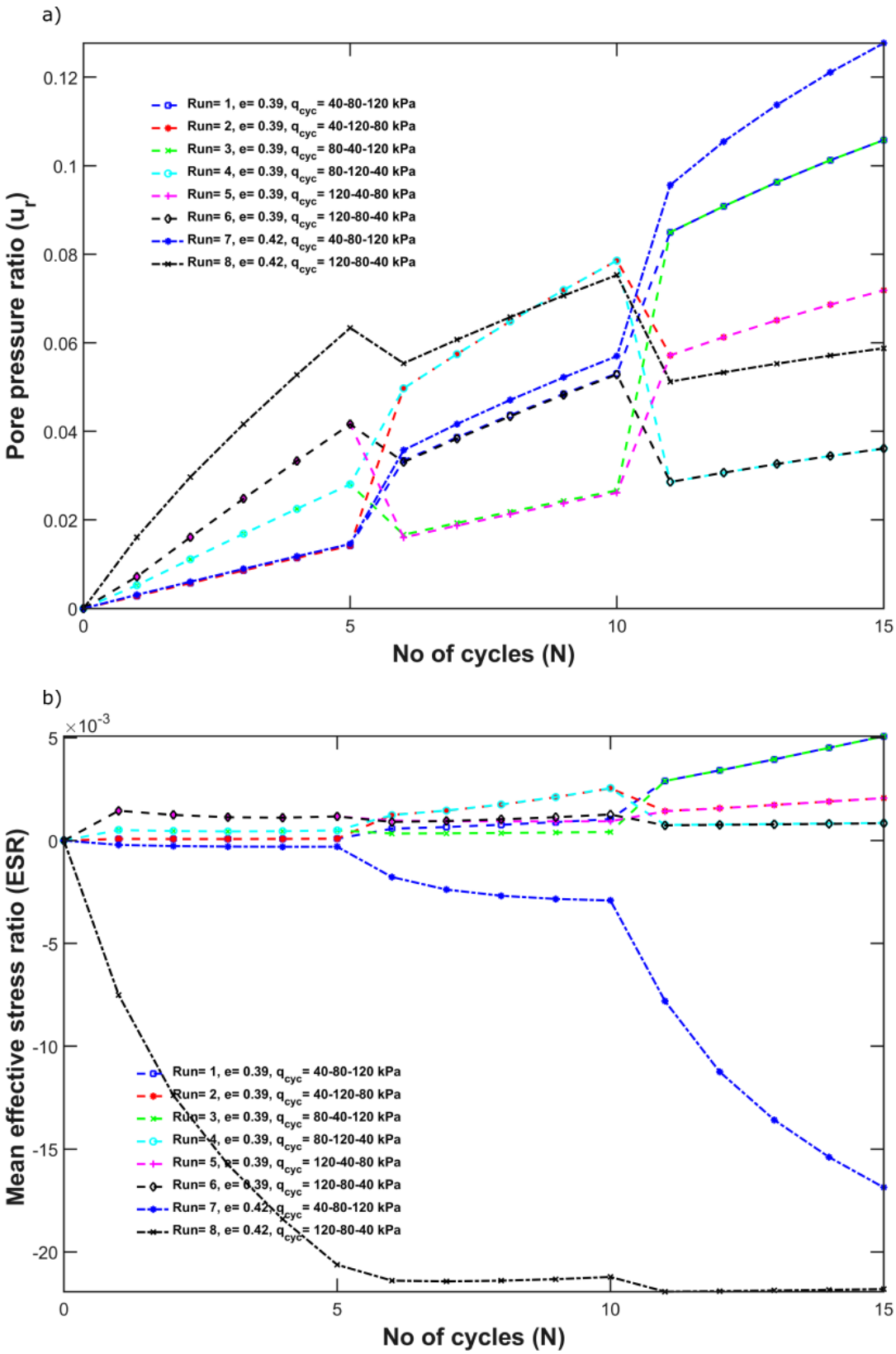

Figure 5.18: Cyclic behaviour plot for the eight simulations described in Table 5.6: a) pore pressure ratio (u_r) vs loading cycles (N); b) Mean effective stress ratio vs loading cycles (N)

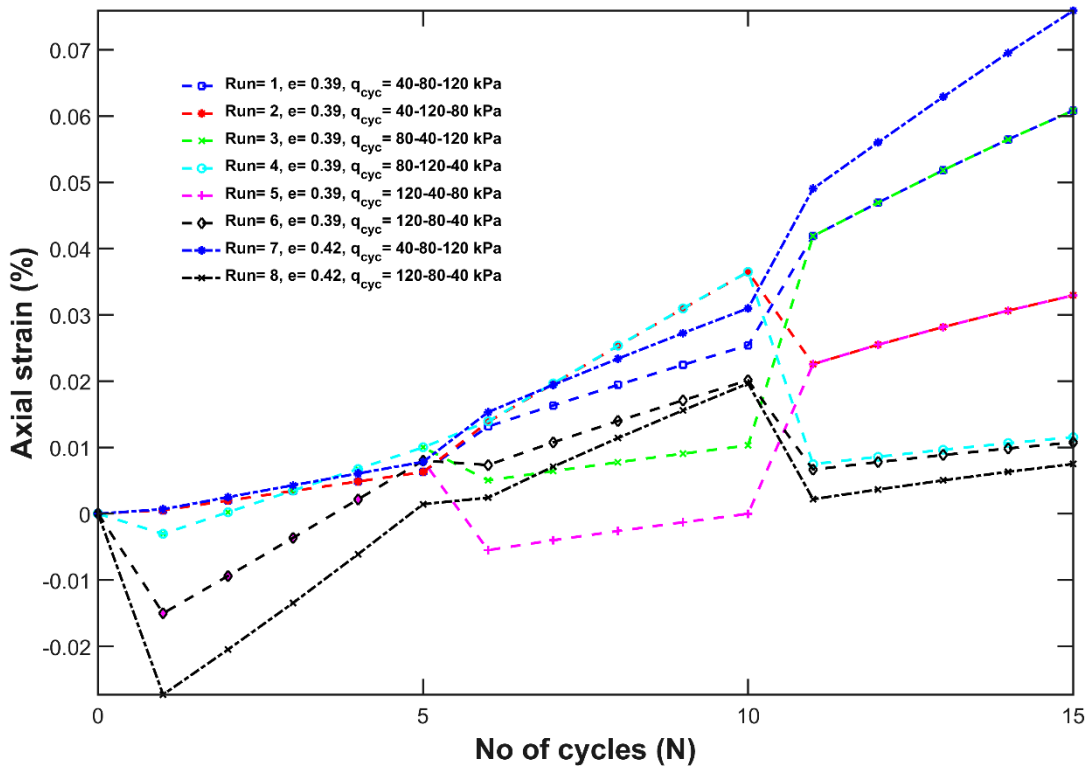

Figure 5.19: Plot of axial strain (%) vs loading cycles (N) for the eight simulations described in Table 5.6.

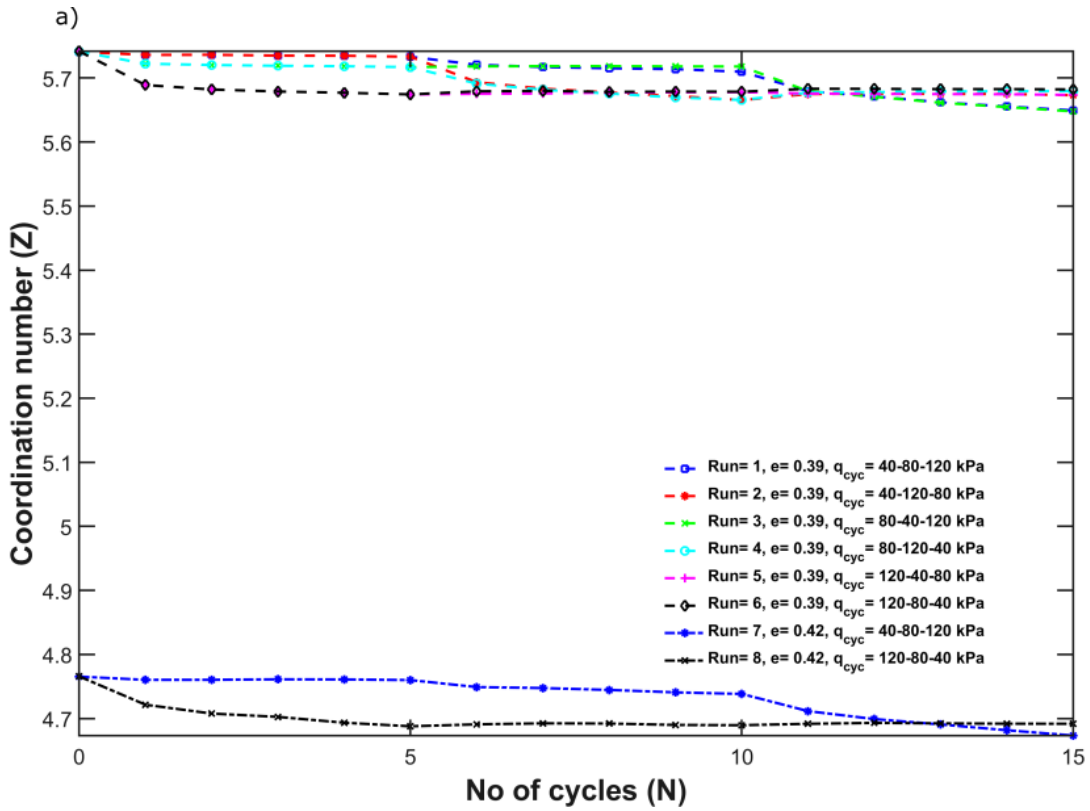

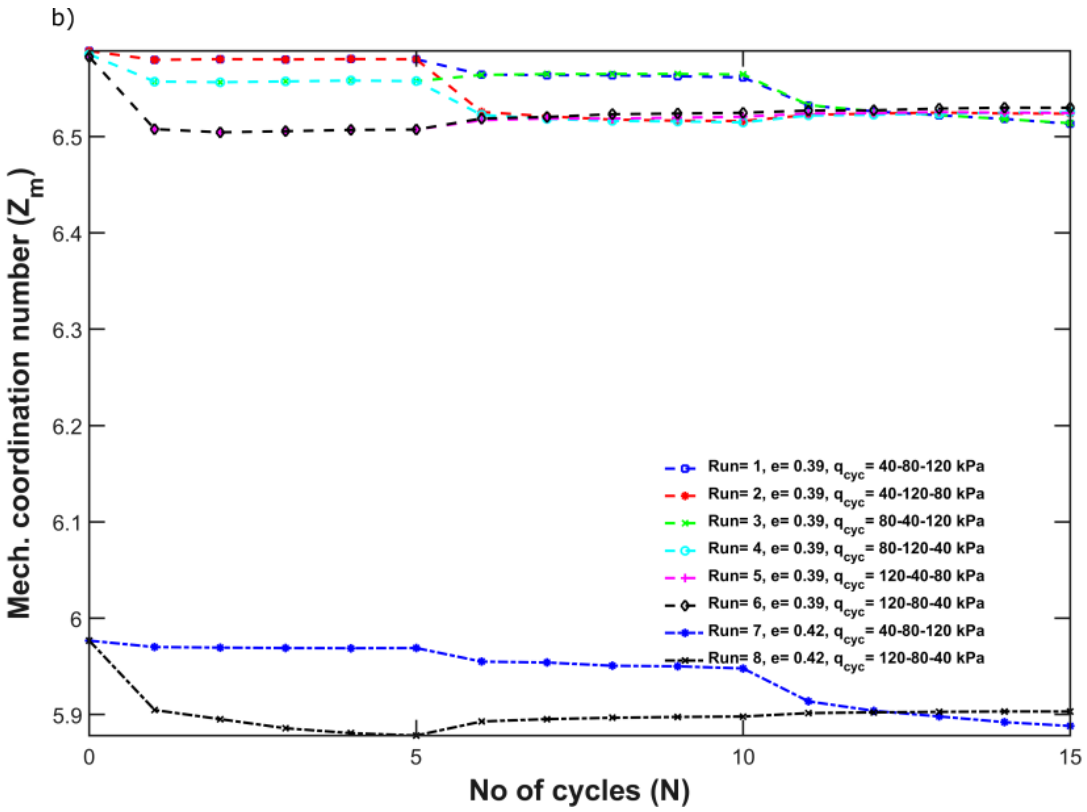

Figure 5.20: Cyclic behaviour plot for the eight simulations described in Table 5.6: a) coordination number (Z) vs loading cycles (N); b) mechanical coordination number (Z_m) vs loading cycles (N)

Chapter 6 Energy dissipation in soil samples during cyclic triaxial simulations

Energy terms were computed in a set of undrained cyclic triaxial discrete-element method simulations which form a parametric study of five factors: void ratio, initial mean effective stress, mean deviator stress, deviator stress amplitude and compressive/extensive initial loading. Void ratio is the only one of these factors which significantly affects the relationship between the excess pore water pressure and the unit energy dissipated (energy dissipated per unit volume). The trends in both the number of complete cycles and the unit energy up to the onset of liquefaction match experimental data. Through analysis of the micro-scale particle and contact information, a preferred contact orientation for frictional dissipation of 30–40° was found. Following a shear reversal, there is a period of negligible frictional dissipation in these simulations of around 0.04% axial strain. This explains, from an energy perspective, why many load cycles are needed to induce liquefaction if their amplitude is very small. A commonly used energy-based model to evaluate the liquefaction potential of a soil was assessed. A substantial improvement in the predictive ability of this model may be achieved by including the mean deviator stress.

6.1 Introduction

Energy is a key consideration when evaluating the response of soil subjected to cyclic loading. The damping ratio is routinely calculated using the areas on a stress–strain plot underneath and enclosed by a hysteresis loop as shown in Fig. 5.3, e.g., (Seed *et al*., 1986; Vucetic and Dobry, 1991). Numerous energy-based methods for liquefaction assessment have been proposed (Berrill and Davis, 1985; Law *et al*., 1990; Figueroa *et al*., 1994; Trifunac, 1995; Dief and Figueroa, 2007; Alavi and Gandomi, 2012; Kokusho, 2013). Liang *et al*. (1995) describe the advantages of energy-based methods for liquefaction assessment compared to the stress- or strain-based methods respectively developed by Seed and Idriss (1971) and Dobry *et al*. (1982).

The damping ratio and models for liquefaction assessment apply to an entire soil sample. They do not give any insight into the motions and interactions of individual soil grains which cause the storage of elastic energy and dissipation of energy measurable at the macro-scale. This limitation is difficult to overcome in physical experiments. However, all of the information needed to compute the kinetic energy of

each grain, the strain energy at each interparticle contact and the energy dissipated during each grain–grain interaction can be obtained from discrete-element method (DEM) simulations with high accuracy. Hanley *et al*. (2018) quantified the energy dissipated by frictional sliding of particles during monotonic, drained triaxial compression. They demonstrated that the frictional dissipation and boundary work were almost equal, found the existence of a preferential orientation for frictional dissipation in triaxial shearing, and recommended the use of a thermodynamically consistent work equation in constitutive modelling of dense sands. This built upon prior monotonic simulation studies which tracked energy dissipation such as Cheng *et al*. (2004), Bolton *et al*. (2008), Bi *et al*. (2011), Wang and Yan (2012), and Zhang *et al*. (2013).

DEM has also been applied to track energy terms during cyclic loading of soil. El Shamy and Denissen (2010) plotted the time histories of individual energy components up to liquefaction, varying the loading conditions applied in the simulations. A follow-up parametric study (El Shamy and Denissen, 2012) varied the sample porosity, maximum strain amplitude and cycle frequency while individual energy terms (boundary work, frictional dissipation, damping, strain and kinetic) were tracked. Zamani and El Shamy (2012) computed the dissipated energy for a range of soil–foundation–structure systems. Tong and Wang (2015) showed the effect of the number of particles, particle aspect ratio and aging (captured by contact creep) on the energy terms per unit volume for cyclic shearing. In these prior studies, the energy data, though computed using micro-scale particle and contact information, have been interpreted at a macro-scale: the important variations in energy that occur within an individual load cycle have not been considered, e.g., the changes that occur upon shear reversal from compression to extension or *vice versa*. This is the key difference between this and prior studies.

This chapter initially presents a comprehensive parametric study in which the void ratio, initial mean effective stress, mean deviator stress, deviator stress amplitude and compressive/extensive initial loading are systematically varied in a set of undrained cyclic loading simulations. The trends in each parameter are compared with experimental data: good agreement is an indicator of the reliability of the simulations. The frictional dissipation, boundary work and strain energy are compared between cycles to show variations from the start of shearing up to the onset of liquefaction. In addition, the significant variations in frictional dissipation during an individual cycle,

e.g., changes upon shear reversal, are studied in detail. The relationship between the accumulated pore water pressure and the dissipated energy per unit volume, a relationship about which there is some uncertainty based on laboratory test data, is explored in this idealised numerical environment. Finally, the applicability of a commonly used energy-based method to evaluate the liquefaction potential of a soil proposed by Figueroa *et al*. (1994) is assessed, and a recommendation is made to improve its predictive ability for samples with initial stress anisotropy.

6.2 DEM Simulations

Cuboidal samples were created which contained 28,309 unbreakable, spherical particles. The grading used was not representative of any specific sand; particle diameters spanned the range 0.1–1 mm (D_{50} = 0.516 mm), with C_u = 3.004 and C_c = 0.573 indicating a poorly graded sand. Periodic boundary conditions were chosen to ensure homogeneous samples (Huang *et al.*, 2014c). The sample preparation approach described by Hanley *et al.* (2014) was adopted. Firstly, particles were sequentially placed within a periodic cell, without contacting any existing particles, at positions chosen at random. Then the periodic boundaries were moved closer together using a servo controller until a stable, equilibrated sample had been achieved at the desired stress state. Stresses were computed from the contact forces (Potyondy and Cundall, 2004). Three different interparticle friction coefficients (μ = 0.15, 0.175 and 0.2) were used during sample preparation to control the void ratio, e. These friction coefficients was selected to get medium dense and loose samples so that the assessment of sample liquefaction could be made with fewer cycles, thereby reducing the computational cost. Five different combinations of effective continuum normal stress were attained (σ_x', σ_y' and σ_z' with respect to conventional Cartesian axes).

After sample preparation, μ was increased to 0.25 (Huang *et al.*, 2014a) and cyclic shearing commenced under stress control as illustrated in Fig. 6.1. The sample volume was maintained constant to capture undrained shearing while the deviator stress, $q = \sigma_z' - \frac{1}{2}\left(\sigma_x' + \sigma_y'\right)$, was varied according to

$$q = q_{mean} \pm q_{cyc} \sin\left(\frac{2\pi t}{T}\right) \tag{6.1}$$

q_{mean} is the mean deviator stress, q_{cyc} is the deviator stress amplitude, T is the cycle period and t is time. The '+' case in Eq. 6.1 corresponds to initial compressive loading (IC); the '–' case to initial extensive loading (IE). The servo-control algorithm maintained $\sigma'_x = \sigma'_y$ during shearing.

T was fixed at 0.25 s for all simulations, i.e., loading frequency of 4 Hz. The frequency was not varied as many studies (although not all: Salvati and Anhdan (2008)) have found that frequency has little effect on energy dissipation and the stress–strain response, e.g., Airey and Fahey (1991); El Shamy and Denissen (2012). This frequency ensured quasi-static conditions: inertia numbers were less than the 7.9 x 10^{-5} threshold identified by Perez *et al*. (2016) throughout shearing, except immediately before the onset of liquefaction in cases where the mean effective stress p' approaches zero. For this research, the onset of liquefaction was defined as either $p' \approx 0$ or an axial strain of $\pm$ 5% in the *z* direction. This is the criterion that is typically used in laboratory tests for identifying initial liquefaction and assessing liquefaction potential, e.g., Ishihara (1993); Yang and Sze (2011).

Table 6.1 shows the parameters for the ten simulations run. S1 is the 'base case' with e = 0.4534, p'_0 = 300 kPa, q_{mean} = 0 kPa, q_{cyc} = 80 kPa and initial compression. Individual parameters were varied from these values. For S2 and S3, e was varied while the other parameters were fixed; p'_0 was varied for S4 and S5; q_{mean} for S6 and S7; q_{cyc} for S8 and S9; initial extensive loading conditions for S10. For S4–S7, the changes in p'_0 and q_{mean} also had some effect on e. This is discussed when the results are presented.

Table 6.1: Void ratios, initial mean effective stresses, mean deviator stresses, deviator stress amplitudes and IC/IE loading conditions for the ten simulations. S1 is the 'base case'; a bold font is used to identify the primary changes from this base case for the other nine simulations

Simulation ID	Void ratio, e	Initial mean effective stress, p'_0 (kPa)	Mean deviator stress, q_{mean} (kPa)	Deviator stress amplitude, q_{cyc} (kPa)	Initial compression (IC) / extension (IE)
S1	0.4534	300	0	80	IC

S2	**0.4470**	300	0	80	IC
S3	**0.4586**	300	0	80	IC
S4	0.4516	**350**	0	80	IC
S5	0.4598	**150**	0	80	IC
S6	0.4529	300	**45**	80	IC
S7	0.4513	300	**90**	80	IC
S8	0.4534	300	0	**60**	IC
S9	0.4534	300	0	**100**	IC
S10	0.4534	300	0	80	**IE**

As was the case for the monotonic simulations presented by Hanley *et al.* (2018), these simulations were run using a version of the open-source LAMMPS code (Plimpton, 1995), adapted to include computations of stress and the various energy terms described in this paper. A simplified Hertz-Mindlin contact model was implemented and used for these simulations. The normal component of the contact force, F_n, is given by Eq. 6.2:

$$F_n = \frac{4Gr_g}{3(1-\upsilon)}\alpha_n^{\frac{3}{2}}\boldsymbol{n} \tag{6.2}$$

α_n is the overlap between elastic spheres a and b, G is the particle shear modulus, υ is the particle Poisson's ratio, $r_g = \sqrt{\frac{r_a r_b}{r_a + r_b}}$ with particle radii r_a and r_b, and $\boldsymbol{n}$ is a unit vector along the line connecting the sphere centres. The shear or tangential component of the contact force, F_t, is incrementally calculated using Eqs. 6.3 and 6.4:

$$F_t^{\beta} = F_t^{\beta-1} - k_t \delta \boldsymbol{\alpha}_t \tag{6.3}$$

$$k_t = \frac{4Gr_g}{2-\upsilon}\sqrt{\alpha_n} \tag{6.4}$$

k_t is the contact shear tangent stiffness, $\beta - 1$ and β represent consecutive time-steps and $\delta \boldsymbol{\alpha}_t$ is the increment of relative tangential displacement during time-step β. A Coulomb slip criterion is imposed to limit the tangential force:

$$|F_t^{\beta}| \leq \mu |F_n| \tag{6.5}$$

G was set at 1.46 GPa based on Chapter 4. This value gives a more realistic stress–strain response in these constant-volume simulations than a realistic G for quartz. The particle density was 2650 kg/m^3 and υ = 0.2. Gravity and damping were both inactive during shearing.

6.3 Energy Calculations

Apart from allowing q to become negative, the other energy terms computed during these cyclic simulations are the same as those described by Hanley *et al.* (2018) and so a summary is given here. The increment of boundary work per unit volume is (Wood, 1990):

$$\delta W = \sigma_x' \delta \varepsilon_x + \sigma_y' \delta \varepsilon_y + \sigma_z' \delta \varepsilon_z \tag{6.6}$$

The incremental normal strains, $\delta \varepsilon_x$, $\delta \varepsilon_y$, $\delta \varepsilon_z$, were determined from the movements of the periodic boundaries. In general, Eq. 6.6 can be decomposed into increments of distortional and volumetric work per unit volume (Wood, 1990). For these constant-volume simulations, it was verified that δW matches the former (the product of q and increment of triaxial shear strain). In each time-step, β, Eq. 6.6 was multiplied by the current sample volume, V^{β}, and accumulated as the total boundary work:

$$W^{\beta} = W^{\beta - 1} + \delta W^{\beta} V^{\beta} \tag{6.7}$$

The translational and rotational kinetic energies are calculated as

$$E_{kt} = \frac{1}{2} \sum_{i=1}^{N_p} m_i v_i^2 \tag{6.8}$$

$$E_{kr} = \frac{1}{2} \sum_{i=1}^{N_p} I_i \omega_i^2 \tag{6.9}$$

N_p is the number of particles in the simulation, m_i, v_i and ω_i are the respective mass, translational speed and rotational speed of particle i, and $I_i = 0.4 m_i r_i^2$ is the moment of inertia of a spherical particle i of radius r_i.

If sliding occurs at contact j during time-step β, according to the criterion given by Eq. 6.5, then the accumulated energy dissipated by friction at the contact is

$$E_{f\_j}^{\beta} = E_{f\_j}^{\beta-1} + \delta E_{f\_j}^{\beta} \tag{6.10}$$

$$\delta E_{f\_j}^{\beta} = \frac{\left|F_t^{\beta-1} + F_t^{\beta}\right|}{2} \frac{\left|F_{t\_o}^{\beta} - F_t^{\beta}\right|}{k_t} \tag{6.11}$$

where $\boldsymbol{F}_{t\_o}^{\beta}$ is the tangential force computed using Eq. 6.3 before the Coulomb slip criterion has been applied. The normal component of strain energy for a single Hertzian contact, j, is given by (Hanley *et al.*, 2018):

$$E_{sn\_j} = \frac{2}{5} |\boldsymbol{F}_n| \alpha_n \tag{6.12}$$

The tangential component is calculated incrementally after the slip criterion has been applied, if necessary. At contact j,

$$E_{st\_j}^{\beta} = E_{st\_j}^{\beta-1} + \delta E_{st\_j}^{\beta} \tag{6.13}$$

$$\delta E_{st\_j}^{\beta} = \frac{\left|F_t^{\beta-1} + F_t^{\beta}\right|}{2} \frac{\left|F_t^{\beta} - F_t^{\beta-1}\right|}{k_t} \tag{6.14}$$

The total frictional dissipation and the normal and tangential components of strain energy at time-step β are found by summation over all N_c contacts:

$$E_{sn} = \sum_{j=i}^{N_c} E_{sn\_j} \tag{6.15}$$

$$E_{st}^{\beta} = E_{st}^{\beta-1} + \sum_{j=i}^{N_c} \delta E_{st\_j}^{\beta} \tag{6.16}$$

$$E_f^{\beta} = E_f^{\beta-1} + \sum_{j=i}^{N_c} \delta E_{f\_j}^{\beta} \tag{6.17}$$

Finally, the error in the energy balance, ΔE, was computed as

$$\Delta E = W^{\beta} - E_f^{\beta} + E_{sn}^0 + E_{st}^0 + E_{kt}^0 + E_{kr}^0 - E_{sn}^{\beta} - E_{st}^{\beta} - E_{kt}^{\beta} - E_{kr}^{\beta} \tag{6.18}$$

where the '0' and β superscripts respectively indicate the value of that energy term at the start of shearing or at some subsequent time-step. The error for each simulation was negligible, confirming (i) the energy terms were computed correctly in the code, and (ii) there was no spurious generation of energy indicating a numerical instability.

6.4 Results and Discussion

6.4.1 Base case (S1)

Fig. 6.2a shows the stress–strain behaviour for S1 with a 'positive compression' sign convention. p' decreases from its initial value of 300 kPa to 35 kPa at the onset of liquefaction (at 5% axial strain in this case). The corresponding energy terms are shown in Fig. 6.2b. The accumulated energy dissipated by friction increases monotonically as expected, although with a noticeable nonlinearity: upon shear reversal, there is a brief period during which negligible frictional dissipation occurs. This is discussed in more detail along with Fig. 6.8. The normal component of strain energy decreases with each cycle in line with the mean effective stress. The shear component, which is more than one order of magnitude smaller than the normal strain energy, similarly decreases with each cycle. The non-monotonic increase in the boundary work is expected from Eq. 6.18: immediately after a shear reversal, frictional dissipation is negligible, the strain energy decreases and so the boundary work must decrease to maintain the energy balance. Once frictional dissipation resumes following a shear reversal, the boundary work increases once more. The kinetic energy has been omitted from Fig. 6.2b, and all subsequent energy figures, because it is negligible: < 0.1% of the boundary work.

The frictional dissipation and boundary work are almost equal for monotonic loading because the strain energy becomes negligible relative to the boundary work at large strains (Hanley *et al*., 2018). For cyclic loading, this is clearly not the case. The largest

normal strain energy, at the start of shearing, is around one-third of the largest boundary work (at the onset of liquefaction). The boundary work is much less than in a monotonic simulation sheared to critical state because the strains, presented later in Fig. 6.11, are comparatively small.

The onset of liquefaction occurs during the 15th load cycle. Fig. 6.2c shows values of the four key energy terms at the end of each of the 14 preceding load cycles, N. The change in each energy term is nearly constant from cycle to cycle up to the 10th cycle, after which the rate of change increases. Fig. 6.2d plots the same data against p' rather than N. The dotted regression lines in Fig. 6.2d show that there are linear trends for all four energy terms (R^2 > 0.998) up to the onset of liquefaction.

6.4.2 Parametric study

Consider firstly the effect of sample void ratio on the various traced energy terms (Fig. 6.3). Although the range of void ratios considered is small, there are substantial differences in the number of complete cycles until the onset of liquefaction, N_l: 49, 14 and 4 for e = 0.4470, 0.4534 and 0.4586, respectively. p' ≈ 0 kPa for both the densest (S2) and loosest (S3) samples at the onset of liquefaction. As the void ratio increases, the unit energy dissipated (energy dissipated per unit volume) up to the onset of liquefaction, δW_d, decreases from 8 kJ/m^3 (equivalent to 5.8 mJ) at e = 0.4470 to 4.5 kJ/m^3 (3.3 mJ) at e = 0.4586. For these simulations, recall that frictional sliding is the only energy dissipation mechanism. El Shamy and Denissen (2012) observed that a 1% decrease in porosity caused an increase of around one order of magnitude in the energy dissipated at liquefaction. It captures the same trend but with much less sensitivity, more in line with experimental results, e.g., Figueroa *et al.*, 1994; Azeiteiro *et al*. (2017). Fig. 6.3c shows the non-monotonic decrease in strain energy that takes place during cycling. As for the boundary work, the normal strain energy increases approaching a shear reversal, and thereafter decreases sharply due to the sharp change in p' seen on Fig. 6.3a. This makes sense from a consideration of the particle-scale micromechanics. Upon shear reversal, the strong force chains within the sample that bear the compressive load must reconfigure to accommodate the sudden change in loading direction. These strong force chains are also observed by Barreto *et al*. (2012). This leads to a temporary reduction in the heterogeneity of the contact force network and a corresponding sharp drop in strain energy. Once a new strong force network has been established, the strain energy can increase once again. Linear

trends are again apparent in Fig. 6.3d, although a slight curvature is noticeable for S2 with e = 0.4470.

Fig. 6.4 shows the parametric study of initial mean effective stress, p_0'. All three samples showed flow liquefaction behaviour. N_l reduces with p_0': 37, 14 and 0 for p_0' = 350 kPa, 300 kPa and 150 kPa, respectively (sample S5 with p_0' = 150 kPa liquefied during the first cycle). This can be partially attributed to the small changes of e, i.e., the p_0' = 350 kPa sample (S4) is the densest of these three while S5 is the loosest, but p_0' is influential regardless. δW_d decreases from 7.6 kJ/m^3 (5.5 mJ) to 2.0 kJ/m^3 (1.5 mJ) as p_0' decreases from 350 kPa to 150 kPa. The nearly linear decrease with p_0' matches the experimental findings of Baziar and Sharafi (2011). Based on an experimental testing programme using a hollow cylinder apparatus, Figueroa *et al.* (1994) and Liang *et al.* (1995) also found that increasing the effective confining pressure or relative density, i.e., increasing p_0' or reducing e, increased δW_d.

Fig. 6.5 compares the base case, S1, with two initially anisotropic samples (S6 and S7). By increasing the initial stress anisotropy, N_l reduces from 14 (isotropic) to 1 (S7 with q_{mean} = 90 kPa) even though both anisotropic samples are slightly denser than the isotropic one. As the anisotropic stress ratio $K_c = \sigma_{z,0}'/\sigma_{x,0}'$ increases, the cyclic stress path reaches the static failure envelope (instability line) sooner (Konrad, 1993). These three simulations, S1, S6 and S7, have K_c values of 1.0, 1.16 and 1.33, respectively. The reduction in N_l caused by initial stress anisotropy does not lead to a commensurate reduction in the energy dissipated by friction: 5.5 mJ, 6.7 mJ and 8.0 mJ for q_{mean} = 0 kPa, 45 kPa and 90 kPa, respectively. This is the opposite of the behaviour seen in both Fig. 6.3 and Fig. 6.4 where a reduction in N_l, caused by either increasing e or reducing p_0', was associated with a decrease in δW_d.

Fig. 6.6 shows that increasing q_{cyc} reduces N_l from 69 at q_{cyc} = 60 kPa to 4 at q_{cyc} = 100 kPa. No significant effect was observed on δW_d, a result supported by laboratory experiments: Figueroa *et al.* (1994) found no clear relationship between δW_d and the shear strain amplitude, while Baziar and Sharafi (2011) found no dependence on the cyclic stress ratio. This differs from the previous DEM study of El Shamy and Denissen (2012) who found that the energy dissipation increases substantially in line with the shear strain amplitude. More energy dissipation must occur during each load cycle as q_{cyc} increases in order for δW_d to remain unchanged as N_l reduces.

The final comparison in this parametric study was between the equivalent initial compression (S1) and initial extension (S10) cases. These were similar with N_l = 14 for both simulations. This may be because the sample was in an idealised isotropic state before cyclic shearing. It is possible that some differences in N_l would be observed for samples with initial anisotropy; however, it is outside the scope of this study which varies only a single parameter at a time from the base case values. The only noticeable difference was in δW_d: 5.3 kJ/m^3 (3.8 mJ) for S1 compared to 6.0 kJ/m^3 (4.4 mJ) for S10.

6.4.3 Inter- and intra-cycle variations in energy

This subsection focuses on the differences between cycles and within individual cycles of the base case simulation, S1. The rose diagrams in Fig. 6.7 show the frictional dissipation within three individual cycles: cycle 2 shortly after the start of cycling, cycle 8 in the middle of cycling, and cycle 14 which is the last complete cycle before the onset of liquefaction. The rose diagrams are drawn based on the spatial orientation of the branch vectors joining the centres of contacting spheres. In each rose diagram, the length of each segment is proportional to the total frictional dissipation that has occurred during that cycle for contacts with that particular branch vector orientation. The colours of the segments give a numerical indication of the frictional dissipation. 18 angular increments of 10° were considered between 0° and 180° in each Cartesian plane (*x*–*y*, *x*–*z* and *y*–*z*).

For all three cycles considered, frictional dissipation is isotropic for the horizontal *x*–*y* planes. In the vertical direction (*x*–*z* and *y*–*z* planes), more frictional dissipation takes place for contacts oriented between 30° and 40° than for any other orientation. This is reduced from the 40–50° preferred contact orientation for the monotonic simulations presented by Hanley *et al*. (2018). The reason for the reduction in contact orientation is unknown for now and is left for future work. Horizontally oriented contacts are associated with least energy dissipation, as in the monotonic simulations. The *x*–*z* and *y*–*z* rose diagrams also show a systematic variation as cycling proceeds. Cycle 2 has the greatest variation between rose diagram segments while cycle 14 has the least. The heterogeneity of the energy dissipation can be quantified by computing the coefficient of variation, c_v, i.e., the standard deviation divided by the mean, of the 18 friction values shown on each rose diagram. Cycle 2 has a c_v of around 0.2 for the *x*–*z* and *y*–*z* planes: similar to the c_v at critical state for the monotonic simulations of Hanley *et al*. (2018). Since S1 is isotropic with $c_v \approx 0$ before cycling begins, this

significant heterogeneity in the preferred orientation of frictional dissipation must develop rapidly upon shearing. Cycle 8 has a fractionally lower c_v than cycle 2, but c_v has diminished to around 0.09 by cycle 14: less than half of its value at cycle 2. Note also the different scales on the three colourbars. The friction dissipated during cycle 14 is nearly an order of magnitude greater than during cycle 2.

In addition to these differences between load cycles, there are also differences within a single cycle. Fig. 6.8 shows how the frictional dissipation, boundary work and strain energy vary with each individual cycle. Each cycle can be divided into quarters. For S1, loading is compressive from 0–0.25 and 0.75–1 cycles, and extensive from 0.25–0.75 cycles. Shear reversals occur at 0.25 and 0.75 cycles. The horizontal regions in Fig. 6.8a show negligible frictional dissipation immediately following a shear reversal. These 'zero friction' regions extend for around 0.04% axial strain. Beyond this threshold, the frictional dissipation grows quadratically (R^2 > 0.99). This indicates that, provided the applied load cycles have a sufficiently small amplitude, negligible frictional dissipation will occur. This explains why so many load cycles are needed to reach liquefaction if their amplitude is very small: N_l must be very large to accrue sufficient δW_d, which has no dependence on q_{cyc}, to induce liquefaction. The spacing between lines for $N-1$ and N grows increasingly rapidly as the onset of liquefaction is approached. The quadratic growth in friction implies that most frictional dissipation ought to occur towards the end of the compressive or extensive loading phases. This is exactly what is observed: the energy dissipation during the half-cycle 0–0.25 & 0.5–0.75 is around one order of magnitude greater than during the other half-cycle as shown in Fig. 6.9.

The energy balance constrains Fig. 6.8b to have a similar appearance to Fig. 6.8a. One interesting difference is that the boundary work decreases during the entire half-cycle 0.25–0.5 & 0.75–1 (post-shear reversal when the magnitudes of the deviator stress and strain are decreasing); work input is needed solely for the other half-cycle. The normal component of strain energy decreases nonlinearly during a cycle (Fig. 6.8c). Its behaviour is completely different from the shear component (Fig. 6.8d) for which there are prominent local maxima at the shear reversals. This mirrors $|q|$: for S1, $|q|$ = 80 kPa at the shear reversals compared to $|q|$ = 0 kPa at 0 and 0.5 fractional cycles.

The total frictional dissipation for cycle 8 of S1 is given in Fig. 6.7; Fig. 6.9 shows the analogous rose diagram projections onto the *y*–*z* plane for the individual quarter-cycles 7–7.25, 7.25–7.5, 7.5–7.75 and 7.75–8. Although there are seemingly minor differences between these four diagrams, the coefficients of variation reveal a greater heterogeneity in the orientations of contacting particles at which frictional dissipation occurs for the extensive half-cycle than the compressive half-cycle. Apart from confirming that c_v declines during shearing, Fig. 6.10 also shows that extension leads to a higher c_v than compression throughout the simulation, regardless of whether the first quarter-cycle is compressive (Fig. 6.10a) or extensive (Fig. 6.10b). Considering Fig. 6.11, compression, in which one boundary (*z* in this case) moves inwards and the two lateral boundaries outwards, leads to a more homogeneous pattern of frictional dissipation than extension, in which one boundary moves outwards and two inwards. This is a very interesting observation. The trend is unrelated to the magnitude of the frictional dissipation (Fig. 6.8a): dissipation is negligible immediately following a shear reversal regardless of compressive or extensive loading. It is also unrelated to the second-order fabric tensor, Φ_{pq}, proposed by Satake (1982) as a useful measure of fabric anisotropy, $\Phi_{pq} = \sum_{j=1}^{N_c} \boldsymbol{n}_p^j \boldsymbol{n}_q^j$. where $\boldsymbol{n}_p^j$ is the unit contact normal for contact j. The difference between the maximum and minimum eigenvalues of the Φ_{pq} tensor is termed the deviatoric fabric. Fig. 6.12a shows the variation of deviatoric fabric with N for S1. The cyclic trends in deviatoric fabric are linked to trends in q and match the trends in frictional dissipation: increasing deviatoric fabric is associated with increasing $|q - q_{mean}|$ and those quarter-cycles with high frictional dissipation. Conversely, decreasing deviatoric fabric is linked to low dissipation and decreasing $|q - q_{mean}|$. The same observation is true for other simulations such as S6 with initial stress anisotropy (Fig. 6.12b). Comparing Fig. 6.10 and Fig. 6.12 shows that even though the fabric becomes increasingly anisotropic as cycling proceeds, the anisotropy in the pattern of energy dissipation becomes less pronounced.

6.4.4 Relationship between stress and energy

The relationship between the accumulated pore water pressure increase and the dissipated energy per unit volume during undrained cyclic loading has been investigated experimentally (Simcock *et al*., 1983; Towhata and Ishihara, 1985; Law *et al*., 1990; Okada and Nemat-Nasser, 1994; Baziar and Sharafi, 2011; Kokusho, 2013; Azeiteiro *et al*., 2017). Some authors have reported a unique relationship for a given soil type, after normalisation by the initial confining pressure when necessary;

others have found a dependence on the specimen density (Okada and Nemat-Nasser, 1994) or the cyclic deviator stress (Simcock *et al*., 1983).

The dissipated energy is readily and precisely available from DEM; it does not require estimation from the areas of stress–strain hysteresis loops. Fig. 6.13 shows the normalised data for all 10 simulations. Δu was computed for these constant-volume simulations as $\sigma'_x - \sigma'_{x,0}$ (equivalent to $p'_0 - p'$ since q is prescribed by Eq. 6.1). All plots have a similar trend and alignment. The data for the lowest and highest void ratios bound the other data. e is clearly the most influential factor, despite its small variation in these simulations: as e increases from 0.4470 to 0.4586, there is a noticeable upward shift on Fig. 6.13. This is in agreement with the experimental data of Okada and Nemat-Nasser (1994). Apart from e, none of the other factors explored in the parametric study significantly affect the relationship between the pore water pressure and unit energy.

The energy dissipated during a single cycle is plotted against the change in p' during that cycle in Fig. 6.14. A bilinear trend emerges which is most obvious for those simulations with large N_l. During the initial cycles, the particles reorganise so as to bear the applied load. Both the frictional dissipation and change in $|p'|$ per cycle decrease until a minimum is reached. There can then be many cycles in which the changes which occur are almost imperceptible. However, the mechanical coordination number (Thornton, 2000) and indices of redundancy (Kruyt and Rothenburg, 2009; Huang *et al*., 2018) gradually decrease with each cycle until eventually the frictional dissipation and change in $|p'|$ per cycle begin to increase. The rate of increase accelerates until the onset of liquefaction. The decreasing and increasing trends have distinct slopes.

Fig. 6.15 and Fig 6.16 shows the critical state locus points for 27 CV and 9 drained monotonic simulations and the critical state line drawn from these points in $q - p'$ space and $e - p'$ space respectively. The slope of this line, *M* = 0.72, is equivalent to a critical state angle of shearing resistance of 18.95° (see detailed results in Appendix D: Table D.1-D.3). The red square markers shown in Fig. 6.15 and Fig 6.16 are the initial states for the 10 energy tracing simulations before cyclic shearing. Fig 6.17 shows the state parameter at the end of each cycle for S1 (base case) against energy dissipation, δW_d . As p' decreases from cycle to cycle as shown in Fig 6.2, the state parameter becomes increasingly negative. Fig 6.18 shows the state parameter

at the end of each cycle for S1-S10 against energy dissipation, δW_d . There is linearly decreasing trend after the initial cycles on this semi-logarithmic plot.

Fig. 6.19 shows the number of contacts against axial strain for S1 (base case simulation) during the complete cyclic shearing process. The number of contacts decreases as the cycles are applied. Fig. 6.20 shows the sliding fraction, f, against axial strain for S1 (base case). The sliding fraction has a butterfly shape as the sliding fraction becomes zero at stress reversals which correspond to the maxima and minima of strain. This is expected as friction is zero immediately following a shear reversal as shown in Fig 6.8 which indicates no sliding at contacts.

6.4.5 Energy-based models for liquefaction assessment

Many models have been proposed to evaluate the liquefaction potential of soils based on dissipated energy (Alavi and Gandomi, 2012). These models have been derived from experimental data for various sands. Most are a function only of initial effective confining pressure and initial relative density; the model proposed by Baziar and Jafarian (2007) also takes the soil grading into account. In this paper, we focus on the popular model proposed by Figueroa *et al*. (1994) which is conveniently expressed in terms of effective confining pressure (in kPa) and e rather than relative density:

$$\log_{10} \delta W_d = a + b\sigma'_{x,0} - ce \tag{6.19}$$

a, b, c are constants, and δW_d, the unit energy up to the onset of liquefaction, is in J/m^3. The values obtained by Figueroa *et al*. (1994) for these constants, based on 27 laboratory tests of Reid Bedford sand, are given in Table 6.2. Fitting Eq. 6.19 with these constants to the DEM data led to large over-predictions of δW_d by factors between 10 and 35 and an adjusted R^2 of 0.2621. Such a poor fit is unsurprising: our simulations of perfectly smooth spheres do not permit plastic deformation, asperity crushing or grain breakage. At least some of the disparity may be attributed to these omissions. A new set of constants, also given in Table 2, was obtained through best-fitting Eq. 6.19 to the simulation data. This improved the adjusted R^2 to 0.7757: reasonable agreement considering the simplicity of the model. Fig. 6.21a compares the predicted and actual δW_d values. S6 and S7, the two samples with initial stress anisotropy, are the principal outliers. Eq. 6.19 does not take q_{mean} into consideration; this was not one of the factors considered by Figueroa *et al*. (1994) and later models

have also ignored this factor (Alavi and Gandomi, 2012). Consider Eq. 6.20 which includes q_{mean} (kPa):

$$\log_{10} \delta W_d = a + b\sigma'_{x,0} - ce + \mathrm{d}q_{mean} \tag{6.20}$$

The inclusion of q_{mean} improves the adjusted R^2 to 0.97 and brings the δW_d values for S6 and S7 into line with the data for the initially isotropic samples, as shown in Fig. 21b. If an energy-based model is being applied for liquefaction assessment of anisotropic samples, a significant improvement in the accuracy of the model may be achieved by including the mean deviator stress.

Table 6.1: Constants in Eqs 6.19 and 6.20 obtained by Figueroa* et al*. (1994) for Reid Bedford sand and model fitting using the simulation data reported in this paper, along with adjusted R^2 statistics for these models

Source	a	b	c	d	Adjusted R^2
Figueroa *et al*. (1994)	5.697	0.00477	4.339	–	0.2621
Best-fit of equation (20)	13.815	0.00128	22.981	–	0.7757
Best-fit of equation (21)	12.852	0.00164	21.120	0.00156	0.9700

6.5 Conclusions

A set of 10 constant-volume cyclic triaxial simulations with energy tracing active have been conducted in accordance with a parametric study of five factors: void ratio, initial mean effective stress, mean deviator stress, deviator stress amplitude and compressive/extensive initial loading. By increasing the void ratio or decreasing the initial mean effective stress, both the number of complete cycles and the energy dissipated per unit volume up to the onset of liquefaction, respectively denoted as N_l and δW_d, are reduced. Void ratio is the only factor from those investigated which significantly affects the relationship between the excess pore water pressure and δW_d. Initial stress anisotropy reduces N_l but increases δW_d. Increasing the deviator stress amplitude also reduces N_l but this parameter has no significant effect on δW_d.

All of these observed trends in N_l and δW_d match data from physical experiments, where available.

The preferred contact orientation for frictional dissipation is between 30° and 40° for these cyclic simulations: lower than for the monotonic simulations described by Hanley *et al*. (2018). Horizontally oriented contacts are associated with least energy dissipation. A significant heterogeneity in the preferred orientation of frictional dissipation develops rapidly upon shearing; this heterogeneity declines nonlinearly as cycling proceeds. There is a greater heterogeneity for extension than for compression, regardless of whether the initial phase of loading is compressive or extensive. Immediately following a shear reversal, the boundary work decreases and there is a period of negligible frictional dissipation which lasts for around 0.04% axial strain. Thereafter, the frictional dissipation grows quadratically, i.e., most frictional dissipation occurs towards the end of the compressive or extensive loading phases. This explains why so many load cycles are needed to reach liquefaction if their amplitude is very small: load cycles with amplitudes less than a particular threshold (0.04% axial strain for these simulations) cause negligible frictional dissipation. N_l must therefore be very large to accrue sufficient δW_d to induce liquefaction.

The model proposed by Figueroa *et al*. (1994) to evaluate the liquefaction potential of a soil gives reasonable agreement for these data using best-fit parameters (adjusted R^2 of 0.7757). However, the inclusion of mean deviator stress, a factor omitted from all commonly used models of this type (Alavi and Gandomi, 2012), significantly improves the adjusted R^2 to 0.97. This inclusion is strongly recommended to improve the predictive ability for samples with initial stress anisotropy.

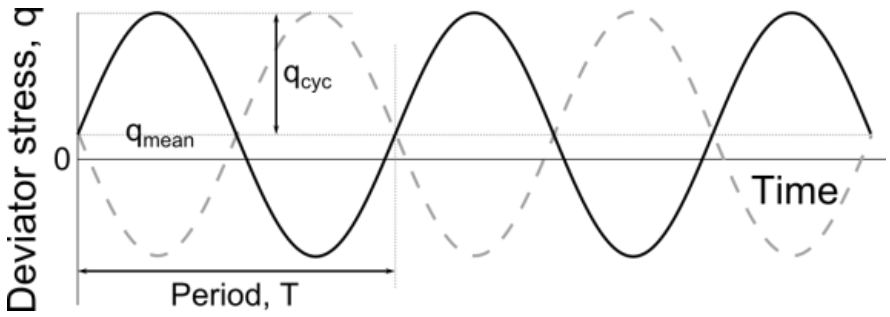

Figure 6.1: Schematic of two stress-controlled cyclic simulations with mean deviator stress q_{mean}, deviator stress amplitude q_{cyc} and period T. The solid black line shows initial compression; the dashed grey line shows initial extension

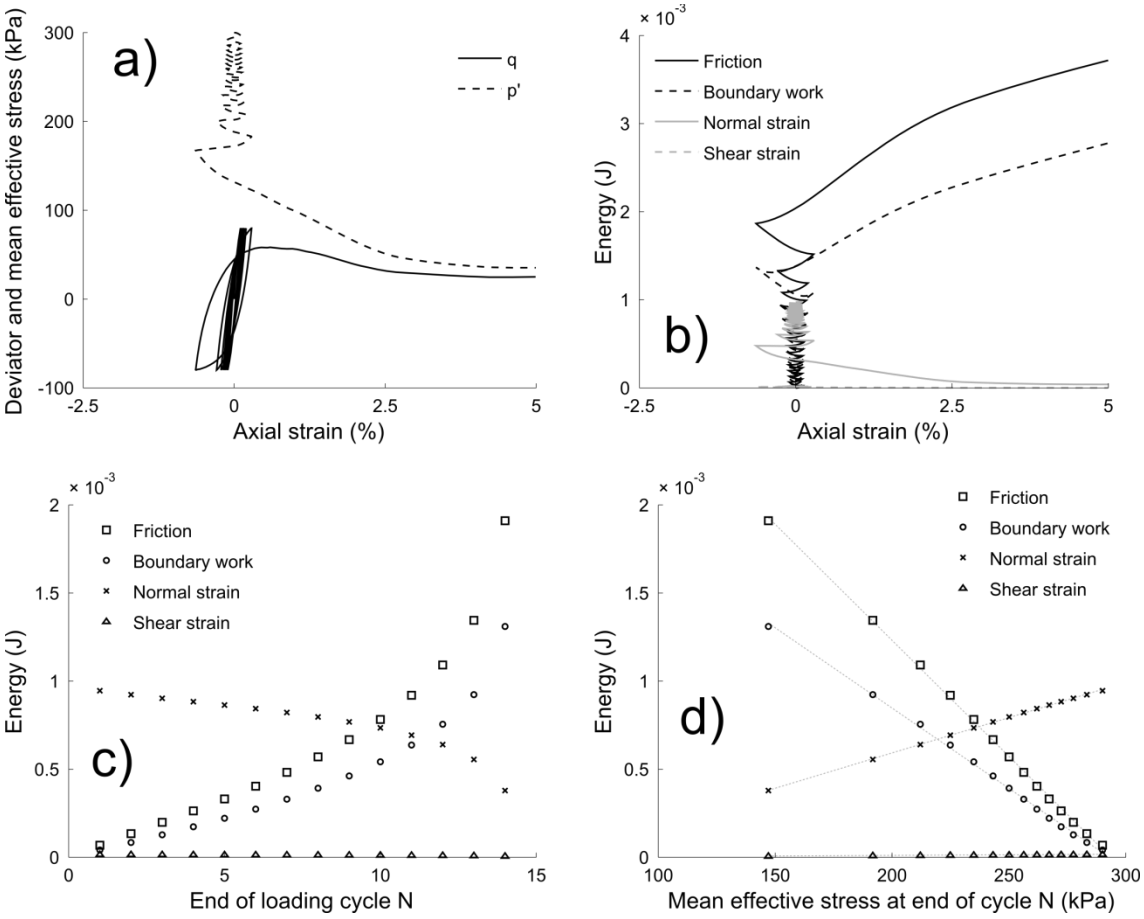

Figure 6.2: Stress–strain behaviour and energy terms for S1 (base case) with e = 0.4534, p'_0 = 300 kPa, q_{mean} = 0 kPa and q_{cyc} = 80 kPa: a) deviator stress, q, and mean effective stress, p', against axial strain (%); b) energy dissipated by frictional sliding, boundary work, and normal and shear components of strain energy, all in J, against axial strain; c) values of these four energy terms at the end of loading cycle N against N; d) the same values plotted against p' (kPa) where the dotted grey lines are linear regressions

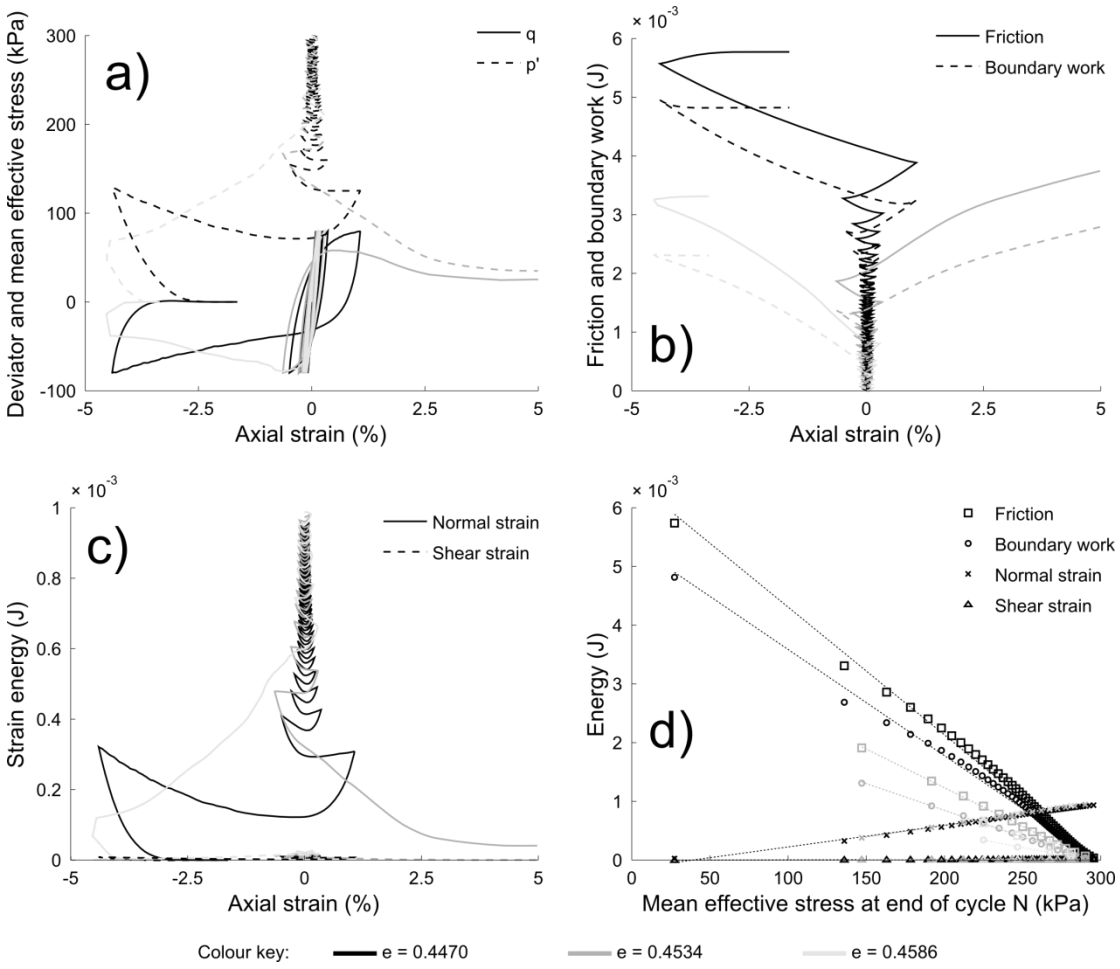

Figure 6.3: Stress–strain behaviour and energy terms for the parametric study of void ratio where e = 0.4470 (S2), e = 0.4534 (S1) and e = 0.4586 (S3) are respectively represented by black, dark grey and light grey colours: a) deviator stress, q, and mean effective stress, p', against axial strain (%); b) boundary work and energy dissipated by frictional sliding, both in J, against axial strain; c) normal and shear components of strain energy (J) against axial strain; d) values of the four tracked energy terms at the end of loading cycle N against p' (kPa), including dotted linear regressions

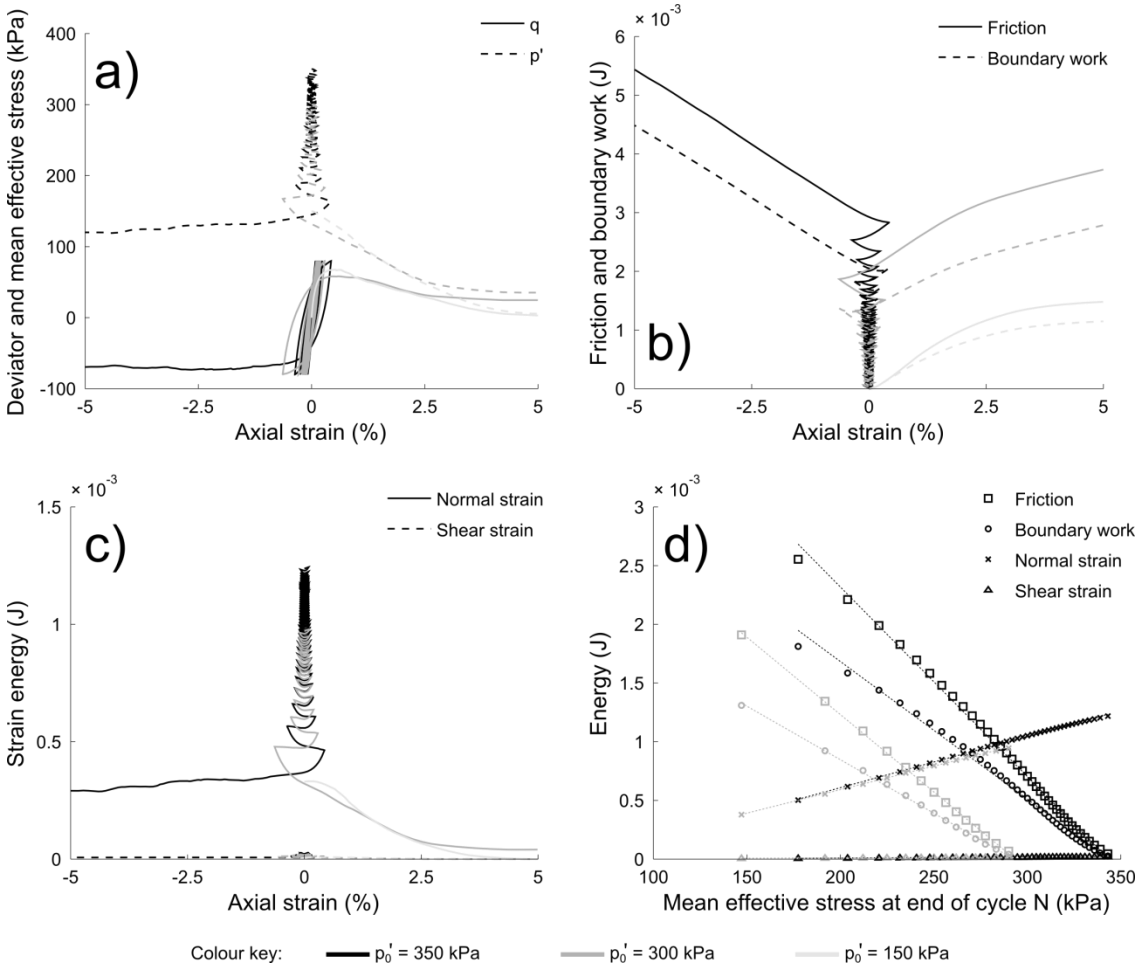

Figure 6.4: Stress–strain behaviour and energy terms for the parametric study of initial mean effective stress where p_0' = 350 kPa (S4), p_0' = 300 kPa (S1) and p_0' = 150 kPa (S5) are respectively represented by black, dark grey and light grey colours. The four subfigures are as described for Fig. 6.3

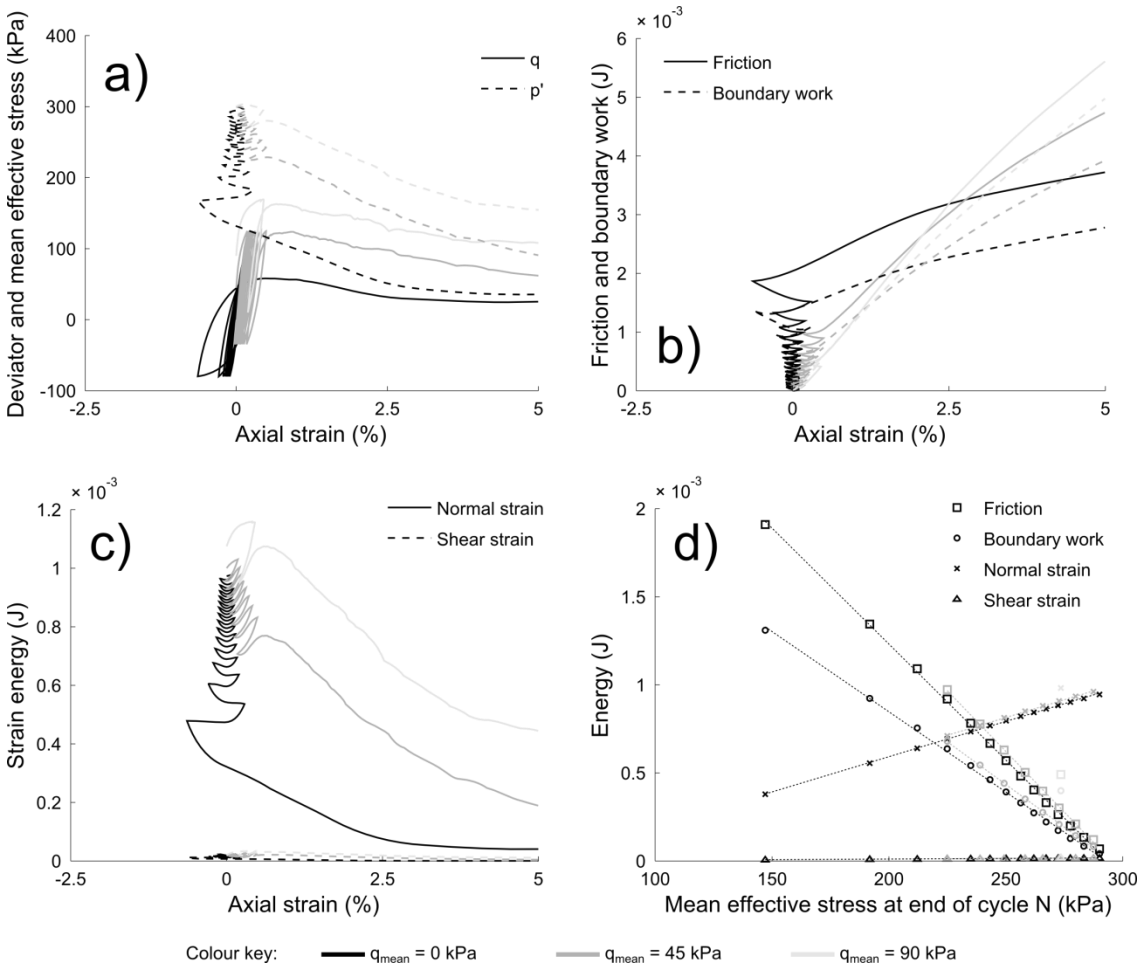

Figure 6.5: Stress–strain behaviour and energy terms for the parametric study of mean deviator stress where q_{mean} = 0 kPa (S1), q_{mean} = 45 kPa (S6) and q_{mean} = 90 kPa (S7) are respectively represented by black, dark grey and light grey colours. The four subfigures are as described for Fig. 6.3

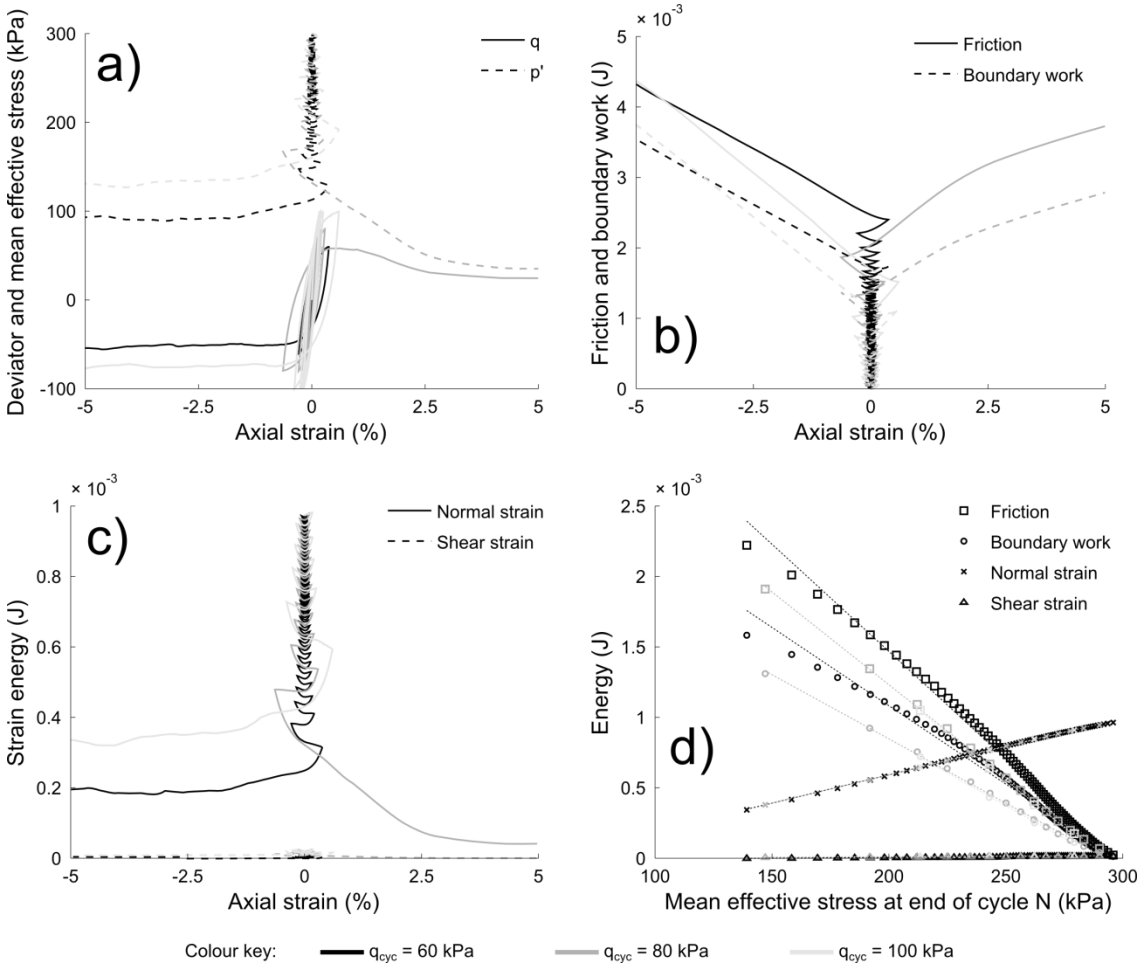

Figure 6.6: Stress–strain behaviour and energy terms for the parametric study of deviator stress amplitude where q_{cyc} = 60 kPa (S8), q_{cyc} = 80 kPa (S1) and q_{cyc} = 100 kPa (S9) are respectively represented by black, dark grey and light grey colours. The four subfigures are as described for Fig. 6.3

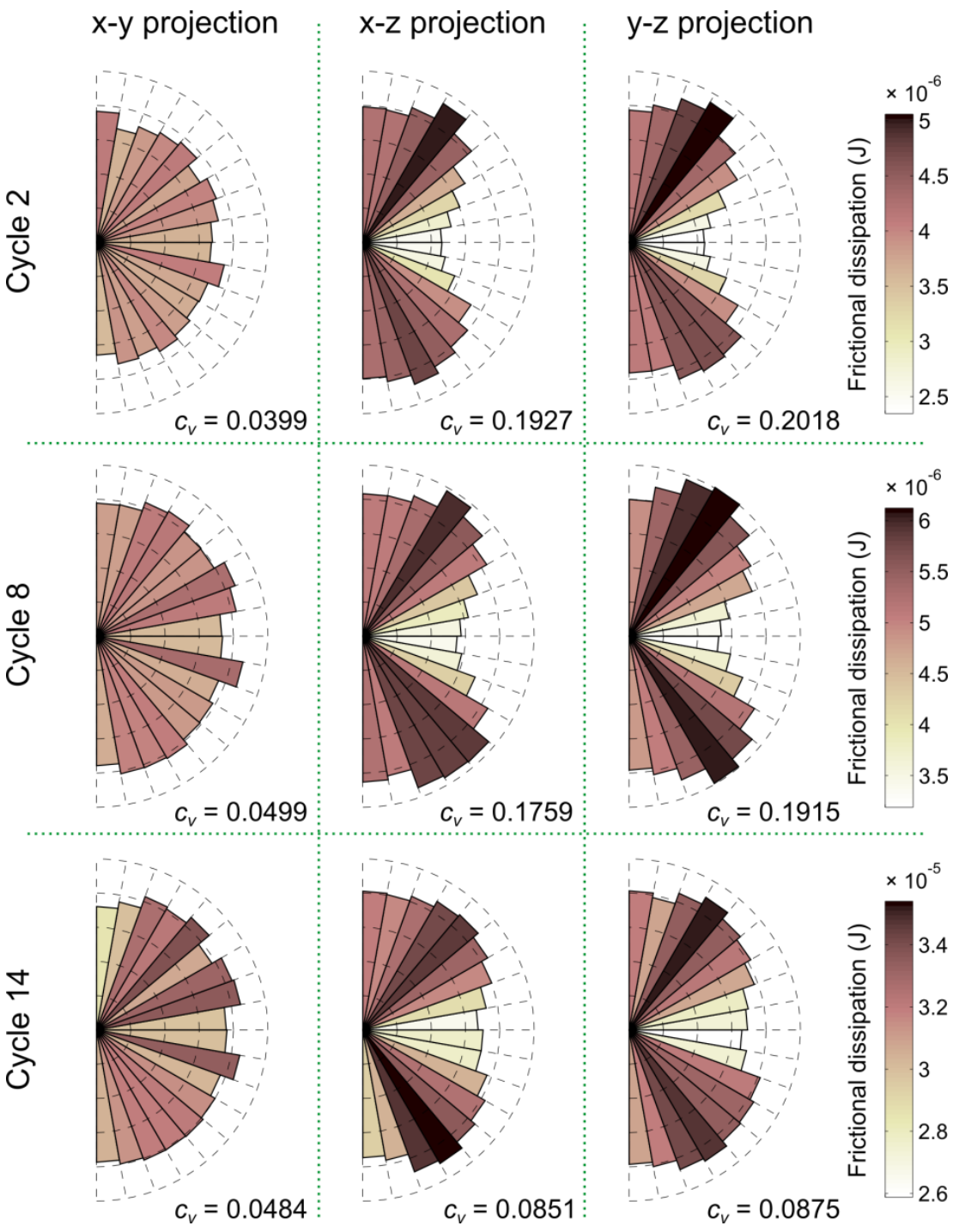

Figure 6.7: Rose diagrams showing the total frictional dissipation (J) at each orientation for specific cycles of the base case simulation, S1. The three rows represent the dissipation during the 2nd (top), 8th (middle) and 14th (bottom) loading cycles. The three columns, from left to right, show projections onto the x–y, x–z and y–z planes. The lengths and colours of each segment show the total frictional dissipation for contacts at that orientation during the specified cycle

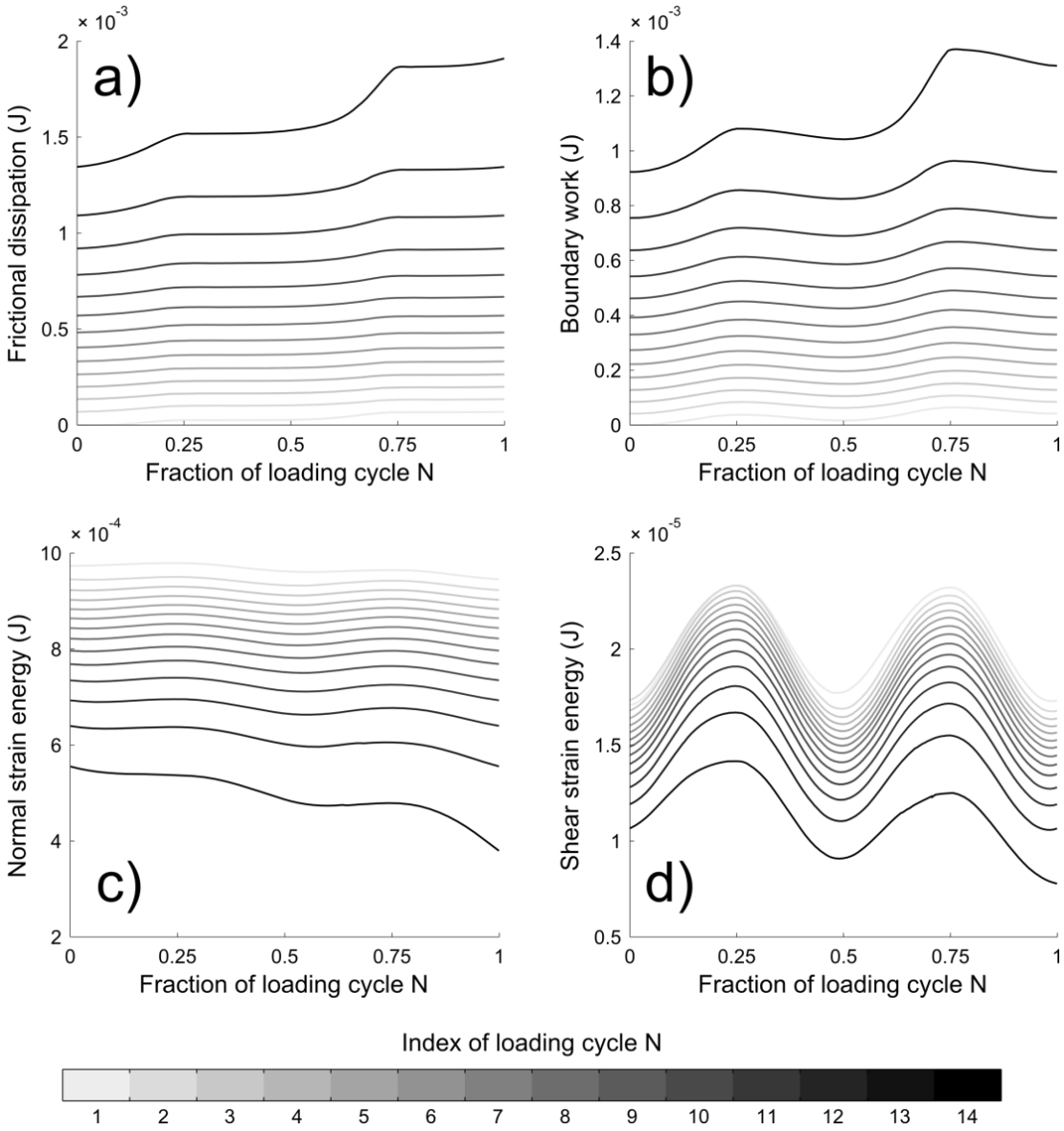

Figure 6.8: Energy dissipated by frictional sliding, boundary work, and normal and shear components of strain energy, all in J, against the fraction of loading cycle N for the base case simulation, S1. Individual cycles are distinguishable by colour, varying from light grey (1st cycle) to black (14th and final cycle before liquefaction) as indicated by the colourbar

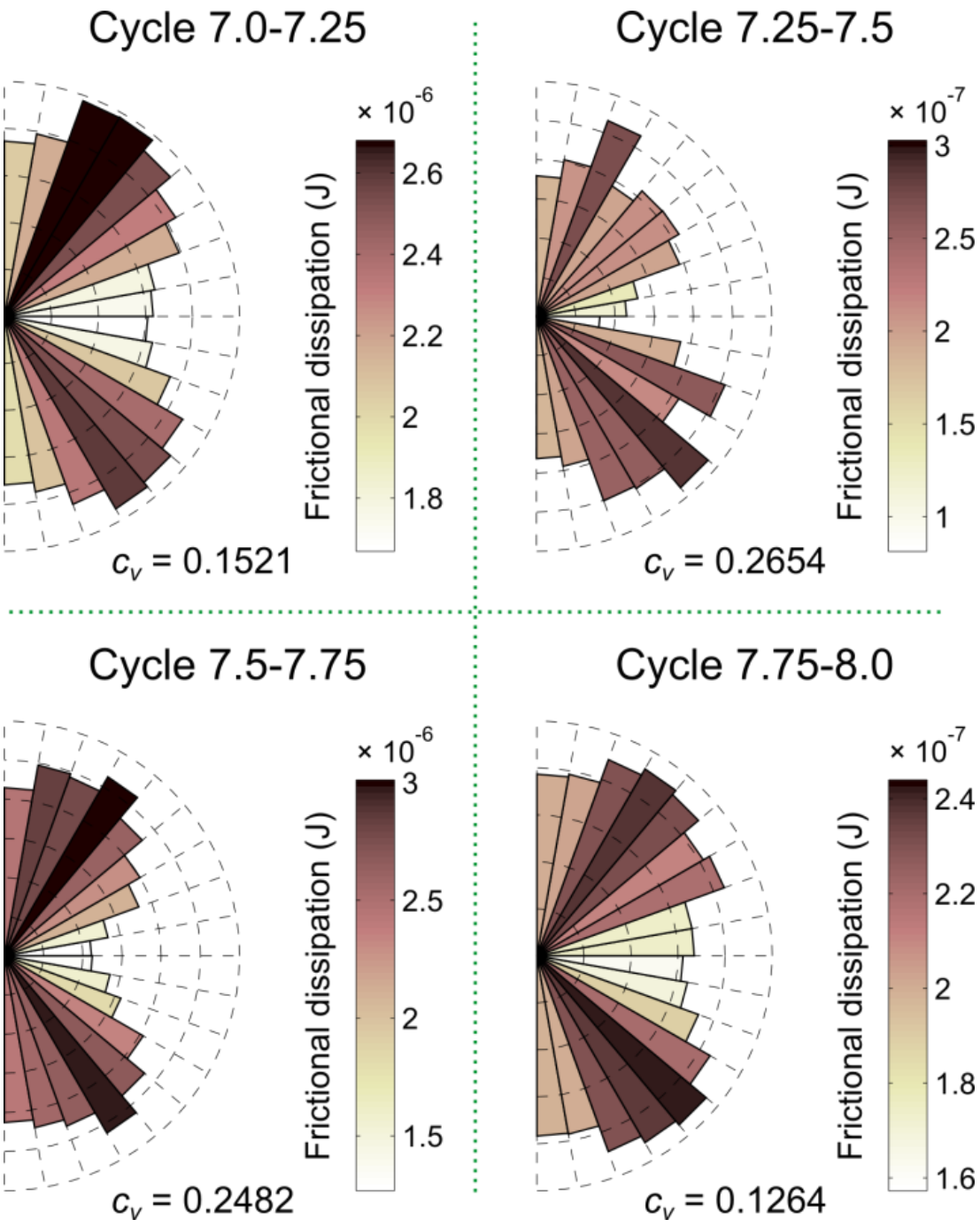

Figure 6.9: Rose diagrams showing the total frictional dissipation (J) at each orientation for four consecutive quarter-cycles comprising one complete loading cycle of the base case simulation, S1. The frictional dissipation is shown for cycle 8, i.e., the middle row of Fig.6.7. Each diagram shows a projection onto the y–z plane

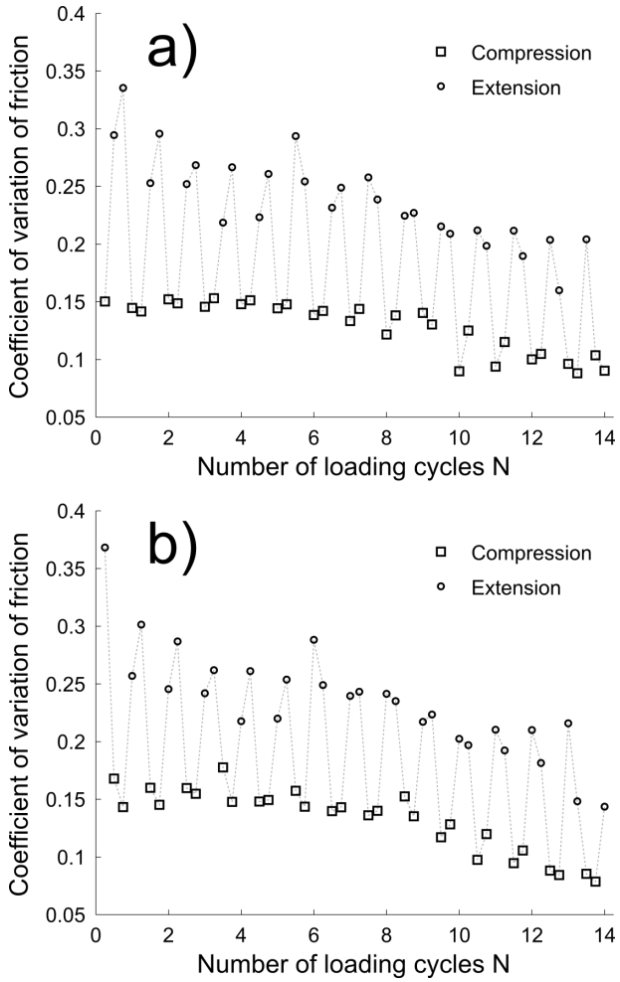

Figure 6.10: Coefficient of variation among the 36 bins for total frictional dissipation for projections onto the x–z and y–z planes against the number of loading cycles N. a) is for the base case IC simulation, S1; b) is for the IE simulation, S10. Each data point is based on a quarter-cycle, as for the rose diagrams in Fig. 6.9. Markers distinguish compressive (□) from extensive (o) loading; the grey dotted lines are a visual aid

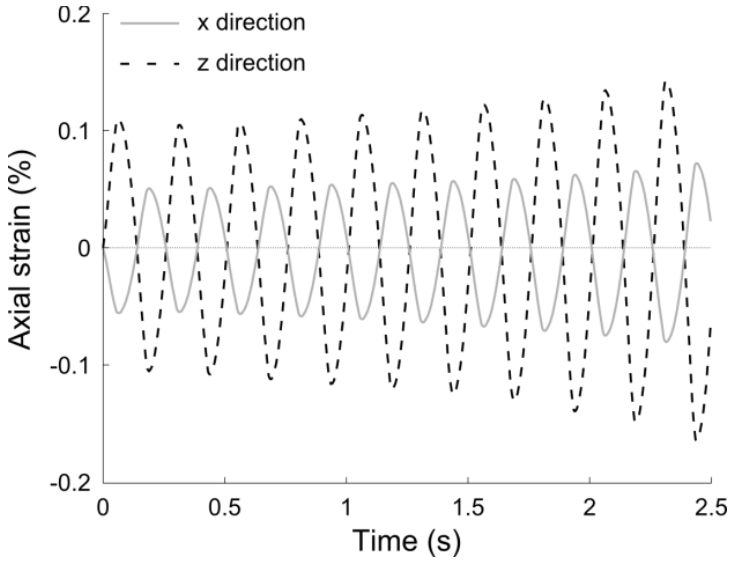

Figure 6.11: Percentage axial strains against time for the initial cycles of S1

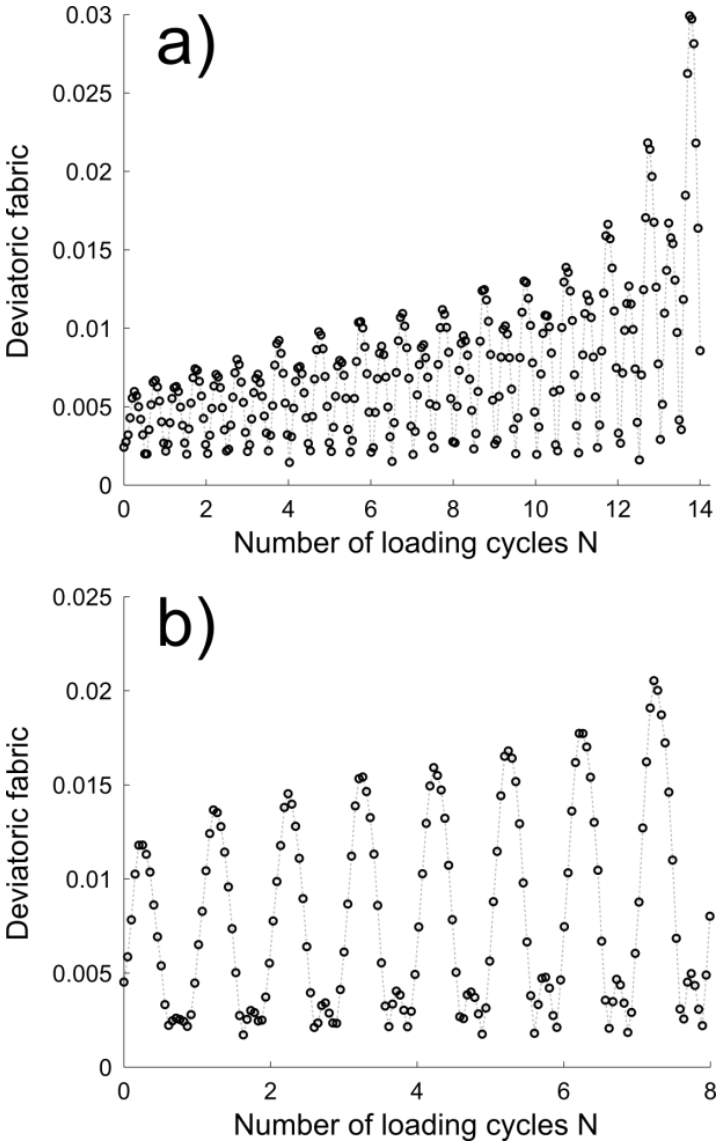

Figure 6.12: Deviatoric fabric of all contacts against the number of loading cycles N for a) the base case simulation, S1 and b) the q_{mean} = 45 kPa simulation, S6. The grey dotted lines are a visual aid

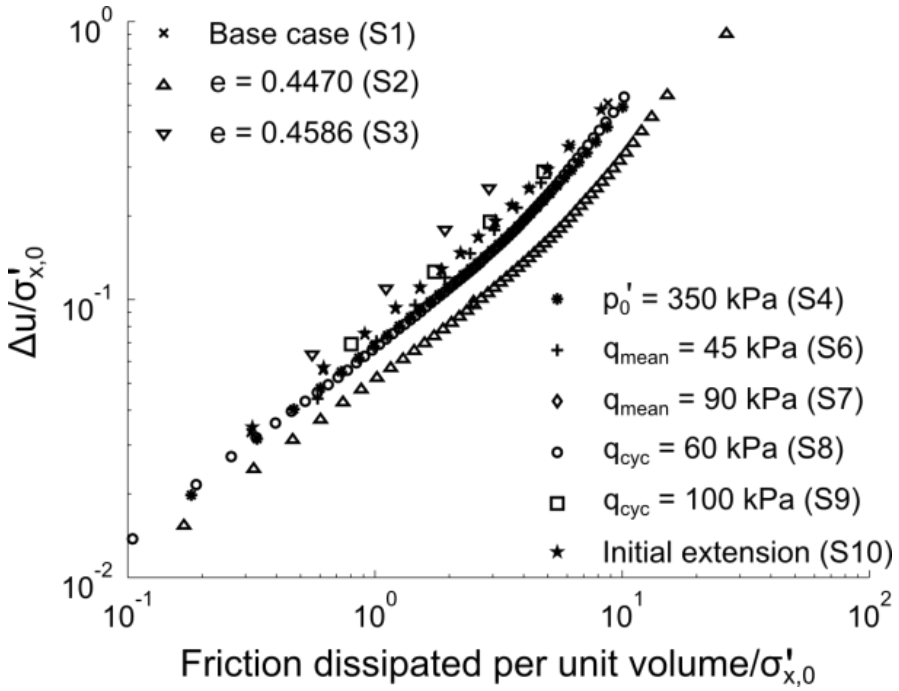

Figure 6.13: Accumulated pore water pressure increase normalised by initial confining pressure, $\sigma'_{x,0}$, against the accumulated friction dissipated per unit volume (unit energy) with the same normalisation. The markers show values at the end of each complete loading cycle

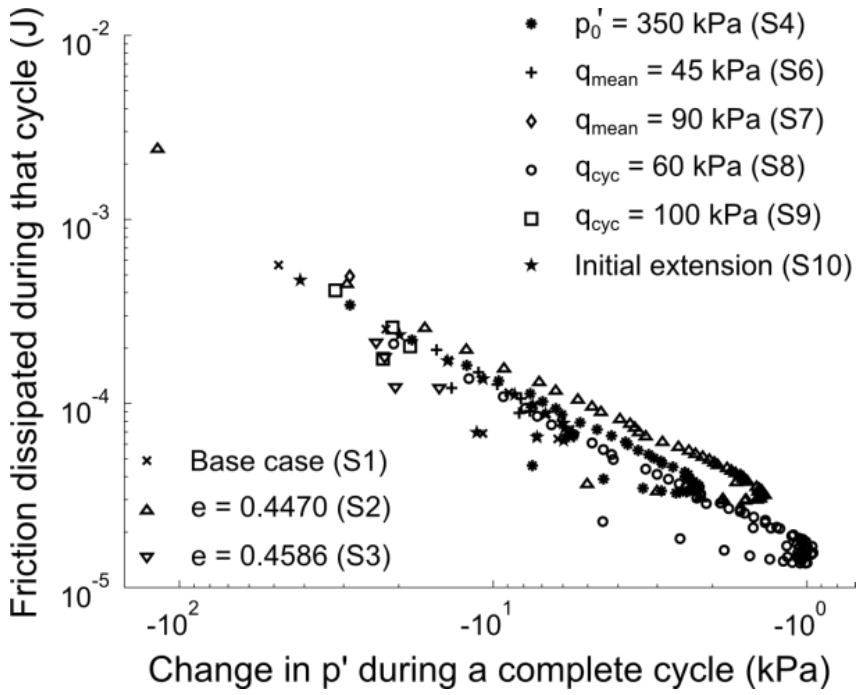

Figure 6.14: Friction dissipated during a single loading cycle (J) against the change in mean effective stress, p', during that cycle (kPa)

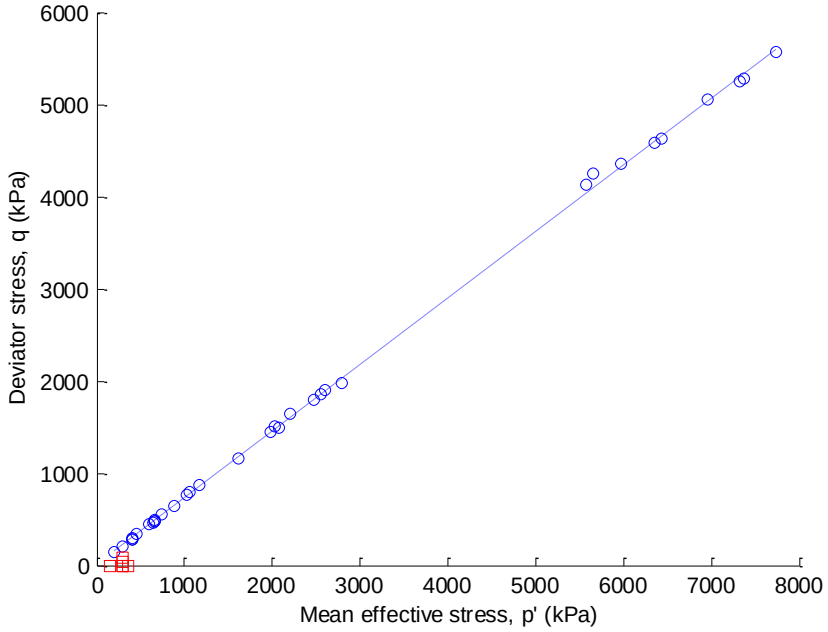

Figure 6.15: Plot of CSL in $q - p'$ space for 27 CV and 9 drained monotonic simulations (simplified Hertz-Mindlin contact model, G = 1.46 GPa, μ_s = 0.25, ϑ = 0.2 and periodic boundaries using LAMMPS).

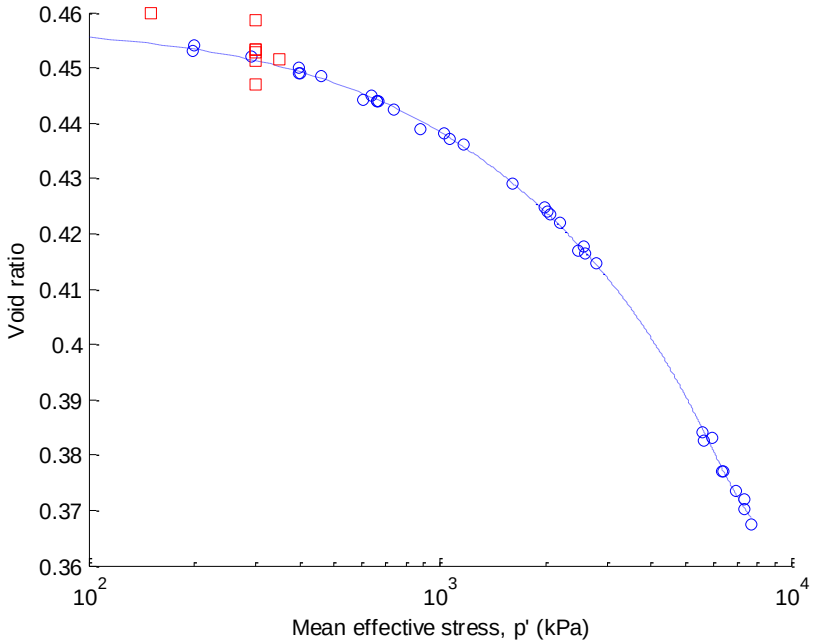

Figure 6.16: Plot of CSL in $e - p'$ space for 27 CV and 9 drained monotonic simulations (simplified Hertz-Mindlin contact model, G = 1.46 GPa, μ_s = 0.25, ϑ = 0.2 and periodic boundaries using LAMMPS).

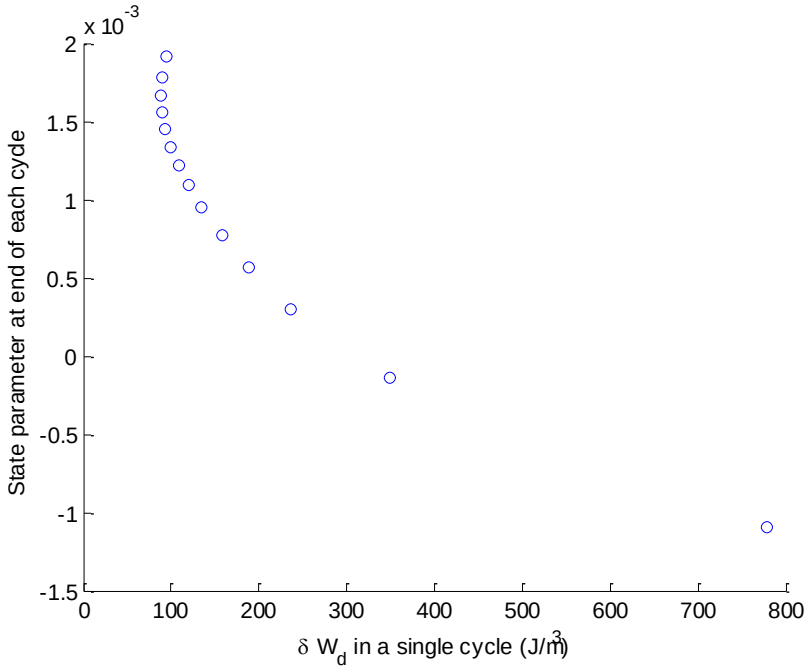

Figure 6.17: Plot of ψ against δW_d for S1 (base case) CV cyclic simulation (simplified Hertz-Mindlin contact model, G = 1.46 GPa, μ_s = 0.25, ϑ = 0.2 and periodic boundaries using LAMMPS).

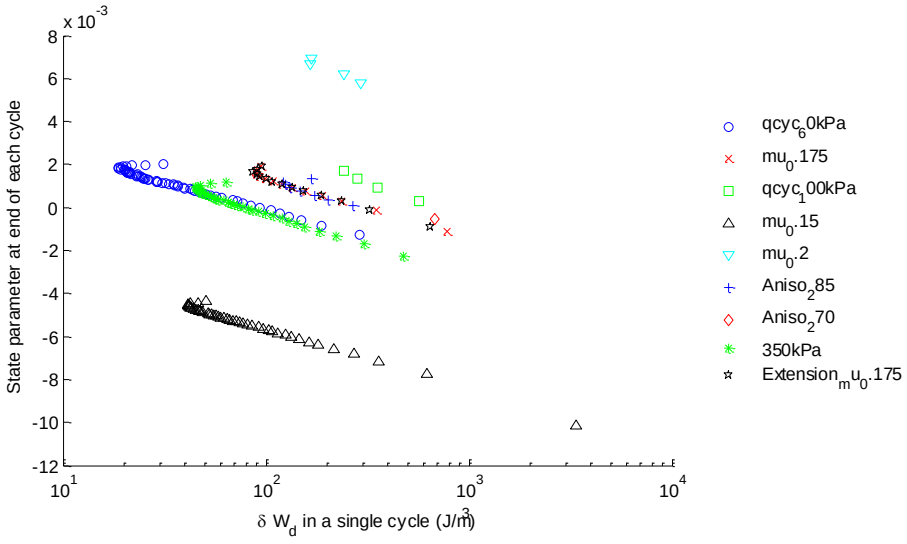

Figure 6.18: Plot of ψ against δW_d for S2-S10 CV cyclic simulations (simplified Hertz-Mindlin contact model, G = 1.46 GPa, μ_s = 0.25, ϑ = 0.2 and periodic boundaries using LAMMPS).

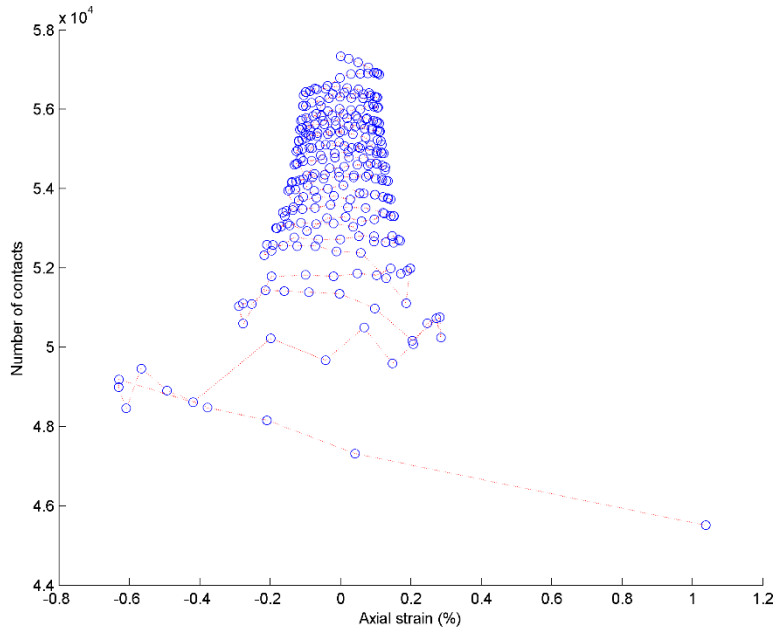

Figure 6.19: Plot of number of contacts against axial strain for S1 (base case) CV cyclic simulation (simplified Hertz-Mindlin contact model, G = 1.46 GPa, μ_s = 0.25, ϑ = 0.2 and periodic boundaries using LAMMPS).

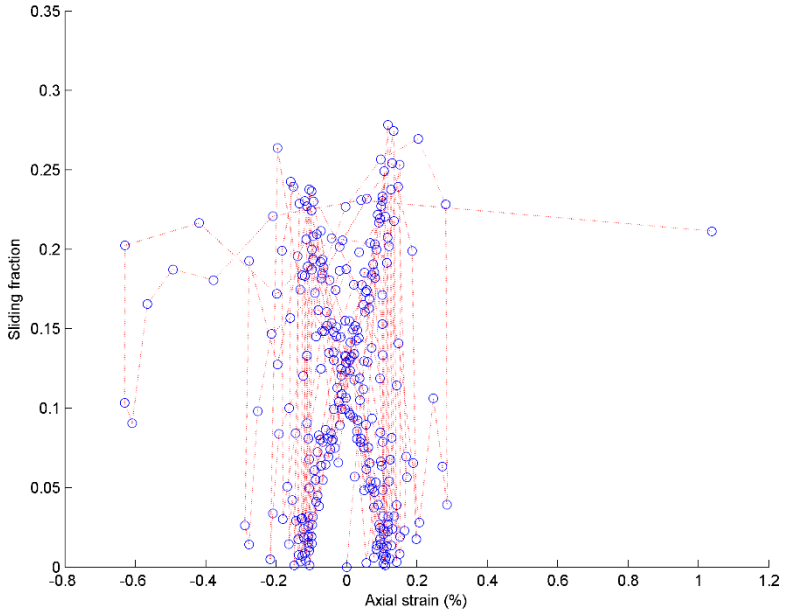

Figure 6.20: Plot of sliding fraction against axial strain for S1 (base case) CV cyclic simulation (simplified Hertz-Mindlin contact model, G = 1.46 GPa, μ_s = 0.25, ϑ = 0.2 and periodic boundaries using LAMMPS).

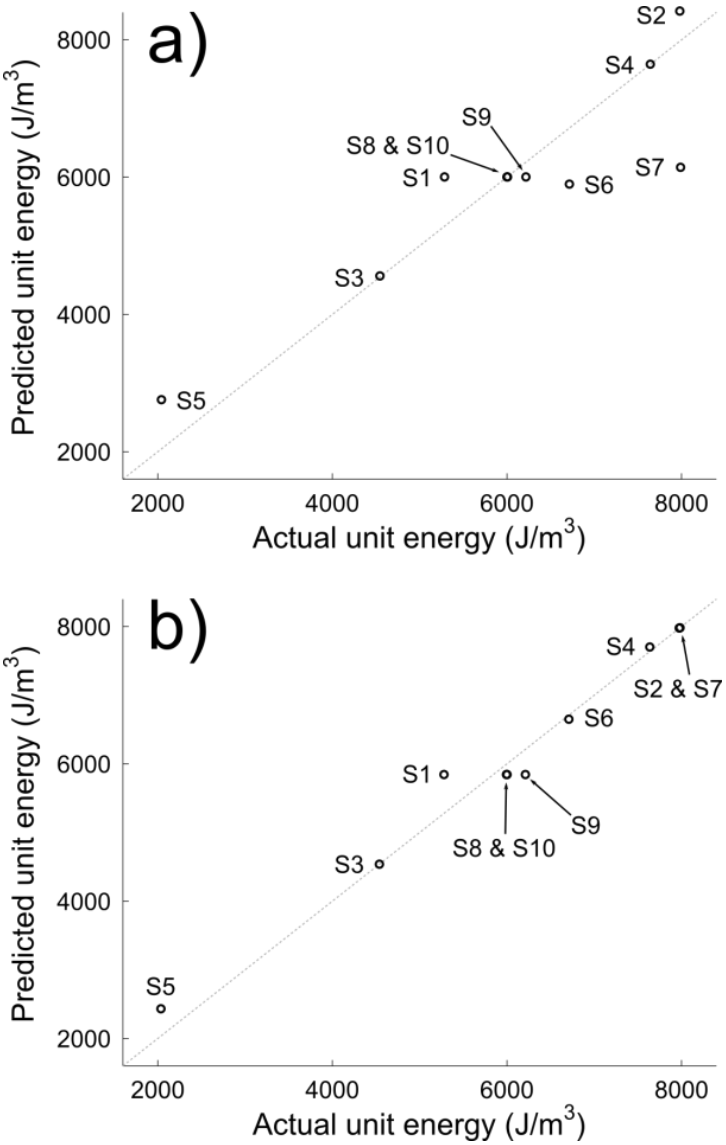

Figure 6.21: Comparison between the total frictional dissipation per unit volume, i.e., unit energy, at the onset of liquefaction (J/m^3) for the ten simulations described in this paper and the predictions made using a) Eq. 6.20; b) Eq. 6.21

Chapter 7 Conclusions

7.1 Summary

The objectives guiding the numerical investigation reported in this thesis were:

1. To validate a common assumption – that fully saturated soils can be simulated effectively by maintaining the sample's volume constant throughout a simulation.
2. To determine the influence of void ratio, frequency, mean deviator stress, deviator stress amplitude and confining pressure on sand behaviour under undrained cyclic triaxial conditions.
3. To understand the role of energy during undrained cyclic loading of a sand.

In order to achieve these objectives, DEM simulations were carried out to analyse the behaviour of sand subjected to both monotonic and cyclic loading under a variety of soil conditions and well-controlled triaxial stress paths. The first objective was addressed in Chapter 4: (Improving constant-volume simulations of undrained behaviour in DEM). In conventional constant-volume undrained triaxial simulations of dense samples, the stresses generated during shearing are unrealistically high as demonstrated in Chapter 3: (Undrained monotonic triaxial DEM simulations). Four alternatives to the constant-volume method with uncrushable spherical particles were proposed, each of which has a physical basis, to try to remedy this well-known problem: the inclusion of particle crushing in the simulations, the presence of highly compressible air within the sample, or the reduction of stiffness due to particle surface asperities or non-spherical particle shapes. These four approaches were all explored using the open-source LAMMPS code.

The second objective was met in Chapter 5: (Evaluating the cyclic triaxial response of sand using Design of Experiments). This chapter presents a systematic investigation of the behaviour of sand subjected to cyclic loading using an established Design of Experiments (DOE) technique: the Taguchi method. Detailed simulation results are presented that relate the influence of the five factors: cycle frequency, mean deviator stress, deviator stress amplitude, confining pressure and void ratio on the dynamic properties of granular materials.

The third objective was addressed in Chapter 6: (Energy dissipation in soil samples during cyclic triaxial simulations). 10 constant-volume cyclic triaxial DEM simulations

were run in accordance with a parametric study of five factors: void ratio, initial mean effective stress, mean deviator stress, deviator stress amplitude and compressive/extensive initial loading. Numerous energy terms were tracked during these simulations: boundary work, frictional dissipation, translational and rotational kinetic energy, and normal and shear components of strain energy. The trends in both the number of complete cycles and the unit energy up to the onset of liquefaction were compared with experimental data, a preferred contact orientation for frictional dissipation was found, the relationship between the accumulated pore water pressure and the dissipated energy per unit volume was explored, and a commonly used energy-based model to evaluate the liquefaction potential of soil (Figueroa *et al*., 1994) was assessed.

The key findings of the research work such as implementing DOE approach and prediction in cyclic loading study; DEM micro-scale information during one cycle; DEM micro-scale information embedded with an energy-based model to assess liquefaction will be helpful to geotechnical engineers and are summarised in section 7.2. Suggested recommendations for future work are given in section 7.3.

7.2 Major findings

The key findings are summarised here; more detail may be found in the conclusions of each chapter.

1. The assumption of a constant volume to simulate fully saturated undrained conditions is not appropriate as it generates extremely unrealistic high stresses for dense samples. These stresses are further increased by incorporating rotational resistance at the contacts between spherical particles in constant-volume simulations: a result which differs from the drained case.
2. Adopting a rough-surface contact model (capturing the effect of asperity crushing) or switching to the bulk modulus method (enabling small changes of sample volume to capture compression of entrained air) reduces stresses. However, both of these approaches are less effective than reducing the particle/sample stiffness to account for non-spherical particle shapes.
3. If particles are crushable, it is important to incorporate particle crushing in the simulations so that stresses are not over-estimated. In the absence of

particle crushing, the most effective method to improve agreement between undrained experiments and DEM simulations is to reduce the particle shear modulus substantially. By reducing the shear modulus by a factor of 20, based on single-particle laboratory experiments (Cavarretta *et al*., 2012), stresses were reduced by 94%. This recommended approach is also computationally beneficial as the simulation time-step may be increased.

4. The Taguchi method is an effective way to study the cyclic response of soil samples, to identify the main effects and the interactive effects, and to predict responses for combinations of parameters not tested. Based on this DOE analysis, the void ratio is the most influential effect on the behaviour of sand subjected to cyclic loading.
5. Introducing initial stress anisotropy reduces the number of complete cycles up to the onset of liquefaction, N_l, but increases the energy dissipated per unit volume, δW_d. Increasing the deviator stress amplitude reduces N_l but has no significant effect on δW_d. The observed trends in N_l and δW_d match data from physical experiments, where available.
6. Immediately after a shear reversal, there is a period where the frictional dissipation is negligible. Thereafter, the frictional dissipation grows quadratically until the end of the compressive or extensive loading phases. This may be the reason why so many load cycles are needed to reach liquefaction if the cyclic amplitude is less than a particular threshold (0.04% axial strain for these simulations).
7. If an energy-based model is being applied for liquefaction assessment of anisotropic samples, a significant improvement in the accuracy of the model may be achieved by including the mean deviator stress.

7.3 Recommendations for future work

1. These simulations used an artificial particle size distribution which is not representative of a real sand. It would be useful to conduct a set of DEM simulations which match the grading of a real sand, enabling a meaningful comparison between the simulation results and physical tests.
2. Similarly this study was restricted to perfectly spherical particle shapes. It is important to investigate the influence of particle shape on soil behaviour, particularly if quantitative agreement with physical experiments is desired.

3. Since this study utilised stress control, a set of strain controlled simulations could be conducted to verify that the results are fundamentally unchanged.
4. The micro-scale information provided by DEM simulations should be embedded into existing soil constitutive models or new models should be developed, informed by the simulations, to explore liquefaction and predict sand behaviour under both monotonic and cyclic loading conditions.
5. The Taguchi method is an effective way to study the cyclic response of soil samples using DEM. It reduces computational cost, is capable of identifying the main effects and the interactive effects, and can be used to predict responses for combinations of parameters that are not being tested.
6. The energy-based model can be applied for liquefaction assessment of both isotropic and anisotropic samples.
7. For CV simulations with a Hertz Mindlin contact model at high density, it is important to incorporate particle crushing in the simulations if particles are crushable. In the absence of particle crushing, the most effective method to achieve more realistic simulation results is to reduce the particle shear modulus so that stresses are not over-estimated. This particle shear modulus reduction approach is also computationally advantageous as the simulation time-step increases.

References

Aghakouchak, A. 2015. Advanced laboratory studies to explore the axial cyclic behaviour of driven piles (Ph.D. thesis). *Imperial College London (University of London)*.

Airey, D. & Fahey, M. 1991. Cyclic response of calcareous soil from the North-West Shelf of Australia. *Géotechnique* 41(1)**,** pp 101-121.

Alarcon-Guzman, A. 1986. Cyclic stress-strain and liquefaction characteristics of sands. Purdue Univ., Lafayette, IN (USA),

Alarcon, A. & Leonards, G. 1988. Discussion of “Liquefaction evaluation procedure” by steve J. poulos, gonzalo castro, and john W. france (june, 1985, vol. 111, no. 6). *Journal of Geotechnical Engineering,* 114(2)**,** pp 232-236.

Alavi, A. H. & Gandomi, A. H. 2012. Energy-based numerical models for assessment of soil liquefaction. *Geoscience Frontiers,* 3(4)**,** pp 541-555.

Altuhafi, F. & Coop, M. R. 2011. Changes to particle characteristics associated with the compression of sands. *Géotechnique,* 61(6)**,** pp 459-471.

Andersen, K., Puech, A. & Jardine, R. Cyclic resistant geotechnical design and parameter selection for offshore engineering and other applications. Proceedings of the TC-209 Workshop, Design for Cyclic Loading: Piles and Other Foundations, Paris. Presses des Ponts, 2013. 9-44.

Assimaki, D., Kausel, E. & Whittle, A. 2000. Model for dynamic shear modulus and damping for granular soils. *Journal of Geotechnical and Geoenvironmental Engineering,* 126(10)**,** pp 859-869.

ASTM. 2011. Method for consolidated drained triaxial compression test for soils.

Azeiteiro, R. J., Coelho, P. A., Taborda, D. M. & Grazina, J. C. 2017. Energy-based evaluation of liquefaction potential under non-uniform cyclic loading. *Soil Dynamics and Earthquake Engineering,* 92(650-665.

Barreto, D. 2009. Numerical and Experimental Investigation into the Behaviour of Granular Materials under Generalised Stress States (Ph. D. thesis). *University of London, Department of Civil Engineering, Imperial College of Science, Technology and Medicine*.

Barreto, D. & O’Sullivan, C. 2012. The influence of inter-particle friction and the intermediate stress ratio on soil response under generalised stress conditions. *Granular Matter,* 14(4)**,** pp 505-521.

Baziar, M. & Jafarian, Y. 2007. Assessment of liquefaction triggering using strain energy concept and ANN model: capacity energy. *Soil Dynamics and Earthquake Engineering,* 27(12)**,** pp 1056-1072.

Baziar, M. & Sharafi, H. 2011. Assessment of silty sand liquefaction potential using hollow torsional tests—An energy approach. *Soil Dynamics and Earthquake Engineering,* 31(7)**,** pp 857-865.

Been, K., Jefferies, M. & Hachey, J. 1991. Critical state of sands. *Géotechnique* 41(3)**,** pp 365-381.

Been, K. & Jefferies, M. G. 1985. A state parameter for sands. *Géotechnique,* 35(2)**,** pp 99-112.

Berrill, J. & Davis, R. 1985. Energy dissipation and seismic liquefaction of sands: revised model. *Soils and Foundations,* 25(2)**,** pp 106-118.

Bi, Z., Sun, Q., Jin, F. & Zhang, M. 2011. Numerical study on energy transformation in granular matter under biaxial compression. *Granular Matter,* 13(4)**,** pp 503-510.

Bishop, A. 1973. The influence of an undrained change in stress on the pore pressure in porous media of low compressibility. *Géotechnique* 23(3)**,** pp.

Bishop, A. W. & Eldin, G. 1950. Undrained triaxial tests on saturated sands and their significance in the general theory of shear strength. *Géotechnique* 2(1)**,** pp 13-32.

Bolton, M., Nakata, Y. & Cheng, Y. 2008. Micro-and macro-mechanical behaviour of DEM crushable materials. *Géotechnique,* 58(6)**,** pp 471-480.

Carrera, A., Coop, M. & Lancellotta, R. Influence of sample preparation techniques and stress path followed on the location of the Critical State Line? An example of a silty-sandy tailing. International Symposium on Deformation Characteristics of Geomaterials, 2011. 526-532.

Casagrande, A. 1940. Characteristics of cohesionless soils affecting the stability of slopes and earth fills. *Contributions to Soils Mechanics, 1925-1940*.

Casto, G. 1975. Liquefaction and cyclic mobility of saturated sands. *Journal of Geotechnical and Geoenvironmental Engineering,* 101(GT6)**,** pp 551-569.

Castro, G. 1969. Liquefaction of sands (Ph. D. thesis). *Harvard Soil Mech.*

Castro, G. & Poulos, S. J. 1977. Factors affecting liquefaction and cyclic mobility. *Journal of Geotechnical and Geoenvironmental Engineering,* 103(6)**,** pp 501-516.

Cavarretta, I. 2009. *The influence of particle characteristics on the engineering behaviour of granular materials. (Ph.D thesis).* Imperial College London (University of London).

Cavarretta, I., Coop, M. & O'SULLIVAN, C. 2010. The influence of particle characteristics on the behaviour of coarse grained soils. *Géotechnique,* 60(6)**,** pp 413-423.

Cavarretta, I. & O'sullivan, C. 2012. The mechanics of rigid irregular particles subject to uniaxial compression. *Géotechnique,* 62(8)**,** pp 681-692.

Cavarretta, I., O'Sullivan, C., Ibraim, E., Lings, M., Hamlin, S. & Wood, D. M. 2012. Characterization of artificial spherical particles for DEM validation studies. *Particuology,* 10(2)**,** pp 209-220.

Chan, S. & Ng, K. 1986. Geometrical characteristics of a computer-generated three-dimensional packed column of equal and unequal sized spheres—with special reference to wall effects. *Chemical Engineering Communications,* 48(4-6)**,** pp 215-236.

Cheng, Y., Bolton, M. & Nakata, Y. 2004. Crushing and plastic deformation of soils simulated using DEM. *Geotechnique,* 54(2)**,** pp 131-141.

Cui, D., Wu, W., Xiang, W., Doanh, T., Chen, Q., Wang, S., Liu, Q. & Wang, J. 2017. Stick-slip behaviours of dry glass beads in triaxial compression. *Granular Matter,* 19(1)**,** pp 1-18.

Cundall, P. 1988. Computer simulations of dense sphere assemblies. *Studies in Applied Mechanics.* Elsevier.

Cundall, P. A. 2001. A discontinuous future for numerical modelling in geomechanics? *Proceedings of the institution of civil engineers-geotechnical engineering,* 149(1)**,** pp 41-47.

Cundall, P. A. & Strack, O. D. 1979. A discrete numerical model for granular assemblies. *Geotechnique,* 29(1)**,** pp 47-65.

D3999-11, A. 2013. Determination of the Modulus and Damping Properties of Soils Using Cyclic Triaxial Apparatus

D5311-11, A. 2013. Load Controlled Cyclic Triaxial Strength of Soil.

de Bono, J. P. & McDowell, G. R. 2014. DEM of triaxial tests on crushable sand. *Granular Matter,* 16(4)**,** pp 551-562.

Dief, H. M. & Figueroa, J. L. 2007. Liquefaction assessment by the unit energy concept through centrifuge and torsional shear tests. *Canadian Geotechnical Journal,* 44(11)**,** pp 1286-1297.

Dobry, R., Ladd, R., Yokel, F. Y., Chung, R. M. & Powell, D. 1982. *Prediction of pore water pressure buildup and liquefaction of sands during earthquakes by the cyclic strain method*: National Bureau of Standards Gaithersburg, MD.

Dubujet, P. & Dedecker, F. 1998. Micro-mechanical analysis and modelling of granular materials loaded at constant volume. *Granular Matter,* 1(3)**,** pp 129-136.

El Shamy, U. & Denissen, C. 2010. Microscale characterization of energy dissipation mechanisms in liquefiable granular soils. *Computers and Geotechnics,* 37(7-8)**,** pp 846-857.

El Shamy, U. & Denissen, C. 2012. Microscale energy dissipation mechanisms in cyclically-loaded granular soils. *Geotechnical and Geological Engineering,* 30(2)**,** pp 343-361.

Favier, J., Curry, D. & LaRoche, R. Calibration of DEM material models to approximate bulk particle characteristics. Proceedings of the 6th World Congress on Particle Technology, Nuremberg, Germany, 2010.

Figueroa, J. L., Saada, A. S., Liang, L. & Dahisaria, N. M. 1994. Evaluation of soil liquefaction by energy principles. *Journal of Geotechnical Engineering,* 120(9)**,** pp 1554-1569.

Finno, R. J., Harris, W. W., Mooney, M. A. & Viggiani, G. 1996. Strain localization and undrained steady state of sand. *Journal of Geotechnical Engineering,* 122(6)**,** pp 462-473.

Gong, G. 2008. *DEM [Discrete Element Method] simulations of drained and undrained behaviour.* University of Birmingham.

Greenwood, J. A. & Tripp, J. H. 1967. The elastic contact of rough spheres. *Journal of Applied Mechanics,* 34(1)**,** pp 153-159.

Gu, X., Huang, M. & Qian, J. 2014. DEM investigation on the evolution of microstructure in granular soils under shearing. *Granular Matter,* 16(1)**,** pp 91-106.

Hanley, K. J. 2011. Experimental quantification and modelling of attrition of infant formulae during pneumatic conveying (Ph.D. thesis). *University College Cork*.

Hanley, K. J., Huang, X. & O'Sullivan, C. 2018. Energy dissipation in soil samples during drained triaxial shearing. *Géotechnique* 68(5)**,** pp 421-433.

Hanley, K. J., Huang, X., O'Sullivan, C. & Kwok, F. Challenges of simulating undrained tests using the constant volume method in DEM. AIP Conference Proceedings, 2013. AIP, 277-280.

Hanley, K. J., Huang, X., O'Sullivan, C. & Kwok, F. C. 2014. Temporal variation of contact networks in granular materials. *Granular Matter,* 16(1)**,** pp 41-54.

Hanley, K. J., O'Sullivan, C. & Huang, X. 2015. Particle-scale mechanics of sand crushing in compression and shearing using DEM. *Soils and Foundations,* 55(5)**,** pp 1100-1112.

Hardin, B. O. & Drnevich, V. P. 1972. Shear modulus and damping in soils: design equations and curves. *Journal of Soil Mechanics & Foundations Div,* 98(sm7)**,** pp.

Head, K. 1994. Manual of soil laboratory testing. Compressibility, shear strength and permeability.

Hsu, C.-C. & Vucetic, M. 2004. Volumetric threshold shear strain for cyclic settlement. *Journal of geotechnical and geoenvironmental engineering,* 130(1)**,** pp 58-70.

Huang, X. 2014. *Exploring Critical-state Behaviour Using DEM (Ph.D. thesis).* Imperial College London London.

Huang, X., Hanley, K., O'Sullivan, C., Kwok, C. & Wadee, M. 2014b. DEM analysis of the influence of the intermediate stress ratio on the critical-state behaviour of granular materials. *Granular Matter,* 16(5)**,** pp 641-655.

Huang, X., Hanley, K. J., O'Sullivan, C. & Kwok, C. Y. 2014a. Exploring the influence of interparticle friction on critical state behaviour using DEM. *International Journal for Numerical and Analytical Methods in Geomechanics,* 38(12)**,** pp 1276-1297.

Huang, X., Hanley, K. J., O'Sullivan, C. & Kwok, F. C. 2014c. Effect of sample size on the response of DEM samples with a realistic grading. *Particuology,* 15(1)**,** pp 107-115.

Huang, X., Hanley, K. J., O'Sullivan, C. & Kwok, C.-Y. 2017. Implementation of rotational resistance models: a critical appraisal. *Particuology,* 34(1)**,** pp 14-23.

Huang, X., Kwok, C.-y., Hanley, K. J. & Zhang, Z. 2018. DEM analysis of the onset of flow deformation of sands: linking monotonic and cyclic undrained behaviours. *Acta Geotechnica,* 13(1061-1074.

Hyodo, M., Tanimizu, H., Yasufuku, N. & Murata, H. 1994. Undrained cyclic and monotonic triaxial behaviour of saturated loose sand. *Soils and Foundations,* 34(1)**,** pp 19-32.

Ishibashi, I. & Zhang, X. 1993. Unified dynamic shear moduli and damping ratios of sand and clay. *Soils and Foundations,* 33(1)**,** pp 182-191.

Ishihara, K. 1993. Liquefaction and flow failure during earthquakes. *Géotechnique* 43(3)**,** pp 351-451.

Ishihara, K. 1996. Soil behaviour in earthquake geotechnics. Oxford engineering science series.

Ishihara, K. & Nagase, H. 1988. Multi-directional irregular loading tests on sand. *Soil Dynamics and Earthquake Engineering,* 7(4)**,** pp 201-212.

Ishihara, K., Okusa, S., Oyagi, N. & Ischuk, A. 1990. Liquefaction-induced flow slide in the collapsible loess deposit in Soviet Tajik. *Soils and Foundations,* 30(4)**,** pp 73-89.

Ishihara, K., Tatsuoka, F. & Yasuda, S. 1975. Undrained deformation and liquefaction of sand under cyclic stresses. *Soils and Foundations,* 15(1)**,** pp 29-44.

Ishihara, K. & Yasuda, S. 1972. Sand liquefaction due to irregular excitation. *Soils and Foundations,* 12(4)**,** pp 65-77.

Itasca Consulting Group, P. D. 2007. Particle Flow Code in 3 Dimensions: User's manual, Version 4.0. Minneapolis, USA.

Iwashita, K. & Oda, M. 1998. Rolling resistance at contacts in simulation of shear band development by DEM. *Journal of Engineering Mechanics,* 124(3)**,** pp 285-292.

Jardine, R. & Standing, J. 2000. *Pile load testing performed for HSE cyclic loading study at Dunkirk, France*: Great Britain, Health and Safety Executive.

Jiang, M., Yu, H.-S. & Harris, D. 2005. A novel discrete model for granular material incorporating rolling resistance. *Computers and Geotechnics,* 32(5)**,** pp 340-357.

Johnstone, M. & Ooi, J. Calibration of DEM models using rotating drum and confined compression measurements [C]. 6th World Congress on Particle Technology, Nuremberg, Germany, 2010.

Keishing, J. & Hanley, K. J. 2019. Improving constant-volume simulations of undrained behaviour in DEM. *Acta Geotechnica (Accepted)*.

Khouri, N. Q. 1984. *Dynamic properties of soils.* Syracuse University.

Kokusho, T. 2013. Liquefaction potential evaluations: energy-based method versus stress-based method. *Canadian Geotechnical Journal,* 50(10)**,** pp 1088-1099.

Konrad, J. 1993. Undrained response of loosely compacted sands during monotonic and cyclic compression tests. *Géotechnique,* 43(1)**,** pp 69-89.

Kruyt, N. P. & Rothenburg, L. Plasticity of Granular Materials: a Structural‐mechanics View. AIP conference proceedings, 2009. AIP, 1073-1076.

Kuhn, M. R., Renken, H. E., Mixsell, A. D. & Kramer, S. L. 2014. Investigation of cyclic liquefaction with discrete element simulations. *Journal of Geotechnical and Geoenvironmental Engineering,* 140(12)**,** pp 04014075.

Kuwano, R. 1999. The stiffness and yielding anisotropy of sand. *Ph. D. Thesis, Imperial College of Science, Technology and Medicine*.

Lade, P. V. & Duncan, J. M. 1973. Cubical triaxial tests on cohesionless soil. *Journal of Soil Mechanics & Foundations Div,* 99(SM10)**,** pp 793-812.

Lade, P. V. & Duncan, J. M. 1975. Elastoplastic stress-strain theory for cohesionless soil. *Journal of Geotechnical and Geoenvironmental Engineering,* 101(GT10)**,** pp 1037-1053.

Lade, P. V. & Pradel, D. 1990. Instability and plastic flow of soils. I: Experimental observations. *Journal of Engineering Mechanics,* 116(11)**,** pp 2532-2550.

Lade, P. V. & Yamamuro, J. A. 1997. Effects of nonplastic fines on static liquefaction of sands. *Canadian Geotechnical Journal,* 34(6)**,** pp 918-928.

Lamei, M. & Mirghasemi, A. A. 2011. A discrete element model for simulating saturated granular soil. *Particuology,* 9(6)**,** pp 650-658.

Law, K. T., Cao, Y. & He, G. 1990. An energy approach for assessing seismic liquefaction potential. *Canadian Geotechnical Journal,* 27(3)**,** pp 320-329.

Lee, G. & Hartmann, B. 1998. Specific damping capacity for arbitrary loss angle. *Journal of sound and vibration,* 211(2)**,** pp 265-272.

Lehane, B., Jardine, R., Bond, A. J. & Frank, R. 1993. Mechanisms of shaft friction in sand from instrumented pile tests. *Journal of Geotechnical Engineering,* 119(1)**,** pp 19-35.

Liang, L., Figueroa, J. L. & Saada, A. S. 1995. Liquefaction under random loading: unit energy approach. *Journal of Geotechnical Engineering,* 121(11)**,** pp 776-781.

Liu, G., Rong, G., Peng, J. & Zhou, C. 2015. Numerical simulation on undrained triaxial behavior of saturated soil by a fluid coupled-DEM model. *Engineering geology,* 193(256-266.

Luzzani, L. & MR, C. 2002. On the relationship between particle breakage and the critical state of sands. *Soils and Foundations,* 42(2)**,** pp 71-82.

Maeda, K., Sakai, H., Kondo, A., Yamaguchi, T., Fukuma, M. & Nukudani, E. 2010. Stress-chain based micromechanics of sand with grain shape effect. *Granular Matter,* 12(5)**,** pp 499-505.

Marketos, G. & Bolton, M. D. 2010. Flat boundaries and their effect on sand testing. *International Journal for numerical and analytical methods in geomechanics,* 34(8)**,** pp 821-837.

Matasović, N. & Vucetic, M. 1993. Cyclic characterization of liquefiable sands. *Journal of Geotechnical Engineering,* 119(11)**,** pp 1805-1822.

Mital, U. & Andrade, J. E. 2016. Mechanics of origin of flow liquefaction instability under proportional strain triaxial compression. *Acta Geotechnica,* 11(5)**,** pp 1015-1025.

Mohamad, R. & Dobry, R. 1986. Undrained monotonic and cyclic triaxial strength of sand. *Journal of Geotechnical Engineering,* 112(10)**,** pp 941-958.

Mulilis, J. P., Arulanandan, K., Mitchell, J. K., Chan, C. K. & Seed, H. B. 1977. Effects of sample preparation on sand liquefaction. *Journal of the Geotechnical Engineering Division,* 103(2)**,** pp 91-108.

Munjiza, A. 2004. *The combined finite-discrete element method*: Wiley Online Library.

Murthy, T., Loukidis, D., Carraro, J., Prezzi, M. & Salgado, R. 2007. Undrained monotonic response of clean and silty sands. *Géotechnique,* 57(3)**,** pp 273-288.

Nakata, A., Hyde, M., Hyodo, H. & Murata 1999. A probabilistic approach to sand particle crushing in the triaxial test. *Géotechnique,* 49(5)**,** pp 567-583.

Newland, P. & Allely, B. 1957. Volume changes in drained taixial tests on granular materials. *Géotechnique,* 7(1)**,** pp 17-34.

Newland, P. & Allely, B. 1959. Volume changes during undrained triaxial tests on saturated dilatant granular materials. *Géotechnique,* 9(4)**,** pp 174-182.

Ng, T.-T. 2009. Discrete element method simulations of the critical state of a granular material. *International Journal of Geomechanics,* 9(5)**,** pp 209-216.

Niemunis, A., Wichtmann, T. & Triantafyllidis, T. 2006. Long-term deformations in soils due to cyclic loading. *Modern Trends in Geomechanics.* Springer.

O'Sullivan, C. & Cui, L. 2009. Micromechanics of granular material response during load reversals: combined DEM and experimental study. *Powder Technology,* 193(3)**,** pp 289-302.

O'Sullivan, C. Advancing geomechanics using DEM. Proc. International Symposium on Geomechanics from Micro to Macro, 2014. 21-32.

Oda, M. 1972. Initial fabrics and their relations to mechanical properties of granular material. *Soils and Foundations,* 12(1)**,** pp 17-36.

Okada, N. & Nemat-Nasser, S. 1994. Energy dissipation in inelastic flow of saturated cohesionless granular media. *Géotechnique,* 44(1)**,** pp 1-19.

Otsubo, M., O'Sullivan, C., Hanley, K. J. & Sim, W. W. 2016. The influence of particle surface roughness on elastic stiffness and dynamic response.

Perez, J. L., Kwok, C., Huang, X. & Hanley, K. 2016. Assessing the quasi-static conditions for shearing in granular media within the critical state soil mechanics framework. *Soils and Foundations,* 56(1)**,** pp 152-159.

Pestana, J. 1994. A unified constitutive model for sands and clays. *ScD thesis*.

Plimpton, S. 1995. Fast parallel algorithms for short-range molecular dynamics. *Journal of computational physics,* 117(1)**,** pp 1-19.

Potyondy, D. O. & Cundall, P. 2004. A bonded-particle model for rock. *International journal of rock mechanics and mining sciences,* 41(8)**,** pp 1329-1364.

Prearo, C., Fioravante, V. & Mazzucato, A. 2015. *Determination of cyclic resistance of clean sands from cone penetration test based on state parameter.* Università degli Studi di Parma. Dipartimento di Ingegneria Civile ed Architettura.

Robertson, P., List, B. & Hofmann, B. 1995. CANLEX (Canadian Liquefaction Experiment): a one year update.

Roscoe, K. H., Schofield, A. & Wroth, C. 1958. On the yielding of soils. *Géotechnique,* 8(1)**,** pp 22-53.

Ross, P. J. & Ross, P. J. 1988. *Taguchi techniques for quality engineering: loss function, orthogonal experiments, parameter and tolerance design*: McGraw-Hill New York.

Salvati, L. & Anhdan, L. 2008. Rate-dependent response of dense sand in cyclic triaxial tests. *Soils and Foundations,* 48(3)**,** pp 447-451.

Satake, M. Fabric tensor in granular materials. IUTAM Conference on Deformation and Flow of Granular Materials, 1982, 1982. AA Balkema, 63-68.

Schofield, A. & Wroth, P. 1968. *Critical state soil mechanics*: McGraw-Hill London.

Seed, B. & Lee, K. L. 1966. Liquefaction of saturated sands during cyclic loading. *Journal of Soil Mechanics & Foundations Div,* 92(SM6)**,** pp 105-134.

Seed, H. B., Idriss, I. & Arango, I. 1983. Evaluation of liquefaction potential using field performance data. *Journal of Geotechnical Engineering,* 109(3)**,** pp 458-482.

Seed, H. B. & Idriss, I. M. 1971. Simplified procedure for evaluating soil liquefaction potential. *Journal of Soil Mechanics & Foundations Div*.

Seed, H. B., Wong, R. T., Idriss, I. & Tokimatsu, K. 1986. Moduli and damping factors for dynamic analyses of cohesionless soils. *Journal of Geotechnical Engineering,* 112(11)**,** pp 1016-1032.

Seed, R. B. SPT-based analysis of cyclic pore pressure and undrained residual soil strength. Proc., H. Boldon Seed Memorial Symp., University of California, Berkeley, 1990. 351-376.

Senetakis, K., Coop, M. R. & Todisco, M. 2013. Tangential load–deflection behaviour at the contacts of soil particles. *Géotechnique Letters,* 3(2)**,** pp 59-66.

Sherif, M. A., Ishibashi, I. & Gaddah, A. 1977. Damping ratio for dry sands. *Journal of Geotechnical and Geoenvironmental Engineering,* 103(GT7)**,** pp 743-756.

Simcock, K. J., Davis, R. O., Berrill, J. B. & Mullenger, G. 1983. Cyclic triaxial tests with continuous measurement of dissipated energy. *Geotechnical Testing Journal,* 6(1)**,** pp 35-39.

Sitharam, T. & Vinod, J. S. 2009. Critical state behaviour of granular materials from isotropic and rebounded paths: DEM simulations. *Granular matter,* 11(1)**,** pp 33-42.

Sitharam, T. & Vinod, J. S. 2010. Evaluation of shear modulus and damping ratio of granular materials using discrete element approach. *Geotechnical and Geological Engineering,* 28(5)**,** pp 591-601.

Suazo, G., Fourie, A., Doherty, J. & Hasan, A. 2016. Effects of confining stress, density and initial static shear stress on the cyclic shear response of fine-grained unclassified tailings. *Géotechnique,* 66(5)**,** pp 401-412.

Sze, H. & Yang, J. 2013. Failure modes of sand in undrained cyclic loading: impact of sample preparation. *Journal of Geotechnical and Geoenvironmental Engineering,* 140(1)**,** pp 152-169.

Taguchi, G. 1987. System of experimental design; engineering methods to optimize quality and minimize costs,

Tatsuoka, F., MAEDA, S., OCHI, K. & FUJII, S. 1986. Prediction of cyclic undrained strength of sand subjected to irregular loadings. *Soils and Foundations,* 26(2)**,** pp 73-90.

Taylor, D. 1948. *Fundamentals of soil mechanics*: Chapman And Hall, Limited.; New York.

Thornton, C. 2000. Numerical simulations of deviatoric shear deformation of granular media. *Géotechnique,* 50(1)**,** pp 43-53.

Thornton, C. & Randall, C. 1988. Applications of theoretical contact mechanics to solid particle system simulation. *Studies in Applied Mechanics.* Elsevier.

Tong, L. & Wang, Y. H. 2015. DEM simulations of shear modulus and damping ratio of sand with emphasis on the effects of particle number, particle shape, and aging. *Acta Geotechnica,* 10(1)**,** pp 117-130.

Towhata, I. & Ishihara, K. 1985. Shear work and pore water pressure in undrained shear. *Soils and foundations,* 25(3)**,** pp 73-84.

Trifunac, M. 1995. Empirical criteria for liquefaction in sands via standard penetration tests and seismic wave energy. *Soil Dynamics and Earthquake Engineering,* 14(6)**,** pp 419-426.

Tsuha, C. d. H. C., Foray, P., Jardine, R., Yang, Z., Silva, M. & Rimoy, S. 2012. Behaviour of displacement piles in sand under cyclic axial loading. *Soils and Foundations,* 52(3)**,** pp 393-410.

Uthayakumar, M. & Vaid, Y. 1998. Static liquefaction of sands under multiaxial loading. *Canadian Geotechnical Journal,* 35(2)**,** pp 273-283.

Vaid, Y. & Chern, J. Cyclic and monotonic undrained response of saturated sands. Advances in the art of testing soils under cyclic conditions, 1985. ASCE, 120-147.

Vaid, Y. & Sivathayalan, S. 2000. Fundamental factors affecting liquefaction susceptibility of sands. *Canadian Geotechnical Journal,* 37(3)**,** pp 592-606.

Verdugo, R. & Ishihara, K. 1996. The steady state of sandy soils. *Soils and Foundations,* 36(2)**,** pp 81-91.

Vucetic, M. & Dobry, R. 1991. Effect of soil plasticity on cyclic response. *Journal of geotechnical engineering,* 117(1)**,** pp 89-107.

Wanatowski, D. 2007. Undrained instability of loose sand under plane-strain conditions and its engineering application. *Foundations of Civil and Environmental Engineering,* 10(1)**,** pp 131-141.

Wang, J. & Yan, H. 2012. DEM analysis of energy dissipation in crushable soils. *Soils and Foundations,* 52(4)**,** pp 644-657.

Wang, J. N. 1989. Pore pressure development during non-uniform cyclic loading. *Soils and Foundations,* 29(2)**,** pp 1-14.

Wichtmann, T. 2005. *Explicit accumulation model for non-cohesive soils under cyclic loading.* Inst. für Grundbau und Bodenmechanik Bochum University, Germany.

Wichtmann, T., Niemunis, A. & Triantafyllidis, T. 2010. Strain accumulation in sand due to drained cyclic loading: on the effect of monotonic and cyclic preloading (Miner's rule). *Soil Dynamics and Earthquake Engineering,* 30(8)**,** pp 736-745.

Wichtmann, T. & Triantafyllidis, T. 2009. Influence of the grain-size distribution curve of quartz sand on the small strain shear modulus G max. *Journal of Geotechnical and Geoenvironmental Engineering,* 135(10)**,** pp 1404-1418.

Wood, D. M. 1990. *Soil behaviour and critical state soil mechanics*: Cambridge university press.

Xia, H. & Hu, T. 1991. Effects of saturation and back pressure on sand liquefaction. *Journal of Geotechnical Engineering,* 117(9)**,** pp 1347-1362.

Yamada, Y. & Ishihara, K. 1983. Undrained deformation characteristics of sand in multi-directional shear. *Soils and Foundations,* 23(1)**,** pp 61-79.

Yamamuro, J. A. & Lade, P. V. 1998. Steady-state concepts and static liquefaction of silty sands. *Journal of geotechnical and geoenvironmental engineering,* 124(9)**,** pp 868-877.

Yan, W. & Dong, J. 2011. Effect of particle grading on the response of an idealized granular assemblage. *International Journal of Geomechanics,* 11(4)**,** pp 276-285.

Yang, J. 2005. Pore pressure coefficient for soil and rock and its relation to compressional wave velocity. *Géotechnique,* 55(3)**,** pp 251-256.

Yang, J. & Luo, X. 2015. Exploring the relationship between critical state and particle shape for granular materials. *Journal of the Mechanics and Physics of Solids,* 84(196-213.

Yang, J. & Sato, T. 2000. Interpretation of seismic vertical amplification observed at an array site. *Bulletin of the Seismological Society of America,* 90(2)**,** pp 275-285.

Yang, J. & Sze, H. 2011. Cyclic behaviour and resistance of saturated sand under non-symmetrical loading conditions. *Géotechnique,* 61(1)**,** pp 59-73.

Yang, J. & Wei, L. 2012. Collapse of loose sand with the addition of fines: the role of particle shape. *Géotechnique,* 62(12)**,** pp 1111-1125.

Yimsiri, S. & Soga, K. 2002. Application of micromechanics model to study anisotropy of soils at small strains. *Soils and Foundations,* 42(5)**,** pp 15-26.

Yimsiri, S. & Soga, K. 2010. DEM analysis of soil fabric effects on behaviour of sand. *Géotechnique,* 60(6)**,** pp 483-495.

Yoon, J. 2007. Application of experimental design and optimization to PFC model calibration in uniaxial compression simulation. *International Journal of Rock Mechanics and Mining Sciences,* 44(6)**,** pp 871-889.

Yoshimine, M. & Ishihara, K. 1998. Flow potential of sand during liquefaction. *Soils and Foundations,* 38(3)**,** pp 189-198.

Yoshimine, M., Ishihara, K. & Vargas, W. 1998. Effects of principal stress direction and intermediate principal stress on undrained shear behavior of sand. *Soils and Foundations,* 38(3)**,** pp 179-188.

Zamani, N. & El Shamy, U. 2012. Discrete-element method simulations of the response of soil-foundation-structure systems to multidirectional seismic motion. *International Journal of Geomechanics,* 13(5)**,** pp 595-610.

Zhang, W., Wang, J. & Jiang, M. 2013. DEM-aided discovery of the relationship between energy dissipation and shear band formation considering the effects of particle rolling resistance. *Journal of Geotechnical and Geoenvironmental Engineering,* 139(9)**,** pp 1512-1527.

Zhao, J. & Shan, T. 2013. Coupled CFD–DEM simulation of fluid–particle interaction in geomechanics. *Powder Technology,* 239(1)**,** pp 248-258.

Appendix A

Table A.1: Summary for CV monotonic undrained simulations at CS with simplified Hertz-Mindlin contact model and periodic boundaries for sand specimens using LAMMPS

Simulation ID	μ_0	$\sigma'_{3,0}$ (kPa)	$\sigma'_{1,0}$ (kPa)	e	I_{ss}	q (kPa)	p' (kPa)	*ASR* (degree)	*Stress ratio*	Z	Z_m	O_p (%)
D1	0.00	150	150	0.3940	0.00	68784.25	95257.86	18.79	0.72	4.97	5.89	3.13
D2	0.05*	150	200	0.3939	0.30	68571.72	94770.26	18.83	0.72	4.98	5.88	3.14
D3	0.06*	150	250	0.3960	0.55	65159.94	89344.49	18.97	0.73	4.95	5.87	3.08
D4	0.00	300	300	0.3926	0.00	69936.01	95682.04	19.01	0.73	5.00	5.88	3.18
D5	0.00	300	350	0.3902	0.16	70662.79	98550.88	18.67	0.72	5.03	5.91	3.24
D6	0.00	300	400	0.3882	0.30	77237.01	105608.1	19.02	0.73	5.04	5.94	3.34
D7	0.00	500	500	0.3912	0.00	72543.11	97599.62	19.31	0.74	5.02	5.91	3.28
D8	0.00	500	550	0.3898	0.10	73656.61	102162.5	18.77	0.72	5.04	5.91	3.31
D9	0.01*	500	600	0.3913	0.19	72885.12	99126.94	19.11	0.73	5.01	5.91	3.22
MD1	0.08	150	150	0.4395	0.00	12972.92	17992.52	18.77	0.72	4.01	5.37	1.14
MD2	0.08	150	200	0.4321	0.30	20285.32	28091.87	18.80	0.72	4.23	5.48	1.52
MD3	0.22*	150	250	0.4393	0.55	12350.92	16993.74	18.91	0.73	3.99	5.37	1.16
MD4	0.08	300	300	0.4392	0.00	14108.51	19363.40	18.95	0.73	4.02	5.39	1.20
MD5	0.08	300	350	0.4361	0.16	16054.81	22124.69	18.88	0.73	4.07	5.42	1.31
MD6	0.08	300	400	0.4323	0.30	20424.05	28569.73	18.62	0.71	4.22	5.49	1.52
MD7	0.08	500	500	0.4383	0.00	15720.23	21437.15	19.07	0.73	4.07	5.42	1.33
MD8	0.08	500	550	0.4373	0.10	15419.91	21090.63	19.02	0.73	4.08	5.43	1.32
MD9	0.08	500	600	0.4348	0.19	17726.91	24349.55	18.93	0.73	4.13	5.45	1.39
L1	0.16	150	150	0.4601	0.00	Liquefied						
L2	0.16	150	200	0.4523	0.30	3675.94	5068.35	18.88	0.72	3.56	5.13	0.52
L3	0.18*	150	250	0.4481	0.55	6179.79	8521.98	18.87	0.72	3.71	5.22	0.73
L4	0.16	300	300	0.4598	0.00	Liquefied						

Simulation ID	μ_0	$\sigma'_{3,0}$ (kPa)	$\sigma'_{1,0}$ (kPa)	e	I_{ss}	q (kPa)	p' (kPa)	*ASR* (degree)	*Stress ratio*	Z	Z_m	O_p (%)
L5	0.16	300	350	0.4590	0.16	Liquefied						
L6	0.16	300	400	0.4527	0.30	3104.92	4328.94	18.68	0.72	3.52	5.12	0.48
L7	0.16	500	500	0.4597	0.00	Liquefied						
L8	0.16	500	550	0.4594	0.10	Liquefied						
L9	0.16	500	600	0.4579	0.19	Liquefied						
* Friction coefficient μ_0 increased to get desired I_{ss}												

Table A.2: Summary for CV monotonic undrained simulations with/without rotational resistance at CS: simplified Hertz-Mindlin contact model and periodic boundaries for sand specimens using LAMMPS

Simulation ID	$\sigma'_{3,0}$ (kPa)	κ	e	q (kPa)	p' (kPa)	*ASR (degree)*	*Stress ratio*	Z
D1	150	-	0.3940	68784.25	95257.86	18.79	0.72	4.97
DR1	150	0.1	0.3916	127947.8	128050.2	25.36	0.99	4.93
DR2	150	0.3	0.3916	113009.9	112135.6	25.56	1.00	4.96
DR3	150	0.5	0.3916	109386.3	110301.0	25.18	0.99	5.00

Appendix B

The change in sample volume, ΔV_{total}, during shearing at every time-step is given by Eq. 4.6, which is based on a discontinuous jump from time-step t to time-step $t + \Delta t$. However, when Δt is divided into infinitely many smaller time increments, the required volume change is smaller than the original volume, ΔV_{total}. Consider, for example, the case where Δt is divided into 3 increments ($q_{inc} = 3$), as illustrated in Fig. 4.16. The black line on Fig. 4.16 shows the stress profile for the application of $\Delta\sigma_3'$ in one step at $t + \Delta t$, assuming a linear profile on the figure, with the corresponding volume change on the lower figure. The green line is for a similar situation in which $\Delta\sigma_3'$ is applied in three smaller increments.

Let $\propto = \frac{\eta V_{total}}{K_f}$ and assume this term is constant throughout the time-step (valid as $\Delta V_{total} \ll V_{total}$). By using Eq. 4.4 and the definition of K_f (Eq. 4.5), α can be written as:

$$\propto = \frac{\Delta V_s}{\Delta\sigma_3'} \tag{B.1}$$

The volume change, ΔV_1, at point (a) calculated using $\sigma_{3,a}'$ is equal to

$$\Delta V_1 = \propto \left(\frac{\Delta\sigma_3'}{3}\right)$$

The volume change, ΔV_2, at point (b) calculated using $\sigma_{3,b}'$ is equal to

$$\Delta V_2 = \propto \left(\frac{\Delta\sigma_3'}{3} - X_1\right) \tag{B.2}$$

where $\left(\frac{\Delta\sigma_3'}{3} - X_1\right)$ is the stress difference $(\sigma_{3,b}' - \sigma_{3,a}')$. Similarly,

$$\Delta V_3 = \propto \left(\frac{\Delta\sigma_3'}{3} - X_2\right) \tag{B.3}$$

X_1 and X_2 therefore represent the drops in σ_3' that result when ΔV_1 and ΔV_2 are added, respectively.

$$X_1 = \frac{\Delta V_1}{\propto}$$

$$X_2 = \frac{\Delta V_2}{\propto}$$

Substituting X_1 and X_2 into Eq. B.2 and Eq. B.3, respectively, we get

$$\Delta V_2 = 0$$

$$\Delta V_3 = \propto \left(\frac{\Delta \sigma_3'}{3}\right)$$

The total volume change over the time-step Δt is obtained by summation: $\Delta V_1 + \Delta V_2 + \Delta V_3 = \frac{2\Delta\sigma_3'}{3}$. When $q_{inc} = 3$, the required volume change is thus $\frac{2}{3}$ of the original volume increment, ΔV. When $q_{inc} = 4$, the volume change is equal to $\propto \left(\frac{\Delta\sigma_3'}{2}\right)$. For $q_{inc} = 5$, the volume change is equal to $\propto \left(\frac{3\Delta\sigma_3'}{5}\right)$. For odd numbers of increments (q), the total volume change is

$$\Delta V_* = \propto \left(\frac{\Delta \sigma_3'}{q}\right)$$

For even numbers of increments, the total volume change is

$$\Delta V_* = 0$$

As $q_{inc} \rightarrow \infty$, it is straightforward to show that the total required volume change is equal to

$$\sum \Delta V_i \rightarrow \propto \left(\frac{\Delta \sigma_3'}{2}\right)$$

This is half of the ΔV_{total} assuming a discontinuous jump from time-step t to time-step $t + \Delta t$. This volume increment for a continuous time scenario was implemented in the code.

Appendix C

This appendix contains the L_{27} orthogonal array used for the Taguchi experimental design in Chapter 5 of this thesis, shown in Section (C.1). The corresponding triangular table is provided in Section (C.2) which identifies the pairs of columns containing interactions between three-level factors.

C.1 Orthogonal array

The standard L_{27} orthogonal array below denotes the factor levels as 1, 2 and 3. Number 1 represents the lowest setting of the factor. For further detail, the reader is directed to (Ross and Ross, 1988).

Table C.1: Standard form of the L_{27} orthogonal array (Ross and Ross, 1988)

Row	Column												
	1	2	3	4	5	6	7	8	9	10	11	12	13
1	1	1	1	1	1	1	1	1	1	1	1	1	1
2	1	1	1	1	2	2	2	2	2	2	2	2	2
3	1	1	1	1	3	3	3	3	3	3	3	3	3
4	1	2	2	2	1	1	1	2	2	2	3	3	3
5	1	2	2	2	2	2	2	3	3	3	1	1	1
6	1	2	2	2	3	3	3	1	1	1	2	2	2
7	1	3	3	3	1	1	1	3	3	3	2	2	2
8	1	3	3	3	2	2	2	1	1	1	3	3	3
9	1	3	3	3	3	3	3	2	2	2	1	1	1
10	2	1	2	3	1	2	3	1	2	3	1	2	3
11	2	1	2	3	2	3	1	2	3	1	2	3	1
12	2	1	2	3	3	1	2	3	1	2	3	1	2
13	2	2	3	1	1	2	3	2	3	1	3	1	2
14	2	2	3	1	2	3	1	3	1	2	1	2	3
15	2	2	3	1	3	1	2	1	2	3	2	3	1
16	2	3	1	2	1	2	3	3	1	2	2	3	1
17	2	3	1	2	2	3	1	1	2	3	3	1	2
18	2	3	1	2	3	1	2	2	3	1	1	2	3
19	3	1	3	2	1	3	2	1	3	2	1	3	2
20	3	1	3	2	2	1	3	2	1	3	2	1	3
21	3	1	3	2	3	2	1	3	2	1	3	2	1
22	3	2	1	3	1	3	2	2	1	3	3	2	1
23	3	2	1	3	2	1	3	3	2	1	1	3	2
24	3	2	1	3	3	2	1	1	3	2	2	1	3
25	3	3	2	1	1	3	2	3	2	1	2	1	3
26	3	3	2	1	2	1	3	1	3	2	3	2	1
27	3	3	2	1	3	2	1	2	1	3	1	3	2

C.2 Triangular table

The triangular table below shows the columns where any interaction between factors is contained. For identifying the confounding effects, one number (first factor) from

the top row of the column is read and the other (second factor) from the left-most column of the table. For example, the interaction between the factors in columns 1 and 2 of an L_{27} array is distributed between columns 3 and 4 and the interaction between columns 4 and 7 of an L_{27} array is contained in columns 9 and 11 as shown in Table C.2. For further detail, the reader is directed to (Ross and Ross, 1988).

Table C.2: Triangular table for the L_{27} orthogonal array (Ross and Ross, 1988)

I	Column												
	1	2	3	4	5	6	7	8	9	10	11	12	13
1		3 4	2 4	2 3	6 7	5 7	5 6	9 10	8 10	8 9	12 13	11 13	11 12
2			1 4	1 3	8 11	9 12	10 13	5 11	6 12	7 13	5 8	6 9	7 10
3				1 2	9 13	10 11	8 12	7 12	5 13	6 11	6 10	7 8	5 9
4					10 12	8 13	9 11	6 13	7 11	5 12	7 9	5 10	6 8
5						1 7	1 6	2 11	3 13	4 12	2 8	4 10	3 9
6							1 5	4 13	2 12	3 11	3 10	2 9	4 8
7								3 12	4 11	2 13	4 9	3 8	2 10
8									1 10	1 9	2 5	3 7	4 6
9										1 8	4 7	2 6	3 5
10											3 6	4 5	2 7
11												1 13	1 12
12													1 11

Table C.3: Summary for mean effective stress ratio (SR) and coordination number (Z) responses at the end of 1 and 9 cycle under undrained triaxial cyclic loading.

Row	q_{cyc} (kPa)	q_{mean} (kPa)	Freq. f (Hz)	e	$\sigma'_{3,0}$ (kPa)	CSR	$\frac{\Delta p'}{p'_0}$ (%) at end of 1 cycle	$\frac{\Delta p'}{p'_0}$ (%) at end of 9 cycles	Z at end of 1 cycle	Z at end of 9 cycles	Comment
1	40	0	2	0.39	150	0.267	0.059667	0.231259	5.517	5.489	
2	40	0	4	0.42	300	0.133	-0.02083	0.007021	4.761	4.759	
3	40	0	6	0.45	500	0.080	-0.04436	0.008669	4.293	4.290	
4*	40	50	2	0.42	300	0.126	-0.00666	0.26743	4.792	4.782	*
5*	40	50	4	0.45	500	0.077	-0.02675	0.100822	4.309	4.305	*
6*	40	50	6	0.39	150	0.240	-0.0174	0.326165	5.405	5.394	*
7*	40	100	2	0.45	500	0.075	-0.01543	0.25253	4.327	4.321	*
8*	40	100	4	0.38	150	0.218	-0.07555	0.556958	5.051	5.040	*
9*	40	100	6	0.42	300	0.120	-0.01377	0.31303	4.786	4.782	*
10	80	0	2	0.39	300	0.267	0.047867	0.231243	5.723	5.699	
11	80	0	4	0.42	500	0.160	-0.02964	0.008395	4.964	4.959	
12	80	0	6	0.45	150	0.533	-100 (L)	L	0 (L)	L	Liquefaction at 1 cycle
13	80	50	2	0.42	500	0.155	-0.01225	0.231035	4.980	4.971	
14	80	50	4	0.45	150	0.480	-100 (L)	L	0 (L)	L	Liquefaction at 1 cycle
15	80	50	6	0.38	300	0.253	-0.05378	0.18539	5.751	5.742	
16*	80	100	2	0.45	150	0.436	-0.26307	0.92312	3.748	3.705	*
17*	80	100	4	0.39	300	0.240	-0.01206	0.312625	5.629	5.620	*
18*	80	100	6	0.42	500	0.150	-0.01166	0.203754	4.986	4.982	*
19	120	0	2	0.38	500	0.240	0.03242	0.20811	5.902	5.879	
20	120	0	4	0.42	150	0.800	-4.48393	L	4.059	L	Liquefaction at 6 cycle
21	120	0	6	0.45	300	0.400	-7.51113	L	4.007	L	Liquefaction at 5 cycle
22	120	50	2	0.42	150	0.720	-4.1634	0.923314	4.240	3.763	
23	120	50	4	0.45	300	0.379	-8.63902	L	4.008	L	Liquefaction at 5 cycle
24	120	50	6	0.39	500	0.232	-0.00906	0.122003	5.922	5.917	

Row	q_{cyc} (kPa)	q_{mean} (kPa)	Freq. f (Hz)	e	$\sigma'_{3,0}$ (kPa)	*CSR*	$\frac{\Delta p'}{p'_0}$ *(%) at end of 1 cycle*	$\frac{\Delta p'}{p'_0}$ *(%) at end of 9 cycles*	*Z at end of 1 cycle*	*Z at end of 9 cycles*	Comment
25	120	100	2	0.45	300	0.360	-12.0761	L	3.874	L	Liquefaction at 4 cycle
26	120	100	4	0.38	500	0.225	-0.03994	0.199313	5.915	5.912	
27	120	100	6	0.42	150	0.655	-4.60871	0.61504	4.055	3.924	
Asterisk * denoted one-way cyclic where $q_{cyc} < q_{mean}$ and liquefaction occurred during the cyclic shearing is denoted capital letter L and number (no of cyclic when liquefaction occurred)											

Table C.4: Summary for damping ratio (DR) and shear modulus (G) responses at the end of 1 and 9 cycles under undrained triaxial cyclic loading

Row	q_{cyc} (kPa)	q_{mean} (kPa)	Freq. f (Hz)	e	$\sigma'_{3,0}$ (kPa)	*CSR*	G (kPa) at end of 1 cycle	G (kPa) at end of 9 cycles	D at end of 1 cycle	D at end of 9 cycles	Comment
1	40	0	2	0.39	150	0.267	41148.94	41931.06	0.050935	0.045135	
2	40	0	4	0.42	300	0.133	48408.77	48848.3	0.017898	0.014485	
3	40	0	6	0.45	500	0.080	49809.27	50666.78	0.012298	0.006361	
4*	40	50	2	0.42	300	0.126	50560.72	50577.14	0.016916	0.01516	*
5*	40	50	4	0.45	500	0.077	51838.9	51685.36	0.007989	0.006404	*
6*	40	50	6	0.38	150	0.240	45826.09	45411.5	0.034337	0.03515	*
7*	40	100	2	0.45	500	0.075	52657.42	52459.3	0.008509	0.006729	*
8*	40	100	4	0.39	150	0.218	44122.91	43822.54	0.037607	0.03774	*
9*	40	100	6	0.42	300	0.120	50905.06	51004.72	0.018559	0.016555	*
10	80	0	2	0.38	300	0.267	54386.82	55352.54	0.050173	0.044768	
11	80	0	4	0.42	500	0.160	59516.32	60227.12	0.022814	0.018384	
12	80	0	6	0.45	150	0.533	0 (L)	L	0.333 (L)	L	Liquefaction at 1 cycle
13	80	50	2	0.42	500	0.155	61853.65	61818.38	0.020045	0.018235	
14	80	50	4	0.45	150	0.480	0 (L)	L	0.333 (L)	L	Liquefaction at 1 cycle
15	80	50	6	0.39	300	0.253	59194.07	59891.42	0.040842	0.036734	
16*	80	100	2	0.45	150	0.436	5797.411	4401.682	0.052936	0.045105	*
17*	80	100	4	0.38	300	0.240	60629.93	60115.6	0.035502	0.033646	*
18*	80	100	6	0.42	500	0.150	62616.79	62581.52	0.020432	0.018489	*
19	120	0	2	0.39	500	0.240	69285.65	70018.77	0.038839	0.03525	
20	120	0	4	0.42	150	0.800	9356.754	L	0.318078	L	Liquefaction at 6 cycle
21	120	0	6	0.45	300	0.400	19952.65	L	0.203208	L	Liquefaction at 5 cycle
22	120	50	2	0.42	150	0.720	9224.85	2330.668	0.150189	0.103277	
23	120	50	4	0.45	300	0.379	11135.42	L	0.071259	L	Liquefaction at 5 cycle
24	120	50	6	0.38	500	0.232	72449.91	73133.63	0.035163	0.031937	
25	120	100	2	0.45	300	0.360	5075.741	L	0.039409	L	Liquefaction at 4 cycle

Row	q_{cyc} (kPa)	q_{mean} (kPa)	Freq. f (Hz)	e	$\sigma'_{3,0}$ (kPa)	*CSR*	G (kPa) at end of 1 cycle	G (kPa) at end of 9 cycles	D at end of 1 cycle	D at end of 9 cycles	Comment
26	120	100	4	0.39	500	0.225	75544.05	76078.14	0.031074	0.028306	
27	120	100	6	0.42	150	0.655	8543.567	6772.331	0.114295	0.096496	
Asterisk * denoted one-way cyclic where $q_{cyc} < q_{mean}$ and liquefaction occurred during the cyclic shearing is denoted capital letter L and number (no of cyclic when liquefaction occurred)											

Table C.5: Summary for mean effective stress ratio (ESR) at the end of each cycle under undrained triaxial cyclic loading

Row	q_{cyc} (kPa)	q_{mean} (kPa)	Freq. f (Hz)	e	$\sigma'_{3,0}$ (kPa)	Mean effective stress ratio (ESR) in (%) at the end each cycle									
						Cycles									
						1	2	3	4	5	6	7	8	9	10
1	40	0	2	0.38	150	0.059667	0.059867	0.0602	0.060333	0.060533	0.0604	0.060667	0.0606	0.0608	0.060867
2	40	0	4	0.42	300	-0.02083	-0.027	-0.03043	-0.03287	-0.03477	-0.0363	-0.0377	-0.03887	-0.03997	-0.04097
3	40	0	6	0.45	500	-0.04436	-0.05464	-0.0599	-0.0635	-0.06632	-0.06864	-0.07066	-0.07244	-0.07402	-0.07552
4*	40	50	2	0.42	300	-0.00666	-0.00906	-0.01036	-0.01121	-0.01191	-0.01247	-0.01285	-0.01317	-0.01352	-0.01371
5*	40	50	4	0.45	500	-0.02675	-0.03271	-0.03606	-0.03848	-0.04039	-0.04208	-0.04351	-0.04479	-0.04595	-0.04705
6*	40	50	6	0.39	150	-0.0174	-0.0162	-0.01602	-0.0162	-0.01638	-0.01686	-0.01692	-0.01716	-0.01728	-0.01734
7*	40	100	2	0.45	500	-0.01543	-0.02001	-0.02263	-0.02453	-0.02606	-0.02734	-0.02843	-0.02936	-0.03023	-0.03094
8*	40	100	4	0.38	150	-0.07555	-0.06147	-0.05302	-0.04636	-0.04025	-0.03447	-0.02913	-0.02378	-0.01898	-0.01407
9*	40	100	6	0.42	300	-0.01377	-0.01536	-0.01677	-0.018	-0.01905	-0.0201	-0.02103	-0.02202	-0.02295	-0.02388
10	80	0	2	0.39	300	0.047867	0.0455	0.0517	0.065467	0.086133	0.112533	0.142067	0.174067	0.20506	0.234033
11	80	0	4	0.42	500	-0.02964	-0.0395	-0.04522	-0.04928	-0.05258	-0.0551	-0.05748	-0.05964	-0.0615	-0.06328
12	80	0	6	0.45	150	-100 (L)									
13	80	50	2	0.42	500	-0.01225	-0.01765	-0.02102	-0.0234	-0.02537	-0.02696	-0.02841	-0.02955	-0.03058	-0.03155
14	80	50	4	0.45	150	-100 (L)									
15	80	50	6	0.38	300	-0.05378	-0.05419	-0.05454	-0.05466	-0.05482	-0.05498	-0.05504	-0.05523	-0.05542	-0.05529
16*	80	100	2	0.45	150	-0.26307	-1.29922	-2.22322	-2.93138	-4.01847	-4.91356	-5.97044	-6.51338	-7.81435	-8.51837
17*	80	100	4	0.39	300	-0.01206	-0.00912	-0.0072	-0.00537	-0.00348	-0.00159	0.00036	0.00228	0.0042	0.00636
18*	80	100	6	0.42	500	-0.01166	-0.01571	-0.01845	-0.02049	-0.02224	-0.02376	-0.02516	-0.02642	-0.02768	-0.02882
19	120	0	2	0.38	500	0.03242	0.0341	0.04168	0.05478	0.07276	0.09432	0.11866	0.14352	0.16786	0.18952
20	120	0	4	0.42	150	-4.48393	-15.4535	-28.9319	-51.8153	-78.9481	L6				
21	120	0	6	0.45	300	-7.51113	-14.4327	-22.5332	-36.1375	L5					
22	120	50	2	0.42	150	-4.1634	-6.95274	-10.1006	-13.9546	-18.6392	-24.8196	-33.0588	-43.7465	-55.604	-61.749
23	120	50	4	0.45	300	-8.63902	-15.0439	-24.119	-47.8067	L5					
24	120	50	6	0.39	500	-0.00906	-0.00921	-0.00933	-0.0096	-0.00962	-0.00977	-0.00985	-0.00999	-0.00999	-0.0101
25	120	100	2	0.45	300	-12.0761	-25.6021	-56.9997	L4						
26	120	100	4	0.38	500	-0.03994	-0.03862	-0.03722	-0.03581	-0.03427	-0.0327	-0.03114	-0.02961	-0.02805	-0.02644
27	120	100	6	0.42	150	-4.60871	-4.59398	-5.08156	-5.7684	-6.05749	-6.31015	-6.40707	-7.05049	-8.1828	-9.31091

Asterisk * denoted one-way cyclic where $q_{cyc} < q_{mean}$ and liquefaction occurred during the cyclic shearing is denoted capital letter L and number (no of cyclic when liquefaction occurred)

Table C.6: Summary for coordination number (Z) at the end of each cycle under undrained triaxial cyclic loading

Row	q_{cyc} (kPa)	q_{mean} (kPa)	Freq. f (Hz)	e	$\sigma'_{3,0}$ (kPa)	Coordination number (Z) at the end each cycle									
						Cycles									
						1	2	3	4	5	6	7	8	9	10
1	40	0	2	0.39	150	5.517	5.512	5.509	5.504	5.501	5.500	5.495	5.493	5.489	5.489
2	40	0	4	0.42	300	4.761	4.761	4.761	4.760	4.761	4.761	4.760	4.759	4.759	4.759
3	40	0	6	0.45	500	4.293	4.293	4.292	4.291	4.291	4.291	4.290	4.289	4.290	4.290
4*	40	50	2	0.42	300	4.792	4.790	4.788	4.789	4.787	4.785	4.784	4.783	4.782	4.781
5*	40	50	4	0.45	500	4.309	4.308	4.307	4.307	4.307	4.307	4.308	4.307	4.305	4.305
6*	40	50	6	0.39	150	5.405	5.401	5.401	5.399	5.398	5.397	5.396	5.395	5.394	5.394
7*	40	100	2	0.45	500	4.327	4.325	4.326	4.326	4.326	4.325	4.324	4.323	4.321	4.320
8*	40	100	4	0.39	150	5.051	5.048	5.048	5.046	5.045	5.043	5.043	5.042	5.040	5.040
9*	40	100	6	0.42	300	4.786	4.786	4.784	4.783	4.783	4.783	4.782	4.782	4.782	4.782
10	80	0	2	0.39	300	5.723	5.720	5.719	5.716	5.713	5.708	5.705	5.702	5.699	5.697
11	80	0	4	0.42	500	4.964	4.962	4.962	4.962	4.961	4.961	4.960	4.960	4.959	4.959
12	80	0	6	0.45	150	0 (L)									
13	80	50	2	0.42	500	4.980	4.979	4.977	4.977	4.975	4.973	4.973	4.971	4.971	4.970
14	80	50	4	0.45	150	0 (L)									
15	80	50	6	0.39	300	5.751	5.747	5.745	5.744	5.744	5.744	5.743	5.742	5.742	5.741
16*	80	100	2	0.45	150	3.748	3.711	3.708	3.706	3.714	3.718	3.715	3.721	3.705	3.702
17*	80	100	4	0.39	300	5.629	5.625	5.624	5.622	5.622	5.622	5.621	5.620	5.620	5.619
18*	80	100	6	0.42	500	4.986	4.986	4.985	4.986	4.984	4.985	4.983	4.984	4.982	4.984
19	120	0	2	0.39	500	5.902	5.900	5.896	5.893	5.890	5.887	5.885	5.880	5.879	5.878
20	120	0	4	0.42	150	4.059	3.867	3.687	3.482	3.171	L6				
21	120	0	6	0.45	300	4.007	3.935	3.849	3.704	L5					
22	120	50	2	0.42	150	4.240	4.152	4.081	4.039	3.972	3.922	3.865	3.811	3.763	3.758
23	120	50	4	0.45	300	4.008	3.934	3.838	3.582	L5					
24	120	50	6	0.39	500	5.922	5.920	5.920	5.919	5.920	5.918	5.918	5.917	5.917	5.916

Row	q_{cyc} (kPa)	q_{mean} (kPa)	Freq. f (Hz)	e	$\sigma'_{3,0}$ (kPa)	Coordination number (Z) at the end each cycle									
						Cycles									
						1	2	3	4	5	6	7	8	9	10
25	120	100	2	0.45	300	3.874	3.707	3.552	L4						
26	120	100	4	0.39	500	5.915	5.913	5.913	5.913	5.912	5.911	5.912	5.911	5.912	5.911
27	120	100	6	0.42	150	4.055	4.016	4.003	4.005	3.985	3.983	3.968	3.942	3.924	3.931
Asterisk * denoted one-way cyclic where $q_{cyc} < q_{mean}$ and liquefaction occurred during the cyclic shearing is denoted capital letter L and number (no of cyclic when liquefaction occurred)															

Table C.7: Summary for shear modulus (kPa) at the end of each cycle under undrained triaxial cyclic loading

Row	q_{cyc} (kPa)	q_{mean} (kPa)	Freq. f (Hz)	e	$\sigma'_{3,0}$ (kPa)	Shear modulus (kPa) at the end each cycle									
						Cycles									
						1	2	3	4	5	6	7	8	9	10
1	40	0	2	0.39	150	41148.94	41925.93	41965.74	41971.21	41968.53	41963.62	41958.05	41941.83	41931.06	41922.04
2	40	0	4	0.42	300	48408.77	48873.1	48882.52	48886.39	48880.6	48872.09	48863.75	48856.98	48848.3	48841.93
3	40	0	6	0.45	500	49809.27	50647.5	50683.65	50690.36	50689.45	50685.1	50679.93	50674.85	50666.78	50661.93
4*	40	50	2	0.42	300	50560.72	50712.67	50691.82	50665.32	50651.27	50630.73	50612.41	50594.45	50577.14	50559.46
5*	40	50	4	0.45	500	51838.9	51880.028	51837.19	51800.27	51768.96	51745.69	51723.11	51701.85	51685.36	51664.11
6*	40	50	6	0.39	150	45826.09	45838.48	45751	45679.45	45615.13	45558	45510.26	45463.37	45411.5	45364.59
7*	40	100	2	0.45	500	52657.42	52687.886	52636.51	52596.66	52562.68	52528.55	52505.74	52479.6	52459.3	52437.35
8*	40	100	4	0.39	150	44122.91	44258.4	44180.45	44107.73	44041.1	43980.44	43928.97	43874.9	43822.54	43780.3
9*	40	100	6	0.42	300	50905.06	51111.5	51103.01	51087.62	51070.89	51048.6	51037.42	51023.13	51004.72	50993.21
10	80	0	2	0.39	300	54386.82	55337.47	55389.76	55397.74	55391.9	55382.9	55379.1	55363.23	55352.54	55334.34
11	80	0	4	0.42	500	59516.32	60263.04	60285.66	60286	60274.03	60263	60252.83	60237.24	60227.12	59516.32
12	80	0	6	0.45	150	0 (L)									
13	80	50	2	0.42	500	61853.65	62022.89	61990.68	61951.18	61922.52	61893.29	61867.42	61840.22	61818.38	61795.66
14	80	50	4	0.45	150	0 (L)									
15	80	50	6	0.39	300	59194.07	59947.19	59977.97	59972.8	59964.24	59946.15	59923.8	59905.52	59891.42	59870.35
16*	80	100	2	0.45	150	5797.411	6362.861	6461.878	6643.416	6599.566	6429.065	6293.479	5241.564	4401.682	3812.23

Row	q_{cyc} (kPa)	q_{mean} (kPa)	Freq. f (Hz)	e	$\sigma'_{3,0}$ (kPa)	Shear modulus (kPa) at the end each cycle									
						Cycles									
						1	2	3	4	5	6	7	8	9	10
17*	80	100	4	0.39	300	60629.93	60622.29	60516.06	60429.76	60354.07	60289.36	60226.12	60168.36	60115.6	60061.91
18*	80	100	6	0.42	500	62616.79	62800.66	62764.33	62726.74	62696.09	62666.34	62636.61	62608.01	62581.52	62556.72
19	120	0	2	0.39	500	69285.65	70082.92	70108.59	70103.23	70086.8	70070.21	70055.15	70037.76	70018.77	69996.46
20	120	0	4	0.42	150	9356.754	4160.534	2801.101	1762.687	909.4625	L6				
21	120	0	6	0.45	300	19952.65	18868.19	15871.85	11164.92	L5					
22	120	50	2	0.42	150	9224.85	7165.818	6674.045	6135.114	5516.371	4904.287	4311.195	3301.373	2330.668	1804.888
23	120	50	4	0.45	300	11135.42	8328.303	5821.052	3018.262	L5					
24	120	50	6	0.39	500	72449.91	73177.9	73203.21	73201.85	73188.96	73177.77	73166.77	73151.04	73133.63	73117.84
25	120	100	2	0.45	300	5075.741	2677.961	877.0699	L4						
26	120	100	4	0.39	500	75544.05	76182.8	76193.829	76182.23	76163.68	76143.19	76123.04	76101.02	76078.14	76051.3
27	120	100	6	0.42	150	8543.567	7291.635	7356.193	7377.293	7174.221	7082.09	6946.651	6901.331	6772.331	6690.026
Asterisk * denoted one-way cyclic where $q_{cyc} < q_{mean}$ and liquefaction occurred during the cyclic shearing is denoted capital letter L and number (no of cyclic when liquefaction occurred)															

Table C.8: Summary for damping ratio responses at the end of each cycle under undrained triaxial cyclic loading

Row	q_{cyc} (kPa)	q_{mean} (kPa)	Freq. f (Hz)	e	$\sigma'_{3,0}$ (kPa)	Damping ratio (D) at the end each cycle								
						Cycles								
						1	2	3	4	5	6	7	8	9
1	40	0	2	0.39	150	0.050935	0.046069	0.04567	0.045452	0.045364	0.045251	0.045207	0.045174	0.045135
2	40	0	4	0.42	300	0.017898	0.014994	0.014766	0.014655	0.014591	0.014547	0.014514	0.014495	0.014485
3	40	0	6	0.45	500	0.012298	0.007267	0.006839	0.00665	0.006553	0.006482	0.006424	0.006385	0.006361
4*	40	50	2	0.42	300	0.016916	0.015622	0.015447	0.015356	0.01529	0.015238	0.015205	0.015191	0.01516

Row	q_{cyc} (kPa)	q_{mean} (kPa)	Freq. f (Hz)	e	$\sigma'_{3,0}$ (kPa)	Damping ratio (D) at the end each cycle								
						Cycles								
						1	2	3	4	5	6	7	8	9
5*	40	50	4	0.45	500	0.007989	0.006897	0.006682	0.006591	0.006529	0.00648	0.006455	0.006426	0.006404
6*	40	50	6	0.39	150	0.034337	0.036013	0.035729	0.035551	0.035448	0.035366	0.035298	0.035219	0.03515
7*	40	100	2	0.45	500	0.008509	0.007316	0.007082	0.006952	0.006879	0.006835	0.006788	0.006758	0.006729
8*	40	100	4	0.39	150	0.037607	0.038928	0.038461	0.038245	0.038098	0.037987	0.037883	0.037787	0.03774
9*	40	100	6	0.42	300	0.018559	0.01701	0.016809	0.016717	0.01666	0.016631	0.016595	0.016561	0.016555
10	80	0	2	0.39	300	0.050173	0.045593	0.045197	0.045046	0.044968	0.044899	0.044827	0.044797	0.044768
11	80	0	4	0.42	500	0.022814	0.019071	0.018762	0.018607	0.018534	0.018482	0.018439	0.018412	0.018384
12	80	0	6	0.45	150	0.333 (L)								
13	80	50	2	0.42	500	0.020045	0.018725	0.018525	0.018423	0.018346	0.018308	0.018272	0.018263	0.018235
14	80	50	4	0.45	150	0.333 (L)								
15	80	50	6	0.39	300	0.040842	0.037372	0.037067	0.03697	0.036878	0.036837	0.036811	0.036786	0.036734
16*	80	100	2	0.45	150	0.052936	0.059004	0.060659	0.062534	0.062668	0.061451	0.060915	0.052124	0.045105
17*	80	100	4	0.39	300	0.035502	0.034303	0.034059	0.033913	0.033833	0.033759	0.033711	0.033675	0.033646
18*	80	100	6	0.42	500	0.020432	0.019016	0.018796	0.018697	0.018623	0.018575	0.018545	0.018513	0.018489
19	120	0	2	0.39	500	0.038839	0.035715	0.035489	0.035405	0.03536	0.035312	0.035281	0.035258	0.03525
20	120	0	4	0.42	150	0.318078	0.176516	0.158128	0.111202	0.043656	L6			
21	120	0	6	0.45	300	0.203208	0.221633	0.264343	0.352587	L5				
22	120	50	2	0.42	150	0.150189	0.12458	0.126638	0.128357	0.129628	0.132771	0.135269	0.12021	0.103277
23	120	50	4	0.45	300	0.071259	0.067044	0.066338	0.071978	L5				
24	120	50	6	0.39	500	0.035163	0.032386	0.032175	0.032084	0.032045	0.032008	0.031979	0.031952	0.031937
25	120	100	2	0.45	300	0.039409	0.030782	0.014678	L4					
26	120	100	4	0.39	500	0.031074	0.028657	0.028483	0.028413	0.028378	0.028345	0.028331	0.028319	0.028306
27	120	100	6	0.42	150	0.114295	0.097503	0.099156	0.099188	0.096894	0.097743	0.095847	0.095778	0.096496

Asterisk * denoted one-way cyclic where $q_{cyc} < q_{mean}$ and liquefaction occurred during the cyclic shearing is denoted capital letter L and number (no of cyclic when liquefaction occurred)

Appendix D

Table D.1: Critical state results for 9 (isotropic sample) CV triaxial monotonic simulations (simplified Hertz-Mindlin contact model, G = 1.46 GPa, μ_s = 0.25, ϑ = 0.2 and periodic boundaries using LAMMPS).

Initial void ratio	$\sigma'_{3,0}$ (kPa)	Loading strain rate s^{-1}	Critical state results				
			ASR *(degree)*	M	p' (kPa)	q (kPa)	Z
0.383	150	1	18.89	0.73	5968.02	4355.37	5.14
0.429	150	1	18.85	0.72	1607.18	1164.08	4.30
0.452	150	1	18.67	0.72	289.68	207.82	3.58
0.377	300	1	18.81	0.72	6348.25	4588.36	5.21
0.424	300	1	19.27	0.74	2025.25	1502.07	4.42
0.445	300	1	19.03	0.73	640.08	468.51	3.87
0.372	500	1	18.67	0.72	7329.76	5254.04	5.32
0.417	500	1	18.79	0.72	2480.73	1791.05	4.52
0.439	500	1	19.04	0.73	880.46	644.85	4.01

Table D.2: Critical state results for 9 (isotropic sample) drained triaxial monotonic simulations (simplified Hertz-Mindlin contact model, G = 1.46 GPa, μ_s = 0.25, ϑ = 0.2 and periodic boundaries using LAMMPS).

Initial void ratio	$\sigma'_{3,0}$ (kPa)	Loading strain rate s^{-1}	*Critical state results*						
			Void ratio	*Vol. strain* (%)	ASR *(degree)*	M	p' (kPa)	q (kPa)	Z
0.383	150	1	0.453	5.1	18.59	0.71	198.42	141.63	3.49
0.429	150	1	0.454	1.7	18.77	0.72	199.04	143.49	3.51
0.452	150	1	0.454	0.2	19.04	0.73	200.02	146.43	3.51
0.377	300	1	0.450	5.2	18.77	0.72	398.18	287.20	3.69
0.424	300	1	0.449	1.8	19.03	0.73	400.02	292.77	3.71
0.445	300	1	0.449	0.3	18.75	0.72	397.97	286.69	3.71
0.372	500	1	0.444	5.2	18.80	0.72	664.01	479.59	3.87
0.417	500	1	0.444	1.85	19.06	0.73	667.47	490.26	3.92
0.439	500	1	0.444	0.4	18.68	0.72	659.73	473.21	3.84

Table D.3: Critical state results for 18 (anisotropic sample) CV triaxial monotonic simulations (simplified Hertz-Mindlin contact model, G = G = 1.46 GPa, μ_s = 0.25, ϑ = 0.2 and periodic boundaries using LAMMPS).

Initial void ratio	$\sigma'_{3,0}$ (kPa)	$\sigma'_{1,0}$ (kPa)	Loading strain rate s^{-1}	Critical state results				
				ASR *(degree)*	M	p' (kPa)	q (kPa)	Z
0.3825	150	200	1	19.46	0.75	5660.73	4244.62	5.17
0.3842	150	250	1	19.25	0.74	5566.63	4124.58	5.13
0.4235	150	200	1	18.84	0.72	2068.37	1497.50	4.44
0.4248	150	250	1	18.91	0.73	1985.81	1443.20	4.42
0.4485	150	200	1	19.17	0.74	457.82	337.64	3.75
0.4362	150	250	1	19.23	0.74	1172.56	867.61	4.13
0.3735	300	350	1	18.91	0.73	6961.66	5058.21	5.26
0.3770	300	400	1	18.75	0.72	6434.67	4633.68	5.23
0.4219	300	350	1	19.40	0.75	2202.14	1645.16	4.47
0.4176	300	400	1	18.93	0.73	2557.66	1861.01	4.53
0.4443	300	350	1	19.13	0.74	601.96	443.18	3.87
0.4424	300	400	1	19.37	0.75	741.17	552.92	3.95
0.3703	500	550	1	18.68	0.72	7364.52	5281.61	5.32
0.3675	500	600	1	18.75	0.72	7729.66	5567.57	5.36
0.4164	500	550	1	19.12	0.74	2594.01	1907.83	4.54
0.4147	500	600	1	18.46	0.71	2786.23	1972.75	4.59
0.4381	500	550	1	19.13	0.74	1030.87	758.75	4.06
0.4371	500	600	1	19.39	0.75	1064.56	794.67	4.11